ALKALINE CHEMICAL STABILITY AND ION TRANSPORT IN POLYMERIZED IONIC LIQUID ANION EXCHANGE MEMBRANES

A Dissertation

by

KELLY MARIE MEEK

Submitted to the Office of Graduate and Professional Studies of
Texas A&M University
in partial fulfillment of the requirements for the degree of

DOCTOR OF PHILOSOPHY

Chair of Committee,	Yossef A. Elabd
Committee Members,	Jodie L. Lutkenhaus
	Zheng-Dong D. Cheng
	Lei Fang
Head of Department,	M. Nazmul Karim

May 2016

Major Subject: Chemical Engineering

ABSTRACT

Non-platinum (low-cost), long-lasting, solid-state alkaline fuel cells (AFCs) require anion exchange membranes (AEMs) that have high alkaline chemical stability, high hydroxide ion conductivity, and adequate mechanical properties. In this study, polymerized ionic liquid (PIL) block copolymers were explored as a viable candidate for AFCs. PIL block copolymers are an emerging class of polymers that synergistically combine the benefits of both ionic liquids and block copolymers into one, where the former possesses a unique set of physiochemical properties and the latter self assembles into a range of nanostructures. More importantly, the potential to synthesize a vast array of new block copolymers is almost limitless with numerous IL cations and anions available.

PIL diblock copolymers were first synthesized at various compositions from an imidazolium-based ionic liquid monomer and a non-ionic monomer *via* reverse addition fragmentation chain transfer polymerization. Hydroxide ion conductivities were higher in the PIL diblock copolymers compared to the analogous PIL homopolymer due to the nanostructured morphology in the PIL diblock copolymers. This demonstrates the high hydroxide ion conductivity of PIL block copolymers.

Numerous PILs were then synthesized with various covalently attached cations (butylimidazolium, butylmethylimidazolium, trimethylammonium, butylpyrrolidinium, trimethylphosphonium) and various backbone/cation pairings (backbones: ethyl methacrylate, undecyl methacrylate, undecyl acrylate, styrene; covalently attached

cations: butylimidazolium, trimethylammonium, butylpyrrolidinium) and their alkaline chemical stability was carefully quantified with ^{1}H NMR spectroscopy. The styrene/butylpyrrolidinium pairing proved to be highly chemically stable, with no degradation in 20 meq of KOH at 60 °C for 168 h.

Considering the high hydroxide conductivities of PIL block copolymers, and the high alkaline chemical stability of the styrene/pyrrolidinium-based PIL, conductivity and chemical stability of a PIL block copolymer (ABCBA pentablock terpolymer) with a styrene/pyrrolidinium-based PIL block was investigated. A high hydroxide conductivity of 43.4 mS cm^{-1} at 60 °C in liquid water was achieved and no degradation or loss of conductivity was observed in the membrane after 168 h in 1 M KOH at 60 °C. PIL block copolymers utilizing a styrene/pyrrolidinium backbone/cation pairing in the PIL block represent a promising chemistry for producing highly conductive, chemically stable, robust AEMs for implementation in future solid-state AFCs.

ACKNOWLEDGEMENTS

First and foremost I thank my advisor, the world's best advisor, Professor Yossef A. Elabd. There is a quote which describes you perfectly: "My teacher thought I was smarter than I was, so I was." Because of your faith in me, I have grown more than I could have imagined as a scientist and researcher. I would also like to thank all of the past and present members of the Elabd research group, specifically Yuesheng Ye for his extensive training and mentoring, and Jacob Nykaza for numerous helpful conversations about work and non-work – Team Jelly for life! Thank you to the members of my dissertation committee, for taking time to meet and review my work. Many thanks to all of those who have collaborated with me on this project. Finally, thanks to all my friends and family for their support.

TABLE OF CONTENTS

Page

LIST OF FIGURES

Page

LIST OF TABLES

Page

LIST OF SCHEMES

Page

CHAPTER I

INTRODUCTION*

1.1 Alkaline Fuel Cells

Currently, there are more than 1.1 billion vehicles in the world, largely powered by internal combustion engines. Due to concerns about global pollution increase and the desire to be independent of fossil fuels, environmentally friendly alternative power sources are desirable. If a low-cost electric car with no greenhouse gas emissions could be produced and made broadly available, this would have a significant impact in reducing global CO_2 emissions. Currently, the only zero-emission vehicles available are electric vehicles powered by rechargeable lithium-ion batteries (*e.g.*, Tesla Model S) or hydrogen-fueled proton exchange membrane (PEM) fuel cells (*e.g.*, Toyota Mirai). Fuel cell electric vehicles have several advantages over battery electric vehicles for driving ranges greater than 300 miles, such as significantly lower vehicle weight, six-fold higher specific energy density, and instant re-fueling.

Although automakers have engineered solutions to many of the major hurdles to bringing fuel cell electric vehicles to the market place, the high cost due to the required precious metal platinum (Pt) electrodes is now one of the few major factors that has limited the mass commercialization of low-cost PEM fuel cell electric vehicles. However, alkaline

---

*Reprinted with permission from "Polymerized Ionic Liquid Block Copolymers for Electrochemical Energy" by K. M. Meek and Y. A. Elabd, 2015. *J. Mater. Chem. A*, 3, 24187, Copyright 2015 by The Royal Society of Chemistry.

fuel cells (AFCs) represent a viable alternative; AFCs produce high power densities at low operating temperatures (< 200 °C) and allow for the use of non-platinum electrodes (*e.g.*, nickel), thereby significantly reducing cost relative to PEM fuel cells.[1] An AFC, shown in Figure 1.1, converts hydrogen and oxygen fuels directly into electrical energy. At the anode catalyst, hydrogen oxidizes with hydroxide ions to produce water and electrons. Electrons travel through the circuit to provide the desired electricity,[2] and is reduced with oxygen and water at the cathode catalyst. At the cathode, hydroxide ions are produced and transport from the cathode to the anode; opposite of the direction of protons in a PEM fuel cell. The half-cell and overall reaction are listed here:

Anode: $2H_2 + 4OH^- \rightarrow 4H_2O + 4e^-$ (1.1)

Cathode: $O_2 + 4H_2O + 4e^- \rightarrow 4OH^-$ (1.2)

Overall: $2H_2 + O_2 \rightarrow 2H_2O$ (1.3)

A major drawback of the AFC is related to the use of the liquid potassium hydroxide (KOH) as the electrolyte, as the KOH solution is very sensitive to the presence of CO_2. When the liquid electrolyte is exposed to CO_2 fuel impurities, the hydroxide ions react to form solid potassium carbonate precipitates. These carbonate precipitates degrade catalyst performance, reduce ion conductivity, and block the pores of the diffusion layer to the catalyst sites, causing a severe decline in AFC performance and lifetime.[2]

This key limitation in the AFC may be overcome by using a solid polymer membrane as the electrolyte, *i.e.*, using a solid-state anion exchange membrane (AEM) to replace the liquid electrolyte eliminates leakage and carbonate precipitate issues that lead to fuel cell degradation.[2] An ideal AEM should have high alkaline chemical stability, hydroxide

conductivity, and CO_2 tolerance, while also being durable, mechanically strong, and flexible. There is currently no commercially available membrane material for the solid-state AFC, and thus there is significant motivation to develop highly conductive, chemically stable, robust AEMs and to cultivate a fundamental understanding of ion transport in these membranes, to advance the technology for long-lasting low-cost (non-platinum) AFCs.

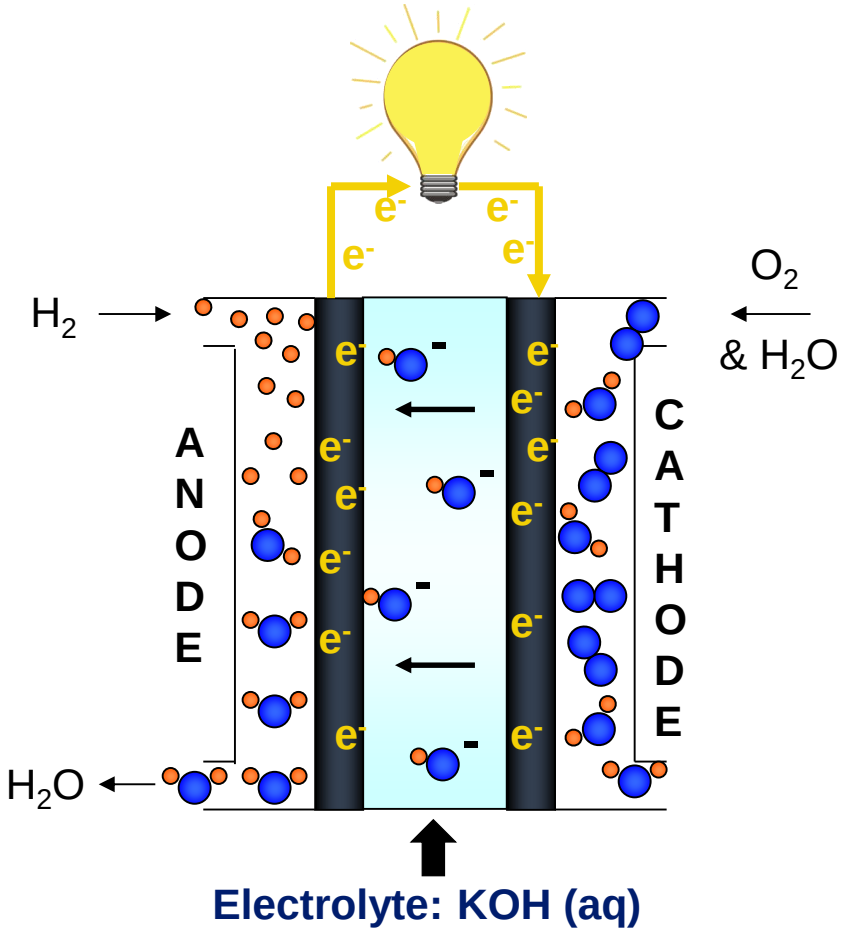

Figure 1.1 Diagram of the alkaline fuel cell (AFC).

1.2 AEMs for AFCs

Numerous AEMs have been developed as solid-state electrolytes for the AFC.[3-35] Currently, the most critical issue limiting the wide scale use of AEMs in the AFC is the alkaline chemical stability of the AEM in hydroxide (OH^-) form. Because of the high nucleophilicity and basicity of the OH^- ions produced in the AFC, a variety of known degradation pathways may be triggered in the AEM for the covalently tethered cationic groups and the polymer backbone. Achieving long-lifetime AFC performance will require that both the polymer backbone, as well as the attached cation, maintain long-term chemical stability in alkaline media at moderate temperatures (60 to 80 °C). Additionally, AEMs for AFC applications require sufficient hydroxide transport (*i.e.*, conductivities >10 mS cm^{-1}) and adequate mechanical properties (*i.e.*, limited membrane swelling from water sorption). Future investigations are required to determine the optimal backbone and cation pairings for long-term AEM stability in the presence of hydroxide, in conjunction with high hydroxide ion conductivity at moderate water uptakes, in order to achieve peak AFC performance and lifetime.

The benzyltrimethylammonium (BTMA) cation, advantageous for its ease of functionalization, high conductivity and thermal stability, and adequate short-term alkaline stability, has been the most ubiquitous cation in AEM chemistry.[17-23] Ultimately, BTMA will degrade in alkaline conditions over time, a major disadvantage, which has spurred consideration of alternative cations: imidazolium,[3-16] phosphonium,[26-29] guanidinium,[30-33] pyrrolidinium.[35,36] One popular measure of chemical stability of AEMs is to monitor ion conductivity over time for an AEM immersed in a concentrated alkaline

solution.[6-8,24,28] Hibbs[24] compared various cations on the polyphenylene backbone: BTMA, benzylic pentamethylguanidinum, benzylic N-methylimidazolium. BTMA had the highest ionic conductivity (18 mS cm^{-1}) and the least significant losses in ionic conductivity (~33% loss after 14 day in 4 M KOH at 90 °C) with a high ion exchange capacity (IEC) of 2.39 mmol g^{-1} and high water uptake of 159 wt%. Including a hexyl spacer between the polymer backbone and BTMA cation dramatically reduced the conductivity losses to only ~5% under the same conditions, while still providing a comparable ion conductivity (17.4 mS cm^{-1}) despite a slightly lowered IEC of 2.27 mmol g^{-1} and reduced water uptake of 126 wt%. These results indicate the potential for alkyl spacing between the tethered cation and polymer backbone to improve alkaline stability, as well as reduce water uptake in AEMs without hindering ion mobility. Yan and coworkers[29] found that an AEM with a bulky phosphonium-based cation, tris(2,4,6-trimethoxyphenyl)polysulfone-methylene quaternary phosphonium hydroxide, maintained a high ionic conductivity of at least 27 mS cm^{-1} for 48 h in 10 M KOH at room temperature and in 1 M KOH at 60 °C, at an IEC of 1.09 mmol g^{-1}. Coates and coworkers[28] demonstrated the high chemical stability and ion conductivity of polyethylene functionalized with a sterically crowded phosphonium cation, tetrakis(dialkylamino)phosphonium; the AEM maintained a high conductivity of 22 mS cm^{-1} over a 20 week period in 15 M KOH at 22 °C and conductivity decreased only slightly to 18 mS cm^{-1} over 22 days in 1 M KOH at 80 °C. Additional properties of the material included a high water uptake (~52 wt%) despite a relatively low IEC (0.67 mmol g^{-1}).

Further insights into chemical stability of the covalently attached cation have also recently been achieved in literature through the use of proton nuclear magnetic resonance (^{1}H NMR) spectroscopy to quantify degradation and identify degradation mechanisms of small molecule ionic salt analogs exposed to alkaline solutions.[10,11,21,35,37] Analogous salts are investigated instead of AEMs, because the polymer backbone typically weakens the ^{1}H NMR signal, making it difficult to determine the mechanism of cation degradation. Additionally, the degraded polymer may no longer be soluble in the same solvent as the non-degraded polymer, therefore making degradation analysis *via* ^{1}H NMR inaccurate. A few studies have successfully quantified AEM degradation with the use of NMR spectroscopy.[5,17,25,35,36,38] Holdcroft and coworkers[39] synthesized a poly(benzimidazolium)-type AEM with OH^- conductivities up to 13.2 mS cm^{-1}, and demonstrated notable chemical stability *via* ^{1}H NMR with no measurable degradation in 2 M KOH at 60 °C for 10 days. Nuñez and Hickner[17] established relatively high chemical stability of BTMA on a polystyrene-based backbone using ^{1}H NMR. Arges and Ramani[25] used 2-D NMR correlation spectroscopy to report on the chemical stability of five different cations tethered to a poly(sulfone) backbone: BTMA, 1,4-dimethylpiperazinium, trimethylphosphonium, 1-methylimidazolium, tris(2,4,6-trimethoxyphenyl)phosphonium. The piperazinium cation was the most chemically stable, followed by BTMA, while trimethylphoshonium and 1-methylimidazolium degraded rapidly in alkaline media.

Comparing the alkaline chemical stability of multiple cations on the same backbone at the same conditions is a useful technique for achieving the most accurate assessment of

cation stability. An additional report by Arges and Ramani[38] took a similar approach to compare poly(sulfone) backbone chemical stability, as opposed to cation stability, *via* 2-D NMR correlation spectroscopy and found that despite the relatively stable nature of poly(sulfone), functionalization with fixed cation groups triggers rapid backbone degradation. Accurate relative cation stability through comparisons of several cation types on the same polymer backbone under the same degradation conditions has been achieved by only a few studies.[24,25,35,36] Accurate relative polymer backbone stability by comparison of several backbone types with the same tethered cations under the same degradation conditions remains relatively unexplored. Additionally, a correlation has yet to be established between alkaline chemical degradation of small molecule cations and of AEMs with the same corresponding covalently linked cation. The usefulness of past and future small molecule ionic salt degradation studies as tools for predicting relative cation stability in AEMs is dependent upon proof of a correlation, by means of a tandem study comparing free cation and polymeric cation chemical stability. The usefulness of AEM degradation studies for determining relative alkaline chemical stability between different AEM chemistries is dependent upon a comprehensive study comparing several cation types tethered to the same polymer backbone type and comparing several polymer backbone types with the same tethered cation, all under the same degradation conditions. This study seeks to fill the significant gaps remaining in AEM chemical stability literature by comparing multiple polymer backbone/cation pairings, as well as analogous ionic salts, to determine the most promising chemistries for AEMs for AFCs.

1.3 Polymerized Ionic Liquid Block Copolymers as AEMs

In addition to requiring high conductivity and chemical stability, electrochemical devices, such as AFCs, also require electrolyte films to be robust. Polymerized ionic liquid (PIL) block copolymers are a unique class of block copolymers that combine the benefits of both ionic liquids (ILs) and block copolymers to provide a unique opportunity for achieving robust, highly hydroxide-conductive AEMs. ILs are salts composed of an organic cation and an organic or inorganic anion, which typically have a melting point below 100 °C; they are also referred to as room temperature ionic liquids (RTILs), when the melting point is below room temperature. ILs possess unique physiochemical properties, such as negligible vapor pressure, non-flammability, a wide electrochemical window, high ionic conductivity, high chemical and thermal stability, and a broad chemical diversity owing to a large number of cations and anions available that can form ILs. In 1998, Ohno[40] reported on the first polymerized ionic liquid (PIL): a polymeric form of an IL, where the cations of the IL are covalently attached to each monomeric unit of the polymer chain and are neutralized by mobile anions. Unlike other ion-containing polymers that are typically constrained to high glass transition temperatures due to strong electrostatic ion pair interactions, PILs can possess low glass transition temperatures due to weak electrostatic ion pair interactions, while maintaining high charge densities.[41] Unlike ILs where both cations and anions are mobile in a liquid phase, polymerization of an IL monomer results in a single-ion (anion) conductor, where the cations are covalently attached to the polymer chain.

PILs have a limited range of mechanical properties, and thus PIL block copolymers emerged as a new material that can possess orthogonal properties, such as high modulus (from the non-ionic polymer) and high conductivity (from the ionic polymer or PIL) through the self-assembly of two distinct polymers into well-defined nanostructures of long-range order (*e.g.*, body-centered-cubic spheres, hexagonal cylinders, bicontinuous gyroid, lamellae) with tunable morphology and domain size. An example chemical structure of a PIL block copolymer is shown in Figure 1.2 including a variety of typical cations and anions that have been investigated, where, to date, imidazolium has been the most frequently explored cation. The first PIL block copolymer was reported by Waymouth, Gast, and coworkers[42,43] in 2004. More recently, there has been an increasing number of publications on PIL block copolymers.[4,15,16,27,34,44-73] Although some block copolymers containing covalently attached ammonium cations can be classified as PIL block copolymers, they have typically not been referred to as PIL block copolymers in the literature and therefore are not discussed in detail here.

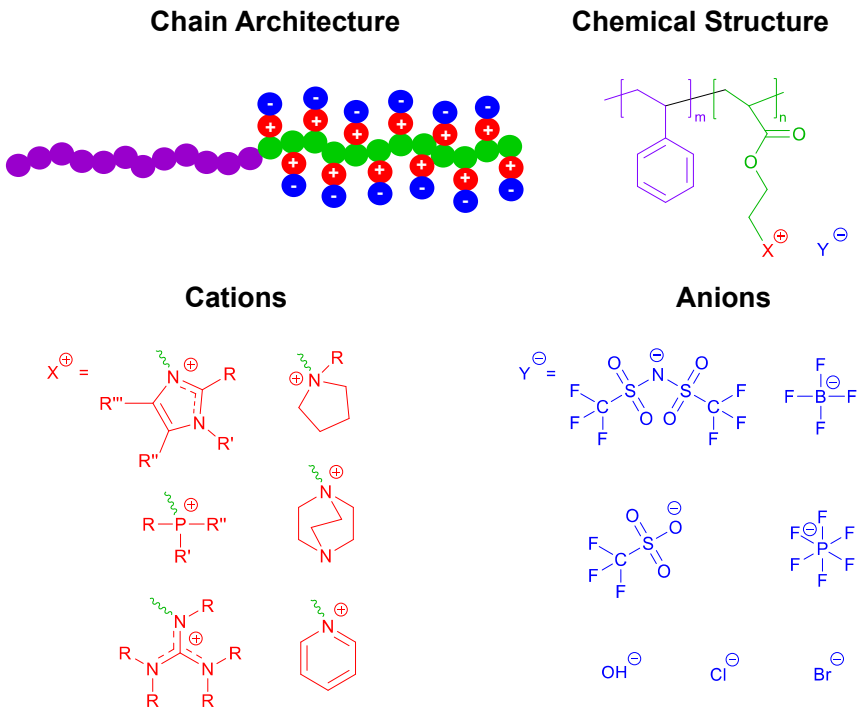

Figure 1.2 PIL block copolymer: (upper left) illustration of polymer chain architecture, (upper right) example chemical structure, (lower left) example cations, (lower right) example anions.

To date, investigators have explored the solution properties of PIL block copolymers, such as micelle behavior[42,43,50,51,55,57,70] and stimuli-responsive behavior,[51,52,55,57,70] and solid-state properties, such as ion and gas transport,[27,34,44-46,48,53,54,56,60,63,64,69] thermo-mechanical properties,[46] and magnetic properties.[49,59] A key interest in PIL block copolymers is not only the combination of PIL and block copolymer properties in one material, but also the ability to significantly impact properties through subtle chemical changes (*e.g.*, *via* anion exchange). This provides an excellent chemical platform to investigate PIL block copolymers as AEMs for AFCs, the topic of this work. The sections

below highlight recent literature findings on the synthesis and properties of PIL block copolymers.

1.3.1 PIL Block Copolymer Synthesis

Table 1.1 lists various controlled polymerization techniques (*e.g.*, NMP, RAFT, anionic, CMRP, ROMP, ATRP) that have recently been explored to prepare PIL block copolymers.[4,15,16,27,34,42-73] Within these techniques, generally two overarching strategies have been used to produce PIL block copolymers: the sequential polymerization of multiple non-ionic monomers followed by subsequent functionalization or quaternization of one of the monomers[4,16,27,42-44,56,59,60,68,69] and the direct sequential polymerization of a non-ionic monomer and an IL monomer.[15,34,45-55,57,58,61-67,70-73] The former allows for facile molecular weight determination of the non-ionic precursor block copolymer with conventional techniques, such as gel permeation chromatography (GPC). The latter requires the addition of salt to minimize the aggregation of the charged polymer in solution when using techniques such as GPC.[41,74,75] For both strategies, a wide range of cations and anions can be explored, where a variety of anions can easily be accessed *via* simple ion exchange of the PIL block copolymer. Here, we briefly highlight various chemistries from each of the polymerization techniques shown in Table 1.1.

Table 1.1 Examples of PIL block copolymers and their polymerization techniques

Polymerization Techniques	Example Structures	References	Additional References
Nitroxide-mediated polymerization (NMP)	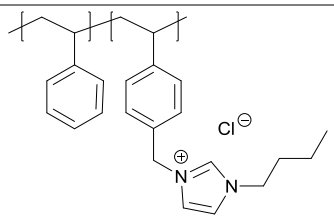	34	42-47
Reversible addition-fragmentation chain transfer (RAFT)	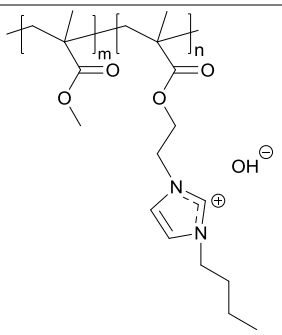	15,48	4,16,27,49-58
Anionic	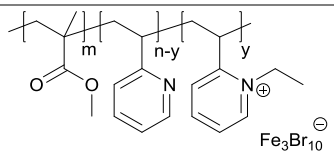	59	60
Cobalt-mediated radical polymerization (CMRP)	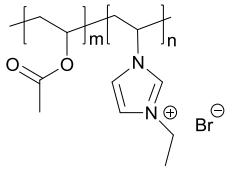	61	62
Ring opening metathesis polymerization (ROMP)	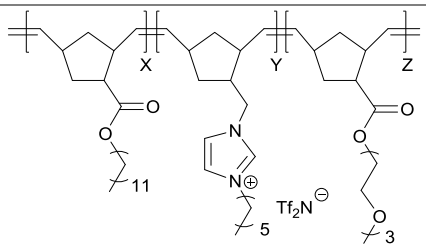	63	64-68
Atom transfer radical polymerization (ATRP)	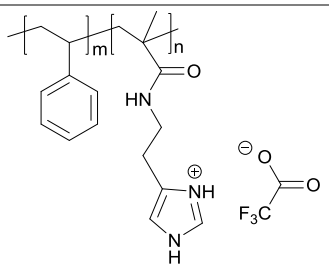	69	70-73

Nitroxide-mediated free radical polymerization (NMP) has been used to synthesize several PIL block copolymers.[34,42-47] In fact in 2004, the first PIL block copolymer was synthesized *via* NMP by Waymouth, Gast, and coworkers.[42,43] In this study, NMP was used to polymerize styrene and subsequently grow poly(chloromethylstyrene) (PCMS), followed by post-functionalization with 1-methyimidazole and anion exchange from chloride (Cl^-) to tetrafluoroborate (BF_4^-). Recently, Balsara and coworkers[34] (see structure in Table 1.1) and others[44,46] have reported on the synthesis of PIL diblock copolymers similar to Waymouth, Gast, and coworkers[42,43] with a variety of cations and anions. Recently, Long and coworkers[45] were the first to report on the synthesis of a phosphonium-containing PIL triblock copolymer using NMP from the polymerization of a phosphonium-based ionic liquid monomer.

Reversible addition-fragmentation chain transfer (RAFT) polymerization has been the most frequently used technique for producing PIL block copolymers.[4,15,16,27,48-58] Mecerreyes, Taton, Gnanou, *et al.*[50] reported on the first use of RAFT to synthesize a PIL block copolymer. More recently, Elabd and coworkers[15,48,54] synthesized imidazolium-containing methacrylate-based PIL block copolymers at various compositions by first polymerizing methyl methacrylate (MMA) as the macro chain transfer agent (macro-CTA), followed by copolymerization with an ionic liquid methacrylate monomer with a tethered butylimidazolium (BIm^+) cation and mobile bromide (Br^-) anion. In the resulting PIL block copolymer, poly(MMA-*b*-MEBIm-Br), Br^- was ion exchanged to other anions, such as the fluorinated anion bis((trifluoromethyl)sulfonyl)-imide ($TFSI^-$),[54] as well as the hydrophilic anion hydroxide (OH^-) (see structure in Table 1.1).[15,48] Elabd and coworkers[56]

also produced a similar PIL block copolymer, where the non-ionic block was styrene instead of MMA and the imidazolium-based cation was tethered *via* post-functionalization of the non-ionic precursor block copolymer instead of polymerization of the IL monomer. Similarly, Balsara and coworkers[27] used RAFT to synthesize a styrene-based PIL block copolymer with a phosphonium-based cation.

Garcia and coworkers[59,60] used anionic polymerization to synthesize poly(styrene-*b*-2-vinylpyridine) (PS-*b*-P2VP) followed by post-functionalization with 1-ethyl-2-vinylpyridine (see structure in Table 1.1). Br^- was ion exchanged to $TFSI^-$, nonafluoro-1-butanesulfonic acid ($CF_3(CF_2)_3SO_3^-$),[60] as well as iron bromide ($Fe_3Br_{10}^-$)[59].

Taton and coworkers[61] introduced a new family of PIL block copolymers based on poly(N-vinyl-3-ethylimidazolium bromide) (PVEtImBr) and poly(vinyl acetate) (PVAc) by sequential cobalt-mediated radical polymerization (CMRP) (see structure in Table 1.1). In addition to obtaining PVAc-*b*-PVEtImBr diblock copolymers, synthesis of PVAc-*b*-PVEtImBr-*b*-PVAc triblock copolymers was achieved by radical coupling of parent diblocks in the presence of coupling agent isoprene. Taton and coworkers[62] also produced a similar PIL diblock copolymer with poly(N-vinyl-3-butylimidazolium bromide) (PVBImBr) as the PIL using a commercially available controlling agent.

Ring opening metathesis polymerization (ROMP) has recently been used by Gin and coworkers[64] to synthesize a norbonene and alkylimidazolium-based PIL block copolymer with the aid of a Grubbs' first-generation catalyst. Further research from this group yielded the first ABC PIL triblock copolymer, based on norbonene backbones, with alternating hydrophobic–ionic-hydrophilic substituents (see structure in Table 1.1).[63] More recently,

Nishide and coworkers[67] used ROMP and a Grubbs' third-generation catalyst to yield a norbornene-based PIL block copolymer with a redox-active block and an ethylimidazolium-containing PIL block.

Atom transfer radical polymerization (ATRP) is another relatively popular route to produce PIL block copolymers.[69-73] Segalman and coworkers[69] synthesized poly(styrene-*b*-histamine methacrylamide) (PS-*b*-PHMA) diblock copolymers *via* ATRP using the activated ester strategy, followed by post-functionalization with trifluoroacetic acid (TFA) resulting in the protic diblock copolymer, PS-*b*-PIL (see structure in Table 1.1). More recently, ATRP was utilized by Matyjaszewski and coworkers[72] to produce ABA PIL triblock copolymers with either polyketone (PEEK) or polysulfone (PAES) center blocks and butylimidazolium-containing PIL outer blocks. An ABA PIL triblock copolymer was also synthesized by Tenhu and coworkers[73] with a poly(N-isopropyl acrylamide) (PNIPAm) center block and styrenic outer blocks functionalized with methylimidazole.

1.3.2 PIL Block Copolymer Solid-State Conductivity-Morphology Properties

Block copolymers are known to self-assemble into a wide range of nanostructured morphologies based on the incompatibility between the different polymers that are covalently attached to one another. For PIL block copolymers in the solid-state, these self-assembled morphologies result in robust films that can accelerate the transport of ions and small molecules within continuous PIL nanostructured channels. The PIL chemistry within these channels offers unique physiochemical property advantages, such as high electrochemical stability for specific ions (*e.g.* hydroxide, lithium). The transport of these

ions is of particular interest as it applies to PIL block copolymers as electrolyte separators in membrane-based AFCs and solid-state lithium-ion batteries. Although the fuel cell and battery performance has been demonstrated with block copolymers and PILs as the solid-state electrolyte separator,[76-83] there have been no papers to date that show fuel cell or battery performance with a PIL block copolymer. Since PIL block copolymers conjoin the properties of both PILs and block copolymers, future fuel cells and batteries containing this material will be of high interest. Here, we highlight findings with regard to conductivity-morphology relationships in solid-state PIL block copolymers as these properties apply to AFC and lithium-ion battery performance.

1.3.3 Water-assisted Ion Transport (Membrane-Based AFCs)

For AFCs, solid-state single ion conductor PIL block copolymer AEMs that achieve high hydroxide conductivity under wet conditions are of interest. Additionally, other model hydrophilic mobile anions (*e.g.*, Br^-, Cl^-) have been investigated. The transport of hydrophilic anions in PIL block copolymers is dictated by a water-assisted process, where the conductivity is a strong function of water content and follows an Arrhenius behavior as a function of temperature.[4,15,27,34,48,54]

Elabd and coworkers[48] evaluated the Br^- and OH^- conductivity of methacrylate-based, butylimidazolium containing PIL block copolymers, poly(MMA-*b*-MEBIm-Br) and poly(MMA-*b*-MEBIm-OH). At a fixed PIL composition of 17.3 mol%, the Br^- and OH^- conductivity of PIL block copolymer was an order of magnitude higher than its analogous PIL random copolymer (at the same PIL composition and water content). The difference

in conductivity was attributed to the strong microphase separated lamaller morphology in the PIL block copolymer, where no microphase separation was observed in the PIL random copolymer. The Br^- and OH^- conductivity of the PIL copolymer was also higher than the PIL homopolymer (control) (shown in Figure 1.3) at the same experimental conditions, even though the homopolymer possessed a higher PIL composition (100 mol%) and a 2-fold higher water content compared to the block copolymer. These results were unique and suggest that PIL microdomains accelerate water-assisted ion transport compared to bulk PIL homopolymers.

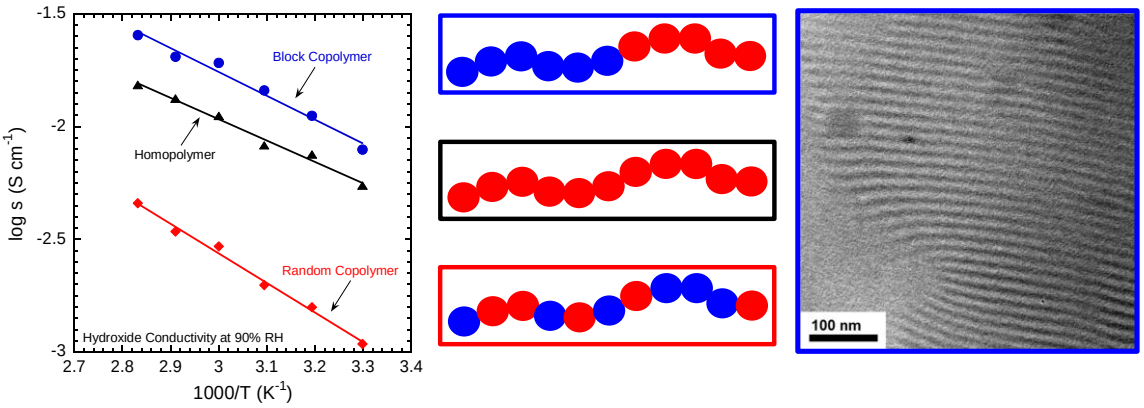

Figure 1.3 PIL block copolymer, PIL homopolymer, PIL random copolymer from ref. [48]: (left) hydroxide conductivity, (middle) illustration of polymer chain architectures, (right) transmission electron micrograph of PIL block copolymer. Figure adapted from ref. [48].

Elabd and coworkers[4] investigated a similar PIL block copolymer with a longer alkyl spacer chain between the tethered imidazolium cation and the methacrylate backbone (11 carbon chain versus 2 carbon chain from previous study). Similarly, a high Br^- conductivity was measured, which was 3-fold higher than its analogous PIL homopolymer

and an order of magnitude higher than the shorter-chain PIL block copolymer from the previous studies despite similar chemistry, similar ion exchange capacity (IEC), similar morphology, and higher water content (shown in Figure 1.4).

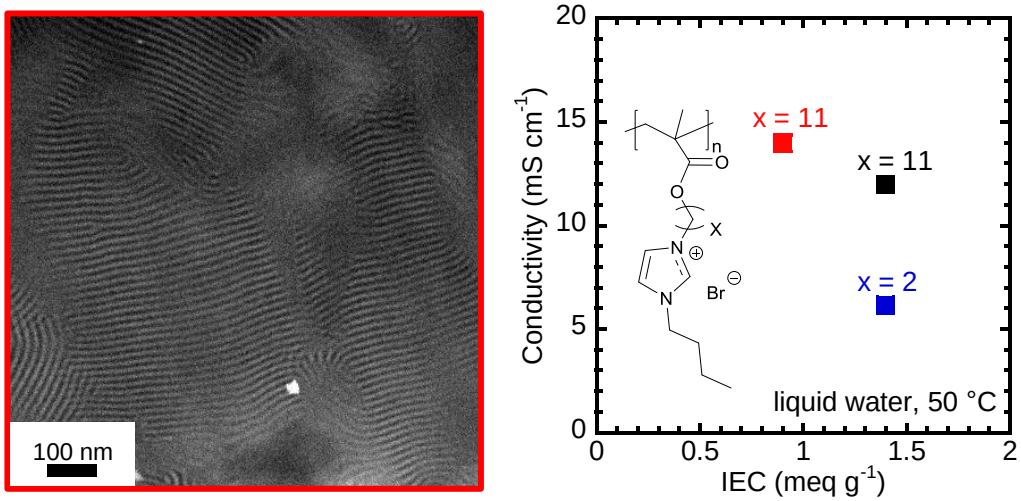

Figure 1.4 PIL block copolymers from refs. [4,15,16,48] comparing long (x=11) and short (x=2) alkyl spacer chain lengths between imidazolium and backbone: (left) transmission electron micrograph, (right) bromide ion conductivity. Figure adapted from ref. [16].

Balsara and coworkers[34] used NMP to produce butylimidazolium- and trimethylammonium-functionalized PIL diblock copolymers over a range of molecular weights and volume fractions. Lamellar morphology was obtained for both bound cations at all volume fractions; domain size of the imidazolium polymer was slightly larger, while the scaling of domain size with chain length showed weak dependency on the nature of the bound cation. Overall, the choice of bound cation had limited effect on the self-assembly, water uptake, and ionic conductivity of the PIL block copolymers. Cl^- conductivity of the membranes was measured in liquid water as a function of temperature

(from 25 to 40 °C), and was found to be ~10^{-2} S cm^{-1} for both cations at higher temperature, although the imidazolium AEM took longer to equilibrate. OH^- conductivity was also measured and was higher than Cl^- conductivity. Similar results were obtained by Elabd and coworkers, where OH^- conductivity exceeded Br^- conductivity.

Balsara and coworkers[27] also produced diblock copolymers of the precursor poly(styrene-*b*-bromoethyl acrylate) *via* RAFT and post-functionalized with a tributylphosphonium cation; overall molecular weights ranged from 31 to 87 kg/mol with a fixed volume fraction of the PIL block of ~0.57. These PIL block copolymers self-assembled into lamellar morphologies with domain sizes increasing with molecular weight. Br^- ion conductivity and water uptake were measured in samples equilibrated in liquid water; conductivity increased 3-fold with a 2-fold increase in domain size, while water uptake was unaffected by domain size. Overall, high conductivity at relatively low water uptake was achieved as a result of the butyl substituents on the pendant phosphonium cations, which provided a somewhat hydrophobic nature to the cation.

1.3.4 Dry Ion Transport (Lithium-Ion Batteries)

In addition to being suitable AEMs for AFCs, PIL block copolymers, with chemistry that is widely tunable *via* anion exchange, also make suitable electrolytes for applications requiring dry ion transport, such as lithium-ion batteries. Replacing liquid-based electrolytes with PIL block copolymers as solid-state polymer electrolytes (SPEs) can alleviate safety and stability concerns, while in turn offering desirable properties, such as thin-film forming ability, flexibility, and transparency.[84] The ideal SPE for a solid-state

battery would have the high ionic conductivity of a liquid (for high overall storage capacity/energy density), mechanical properties of a solid (for improved stability and cyclability), and the formability of a thermoplastic (for good processability). Through the use of PIL block copolymers as SPEs for lithium ion batteries, one of the block components can solvate (*i.e.*, dissolve) lithium salt to provide a continuous, nanoscopic, ion-conductive pathway, while the other block component provides mechanical rigidity in an ordered nanostructured morphology. Therefore, lithium ion conductive block copolymers conjoin the desired multicomponent properties of high ionic conductivity, robust mechanical properties, and good film forming properties, within a unique nanoscale morphology.[77,79,85-87]

To date, the focus of the ion conductivity studies in PIL block copolymers for lithium-ion battery application has focused on fluorinated counter anions (*e.g.*, $TFSI^-$, PF_6^-, BF_4^-) and not systems that contain lithium salt. However, many common lithium salts used in SPEs are compatible with imidazolium salts and therefore systems with added lithium salt represent an area for future exploration. Typically, when the counter anions in a PIL are fluorinated, this results in a hydrophobic polymer, where ion transport is dictated by the segmental dynamics of the polymer chains (Vogel-Fulcher-Tammann (VFT) behavior).[41]

Mahanthappa and coworkers[44] functionalized a series of poly(styrene-*b*-4-vinylbenzyl chloride) precursors at various compositions (2.7-17.0 mol%) using NMP and subsequently post-functionalized with alkylimidazolium (methyl, butyl, hexyl) cations followed by ion exchange with $TFSI^-$ anions. These PIL block copolymers microphase separated into various morphologies: cylinders, lamellae, and coexistence of cylinders and

lamellae with varying degrees of long-range order depending on composition and film preparation technique. $TFSI^-$ conductivity was highly dependent on PIL composition, morphology type, and degree of long-range order. Specifically, a single PIL block copolymer at 8.6 mol% PIL composition exhibited an order of magnitude difference in conductivity when comparing two different film processing techniques (solvent cast versus melt pressing) resulting from differences in long-range ordered morphologies. Morphology factors (conductivity normalized by PIL homopolymer conductivity and block copolymer PIL volume fraction) approached 0.6 for lamellar samples. Overall, these results indicated the importance of PIL microdomain connectivity and long range ordered morphologies as it relates to ion conductivity.

Long and coworkers[46] reported on a PIL ABA triblock copolymer synthesized *via* NMP with styrene end blocks and a styrenic imidazolium functionalized mid-block with $TFSI^-$ anions. Films with a modulus of 100 MPa were achieved and conductivity followed a VFT behavior with temperature. Conductivity approaching 20 mS/cm at 150 °C was achieved when 40 wt% IL was added to the films. A microphase separated morphology without long-range order was measured. Wang and coworkers[53] synthesized PIL ABA triblock copolymers with a fluorinated mid-block of poly(vinylidene fluoride-co-hexafluoropropylene) and methacrylate-based imidazolium end blocks over a range of molecular weights and compositions. No microphase separation was observed due to the compatibility of between the PIL with fluorinated anions and the fluoropolymer mid-block. Temperature-dependent conductivity scaled with VFT behavior and the

conductivity of $TFSI^-$ was higher than BF_4^- due to faster polymer chain segmental dynamics (*i.e.*, lower glass transition temperature (T_g)).

Elabd and coworkers[54] synthesized a series of PIL diblock copolymers *via* RAFT polymerization with methyl methacrylate (MMA) blocks and methacrylate imidazolium-based PIL blocks with $TFSI^-$ counter anions at various PIL compositions. The ionic conductivities of the PIL block copolymers were approximately 2 orders of magnitude higher than their analogous PIL random copolymers at similar PIL compositions. The PIL block copolymers exhibited weakly microphase-separated morphologies with no evident long-range periodic structure, while the PIL random copolymers revealed no microphase separation. The higher conductivity in the block copolymers was attributed to the microphase-separated morphology, as significant differences in conductivity were still observed even when differences in glass transition temperature were considered. Interestingly, strong-microphase separated morphology was not a requirement for significant enhancements in conductivity, suggesting that local confinement and connectivity of nanoscale ionic domains in PIL block copolymers also impact conductivity. Contrastingly, Elabd and coworkers[56] compared these results to a strong microphase-separated PIL diblock copolymer with styrene (S) and acrylate imidazolium-based PIL blocks at various PIL compositions. At comparable PIL composition, the S-based PIL block copolymer with strong microphase separation exhibited ~1.5−2 orders of magnitude higher ionic conductivity than the MMA-based PIL block copolymer with weak microphase separation. Similar to the results shown by the Mahanthappa and coworkers[44], various morphology types were observed as a function of PIL content:

hexagonally packed cylinders, lamellae, coexisting lamellae and network. Conductivity increased with PIL content, as morphology transitioned from 1-D hexagonally packed cylinders to 2-D lamellae to a coexisting 2-D lamellae and 3-D continuous network (see Figure 1.5). Morphology types, and subsequently conductivity of these solution-cast membranes, were also found to be dependent on the solvent casting conditions. Overall, the strongly segregated S-based PIL block copolymers exhibited improved transport properties over the PMMA-based PIL block copolymers signifying the impact of the strength of microphase separation on conductivity.

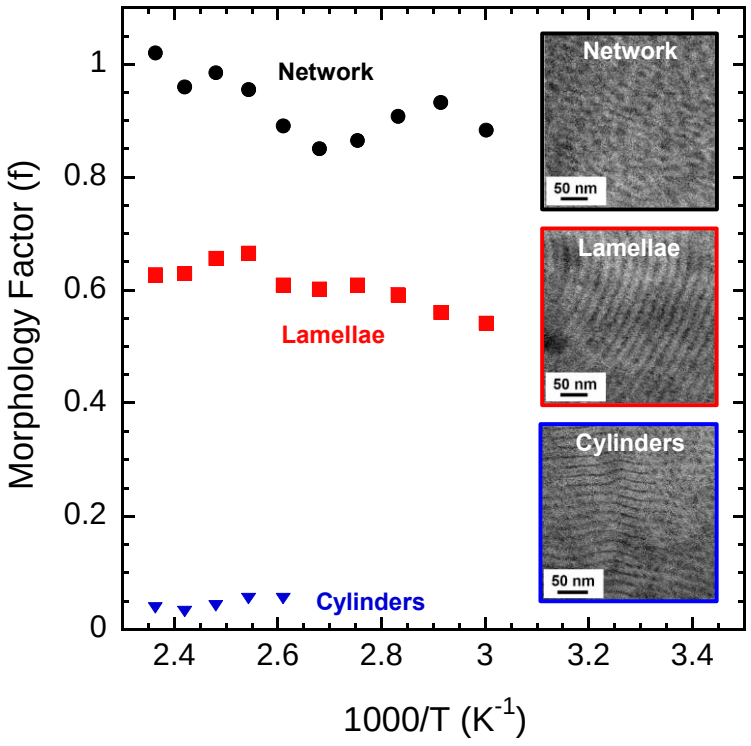

Figure 1.5 Temperature-dependent morphology factor (normalized ionic conductivity) of PIL diblock copolymers from ref. [56]. Figure adapted from ref. [56].

Segalman and coworkers[69] used ATRP to synthesize poly(styrene-block-histamine methacrylamide), PS-*b*-PHMA, which was subsequently treated with trifluoroacetic acid (TFA) to form a protic PIL diblock copolymer. Hexagonally packed cylindrical morphologies were observed for 8 to 20 wt% PHMA, whereas lamellar morphologies were observed in samples containing 32 to 54 wt% PHMA; domain size increased 20-30% with the addition of TFA. Conductivity of the PIL diblock copolymer increased with increasing microdomain channel size (see Figure 1.6), an atypical result, as usually only volume fraction of conducting domains directly affects conductivity. This result suggests that reduced domain size may hinder ion mobility.

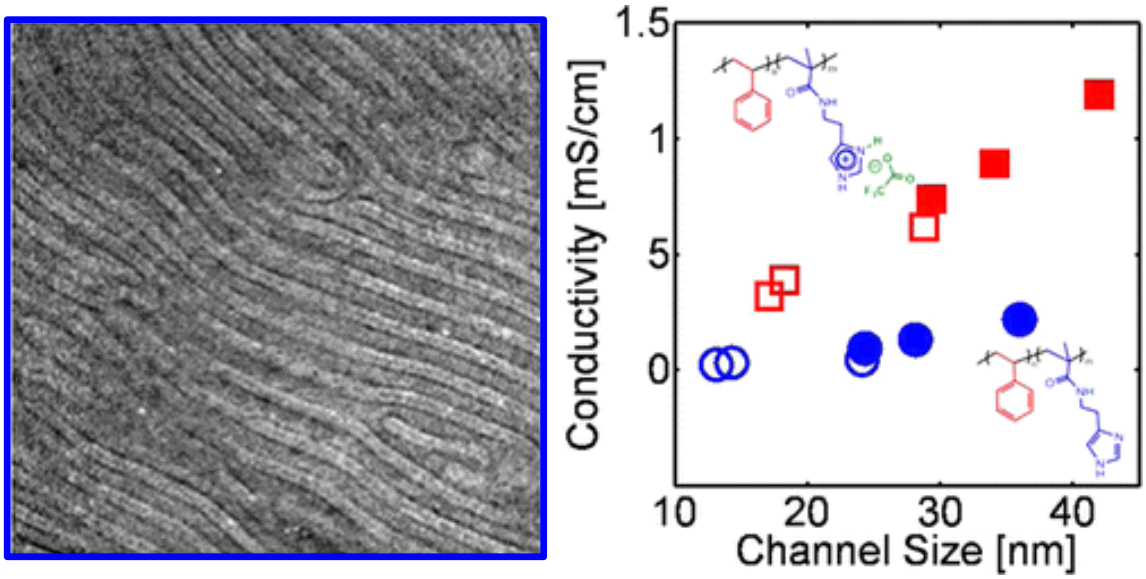

Figure 1.6 (left) Transmission electron micrograph and (right) conductivity versus microdomain channel size of PIL diblock copolymers (squares) and non-ionic precursor diblock copolymers (circles) from ref. [[69]]. Open and closed symbols refer to 33 and 53 wt% of PHMA block, respectively. Figure adapted from ref. [69].

In summary, for work focused on dry fluorinated anion transport (*e.g.*, $TFSI^-$, BF_4^-), the morphology type, extent of long-range order, strength of microphase separation, processing conditions, and glass transition temperature of the PIL have all been shown to have a significant impact on ion conductivity in PIL block copolymers. Network morphology resulted in increased conductivity relative to lamellae,[56] while PIL block copolymers with hexagonally packed cylindrical morphologies exhibited poor ionic conductivity potentially due to increased defects and grain boundaries.[44,56] Increasing long-range order through processing conditions was shown to improve ion conductivity.[44,56] Faster segmental chain motion, and in turn higher conductivity, was achieved through a lower T_g in the PIL microdomain.[53]

PIL block copolymers represent an exciting opportunity for applications that require dry ion transport, as well as water-assisted transport. Only subtle changes in the chemistry were required to transition between these two modes of transport, and increase the potential applications of the material. Continuing along this theme, it may be possible to employ additional subtle changes in the chemistry of PIL block copolymers to open the door to a vast array of applications suitable for ion conducting polymer (*e.g.*, gas separations, drug delivery, electrodialysis, bipolar membranes, capacitors).

1.4 Outline and Summary

In this study, AEMs were developed for electrochemical applications; PILs and PIL block copolymers as AEMs for AFC applications were of particular interest. It is imperative that AEMs for AFCs have both high ion conductivity and high alkaline

chemical stability. The transport properties, self-assembled morphology, and alkaline chemical stability of these AEMs were investigated. Significant progress was achieved in the optimization of AEM chemistry for attaining the desired transport and membrane stability properties.

The versatility in synthesis of PIL block copolymers allows for the inclusion of numerous cations and anions, as well as a broad range of molecular weights and compositions. The careful selection of these parameters results in PIL block copolymer where the morphology and ionic conductivity can be tailored in the solid-state; this is of high interest as it relates to developing electrolyte separators for AFCs. For PIL block copolymer work focused on water-assisted ion transport (*e.g.*, OH^-, Br^-, Cl^-) for AFCs, microphase separated morphology of the PIL block copolymer allows the conductivity to exceed that of its analogous PIL random copolymer,[48] as well as its analogous PIL homopolymer,[4,48] owing to increased transport as a result of ion confinement in PIL nanochannels. Thus, PIL block copolymers are of substantial interest as AEM material components in AFCs. Specifically, the future opportunity to explore a richer set of chemistries and therefore properties for PIL block copolymers is promising. Numerous chain sequences (*e.g.*, AB, ABA, ABC, ABCBA), monomers, functional groups and cation/anion combinations can be considered, all leading to a larger set of block copolymers with unique PIL properties to be explored. This study utilizes the flexibility within PIL block copolymer chemistry to optimize AEM chemistry and produce membranes with desirable properties for AFCs. Within this study, chain sequences were varied: PIL diblock copolymers, as well as PIL pentablock terpolymers, are investigated.

A variety of monomers were examined for optimizing AEM backbone chemistry: ethyl methacrylate, undecyl methacrylate, undecyl acrylate, and styrene. Note, to date, most PIL block copolymers contain imidazolium as the cation, though there are many more cations in the IL family. Within this work, numerous other cations were explored: trimethylammonium, trimethylphosphonium, pentamethylguanidinium, butylpyrrolidinium, methylpyrrolidinium. This vast set of backbone/cation combinations provided the unique opportunity to synthesize PIL block copolymers where many properties can be significantly altered with subtle chemical changes, *e.g.*, mechanical properties, hydrophilicity, ion conductivity, morphology (morphology type, long-range order, strength of microphase separation), to achieve the desirable AEM properties of high conductivity, high chemical stability, low water uptake, and high mechanical strength.

Chapter II is a study of the bromide and hydroxide transport-morphology relationship in PIL diblock copolymers functionalized with butylimidazolium cations at various PIL compositions, in relation to ion transport in their analogous PILs. Chapter III investigates the alkaline chemical stability of a set of ethyl methacrylate-based PILs with five different cation types: butylimidazolium, butylmethylimidazolium, trimethylammonium, butylpyrrolidinium, trimethylphosphonium. The alkaline chemical stability of these PILs was examined in tandem with their analogous ionic salts: 1-butyl-3-methylimidizolium chloride, 1-butyl-2,3-dimethylimidazolium chloride, tetramethylammonium chloride, benzyltrimethylammonium chloride, 1,1-butylmethylpyrrolidinium chloride, tetramethylphosphonium chloride. In Chapter IV, the stability analysis was expanded to compare the alkaline chemical stability and transport properties of a total of twelve PILs

with ethyl methacrylate, undecyl methacrylate, undecyl acrylate, and polystyrene-based backbones with various covalently attached cations: butylimidazolium, trimethylammonium, butylpyrrolidinium.

In addition to achieving high ion conductivity and high alkaline cation and backbone chemical stability, AEMs that are robust and resistant to carbonation (*i.e.*, conversion of the mobile hydroxide anion to carbonate and bicarbonate forms) are desirable for maintaining optimal hydroxide transport. Chapter V examines ion transport and alkaline chemical stability, as well as AEM carbonation, of a mechanically robust PIL multiblock polymer with a methylpyrrolidinium cation.

Because of the widely tunable chemistry of PIL block copolymers, significant changes in physical properties can be achieved *via* subtle changes in chemistry, allowing for the use of PIL block copolymers in additional electrochemical applications outside of AFCs (*e.g.*, Li-ion batteries, gas separations, *etc.*). In Chapter VI, the synthesis and property characterization of a novel sulfonated PIL diblock copolymer, containing both sulfonated blocks and PIL blocks with both mobile cations and mobile anions, is presented; this material represents an exciting new opportunity in PIL block copolymers for applications which take advantage of the use of both mobile cations and mobile anions (*e.g.*, drug delivery, electrodialysis, bipolar membranes, solid-state capacitors).

Chapter VII concludes with a summary of the contributions this research toward the advancement of AEMs for electrochemical applications, as well as proposed future directions for the work outlined in this dissertation.

CHAPTER II

BROMIDE AND HYDROXIDE CONDUCTIVITY-MORPHOLOGY RELATIONSHIPS IN POLYMERIZED IONIC LIQUID DIBLOCK COPOLYMERS*

2.1 Introduction

PIL block copolymers are a relatively new class of electrolytes, which provide an exciting opportunity to produce solid state hydroxide-conductive AEMs for AFCs. In previous work from our laboratory, we investigated the water-assisted ion conductivity in a PIL diblock copolymer poly(methyl methacrylate-*b*-1-[(2-methyacryloyloxy)ethyl]-3-butylimidazolium bromide) (poly(MMA-*b*-MEBIm-Br)) in comparison to its analogous PIL random copolymer at the same fixed PIL composition (17.3 mol% PIL) or IEC of 1.4 mmol g^{-1}.[48] The PIL block copolymer in that study possessed a high bromide conductivity of 5.67 mS cm^{-1} at 80 °C and 90% RH, which was over an order of magnitude higher than its analogous PIL random copolymer (at the same IEC and water content). This difference in conductivity was due to the nanoscale morphology (isotropic lamellae) in the PIL block copolymer evidenced by both small-angle X-ray scattering (SAXS) and transmission electron microscopy (TEM), while no microphase separation was observed in the PIL random copolymer. Surprisingly, the bromide ion conductivity in the PIL block copolymer

*Reprinted with permission from "Bromide and Hydroxide Conductivity-Morphology Relationships in Polymerized Ionic Liquid Block Copolymers" by K. M. Meek, S Sharick, Y. Ye, K. I. Winey, and Y. A. Elabd, 2015. *Macromolecules*, 48, 4850-4862, Copyright 2015 by American Chemical Society.

was also higher than the PIL homopolymer (control) at the same experimental conditions, even though the homopolymer possessed a 3-fold higher IEC and a 2-fold higher water content compared to the block copolymer. Similar conductivity trends were observed for the hydroxide form of these PIL polymers, where the PIL block copolymer and the homopolymer had hydroxide conductivities of 25.46 and 15.29 mS cm^{-1}, respectively, at 80 °C and 90% RH. These are surprising results as they have not been evidenced elsewhere in water-assisted ion transport in block copolymers and the details of why the ion conductivity was higher in the block copolymer compared to the homopolymer remain unclear. While higher ionic conductivity in a block copolymer compared to its random copolymer has been previously reported in literature for proton-conducting block copolymers,[88-90] the observation of higher ion transport in a block copolymer compared to its homopolymer is unique and necessitates further investigation.

In this study, we investigate PIL block copolymers, poly(MMA-*b*-MEBIm-Br) and poly(MMA-*b*-MEBIm-OH), at varying PIL composition in order to explore the unique relationship between ion conductivity and morphology, specifically the conductivity of the PIL block copolymer in relation to the conductivity of its analogous PIL homopolymer. The PIL diblock copolymer, poly(MMA-*b*-MEBIm-Br), was synthesized at various PIL compositions (6.6, 11.9 and 26.5 mol%), *via* the reverse addition fragmentation chain transfer (RAFT) polymerization technique, where the block copolymer consists of an ionic PIL component (1-[(2-methacryloyloxy)ethyl]-3-butylimidazolium bromide) (MEBIm-Br) and a non-ionic component methyl methacrylate (MMA) (Figure 2.1a). As a control, an analogous PIL homopolymer, poly(MEBIm-Br), was synthesized by conventional free

radical polymerization (Figure 2.1b). Hydroxide-exchanged PIL diblock copolymers and homopolymer, poly(MMA-*b*-MEBIm-OH) and poly(MEBIm-OH), were prepared *via* anion exchange metathesis of the bromide-conducting polymers, at various PIL compositions as well. The conductivity, water uptake, and morphology of these bromide- and hydroxide-conducting PILs were investigated in this study. This broader set of data (conductivity at various PIL compositions) allows for a more in depth analysis of the conductivity-morphology data, where both the morphology factor, *f*, and percolation theory were examined. Both approaches suggest that the local confinement of ions and water in block copolymer microdomains results in higher conductivity compared to the bulk homopolymer over a critical PIL composition.

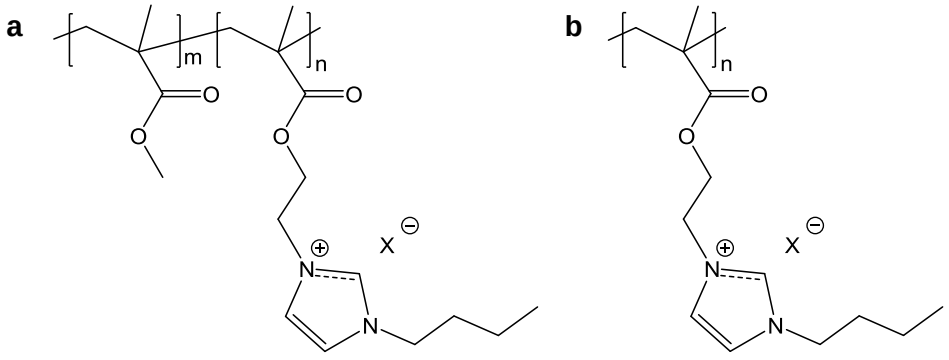

Figure 2.1 Chemical structures of (a) poly(MMA-*b*-MEBIm-X) block copolymer (b) poly(MEBIm-X) homopolymer and, where X^- is Br^- or OH^-.

2.2 Experimental Section

2.2.1 Materials

4-Cyano-4-(phenylcarbonothioylthio)pentanoic acid (chain transfer agent (CTA), >97%, HPLC), tetrahydrofuran (THF, ≥99.9%), N, N-dimethylformamide (DMF, 99.9%,

HPLC), lithium bromide (LiBr, anhydrous, ≥99.9%), methanol (99.9%, HPLC), acetonitrile (anhydrous, 99.8%), calcium hydride (CaH_2, 95%), potassium hydroxide (KOH, ≥90%, reagent grade), and dimethyl sulfoxide-d_6 (DMSO-d_6, 99.9 atom % D, contains 0.03% v/v TMS) were used as received from Sigma-Aldrich. Azobis(isobutyronitrile) (AIBN, 98%, Sigma-Aldrich) was purified by recrystallization twice from methanol. Methyl methacrylate (MMA, 99%, Sigma-Aldrich) was purified by distillation over CaH_2 at a reduced pressure. Ionic liquid monomer, 1-[(2-methacryloyloxy)ethyl]-3-butylimidazolium bromide (MEBIm-Br), was prepared according to literature.[41] Dialysis tubing (Spectra/Por biotech membrane, molecular weight cutoff (MWCO) = 500) was purchased from Fisher Scientific. Ultrapure deionized (DI) water with resistivity *ca.* 16 MΩ cm was used as appropriate.

2.2.2 Synthesis of PIL Block Copolymers

A PIL diblock copolymer, poly(MMA-*b*-MEBIm-Br), was synthesized at various compositions from an ionic liquid monomer, 1-[(2-methacryloyloxy)ethyl]-3-butylimidazolium (MEBIm-Br), and a non-ionic monomer, methyl methacrylate (MMA) *via* the reverse addition fragmentation chain transfer (RAFT) polymerization technique (see Scheme 2.1) using a procedure in literature.[91] Previously, we reported on the synthesis of this PIL block copolymer at one PIL composition: 17.3 mol% (39.2 vol%). Herein, we report on this PIL block copolymer at three additional PIL compositions: 6.6, 11.9, 26.5 mol% (17.9, 29.3, 52.5 vol%), where the PIL composition of the block copolymer was varied by modifying the ratio of IL monomer to PMMA macro-CTA to initiator (see Table

2.1). From these bromide (Br^-)-conducting PIL diblock copolymers, poly(MMA-*b*-MEBIm-Br), a series of hydroxide (OH^-)-exchanged or hydroxide-conducting PIL diblock copolymers, poly(MMA-*b*-MEBIm-OH), were prepared *via* anion exchange metathesis of the bromide-conducting block copolymer annealed films and this procedure is described elsewhere.[48] For comparison, PIL homopolymer analogs, poly(MEBIm-Br) and poly(MEBIm-OH) (both 100 mol% PIL) were prepared, where poly(MEBIm-Br) was synthesized according to the literature *via* free radical polymerization and poly(MEBIm-OH) was prepared by anion exchange metathesis of the poly(MEBIm-Br).[5] ^{1}H NMR were previously published for the bromide- and hydroxide-conducting block copolymers at 17.3 mol% (39.2 vol%) PIL composition and results for the additional PIL compositions synthesized in this paper are similar (Appendix A Figure A1).[48,91] PIL composition (mol%) of block copolymers was determined with ^{1}H NMR by relative integrations of resonance of OCH_3 from the MMA block versus resonance of N−C*H*=C*H*−N from the imidazolium ionic block. Molecular weights and molecular weight distributions of the PIL block copolymers determined by size exclusion chromatography (SEC) are reported in Table 2.1. Synthesis of additional of molecular weights and compositions of PMMA-based block copolymers are reported in Appendix A Table A2.

Scheme 2.1 Synthesis of PIL diblock copolymers: poly(MMA-*b*-MEBIm-Br) and poly(MMA-*b*-MEBIm-OH)

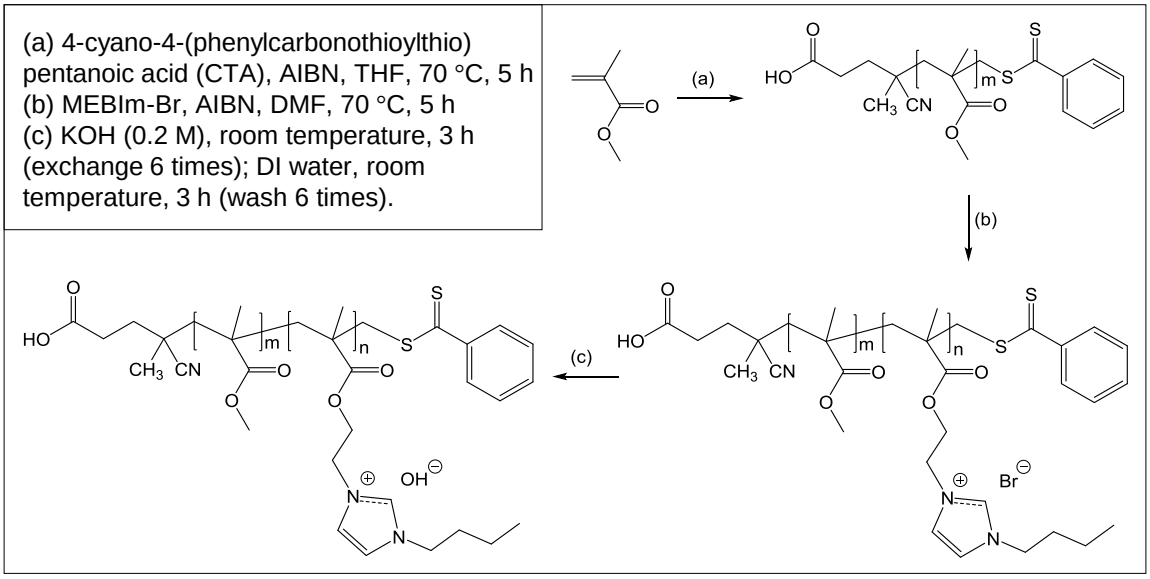

2.2.3 Solvent-Casting PIL Block Copolymers and Homopolymer Films

The bromide-conducting PIL block copolymers, poly(MMA-*b*-MEBIm-Br), were first dissolved in anhydrous acetonitrile (10% w/w) and cast onto Teflon substrates (ca. 35 mm (L) × 4 mm (W) × 0.525 mm (T)) under ambient conditions for *ca.* 2 days, and subsequently annealed under vacuum at 150 °C for 72 h. Bromide-conducting PIL homopolymer, poly(MEBIm-Br), films were fabricated by dissolving the polymer in anhydrous acetonitrile (10% w/w) and casting on glass substrates under ambient conditions for 24 h followed by annealing under vacuum at room temperature for 72 h. As described earlier, the hydroxide-conducting PIL block copolymers, poly(MMA-*b*-MEBIm-OH), were prepared by anion exchange of the poly(MMA-*b*-MEBIm-Br) annealed films. Hydroxide-conducting PIL homopolymer, poly(MEBIm-OH), films were

solution cast from DI water (10% w/w) on a glass substrate and dried under nitrogen environment overnight at room temperature. The hydroxide-conducting PIL homopolymer was not soluble in acetonitrile as was the bromide-conducting PIL homopolymer. No microphase separation was observed for PIL homopolymers in this study, therefore differences in solid-state properties due to different casting solvents is not anticipated. These films were used to determine ionic conductivity and water uptake. The film thicknesses, ranging between 80 to 200 μm, were measured with a Mitutoyo digital micrometer with ± 1 μm accuracy.

2.2.4 Characterization

All chemical structures, PIL compositions, and number-average molecular weights of the PIL block copolymers were characterized by ^{1}H NMR spectroscopy using a Varian 500 MHz spectrometer at 23 °C with DMSO-d_6 as the solvent. The chemical shifts were referenced to tetramethylsilane (TMS). The molecular weights and molecular weight distributions of PMMA macro-CTA and PIL block copolymers were determined by size exclusion chromatography (SEC) using a Waters GPC system equipped with two DMF Styragel columns (Styragel@HR 3 and Styragel@HR 4, effective separation of molecular weight ranges: 500−30 000 and 5000−600 000) and a 2414 reflective index (RI) detector. All measurements were performed at 40 °C. A mixture of DMF and 0.05 M LiBr was used as a mobile phase at a flow rate of 1.0 mL/min. Poly(ethylene glycol)/poly(ethylene oxide) (PEG/PEO) standards (Fluka) with molecular weights ranging from 628 to 478 000 g mol^{-1} were used for calibration.

SAXS was performed using a multi-angle X-ray scattering system generates Cu-Kα X-rays, λ = 0.154 nm, from a Nonius FR 591 rotating anode operated at 40 kV and 85 mA. The bright, highly collimated beam was obtained via Osmic Max-Flux optics and pinhole collimation in an integral vacuum system. The scattering data were collected using a Bruker Hi-Star two-dimensional detector with a sample-to-detector distance of 150 cm. Room temperature data were collected for 1 h for each block copolymer film. Data were analyzed using Datasqueeze software.[92] The intensities were first corrected for primary beam intensity, and then background scattering was subtracted. The isotropic 2-D scattering patterns were then azimuthally integrated to yield 1-D intensity versus scattering angle (q) profiles. The intensities were reported in arbitrary units (a.u.). Morphologies were classified by taking the ratio of the positions of higher order X-ray scattering correlation peaks to the primary peak position, q^*, and comparing to known peak position ratios.[93] The humidity- and temperature-dependent morphologies of poly(MMA-*b*-MEBIm-Br) and poly(MMA-*b*-MEBIm-OH) were characterized by *in situ* X-ray scattering, conducted through the plane of the film, using a custom designed environmental chamber.[94] Relative humidity (RH) was varied by regulating the flow of compressed air/water vapor mixture into the chamber and the sample temperature was controlled by flowing heated or cooled water through the chamber walls, as well as varying the temperature of the water vapor. This is operated by a LabView® program, which employs a proportional-integral-derivative feedback control loop to minimize the error between actual and desired relative humidity and temperature during X-ray scattering data collection. The environmental chamber is able to access a temperature range of 25-90 °C

with a precision of 0.05-0.5 °C and humidity range of 0-95% RH with a precision of 1.5% RH at 30 °C and 3% RH at 80 ºC. For the humidity study, each sample was held at 30 ºC and the percent relative humidity was adjusted to 30, 60, 90, and 30% RH (reverse). For the temperature study, a separate sample was held at 90% RH and the temperature was set to 50 °C and 80 °C. Samples were equilibrated for at least 2 h at each condition before collecting X-ray scattering data. This equilibration time matches that of the conductivity and water sorption experiments.

The ionic conductivities of polymer films were measured with electrochemical impedance spectroscopy (EIS; Solartron, 1260 impedance analyzer, 1287 electrochemical interface, Zplot software) over a frequency range of $1-10^6$ Hz at 200 mV. Conductivities were collected in an environmental chamber (Tenney, BTRS model), where temperature and relative humidity were controlled. The in-plane conductivities of the polymer films were measured in a cell with four-parallel electrodes, where an alternating current was applied to the outer electrodes and the real impedance or resistance, *R*, was measured between the two inner reference electrodes. The resistance was determined from a high x-intercept of the semicircle regression of the Nyquist plot. Conductivity was calculated by using the following equation: $\sigma = L/AR$, where L is the distance between two inner electrodes and A is the cross-sectional area of the polymer film ($A = Wl$; W is the film width and l is the film thickness). Samples were allowed to equilibrate for 2 h at each temperature and humidity followed by six measurements at the equilibrium condition. The values reported are an average of these steady-state measurements. An average error of < 5% was observed among repeated experiments. Note that CO_2 was not removed from

humid air in these experiments. However, significant differences between hydroxide, carbonate, and bicarbonate conductivities in imidazolium-based polymers was observed in our previous work under the same conditions within similar experimental times, suggesting that imidazolium-based polymers may have a high tolerance to the deleterious effect of CO_2.[5]

Water uptake or content was measured with dynamic vapor sorption (DVS, TA Instruments Q5000). A dry film sample was first loaded into the DVS and preconditioned at 0% RH and 30 °C for 2 h. Only a small weight loss (< 0.5%) was observed during this 2 h period and the loss in mass did not change well before the end of this 2 h time period. The relative humidity was then systematically changed to a constant value at a fixed temperature or the temperature was systematically changed to a constant value at a fixed humidity and the film was allowed to equilibrate at that condition for 2 h. The water uptake (content) [wt%; (g H_2O/g dry polymer) × 100] in the polymer was calculated as follows:

$$W_W = \frac{W - W_0}{W_0} \times 100 \tag{2.1}$$

where W_0 and W are dry and wet polymer weights measured before and after the DVS experiment, respectively. The hydration number (λ), defined as the moles of water per mole of imidazolium cations in the hydrated polymer [mol H_2O/mol Im^+], was calculated using the following equation.

$$\lambda = \left[\frac{W_W}{100}\right]\left[\frac{MW_{CP}}{MW_W}\right]\left[\frac{1}{x_{PIL}}\right] \tag{2.2}$$

$$MW_{CP} = (1 - x_{PIL})MW_{MMA} + x_{PIL}MW_{IL} \quad (2.3)$$

x_{PIL} is the PIL composition (mole fraction) in the PIL block copolymer determined from NMR, MW_{CP} is the average molecular weight of the repeat unit of the copolymer (with counter anion), and MW_W and MW_{IL} are the molecular weights of water (18.02 g mol^{-1}) and IL monomeric unit (where MW_{IL} for MEBIm-Br = 317.23 g mol^{-1} and MW_{IL} for MEBIm-OH = 254.34 g mol^{-1}), respectively.

The PIL composition in the dry PIL block copolymers was calculated in terms of volume percent [vol%; (cm^3 PIL/cm^3 copolymer) × 100] using the following equation:

$$vol\% = [x_{PIL}]\left[\frac{MW_{IL}}{MW_{CP}}\right]\left[\frac{\rho_{CP}}{\rho_{IL}}\right]\times 100 \quad (2.4)$$

Similarly, the volume fraction corresponding to the PIL composition can be defined:

$$\phi_{PIL} = \frac{vol\%}{100} \quad (2.5)$$

In Equation 2.4, ρ_{CP} is the density of the copolymer, which is given by:

$$\frac{1}{\rho_{CP}} = \frac{w_{PMMA}}{\rho_{PMMA}} + \frac{w_{PIL}}{\rho_{PIL}} \quad (2.6)$$

where w_{PMMA} and w_{PIL} are the weight fractions of PMMA and PIL, respectively, and ρ_{PMMA} and ρ_{PIL} are the densities of PMMA and PIL. Equation 2.5 represents the volume fraction of the PIL in the block copolymer when no water is present in the polymer, *i.e.*, the dry PIL volume fraction. If one assumes that when water is absorbed by the block copolymer that all of the water is absorbed into the PIL phase, since the water solubility in PMMA is negligible, then a volume fraction of the conducting phase can be determined

at any given relative humidity or temperature. In other words, the volume fraction of the conducting phase is the volume of the PIL phase plus water determined from the known PIL composition (determined from NMR) and the water content (determined from DVS). Therefore, the volume fraction of the conducting phase can be determined using the following expression:

$$\phi_{PIL+W} = \frac{\left[\frac{W_W}{100}\right]\left[\frac{\rho_{CP}}{\rho_W}\right] + [\phi_{PIL}]}{1 + \left[\frac{W_W}{100}\right]\left[\frac{\rho_{CP}}{\rho_W}\right]} \tag{2.7}$$

where ρ_W is the density of water, W_W is the water content in Equation 2.1, and ϕ_{PIL} is the PIL volume fraction in Equation 2.5.

2.3 Results

2.3.1 PIL Block Copolymer Synthesis

We synthesized a series of bromide-conducting PIL diblock copolymers (poly(MMA-*b*-MEBIm-Br)) at various MEBIm-Br (or PIL) compositions and an analogous PIL homopolymer (poly(MEBIm-Br)). The bromide-conducting PIL block copolymers and PIL homopolymer were synthesized using reversible addition-fragmentation chain transfer (RAFT) polymerization and conventional free-radical polymerization techniques, respectively. The bromide-conducting block copolymers and homopolymer were subsequently converted into hydroxide counterion form *via* anion exchange metathesis (Scheme 2.1c) to form hydroxide-conducting block polymers (poly(MMA-*b*-MEBIm-OH)) and homopolymer (poly(MEBIm-OH)). The reaction conditions, molecular weights,

and polydispersities of the PIL block copolymers and homopolymer are listed in Table 2.1. Note the molecular weights (M_w) of the PIL block copolymers and the homopolymers are similar. The synthesis, conductivity, and morphology of the PIL block copolymer at 17.3 mol% (39.2 vol%) PIL composition and the PIL homopolymer (100 mol% or vol% PIL) have previously been published in both bromide and hydroxide forms.[48] Herein, we report the synthesis, conductivity, and morphology of this PIL block copolymer as a function of PIL composition, where the additional PIL compositions of 6.6, 11.9, 26.5 mol% (17.9, 29.3, 52.5 vol%) are listed in Table 2.1.

Table 2.1. Reaction Conditions, Molecular Weights, and Composition of PIL Block Copolymers and Homopolymers.

PIL Block Copolymers[a]	mol %	vol%[c]	IEC (meq/g)[d]	Recipe[e]	M_n (kg mol^{-1})	M_n (kg mol^{-1})	PDI
Poly(MMA-*b*-MEBIm-Br)	6.6[b]	17.9	0.60	20:1:0.1	13.1 + 2.94[f]	18.23[g]	1.22[g]
	11.9[b]	29.3	1.02	40:1:0.1	13.1 + 5.60[f]	20.38[g]	1.44[g]
	17.3[b]	39.2	1.40	60:1:0.1	13.1 + 8.68[f]	18.90[g]	1.26[g]
	26.5[b]	52.5	1.56	100:1:0.1	13.1 + 14.96[f]	26.50[g]	1.33[g]
	100.0	100.0	4.20			29.90[g]	2.20[g]
Poly(MMA-*b*-MEBIm-OH)	6.6	16.4	0.60		13.1 + 2.36[h]	17.99[h]	1.22
	11.9	27.3	1.02		13.1 + 4.49[h]	19.90[h]	1.44
	17.3	36.7	1.40		13.1 + 6.96[h]	18.25[h]	1.26
	26.5	50.0	1.56		13.1 + 12.00[h]	25.10[h]	1.33
	100.0	100.0	4.20			23.99[h]	2.20

[a]*b* = block copolymer, Br = bromide counterion (Br^-), OH = hydroxide counterion (OH^-); [b]PIL (MEBIm-Br) mol% was determined from ^{1}H NMR spectroscopy; [c]dry PIL vol% values were calculated from weight fractions and densities of PMMA (1.18 g cm^{-3}) and PIL homopolymers ($\rho_{poly(MEBIm\text{-}Br)}$ = 1.22 g cm^{-3} and $\rho_{poly(MEBIm\text{-}OH)}$ = 1.08 g cm^{-3}, see Appendix A); [d]calculated as mmeq Im^+ per g of polymer, see Supporting Information. [e]A:B:C = MEBIm-Br:PMMA-CTA:AIBN (in mol); [f]calculated from ^{1}H NMR spectroscopy; [g]determined by SEC. [h]calculated from bromide-conducting PIL polymers.

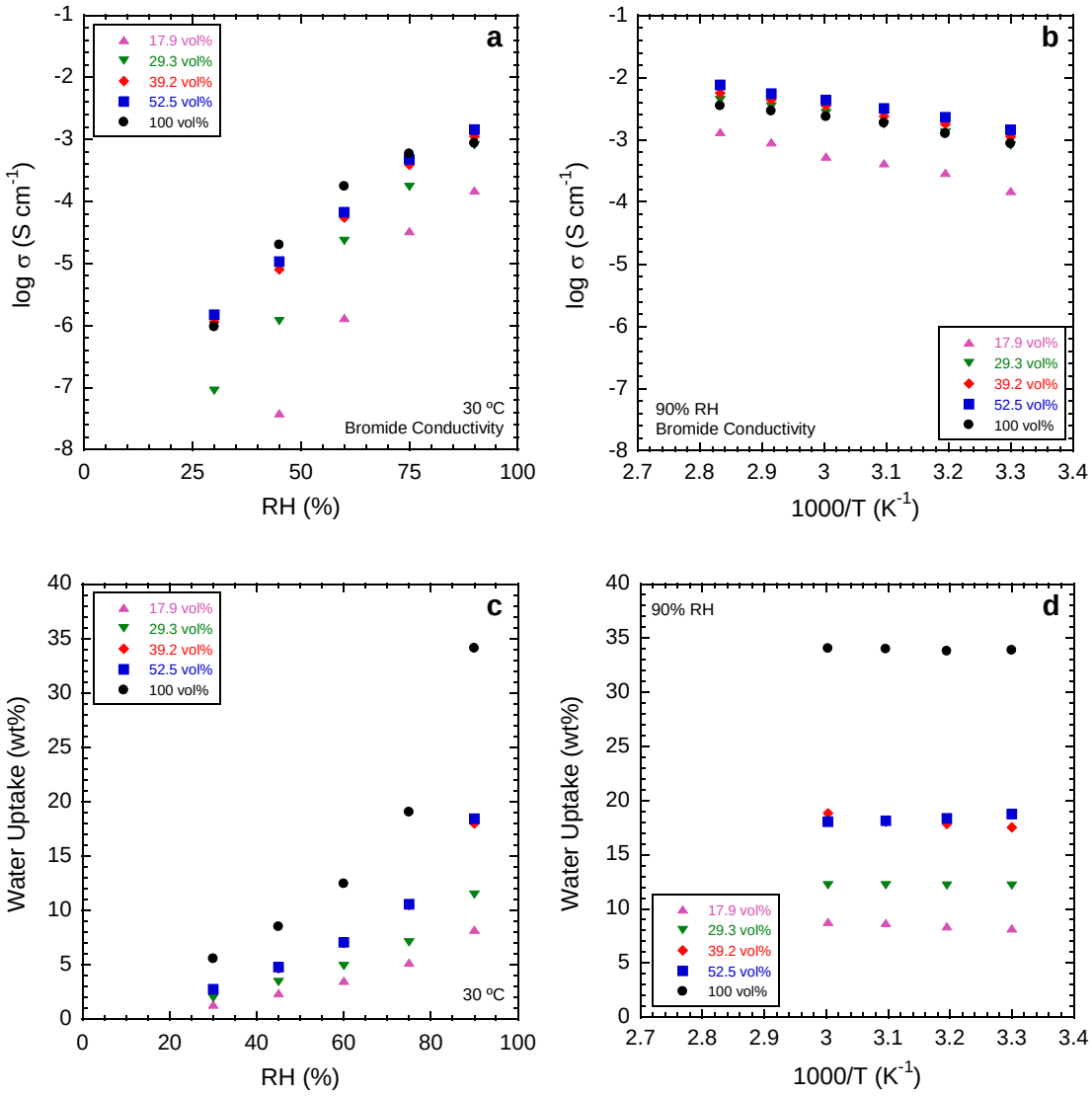

Figure 2.2 Bromide conductivity (a, b) and water uptake (c, d) as a function of relative humidity at 30 °C (a, c) and temperature at 90% RH (b, d) for the PIL block copolymer, poly(MMA-*b*-MEBIm-Br), at various PIL compositions (17.9, 29.3, 39.2, 52.5 vol%; eq 4) and the PIL homopolymer, poly(MEBIm-Br) (100 vol% PIL).

2.3.2 Bromide-Conducting PIL Block Copolymers

Figure 2.2 shows the bromide ion conductivity and water uptake of the block copolymers at various PIL compositions (in vol%; eq 2.4) and the analogous homopolymer (100 vol%

PIL) over a range of humidities and temperatures. Figure 2.2a specifically shows the bromide conductivity at 30 °C as a function of relative humidity (RH) from 30 to 90% RH for the block copolymers and the homopolymer. The bromide conductivity increases over 3-4 orders of magnitude with increasing RH for all polymers. This can be attributed to a water-assisted transport mechanism similar to water-Nafion systems, where an increase in water content in the polymer (1 to 34 wt%; Figure 2.2c) is observed over this humidity range for all polymers. This ion transport mechanism differs from ion transport in anhydrous polymers (*e.g.*, lithium salt-poly(ethylene oxide) systems), where ion transport is dictated by the segmental dynamics of the polymer chains. Conductivity also increases with PIL composition, where conductivity increases by several orders of magnitude at low humidity and by one order of magnitude at high humidity when comparing the lowest and highest PIL composition block copolymers. The PIL block copolymers at the two highest PIL compositions of 39.2 and 52.5 vol% have higher bromide conductivities compared to the homopolymer (100 vol% PIL): 1.14×10^{-3} and 1.49×10^{-3} versus 9.6×10^{-4} mS cm^{-1} at 30 °C and 30% RH, and 1.12 and 1.44 versus 0.87 mS cm^{-1} at 30°C and 90% RH, respectively. Note that at both 30 and 90% RH, this cannot be attributed to water uptake as the water content is 2-fold higher in the homopolymer versus the block copolymers at 39.2 and 52.5 vol% PIL (which have relatively equal water uptake; Figure 2.2c). Also, the normalized water uptakes (mol water/mol imidazolium charged group) for homopolymer and PIL block copolymers at all PIL compositions are similar at all experimental conditions. This unusual behavior of higher conductivity in the block copolymer versus its homopolymer (despite lower ionic content and water content in the block copolymer)

was observed for the 39.2 vol% PIL block copolymer in our previous work and similar results were also observed here for the 52.5 vol% PIL block copolymer.[48]

The block copolymers at the two lowest PIL compositions of 17.9 and 29.3 vol% have lower bromide conductivities compared to the homopolymer for all relative humidities at 30 °C. In Figure 2.2a, the block copolymer at 29.3 vol% PIL has conductivities an order of magnitude below the homopolymer at 30, 45, and 60% RH and half an order of magnitude lower at 75% RH, but at 90% RH the block copolymer conductivity is comparable to the homopolymer (0.81 versus 0.87 mS cm^{-1}, respectively). The lowest composition block copolymer at 17.9 vol% PIL has conductivities two orders of magnitude below the homopolymer at low humidity and approximately an order of magnitude lower at 75% and 90% RH. It is evident that the relationship between block copolymer and homopolymer conductivity is PIL composition dependent, considering the lowest PIL content block copolymer never surpasses the conductivity of the homopolymer while greater conductivity compared with the homopolymer is observed at various conditions for all three higher composition PIL block copolymers. It is interesting that increasing relative humidity has a more significant effect on the conductivity in the lower composition block copolymers than in the higher composition block copolymers.

In Figure 2.2b, the bromide conductivity at 90% RH versus temperature follows an Arrhenius behavior with activation energies of 37, 30, 29, 29, and 25 kJ mol^{-1} for the 17.9, 29, 39.2, 52.5, and 100 vol% PIL compositions, respectively. This ion transport mechanism differs from ion transport in anhydrous polymers, where ion transport versus temperature follows a VFT behavior due to the impact of polymer chain segmental

dynamics on ion transport. It was previously reported that at 90% RH, the block copolymer with 39.2 vol% PIL has higher conductivities than the PIL homopolymer for all temperatures in the range 30-80 °C. In this work, the block copolymer with 52.5 vol% PIL was also observed to have higher conductivities compared to the homopolymer for all temperatures at 90% RH. Interestingly, at 90% RH and higher temperatures (60, 70, 80 °C), the block copolymer at 29.3 vol% PIL has higher conductivities compared to the homopolymer as well. For example, at 80 °C and 90% RH, bromide conductivities are 4.35, 5.67, 7.64 mS cm^{-1} versus 3.55 mS cm^{-1} for compositions of 29.3, 39.2, 52.5 vol% PIL versus 100 vol% PIL, respectively. Only the lowest composition block copolymer (17.9 vol% PIL) has conductivities below that of the homopolymer for all temperatures at 90% RH. Note that in Figure 2.2d, at 90% RH, the polymer equilibrium water contents are constant over the temperature range and are increasing with increasing PIL content (with the exception of relatively equal water uptake in the 39.2 and 52.5 vol% PIL composition block copolymers) from approximately 8 to 34 wt%, where the water uptake of the highest composition block copolymer is ~18 wt% and the homopolymer is ~34 wt%. Therefore, the PIL block copolymers at the two highest compositions (52.5, 39.2 vol%) are ~1.8- and ~1.4-fold higher in conductivity compared to the homopolymer at all temperatures at 90% RH despite a 2-fold lower water content. The lowest two PIL content block copolymers have conductivities at or below the value of the PIL homopolymer, indicating that these high conductivity results are composition-dependent, *i.e.*, once the composition is below a certain threshold, higher conductivities are no longer observed in the block copolymer compared with the homopolymer.

It was previously shown that the bromide-conducting block copolymer at 39.2 vol% PIL exhibits strongly microphase-separated isotropic lamellar morphology with long-range order.[48] Representative *in situ* small-angle X-ray scattering profiles for the bromide-conducting PIL block copolymer with 52.5 vol% PIL are shown in Figure 2.3. At 30 °C, under vacuum, the scattering data contains a narrow primary peak at position $q^* = 0.17$ nm^{-1} and higher-order peaks at positions $2q^*$, $3q^*$, and $4q^*$, indicative of a strongly microphase-separated lamellar morphology. This is interesting given the identical backbone structures of the PMMA and PIL units. It is apparent that the addition of charged pendant groups, specifically a charged imidazolium pendant group and hydrophilic bromide counterion with highly localized charge, to the PIL results in a large degree of immiscibility between the two polymers. As humidity increases, the peak positions shift to lower scattering vectors, which corresponds to the swelling of PIL microdomains with water. At 30 °C and 90% RH, the third peak becomes weak, but the first and second peaks remain well defined and the ratio of their intensities does not change (Figure 2.3a). At 90% RH, as temperature is increased, the data becomes noisier, but the change in scattering is minimal (Figure 2.3b). These results reveal that this PIL block copolymer maintains a lamellar morphology and strong microphase separation over the investigated humidity and temperature conditions. In fact, all of the bromide-conducting PIL block copolymers films at other PIL compositions in this study exhibit strong microphase separation and their morphology types remain constant at various humidities and temperatures. SAXS profiles for the 17.9 and 29.3 vol% PIL compositions, shown in Appedix A Figures A3 and A4 contain two scattering peaks at positions q^* and $2q^*$,

indicative of microphase separated morphology. Table 2.2 provides a summary of X-ray scattering results for all compositions of the block copolymer.

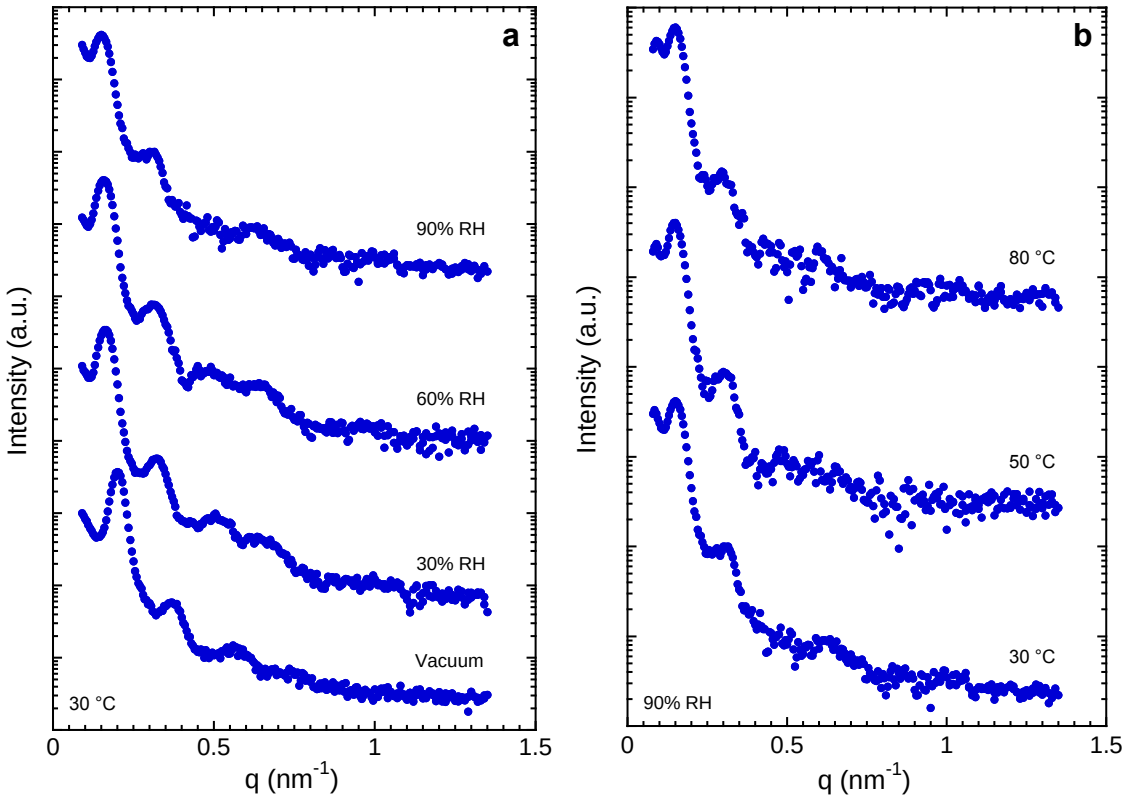

Figure 2.3 Representative *in situ* small-angle X-ray scattering data for poly(MMA-*b*-MEBIm-Br) with 52.5 vol% PIL (a) at 30 °C as a function of relative humidity and (b) at 90% RH as a function of temperature, indicating that a lamellar morphology is maintained over all investigated relative humidities and temperatures. Data are offset vertically for clarity. SAXS profiles for PIL block copolymer at other PIL compositions are shown in Appendix A Figures A3 and A4.

Further insight can be gained by investigating the size of block copolymer microdomains, which can be quantified from the SAXS data. The domain spacing, d^*, is equal to $2\pi/q^*$ and corresponds to the average center-to-center distance between PIL microdomains. Values of d^* were determined for the bromide-conducting PIL block

copolymers at various PIL compositions and increase with increasing PIL composition from 21.7 to 35.1 nm at room temperature, under vacuum, and 22.1 to 40.5 nm at 30 °C and 90% RH. The size of the PIL and water microdomain, L_{PIL+W}, is given by $L_{PIL+W} = \phi_{PIL+W} d^*$, where ϕ_{PIL+W} is the total volume fraction of PIL and water (Equation 2.5). For the bromide PIL block copolymers, L_{PIL} varied from 3.9 to 18.6 nm at room temperature, under vacuum, and L_{PIL+W} varied from 5.6 to 24.7 nm at 30 °C and 90% RH. These values suggest differences between the PIL block copolymer and homopolymer. Because their size ranges from only a few nanometers to tens of nanometers, PIL microdomains may have a higher local ion and water concentration than the bulk PIL homopolymer. This may act to enhance ion transport within the PIL microdomain. Furthermore, the structure of water and subsequently the transport mechanism of ions and water molecules in PIL microdomains may be different from that of the bulk PIL homopolymer.

Table 2.2 Morphology of Bromide-Conducting and Hydroxide-Conducting PIL Block Copolymers.

PIL Block Copolymers[a]	PIL % (vol%)[b]	Morphology	d^* [c] (nm)	L_{PIL} [d] (nm)
Poly(MMA-*b*-MEBIm-Br)	17.9	Microphase Separated	21.7	3.9
	29.3	Microphase Separated	24.6	7.1
	39.2	Lamellar	28.6	11.2
	52.5	Lamellar	35.1	18.6
Poly(MMA-*b*-MEBIm-OH)	16.4	Microphase Separated	22.0	3.5
	27.3	Microphase Separated	27.3	7.4
	36.7	Microphase Separated	24.2	9.0
	50.0	Microphase Separated	33.1	16.6

[a]Br = bromide counterion (Br^-), OH = hydroxide counterion (OH^-); [b]dry volume fractions were calculated from weight fractions and density of PMMA and PIL homopolymers (see Supporting Information); [c]correlation distance at room temperature, under vacuum, calculated by $d^* = 2\pi/q^*$, where q^* is the position of the primary peak obtained from 1-D SAXS data; [d]PIL microdomain size at room temperature, under vacuum, calculated by $L_{PIL} = \phi_{PIL} d^*$, where ϕ_{PIL} is the volume fraction of PIL.

2.3.3 Hydroxide-Conducting PIL Block Copolymers

Figure 2.4 shows the hydroxide ion conductivity of the block copolymers and homopolymer over a range of humidities and temperatures. The hydroxide conductivity trends are similar to the bromide conductivity data (Figure 2.2) with the primary difference being the overall higher magnitude in ion conductivity. For example, the bromide and hydroxide conductivities with increasing PIL composition at 90% RH and 80 °C are 1.33 versus 3.89 mS cm^{-1}, 4.35 versus 7.60 mS cm^{-1}, 5.67 versus 25.46 mS cm^{-1}, and 7.64 versus 25.01 mS cm^{-1} respectively, which corresponds to a range of 2- to 4.5-fold increase.

Similarly, a 4-fold increase in conductivity (3.55 versus 15.29 mS cm^{-1}) is apparent in the homopolymer. The magnitude of the water uptake also increases from the bromide to the hydroxide-conducting polymers, with bromide-conducting polymer water contents varying from 1 to 34 wt% compared to the water contents in the hydroxide-conducting polymers varying from 2 to 61 wt% over 30 to 90% RH at 30 °C (Figure 2.4c).

At 30 °C and low relative humidity (30, 45 and 60% RH), the block copolymer at 50.0 vol% PIL has conductivities ~92% higher than that of the homopolymer, however the block copolymers at all other PIL compositions have lower hydroxide conductivities compared to the homopolymer at these humidities. Interestingly, at 30 °C and 90% RH, the block copolymer at 50.0 vol% PIL has a lower conductivity than the homopolymer (~52% less), while the block copolymer at 36.7 vol% PIL has higher conductivity (~38% higher) than the homopolymer. Analogous to bromide conductivity results, Figure 4b shows the block copolymer at 36.7 vol% PIL has higher hydroxide conductivities compared to the homopolymer for all temperatures at 90% RH: 7.91 versus 5.48 mS cm^{-1} at 30 °C and 25.46 versus 15.29 mS cm^{-1} at 80 °C. From our previous work, this result of higher conductivity in a PIL block copolymer than its analogous PIL homopolymer is a unique and surprising result not found elsewhere in literature.[48] However, the PIL block copolymer at a higher PIL composition of 50.0 vol% only has higher hydroxide conductivities than the homopolymer at higher temperature (50, 60, 70, 80 °C): 25.01 versus 15.29 mS cm^{-1} at 80 °C. These results differ from the bromide conductivity results, where the PIL block copolymer at the highest composition had bromide conductivities higher than the homopolymer at all temperatures at 90% RH. The block copolymers with

lower PIL compositions (16.4, 27.3 vol%) have lower hydroxide conductivities compared to the homopolymer for all temperatures at 90% RH (on average ~89 and 58% less, respectively). Note that the bromide conductivity of the block copolymer with 27.3 vol% PIL was comparable to the homopolymer (on average ~7% less) for all temperatures at 90% RH.

Note that the hydroxide conductivity at 30 °C and 90% RH differs in Figure 2.4a compared to Figure 2.4b for the lower PIL composition samples (16.4 and 27.3 vol%). These experiments were conducted on different days on the same samples (Figure 2.4b – day 1; Figure 2.4a – day 2). We postulate that these differences are due to the samples at low PIL composition being in a non-equilibrium state. Similar results (conductivity differences over days) were observed by Balsara and coworkers[34] on imidazolium-based block copolymers.

Figure 2.4d shows relatively small decreases in water uptake for the block copolymers at 90% RH with increasing temperature over this temperature range. The water uptake of the highest PIL composition block copolymer and homopolymer are ~24 wt% and ~61 wt%, respectively, at 30 °C and 90% RH.

Similar to previous results on the block copolymer at 36.7 vol% PIL, the block copolymer at 50.0 vol% PIL also has a higher hydroxide conductivity at 80 °C and 90% RH compared to the homopolymer: 25.01 versus 15.29 mS cm^{-1}. Again, note that water content in this block copolymer (50.0 vol%) is significantly lower than the homopolymer at high temperature and high humidity: 20 versus 54 wt%. Similar to proton conductivity in Nafion, the hydroxide conductivity in these PIL polymers follows an Arrhenius

behavior with temperature at high humidity (Figure 2.4b) with activation energies of 44, 25, 20, 32, and 18 kJ mol^{-1} for the 16.4, 27.3, 36.7, and 50.0 vol% PIL composition block copolymers and homopolymer, respectively. These activation energies are lower than that of bromide conductivity in these PIL polymers (with the exception of the 16.4 vol% PIL composition), but higher than that for proton conductivity in Nafion (10 ± 2 kJ mol^{-1}).[95]

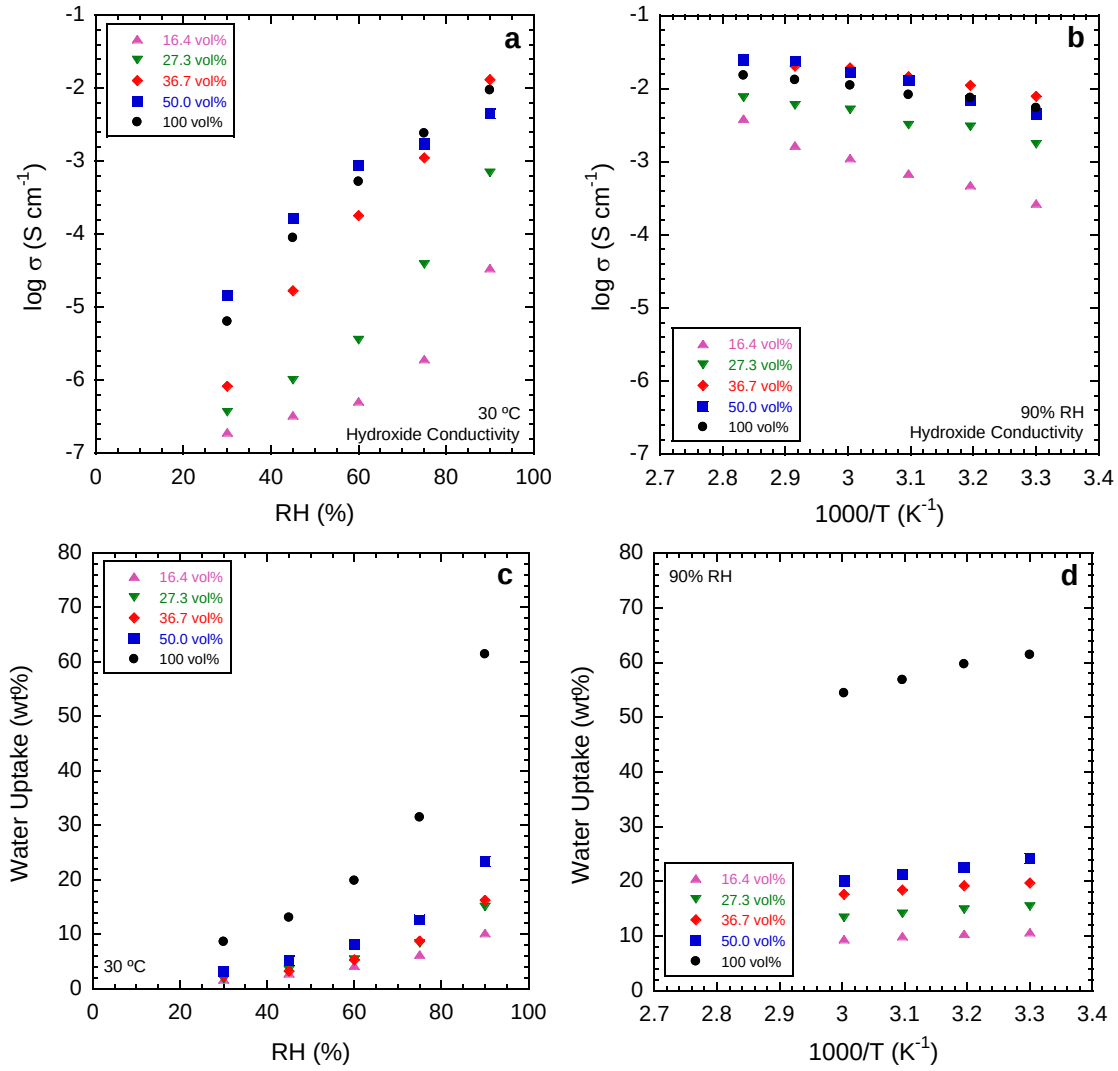

Figure 2.4 Hydroxide conductivity (a, b) and water uptake (c, d) as a function of relative humidity at 30 °C (a, c) and temperature at 90% RH (b, d) for the PIL block copolymer, poly(MMA-*b*-MEBIm-OH), at various PIL compositions (16.4, 27.3, 36.7, 50.0 vol%) and the PIL homopolymer, poly(MEBIm-OH) (100 vol%).

In situ SAXS was also performed for the hydroxide-conducting PIL block copolymers. Representative SAXS profiles as a function of humidity and temperature for the hydroxide-conducting block copolymer at 50.0 vol% PIL are shown in Figure 2.5. At 30 °C, under vacuum, the SAXS data contains one broad peak, indicating a weakly microphase separated morphology. This scattering profile persists as humidity increases to 30 and 60% RH. At 30 °C, 90% RH, the scattering data is featureless, which is attributed to a loss in electron density difference contrast due to the addition of water in the PIL domain rather than a loss in order (Figure 2.5a).[48] This is based on two indicators: the macroscopic state of the block copolymer remains mechanically robust at 90% RH, and it is also known that block copolymers in the disordered state still exhibit a scattering peak, given that they have sufficient contrast. The scattering data remains featureless at 90% RH as temperature is increased to 50 and 80 °C (Figure 2.5b). For all of the hydroxide-conducting PIL block copolymers, scattering profiles with one or two weak peaks were observed at room temperature, under vacuum, and at low humidity (30 and 60% RH), and a featureless profile was observed at 90% RH (Appendix A Figures A5 and A6). The data is consistent with the hydroxide-conducting PIL block copolymers maintaining a weakly microphase separated morphology at all investigated humidities and temperatures, with a loss in scattering contrast at 90% RH. This differs from the strongly microphase separated morphology of the bromide-conducting block copolymers (Figure 2.3). Although the hydroxide-conducting PIL block copolymers exhibit weakly microphase separated morphologies, their conductivities are greater than the conductivities of their bromide-conducting analogs at the same PIL composition. The microdomain sizes of the hydroxide

PIL block copolymers were also on the order of nanometers to tens of nanometers (Table 2.2). The average domain size, *d**, of the hydroxide block copolymers, varies from 22.0 to 33.1 nm with increasing PIL content at room temperature, under vacuum, and from 23.3 to 35.9 nm at 30 °C and 60% RH. The PIL microdomain size, L_{PIL}, varies from 3.5 to 16.6 nm with increasing PIL content at room temperature under vacuum, and L_{PIL+W} varied from 5.9 to 21.8 nm at 30 °C and 60% RH. Again, the confinement of PIL chains and water may contribute to accelerated ion transport, resulting in the conductivities in high PIL composition block copolymers exceeding that of the homopolymer.

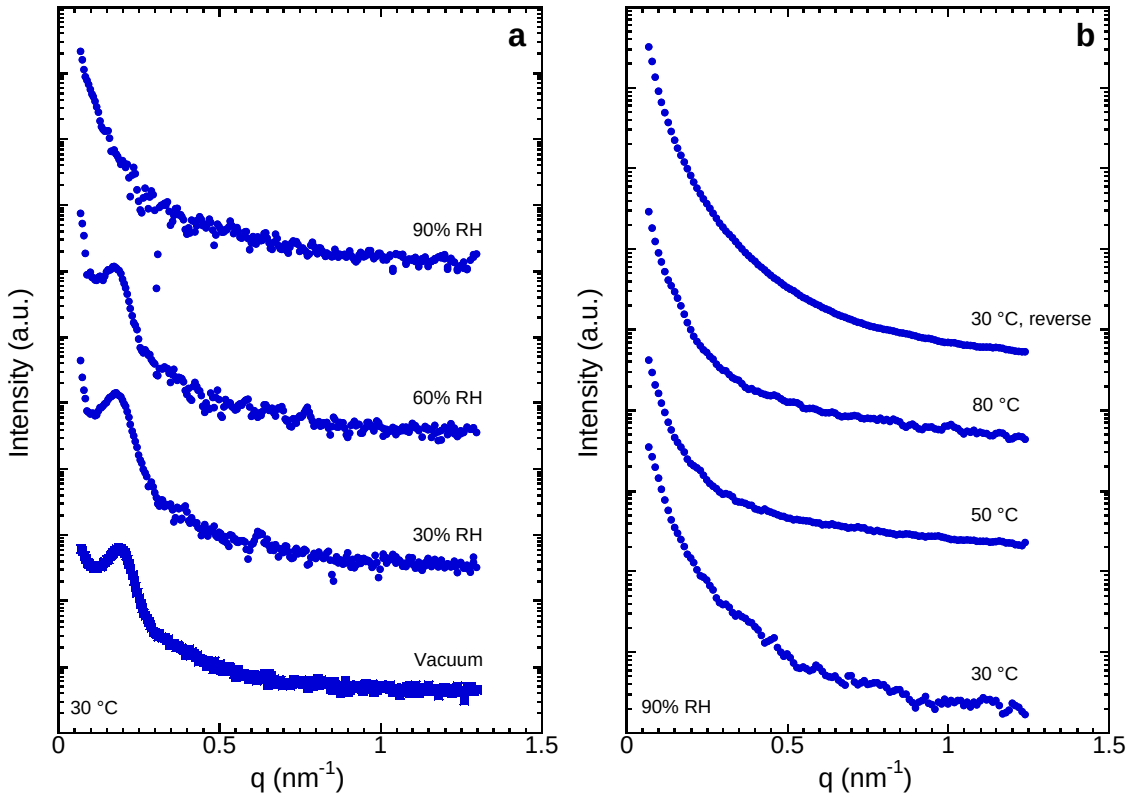

Figure 2.5 Representative *in situ* small-angle X-ray scattering data for poly(MMA-*b*-MEBIm-OH) with 50.0 vol% PIL (a) at 30 °C as a function of relative humidity and (b) at 90% RH as a function of temperature. Data are offset vertically for clarity. SAXS profiles for PIL block copolymers at other PIL compositions are shown in Appendix A Figure A5 and A6.

2.4 Discussion

2.4.1 Morphology Factor

Overall, it is apparent that other mechanisms are impacting transport in this study as the homopolymer exceeds both the PIL content (IEC) and water content compared to that of the block copolymers for all temperatures and humidities studied, but the two highest composition PIL block copolymers have conductivities exceeding that of the homopolymer under several conditions. These results are unusual. As a function of ion composition and water content, there are several different approaches to analyze the data. Two approaches are discussed here: morphology factor and percolation theory.

Others investigators[96,97] have explained the effect of morphology on ion conductivity in block copolymers using a morphology factor (*f*) or normalized conductivity with the following relation.

$$f = \frac{\sigma}{\phi_c \sigma_c} \tag{2.8}$$

In Equation 2.8, σ, ϕ_C, σ_C are the measured ion conductivity of the block copolymer, the volume fraction of the conducting block, and the intrinsic ion conductivity of the conducting microdomain, respectively. Typically, the conductivity of the homopolymer and the volume fraction of the ionic block are used as σ_C and ϕ_C, respectively, to calculate the morphology factor. This provides an estimate of the impact of morphology on transport, where the ion-conducting phase is the minority phase and the theoretical upper limits for the values for *f* in a solid-state block copolymer for a randomly oriented ionic

microdomains in 1-D hexagonally packed cylinders, 2-D lamellae, and 3-D network (gyroid) morphologies are 1/3, 2/3, and 1, respectively.

Recently, several researchers have investigated conductivity-morphology relationships in PIL block copolymers as a function of PIL composition with this approach.[44,96,98-101] Weber *et al.*[44] determined morphology factors in the range of 0.41 to 0.61 for a PIL composition of ϕ_C = 0.5 with a lamellar morphology. This was slightly lower than the predicted f = 2/3 for randomly oriented lamellae. They suggested that there may be some additional resistance due to non-ideal connectivity of microdomains throughout the sample. In this same study, morphology factors in the range of 0.03 to 0.05 were determined for a PIL composition of ϕ_C = 0.34 with a lamellar + cylindrical morphology. The coexistence of cylinders and lamellae should correspond to a theoretical morphology factor in the range of 1/3 to 2/3, however, the morphology factors determined in this study were far below this range suggesting poor macroscopic connectivity of ionic microdomains across the sample and possibly other morphological defects that could hinder ion conduction. In another recent study, Choi *et al.*[98] also determined morphology factors to analyze ion conductivity in a PIL block copolymer. A cylindrical morphology was observed for block copolymers with PIL compositions ϕ_C = 0.18 and 0.32 and morphology factors of less than 0.1 were determined for both of these compositions. These morphology factors were significantly smaller than the theoretical value of f = 1/3 for randomly oriented cylinders. The hexagonally packed cylindrical morphologies in these samples showed limited long-range order as evidenced by SAXS and TEM and therefore suggests the low morphology factors are due to poor connectivity of ionic cylindrical

microdomains across the sample. At higher PIL composition of ϕ_C = 0.41, a lamellar morphology was observed and morphology factors in the range of 0.54 to 0.67 was determined, which was comparable to the theoretical f = 2/3 for randomly oriented lamellae. At an even higher PIL composition of ϕ_C = 0.51, morphology factors ranging from 0.88 to 1.0 were determined for a sample exhibiting a coexisting lamallae + network morphology, which lies between the theoretical limit of f = 2/3 (for lamellae) to f = 1 (for gyroid). It was suggested that at these higher PIL compositions, the degree of microdomain connectivity improves, resulting in higher morphology factors and improved conductivity. Overall, the morphology factor can be used as a tool to not only understand the impact of morphology type on conductivity with changing composition, but the impact of the degree of ion microdomain connectivity, where a high degree of connectivity is required for optimized ion conductivity.

These previous studies lend valuable insights to transport-morphology relationships in PIL block copolymers, but they focused on the conductivity of the TFSI counter anion in anhydrous conditions. In this study, the conductivities of the bromide and hydroxide anions are under investigation under hydrated conditions. To our knowledge, the morphology factor analysis has yet to be applied to water-assisted ion transport in PIL block copolymers.[48] For water-assisted ion transport in block copolymers, we propose a modification to the morphology factor in Equation 2.8.

$$f = \frac{\sigma}{\phi_{PIL+W}\sigma_{HP}} \tag{2.9}$$

Equation 2.9 accounts for not only changing PIL composition, but also different water contents in the block copolymer, where water content is included in the volume fraction of the conducting phase, ϕ_{PIL+W}, or volume fraction of PIL + water in the polymer. Also, to analyze the data in this study, the ion conductivity of the PIL homopolymer, σ_{HP}, is used for the intrinsic ion conductivity of, σ_C, similar to the previous studies on PIL block copolymers.

Figure 2.6 shows normalized conductivity, f (eq 2.8), versus volume fraction of the conducting phase, ϕ_{PIL+W}, for the bromide- and hydroxide-conducting PIL block copolymers and PIL homopolymer at 80 °C and 90% RH (the condition of most interest for the alkaline fuel cell application). Morphology factors at other humidities and temperatures are shown in Appendix A (Figure A7). Morphology factors of 1.5, 3.2, 3.2, and 3.5 were observed for the bromide-conducting block copolymers with PIL compositions of ϕ_C = 0.179, 0.293, 0.392, 0.525, respectively (Figure 2.6a). The homopolymer control is indicated on the graph with a morphology factor of 1.0. The two highest PIL compositions have a lamellar morphology, while the two lower PIL compositions are microphase separated, where a higher order periodic structure could not be determined from the SAXS results for these two compositions (Table 2.2). As previously explained, the maximum theoretical limit for randomly oriented lamellar domains is f = 2/3. Therefore, the block copolymers at all PIL compositions exceed this limit for both lamellar and microphase-separated morphologies, where the three highest PIL compositions have normalized bromide conductivities 3-fold higher than the homopolymer. Figure 2.6b shows morphology factors of 1.0, 1.3, 3.5, and 2.7 for the

hydroxide-conducting block copolymers with PIL compositions of ϕ_C = 0.164, 0.273, 0.367, 0.500, respectively. SAXS results indicate microphase-separated morphologies for all PIL compositions without a higher order periodic structure (Table 2.2). Similar to bromide conductivity results, the hydroxide conductivity results also show unusually high morphology factors that support the previous results of conductivity higher in a block copolymer compared to its analogous homopolymer. Also, similar to the conductivity results (Figures 2.2 and 2.4), the morphology factors are PIL composition dependent, where the lowest PIL composition has the lowest morphology factor. These results suggest that scaling with the homopolymer conductivity to determine the morphology factor may not be an appropriate methodology. In other words, the conductivity in the PIL microdomains may accelerate bromide and hydroxide ion transport due to the local confinement of ions and water within connected network of nanochannels. This confinement results in a higher conductivity in these channels compared to the homopolymer conductivity due to the proximity of ions and water within confined channels and therefore normalizing by the homopolymer conductivity no longer yields meaningful results under this geometric construct. Although this is new to block copolymers, the enhancement of ion conductivity in polymers confined within channels or pores has been observed in other polymer systems.[102,103] To understand the impact of morphology and microdomain confinement on ion transport in more detail, percolation theory was also explored.

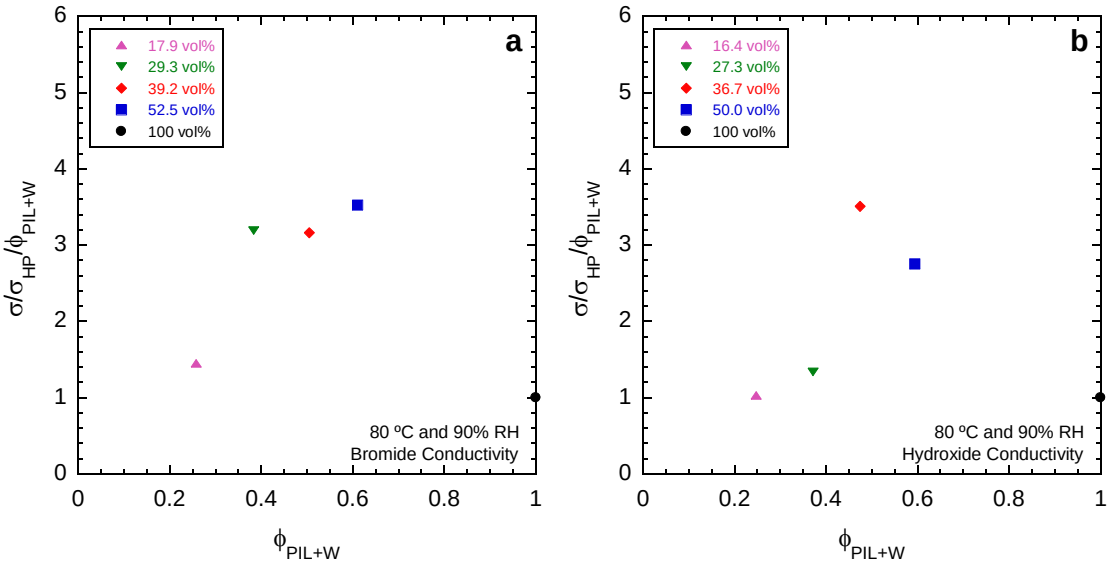

Figure 2.6 Normalized ionic conductivity as a function of volume fraction of the conducting phase (ϕ_{PIL+W}) at 80 °C and 90% RH for (a) poly(MEBIm-Br) and poly(MMA-*b*-MEBIm-Br) and (b) poly(MEBIm-OH) and poly(MMA-*b*-MEBIm-OH). Conductivity is normalized by homopolymer conductivity (σ_{HP}) and volume fraction of conducting phase (ϕ_{PIL+W}) Additional plots for bromide and hydroxide polymers at 30 °C with varying RH and 90% RH with varying temperature are shown in Appendix A Figure A7.

2.4.2 Percolation Theory

Percolation theory describes diffusion through a two-phase system, where one phase is permeable (minority phase) and the other is non-permeable (majority phase).[104,105] The "percolation threshold" is defined as the critical concentration of the minority phase, where isolated domains become interconnected and accessible. According to percolation theory, no transport occurs below the percolation threshold, while transport above the percolation threshold follows a power law dependency on the minority phase volume fraction accordingly:[105]

$$\frac{\sigma}{\sigma_0} \propto \left(\phi_1 - \phi_{1,c}\right)^{\gamma_0} \tag{2.10}$$

In Equation 2.10, σ is the overall measured ionic conductivity of the system, σ_0 is the inherent ionic conductivity (or conductivity of the pure minority phase), γ_D the critical exponent for diffusion; ϕ_1 is the volume fraction of the minority phase, and $\phi_{1,c}$ is the volume fraction of the minority phase at the percolation threshold or the critical volume fraction. Above the percolation threshold, the quantity (ϕ_1 - $\phi_{1,c}$) is known as the excess volume fraction. A plot of measured overall conductivity versus minority volume fraction can be used to determine the critical volume fraction and subsequently a log-log plot of conductivity versus excess volume fraction can be used to determine the inherent conductivity (intercept) and the critical exponent (slope). These two parameters can provide insights into this present study on ion transport in PIL block copolymers. In other words, if confinement of the PIL domain within the block copolymer morphology has no detrimental or enhancing impact on transport, then the inherent conductivity should match that of the measured PIL homopolymer conductivity. Furthermore, the critical exponent provides a measure of morphology and its impact on transport. Kirkpatrick[105] determined values of γ_D = 1.6-1.7 from a 3-D lattice model simulation with a random distribution of the minority phase. When the minority phase was ordered and all domains were accessible to the diffusant, then values of γ_D = 0.3-0.4 were obtained from the simulation.

Others have applied percolation theory to water-assisted ion transport in ion-containing polymers. For proton conductivity in Nafion, a value of γ_D = 1.5 was obtained,[106] while more recently for hydroxide/bicarbonate conductivity in a Tokuyama A201 anion exchange membrane, a value of γ_D = 1.34 was obtained.[107] These values are similar to the simulated values obtained by Kirkpatrick suggesting a random phase-separated

morphology in these systems, which has been experimentally confirmed with other techniques. Elabd *et al.*[104] applied percolation theory to proton conductivity in a block copolymer (sulfonated poly(styrene-isobutylene-styrene) (S-SIBS)) and obtained a value of γ_D = 0.76. This value suggests a more ordered morphology, where a lamellar morphology was confirmed with small-angle X-ray scattering. These examples demonstrate how percolation theory can provide insights into the impact of morphology on water-assisted ion transport in polymers.

Herein, we apply percolation theory to bromide and hydroxide ion transport in PIL block copolymers. We define the percolation model as follows:

$$\frac{\sigma}{\sigma_0} \propto \left(\phi_{PIL+W} - \phi_{PIL+W,c}\right)^{\gamma_D} \tag{2.11}$$

where the volume fraction of the minority phase is defined as ϕ_{PIL+W}, which includes the volume of both the PIL domain and the water that ingresses in that domain, and subsequently, $\phi_{PIL+W,c}$ is the critical volume fraction where percolation occurs. Equation 2.11 differs slightly from others, where only the ingressed water was used as the volume fraction of the minority phase in other reports. Here, we include both the conducting phase (PIL domain) and the ingressed water in the volume fraction of the minority phase.

As described previously, $\phi_{PIL+W,c}$ can be determined from a plot of ion conductivity versus minority phase volume fraction (ϕ_{PIL+W}). For example, Figure 2.7a shows a semi-log plot of bromide conductivity versus the volume fraction of the conducting phase (ϕ_{PIL+W}) for the four different compositions of PIL block copolymers at 80 °C and 90% RH. The homopolymer control is indicated on the graph with a morphology factor of 1.0.

The critical volume fraction can be determined from the x-intercept of a power law regression to the block copolymer data in Figure 2.7a, which was used to produce Figure 2.7b: a log-log plot of bromide conductivity versus excess volume fraction (($\phi_{PIL+W} - \phi_{PIL+W,c}$) at these same conditions). The inherent conductivity, σ_0, and the critical exponent for diffusion, γ_D, were determined from regression of the data (Figure 2.7b) to eq 2.10 as the intercept and slope, respectively. Table 2.3 lists all the values obtained from the percolation model for the bromide- and hydroxide-conducting block copolymers at all temperatures: 30, 40, 50, 60, 70, and 80 °C (see Appendix A for additional plots used in obtained fitting parameters, Figures A8-11). The average critical exponents for diffusion, γ_D, for all temperatures for the bromide- and hydroxide-conducting block copolymers are 0.59 and 0.81, respectively. These values are similar to those obtained from previous work on water-assisted proton conductivity in a block copolymer,[104] which suggests a more ordered morphology and therefore corroborates with the experimental morphology results in this study (Figures 2.3 and 2.5).

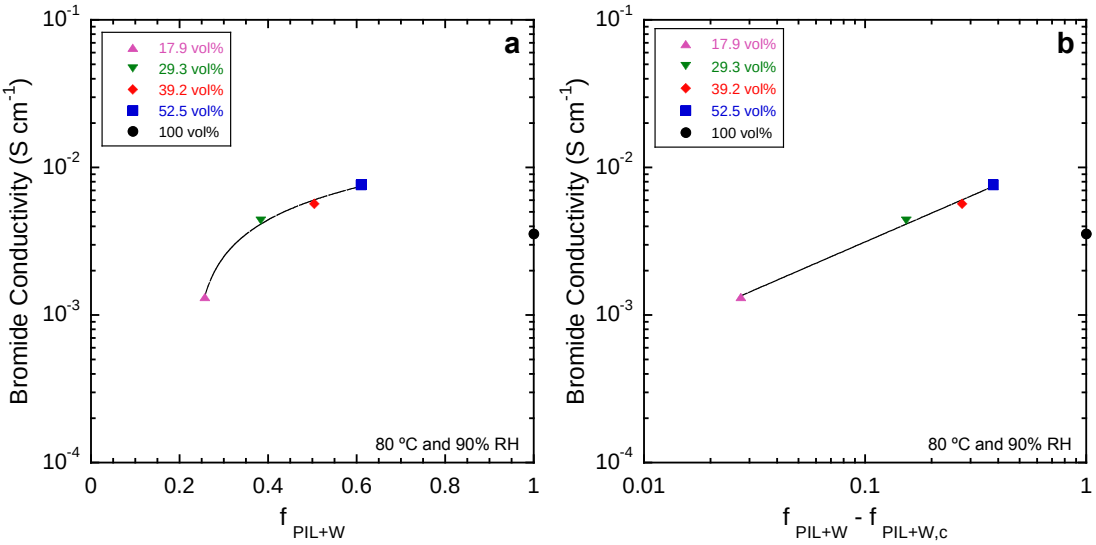

Figure 2.7 Ionic conductivity versus (a) volume fraction of the conducting phase (ϕ_{PIL+W}) and (b) excess volume fraction for poly(MMA-*b*-MEBIm-Br) and poly(MEBIm-Br) at 80 °C and 90% RH. Lines correspond to regressions to Equation 11. Analogous plots for the hydroxide counterpart and for hydroxide- and bromide-conducting polymers at 30, 40, 50, 60, 70 °C are shown in Appendix A Figures A8-11.

More interesting are the values of inherent conductivity obtained from the percolation model, listed in Table 2.3. Specifically, the ratio of the inherent conductivity to the measured PIL homopolymer conductivity, σ_0/σ_{HP}, was on average 3.27 and 3.80 for all temperatures at 90% RH for the bromide- and hydroxide-conducting block copolymers, respectively. As explained previously, if the confinement of the PIL domain with a block copolymer has no detrimental or enhancing effect on conductivity then the inherent conductivity determined from percolation theory should match the measured PIL homopolymer conductivity. These results suggest that the confinement of the PIL domains within the phase-separated block copolymer morphology enhances ion transport over that of the bulk PIL homopolymer. Furthermore, the 3 to 4-fold enhancement in ion conductivity determined from percolation theory corroborates with both the absolute

conductivity results (block copolymer higher conductivity than analogous homopolymer) and the morphology factor analysis. It is possible that block copolymers with higher long-range periodic order and different ionic domain sizes may result in even higher enhancements in conductivity. Overall, these results show that confinement has a significant enhancement effect on conductivity in PIL block copolymers and percolation theory provides valuable insights into quantifying this enhancement effect and on conductivity-morphology relationships in general.

Table 2.3 Percolation Results for Bromide- and Hydroxide-Conducting PIL Block Copolymers.

PIL Block Copolymers	T (°C)[a]	$\phi_{PIL+W,C}$	σ_0 (mS cm^{-1})	Critical Exponent, γ_D	σ_0/σ_{HP}[b]
Poly(MMA-*b*-MEBIm-Br)	30	0.24	2.67	0.63	3.05
	40	0.24	4.21	0.62	3.34
	50	0.24	5.93	0.64	3.19
	60	0.25	7.32	0.51	3.12
	70	0.25	8.80	0.47	3.00
	80	0.23	13.98	0.65	3.93
Poly(MMA-*b*-MEBIm-OH)	30	0.25	10.88	0.58	1.98
	40	0.25	16.11	0.56	2.14
	50	0.25	35.65	0.85	4.31
	60	0.24	42.98	0.78	3.85
	70	0.23	82.55	1.13	6.20
	80	0.21	66.41	0.93	4.34

[a] at 90% RH. [b] Ratio of the inherent conductivity to the measured PIL homopolymer conductivity.

2.5 Conclusions

A series of bromide- and hydroxide-conducting PIL diblock copolymers, poly(MMA-*b*-MEBIm-Br) and poly(MMA-*b*-MEBIm-OH), respectively, were synthesized at various PIL compositions *via* reversible addition-fragmentation chain transfer polymerization. High conductivities in the PIL block copolymers were reported; for example, the bromide and hydroxide conductivities with increasing PIL composition (6.6, 11.9, 17.3, and 26.5 mol%) at 90% RH and 80 °C were 1.33 and 3.89 mS cm^{-1}, 4.35 and 7.60 mS cm^{-1}, 5.67 and 25.46 mS cm^{-1}, and 7.64 and 25.01 mS cm^{-1}, respectively. Under various conditions, especially at high humidity, higher conductivities were observed in the three highest composition PIL block copolymers compared to the analogous PIL homopolymer, despite the significantly higher IEC and water content of the homopolymer. The PIL block copolymers exhibited microphase-separated morphologies, where the confinement of the PIL microdomain within the block copolymer may contribute to these unusually high conductivities. The results from both morphology factor analysis and percolation theory corroborate with these findings and further support this hypothesis. In the future, percolation theory may be an effective tool to optimize the synthesis and design of block copolymers with enhanced ion transport.

This work highlights the promise of PIL block copolymers as AEMS for AFCs, as PIL block copolymers were shown to have enhanced conductivities exceeding that of analogous PILs. The opportunity remains to explore several different polymer backbone/cation chemistries to further tailor PIL block copolymer AEMs and thus achieve other desirable properties, such as high alkaline chemical stability, resistance to

carbonation, limited water uptake, and mechanical robustness, in addition to the high conductivity observed within this study.

CHAPTER III

ALKALINE CHEMICAL STABILITY IN POLYMERIZED IONIC LIQUIDS WITH VARIOUS CATIONS*

3.1 Introduction

Recently, a number of AEMs have been developed for the AFC.[3-13,17-26,28-33,35,108] Alkaline chemical stability remains as one of the critical challenges limiting the wide scale use of solid-state AFCs. Degradation of the covalently tethered cationic groups, as well as the polymer backbone, may be triggered by the high nucleophilicity and basicity of OH^- ions. Further investigations are necessary to determine the most promising AEM chemisty for long-term stability in the presence of hydroxide in order to achieve long-lasting AFC performance. This technique of comparing several cations on the same backbone within one study is useful, as polymer backbone type may contribute to degradation, thus changes in backbone from study to study may lead to inconsistencies when comparing cation stability.

In order to more accurately assess cation stability, it is necessary to compare several cation types on the same polymer backbone under the same degradation conditions. While a few studies have used this approach,[24,25,35] to date, no studies to our knowledge have quantified the alkaline chemical degradation of AEMs with various covalently linked

*Reprinted with permission from "Alkaline Chemical Stability of Polymerized Ionic Liquids with Various Cations" by K. M. Meek and Y. A. Elabd, 2015. *Macromolecules*, 48, 7071-7084, Copyright 2015 by American Chemical Society.

cation types in tandem with their analogous small molecule ionic salts to definitively determine if there is a correlation. The usefulness of past and future small molecule ionic salt degradation studies as tools for predicting relative cation stability in AEMs is dependent upon proof of a correlation between free cation and polymeric cation chemical stability.

In this study, we synthesized polymerized ionic liquids (PILs) containing various covalently attached cations (Scheme 3.1): butylimidazolium, butylmethylimidazolium, trimethylammonium, pentamethylguanidinium, butylpyrrolidinium, trimethylphosphonium. The alkaline chemical stability of these PILs were investigated and compared to their analogous ionic salts (Scheme 3.2): 1-butyl-3-methylimidizolium chloride, 1-butyl-2,3-dimethylimidazolium chloride, tetramethylammonium chloride, benzyltrimethylammonium chloride, hexamethylguanidinium chloride, 1,1-butylmethylpyrrolidinium chloride, tetramethylphosphonium chloride. In order to overcome the aforementioned difficulties in quantifying cation degradation in polymers *via* ^{1}H NMR (*e.g.*, polymer precipitation, weakening of NMR signal by polymer backbone, hydrogen/deuterium exchange), polymers were degraded in D_2O as an alternative to the harsher standard degradation solvent methanol, the PIL chemistry provided high water solubility, such that a significant amount of polymer could be dissolved in D_2O for ^{1}H NMR analysis to enable integration, and small amounts of H_2O were used to suppress H/D exchange where necessary. The degradation pathways and extent of chemical stability of the PILs and ionic salts were determined using ^{1}H NMR spectroscopy after exposure to 2 or 20 molar equivalents (eq) of KOH per cation at 30 °C

or 80 °C for 168 h. This tandem study of AEMs alongside analogous small molecule cations establishes whether small molecule studies provide insight into alkaline chemical stability behavior of polymeric cations. Additionally, these results provide a consistent measure of relative alkaline chemical stability of several major cation types.

Scheme 3.1 Chemical structures of PIL homopolymers with various pendant cations.

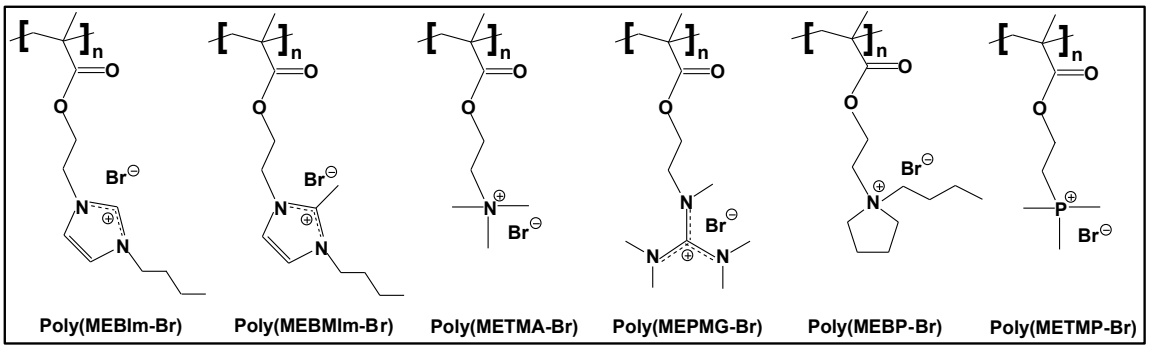

Scheme 3.2 Chemical structures of ionic salts.

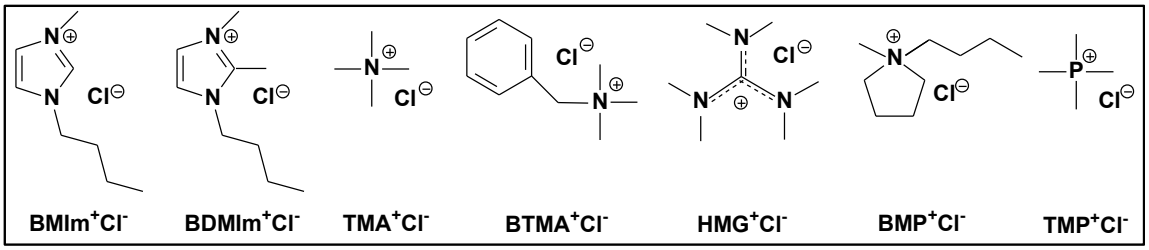

3.2 Experimental Section

3.2.1 Materials

N-dimethylformamide (DMF, ACS Reagent, ≥99.8%), 1-butylimidazole (98%), trimethylamine solution (45 wt% in H_2O), 1-butylpyrrolidine (98%), trimethylphosphine

solution (1 M in THF), tetramethylammonium chloride (≥98%), benzyltrimethylammonium chloride (97%), tetramethylphosphonium chloride (98%), oxalyl chloride (reagent grade, 98%), ethanol, tetramethylurea, 1,2-dichloroethane (anhydrous, 99.8%), methylamine solution (33 wt% in absolute ethanol), magnesium sulfate (anhydrous, ReagentPlus®, 99%), diethyl ether (anhydrous, ≥99.7%, contains 1 ppm BHT inhibitor), hexane (ACS Reagent, ≥98.5%), tetrahydrofuran (THF, ≥99.9%), methanol (ACS Reagent, ≥99.8%,), potassium hydroxide (KOH, ≥90%, reagent grade), deuterium oxide (D_2O, 99.98 atom% D), and dimethyl-d_6 sulfoxide (DMSO-d_6, 99.9 atom% D, contains 0.03% v/v TMS) were used as received from Sigma-Aldrich. 1-Butyl-2-methylimidazole (>98%), 1-butyl-3-methylimidazolium chloride (>99%), 1-butyl-2,3-dimethylimidazolium chloride (>99%), 1-butyl-1-methylpyrrolidinium chloride (99%) were used as received from Iolitec. Hexamethylguanidinium chloride (98%) was used as received from Fisher Scientific. Azobis(isobutyronitrile) (AIBN, 98%, Sigma-Aldrich) was purified by recrystallization twice from methanol.

3.2.2 Synthesis of Poly(BrEMA)

Synthesis of the non-ionic precursor monomer, 2-bromoethyl methacrylate (BrEMA) was performed according to a procedure in literature.[41] The synthesis of the non-ionic precursor homopolymer, poly(BrEMA), was performed using conventional free-radical polymerization as shown in Scheme 3.3(1). A typical example is given as follows. 5.0 g (25.9 mmol) of BrEMA monomer in DMF (BrEMA/DMF 1/1 w/w) and 22.3 mg (0.129 mmol) of AIBN (BrEMA/AIBN 200/1 mol/mol) were mixed in a 200 mL round bottom

flask and reacted under N_2 for 2 h at 60 °C. The resulting polymer was precipitated into methanol twice and dried under vacuum in an oven at room temperature for 24 h. Yield: 0.85 g of solid particles (17.0%). ^{1}H NMR (500 MHz, $CDCl_3$, 23 °C) δ (ppm): 4.47-4.19 (s, 2H, O-C*H*$_2$-CH$_2$-Br), 3.66-3.47 (s, 2H,O-CH$_2$-C*H*$_2$-Br), 2.12-1.84 (d, 3H, CH$_2$-C(C*H*$_3$)), 1.12 (s, 1H, *H*CH-C(CH$_3$)), 0.98 (s,1H, HC*H*-C(CH$_3$)) (NMR, Figure 3.1). SEC (THF, 40°C): M_n = 59.15 kg mol^{-1}, M_w/M_n = 1.85 (against PS standards). Three batches of poly(BrEMA) were synthesized (0.85 g, 0.83 g, and 1.13 g with yields of 17.0%, 16.6%, and 18.8%, respectively) to produce the PILs in this study with similar Mn and PDIs.

3.2.3 Synthesis of Poly(MEBIm-Br)

Synthesis of the PIL homopolymer, poly(MEBIm-Br) [MEBIm-Br = 1-[(2-methacryloyloxy) ethyl]-3-butylimidazolium bromide], is shown in Scheme 3.3(2a), *i.e.*, functionalization of non-ionic precursor homopolymer, 2-bromoethyl methacrylate, to form an ionic homopolymer. A typical example is given as follows. 0.200 g (1.03 mmol) of poly(BrEMA) was first dissolved in ~2 mL DMF in a 50 mL vial. 0.642 g (5.17 mmol) of 1-butylimidazole (poly(BrEMA)/1-butylimidazole, 1/5 mol/mol) was then mixed into the vial. The solution was stirred at 80 °C for 48 h. The resulting polymer was precipitated twice into hexane and dried under vacuum in an oven at room temperature for 24 h. Yield: 0.267 g (0.841 mmol) of solid particles (81.2%). ^{1}H NMR (500 MHz, D_2O, 23 °C) δ (ppm): 9.38-8.76 (s,1H, N-C*H*=N), 7.98-7.17 (s, 2H, N-C*H*=C*H*-N), 4.54-3.91 (m, 6H, N-C*H*$_2$-C*H*$_2$-O, N-C*H*$_2$-CH$_2$-CH$_2$-CH$_3$), 1.89 (s, 5H, CH$_2$-C(C*H*$_3$), N-CH$_2$-C*H*$_2$-CH$_2$-CH$_3$),

1.34 (s, 3H, N-CH_2-CH_2-C*H_2*-CH_3, *H*CH-C(CH_3)), 0.93 (s, 4H, N-CH_2-CH_2-CH_2-C*H_3*, HC*H*-C(CH_3)) (NMR, Figure 3.1).

3.2.4 Synthesis of Poly(MEBMIm-Br)

Synthesis of the PIL homopolymer, poly(MEBMIm-Br) [MEBMIm-Br = 1-[(2-methacryloyloxy) ethyl]-3-butylmethylimidazolium bromide], is shown in Scheme 3.3(2b). A typical example is given as follows. 0.200 g (1.03 mmol) of poly(BrEMA) was first dissolved in ~2 mL DMF in a 50 mL vial. 0.715 g (5.18 mmol) of 1-butyl-3-methylimidazole (poly(BrEMA)/1-butyl-3-methylimidazole, 1/5 mol/mol) was then mixed into the vial. The solution was stirred at 80 °C for 48 h. The resulting polymer was precipitated twice into hexane and dried under vacuum in an oven at room temperature for 24 h. Yield: 0.261 g (0.788 mmol) of solid particles (76.5%). ^{1}H NMR (500 MHz, D_2O, 23 °C) δ (ppm): 7.75-7.37 (s, 2H, N-C*H*=C*H*-N), 4.68-4.01 (m, 6H, N-CH_2-CH_2-O, N-CH_2-CH_2-CH_2), 3.28-3.58 (s, 3H, N-C-CH_3=N), 1.91 (s, 4H, CH_2-C(CH_3), N-CH_2-CH_2-CH_2-CH_3), 1.35 (s, 3H, N-CH_2-CH_2-CH_2-CH_3, *H*CH-C(CH_3)), 0.91 (s, 4H, N-CH_2-CH_2-CH_2-CH_3, HC*H*-C(CH_3)) (NMR, Figure 3.1).

3.2.5 Synthesis of Poly(METMA-Br)

Synthesis of the PIL homopolymer, poly(METMA-Br) [METMA-Br = 1-[(2-methacryloyloxy) ethyl]-trimethylammonium bromide], is shown in Scheme 3.3(2c). A typical example is given as follows. 0.730 g (3.78 mmol) of poly(BrEMA) was first dissolved in ~2 mL DMF in a 50 mL vial. 1.118 g (18.9 mmol) of trimethylamine in aqueous solution (poly(BrEMA)/trimethylamine, 1/5 mol/mol) was then mixed into the

vial. The solution was stirred at room temperature for 48 h. The resulting polymer was precipitated twice into diethyl ether and dried under vacuum in an oven at room temperature for 24 h. Yield: 0.85 g (3.37 mmol) of solid particles (89.2%). ^{1}H NMR (500 MHz, D_2O, 23 °C) δ (ppm): 4.64-4.25 (s, 2H, N-CH_2-C*H*$_2$-O), 3.98-3.62 (s, 2H, N-CH_2-C*H*$_2$-O), 3.64-2.97 (s, 9H, N-(C*H*$_3$)$_3$), 2.17-1.86 (s, 3H, CH_2-C(C*H*$_3$)), 1.28-0.81 (s, 2H, C*H*$_2$-C(CH_3)) (NMR, Figure 3.1).

3.2.6 Synthesis of 1,1,2,3,3-pentamethylguanidine (PMG)

To synthesize a PIL homopolymer with pentamethylguanidinium as the cation, 1,1,2,3,3-pentamethylguanidine was first synthesized (Scheme 4). A 250 ml two-necked flask was charged with 50 mL of dry 1,2-dichloroethane and 4.65 g (40 mmol) of tetramethylurea. Oxalyl chloride (5.65 mL, 64.8 mmol) was added at room temperature and the solution was heated for 2 h at 60 °C. The solvent was removed under vacuum, the residual yellow solid was dissolved in 20 mL of dry ethanol and 33.0 g of 33 wt% methylamine in dry ethanol (11.0 g or 354.8 mmol methylamine) was added dropwise at 0°C. The reaction mixture was allowed to warm slowly to room temperature, stirred overnight and then refluxed for 4 h. The solvent was evaporated under vacuum and the residue was treated with 30% aqueous NaOH. The organic layer was extracted with ether, dried with anhydrous magnesium sulfate and the solvent was evaporated. Distillation of the residue under reduced pressure at 100 °C yielded 3.22 g (62.3%) of PMG. ^{1}H NMR (500 MHz, $CDCl_3$, 23 °C) δ (ppm): 2.90 (s, 3H), 2.80 (s, 6H) and 2.66 (s, 6H) (NMR, Appendix B, Figure B1).

3.2.7 Synthesis of Poly(MEPMG-Br)

Synthesis of the PIL homopolymer, poly(MEPMG-Br) [MEPMG-Br = 1-[(2-methacryloyloxy) ethyl]-pentamethylguanidinium bromide], is shown in Scheme 3.3(2d). A typical example is given as follows. 0.400 g (2.07 mmol) of poly(BrEMA) was first dissolved in ~2 mL DMF in a 50 mL vial. 0.486 g (3.77 mmol) 1,1,2,3,3-pentamethylguanidine (PMG) (poly(BrEMA)/PMG, 1/2 mol/mol) was then mixed into the vial. The solution was stirred at room temperature for 24 h. The resulting polymer was precipitated twice into diethyl ether and dried under vacuum in an oven at room temperature for 24 h. Yield: 0.53 g (1.708 mmol) of solid particles (82.5%). ^{1}H NMR (500 MHz, DMSO-d_6, 23 °C) δ (ppm): 3.55-3.19 (s, 12H, C-(N-(CH_3)$_2$)$_2$) (NMR, Appendix B, Figure B1).

3.2.8 Synthesis of Poly(MEBP-Br)

Synthesis of the PIL homopolymer, poly(MEBP-Br) [MEBP-Br =1-[(2-methacryloyloxy) ethyl]-1-butylpyrrolidinium bromide], is shown in Scheme 3.3(2e). A typical example is given as follows. 0.500 g (2.59 mmol) of poly(BrEMA) was first dissolved in ~2 mL DMF in a 50 mL vial. 0.989 g (7.77 mmol) of 1-butylpyrrolidine (poly(BrEMA)/1-butylpyrrolidine, 1/3 mol/mol) was then mixed into the vial. The solution was stirred at 80 °C for 24 h. The resulting polymer was precipitated twice into hexane and dried under vacuum in an oven at room temperature for 24 h. Yield: 0.819 g (2.442 mmol) of solid particles (94.3%). ^{1}H NMR (500 MHz, D_2O, 23 °C) δ (ppm): 4.64-4.18(s, 2H, N-CH_2-CH_2-O)), 3.90-3.45 (s, 6H, N-CH_2-CH_2-CH_2-CH_2-N, N-CH_2-CH_2-O),

2.35-2.02 (s, 4H, N-CH_2-CH_2-CH_2-CH_2-N), 1.51-1.27 (s, 7H, N-CH_2-CH_2-CH_2-CH_3, CH_2-C(CH_3)), 1.08-0.80 (s, 5H, N-CH_2-CH_2-CH_2-CH_3, CH_2-C(CH_3). (NMR, Appendix B, Figure B1).

3.2.9 Synthesis of Poly(METMP-Br)

Synthesis of the PIL homopolymer, poly(METMP-Br) [METMP-Br =1-[(2-methacryloyloxy) ethyl]-trimethylphosponium bromide], is shown in Scheme 3.3(2f). A typical example is given as follows. 0.500 g (2.59 mmol) of poly(BrEMA) was first dissolved in ~2 mL DMF in a 50 mL vial. 0.591 g (7.77 mmol) of trimethylphosphine in THF solution (poly(BrEMA)/trimethylphosphine, 1/3 mol/mol) was then mixed into the vial. The solution was stirred at room temperature for 24 h. The resulting polymer was precipitated twice into diethyl ether and dried under vacuum in an oven at room temperature for 24 h. Yield: 0.467 g (1.735 mmol) of solid particles (67.0%). ^{1}H NMR (500 MHz, D_2O, 23 °C) δ (ppm): 4.55-4.14 (s, 2H, P-CH_2-CH_2-O), 3.93-3.50 (s, 2H, P-CH_2-CH_2-O), 2.50-1.62 (s, 9H, P-(CH_3)$_3$), 1.44-0.61 (s, 5H, CH_2-C(CH_3)) (NMR, Figure 3.1).

Scheme 3.3 Synthesis of PIL homopolymer, poly(MEX-Br)[a], X = various cations (a-f).

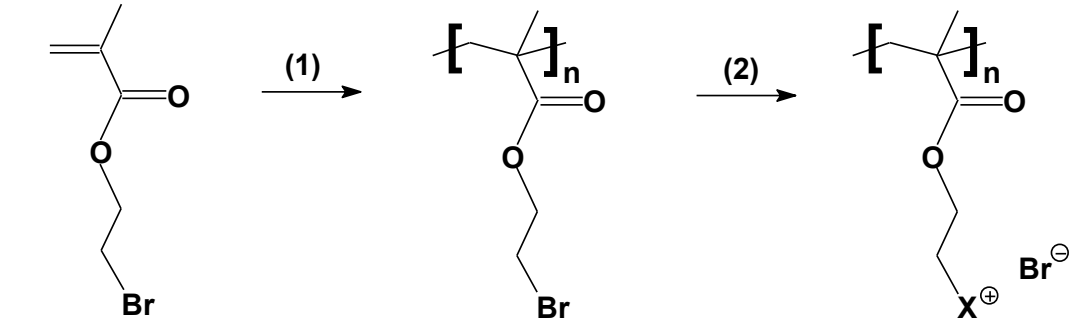

X⊕=

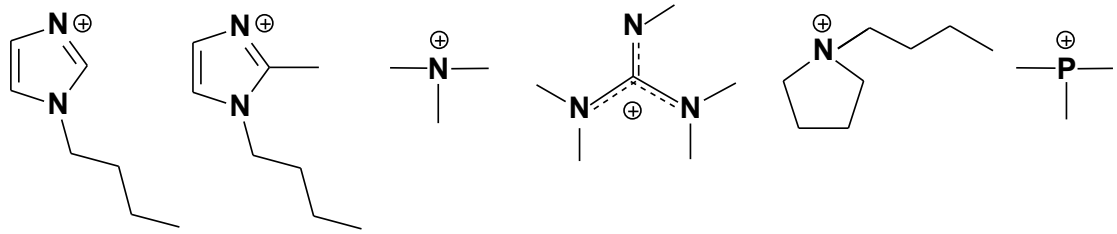

(a) Blm (b) BMIm (c) TMA (d) PMG (e) BP (f) TMP

[a](1) AIBN, DMF, 60 °C, 2 h; (2a) 1-butylimidazole, DMF, 80 °C, 48 h; (2b) 1-butyl-2-methylimidazole, DMF, 80 °C, 48 h; (2c) aqueous trimethylamine, DMF, room temperature, 48 h; (2d) 1,1,2,3,3-pentamethylguanidine (PMG), DMF, room temperature, 24h; (2e) 1-butylpyrrolidine, DMF, 80 °C, 24h; (2f) trimethylphosphine/THF solution, DMF, room temperature, 24h.

Scheme 3.4 Synthesis of 1,1,2,3,3-pentamethylguanidine (PMG)[a]

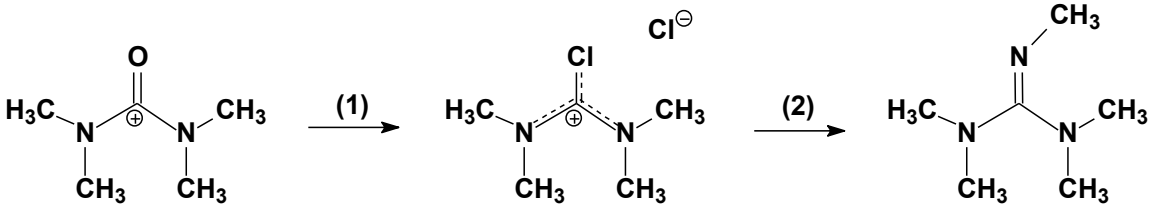

[a](1) Oxalyl chloride, dichloroethane, 60 °C, 2h; (2) methylamine/ethanol solution, dropwise, 0 °C, 1 h.

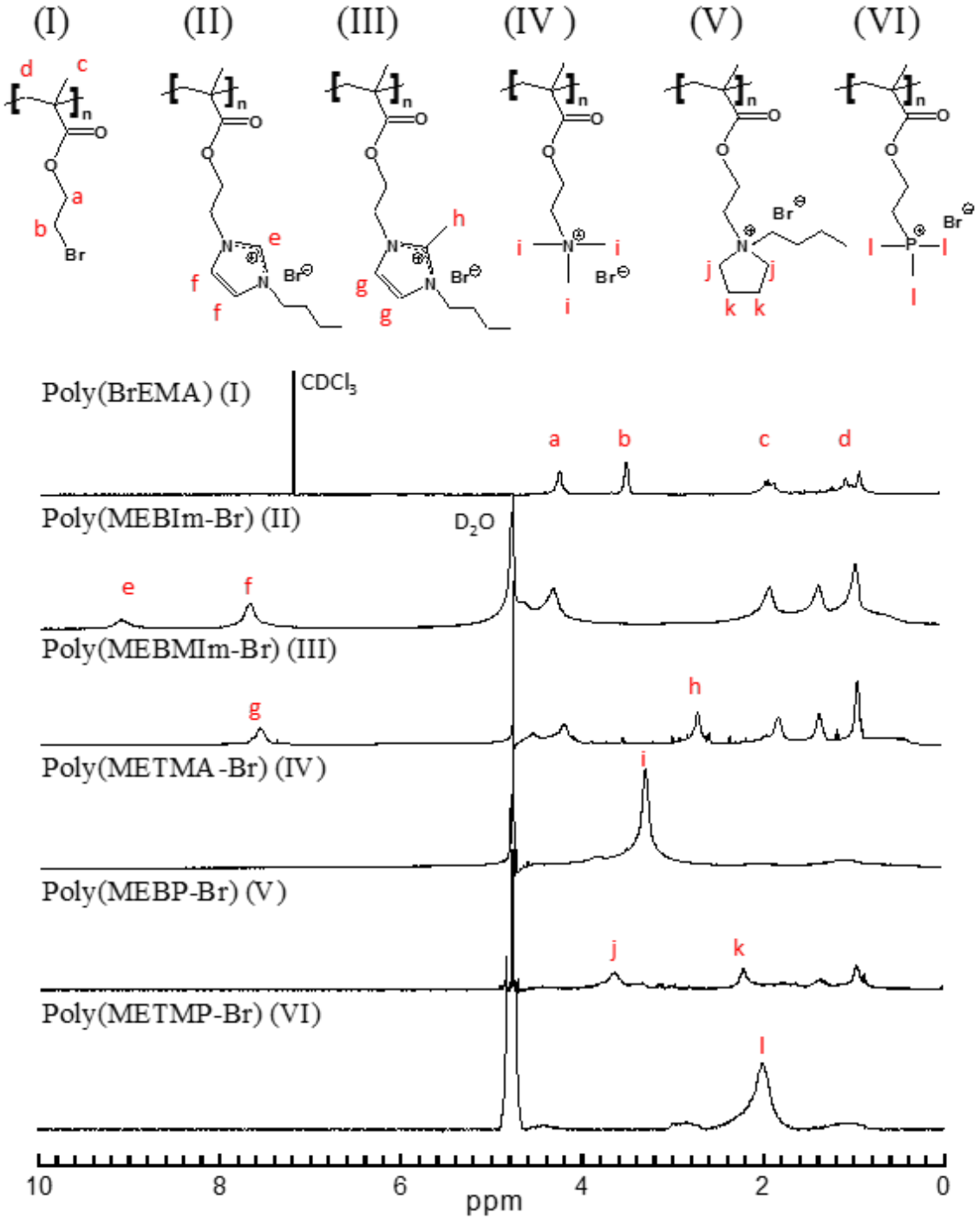

Figure 3.1 ^{1}H NMR spectra for (I) poly(BrEMA), (II) poly(MEBIm-Br), (III) poly(MEBMIm-Br), (IV) poly(METMA-Br), (V) poly(MEBP-Br), (VI) poly(METMP-Br).

3.2.10 Characterization

All chemical structures of the PIL homopolymers were characterized by ^{1}H NMR spectroscopy using a Varian 500 MHz spectrometer at 23 °C with D_2O as the solvent. The chemical shifts were referenced to water at 4.75 ppm. Chemical structure of poly(BrEMA) and PMG were also characterized by ^{1}H NMR spectroscopy and referenced to $CDCl_3$ at 7.27 ppm. The molecular weights and molecular weight distributions of precursor PIL homopolymer were determined by size exclusion chromatography (SEC) using a Waters GPC system equipped with a THF Styragel column (Styragel@HR 5E, effective separation of molecular weight range: 2 to 4000 kg mol^{-1}) and a 2414 reflective index (RI) detector. All measurements were performed at 40 °C. THF was used as the mobile phase at a flow rate of 1.0 mL/min. PS standards (Shodex, Japan) with molecular weights ranging from 2.97 to 983 kg mol^{-1} were used for calibration.

3.2.11 Alkaline Chemical Stability Analysis

The chemical stability of ionic salts and PIL homopolymers was examined using ^{1}H NMR spectroscopy with D_2O as the solvent. The stability study was performed under alkaline conditions in NMR tubes. Ionic salts (25.0 mg) were exposed to different KOH concentrations (2, 20, and 50 molar equivalents (eq)) in 1 mL D_2O at 30 or 80 °C for 168 h, followed by ^{1}H NMR experiments to quantify chemical degradation. PIL homopolymers (8.0 mg) dissolved in 1 mL D_2O were exposed to 2 and 20 eq KOH at 30 or 80 °C for 168 h, followed by ^{1}H NMR experiments. Note that all KOH concentrations are in excess of 1 eq to ensure full ion exchange of ionic salts and PILs.

3.3 Results and Discussion

3.3.1 Ionic Salt Alkaline Chemical Stability

In order to investigate the alkaline stability of PILs with covalently tethered cations, the analogous small molecule model compounds were first studied: 1-butyl-3-methylimidizolium chloride ($BMIm^+$ Cl^-), 1-butyl-2,3-dimethylimidazolium chloride ($BDMIm^+$ Cl^-), tetramethylammonium chloride (TMA^+ Cl^-), benzyltrimethylammonium chloride ($BTMA^+$ Cl^-), hexamethylguanidinium chloride (HMG^+ Cl^-), 1,1-butylmethylpyrrolidinium chloride (BMP^+ Cl^-), tetramethylphosphonium chloride (TMP^+ Cl^-) (Scheme 3.2). The purity and chemical structure of these ionic salts were confirmed by ^1H NMR prior to alkaline chemical stability experiments (Figure 3.2).

The degradation of the ionic salts was quantified by ^1H NMR spectroscopy, where the effects of alkaline concentration and reaction temperature on the alkaline chemical stability of the cations were investigated. Figure 3.2 shows ^1H NMR spectra of each ionic salt after 1 week (168 h) exposure to 2, 20, and 50 eq KOH/D_2O solutions at 30 °C. In Figure 3.2A, the ^1H NMR spectra of $BMIm^+$ Cl^- shows no degradation upon exposure to 2 eq, while exposure to 20 and 50 eq shows a new peak at ~1.8 ppm (labeled 1'), where this peak can be attributed to a ring-opening reaction as described in literature.[5] Scheme 3.5 shows the ring-opening degradation mechanism for $BMIm^+$ Cl^- in alkaline media, where the new peak is attributed to the proton at position 1'. The degree of degradation by this ring-opening reaction was calculated by the relative integrations of the indicated ^1H resonances (*i.e.*, 1'/(1 + 1'), Scheme 3.5), and was calculated to be 20.0% and 88.1% for $BMIm^+$ Cl^- in 20 and 50 eq KOH/D_2O solutions, respectively, at 30 °C for 168 h.

Similarly, a ring opening reaction was observed in the C2-methyl-substituted imidazolium salt (Figure 3.2B), $BDMIm^+ Cl^-$; degree of degradation at 30 °C for 168 h was found to be 0.0%, 2.0%, and 13.8% in 2, 20 and 50 eq KOH/D_2O solutions, respectively, indicating that methyl-substitution in the C2 position of imidazolium salts hinders hydroxide attack compared to the C2-unsubstituted ionic salt ($BMIm^+ Cl^-$). These results corroborate with resent findings in literature.[10] It is also notable that in both salts, the proton peaks associated with the C2, C4, and C5 positions of imidazole rings disappear in the presence of D_2O due to the hydrogen/deuterium (H/D) exchange reaction.

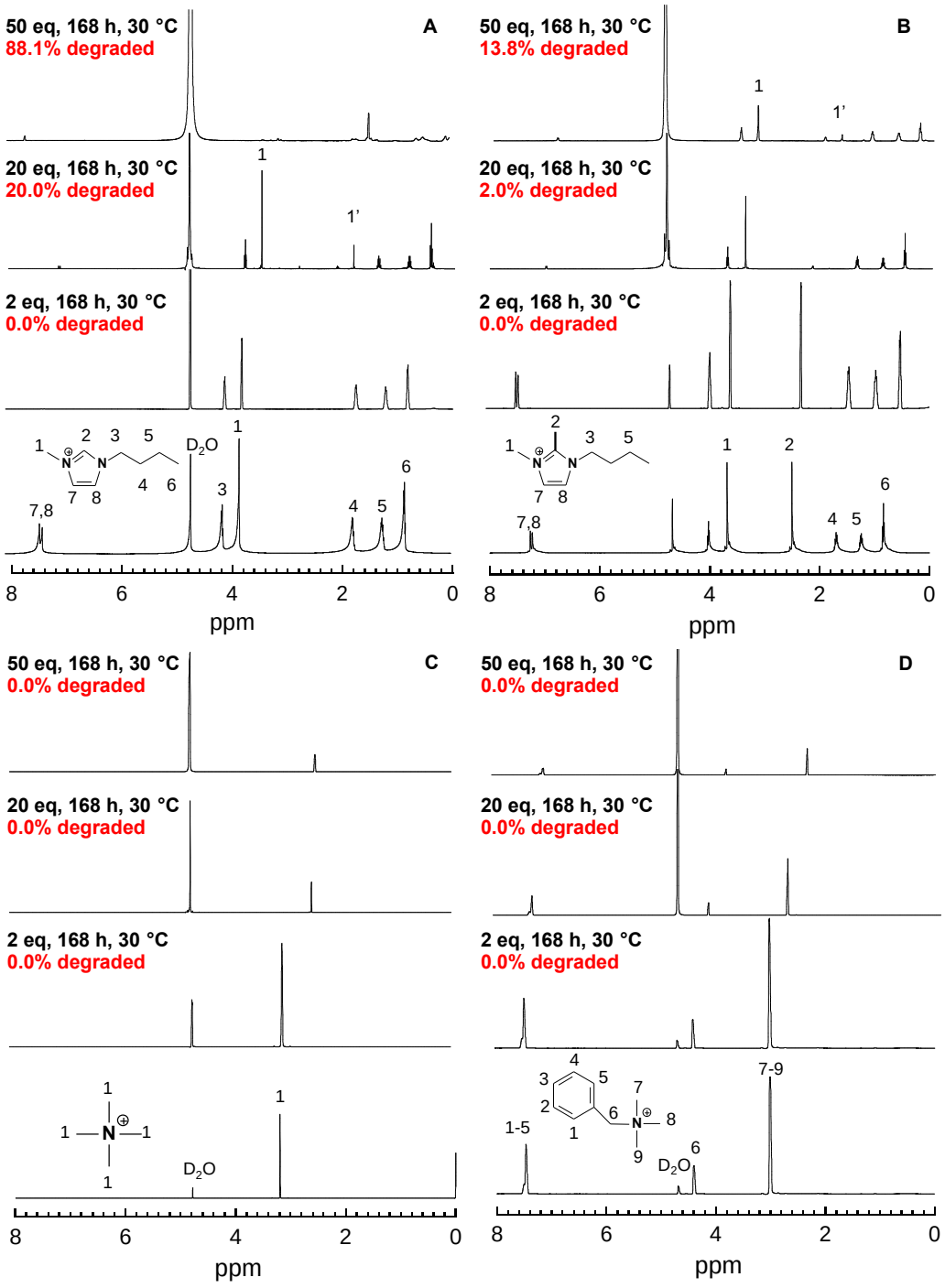

Figure 3.2 ^{1}H NMR spectra for (A) $BMIm^{+}$ Cl^{-}, (B) $BDMIm^{+}$ Cl^{-}, (C) TMA^{+} Cl^{-}, (D) $BTMA^{+}$ Cl^{-}, (E) HMG^{+} Cl^{-}, (F) BMP^{+} Cl^{-}, (G) TMP^{+} Cl^{-} in 2, 20 and 50 eq KOH/D_2O at 30 °C for 168 h.

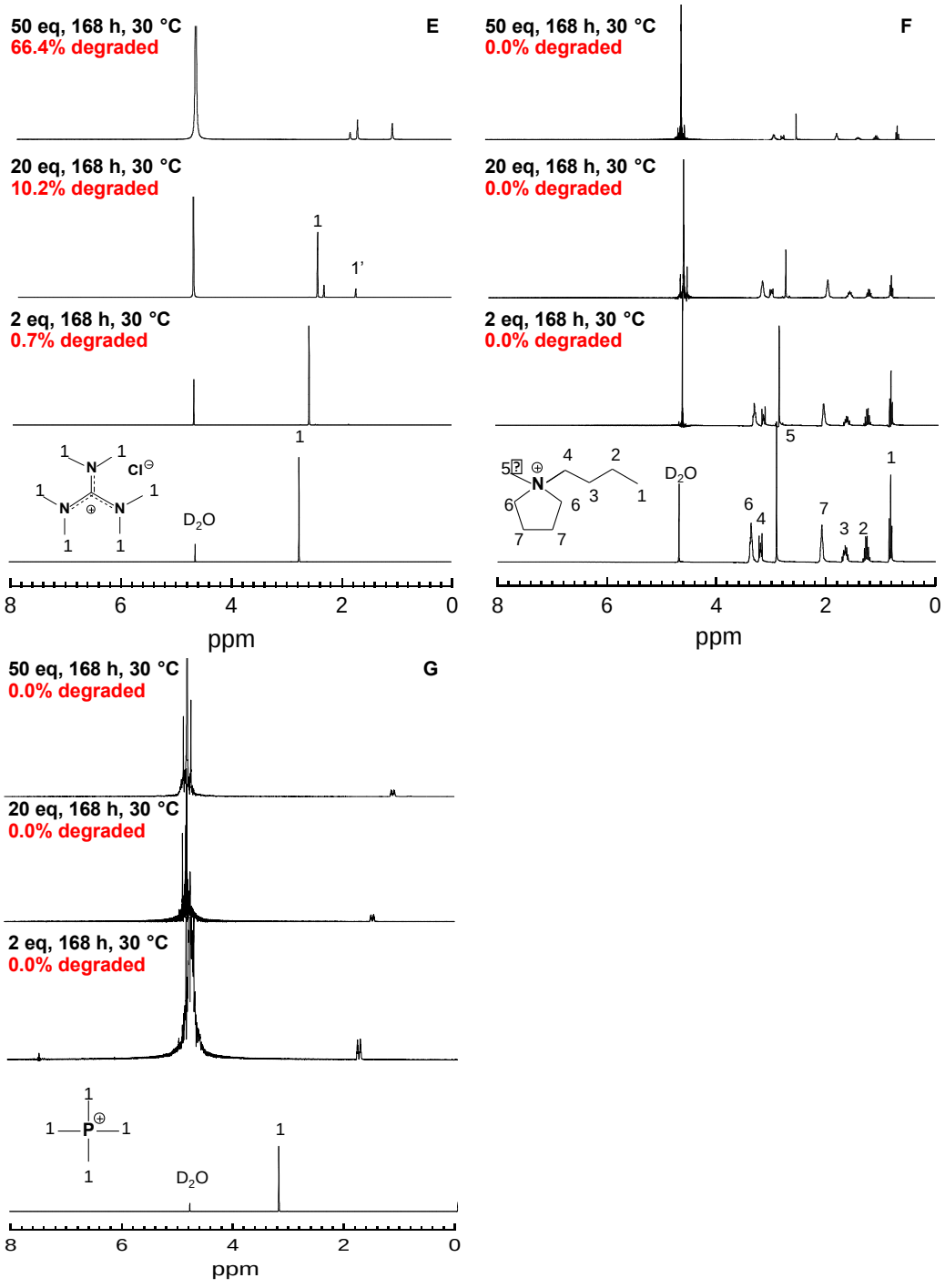

Figure 3.2 Continued

Scheme 3.5 Ring opening reaction of 3-butyl-1-methylimidazolium.

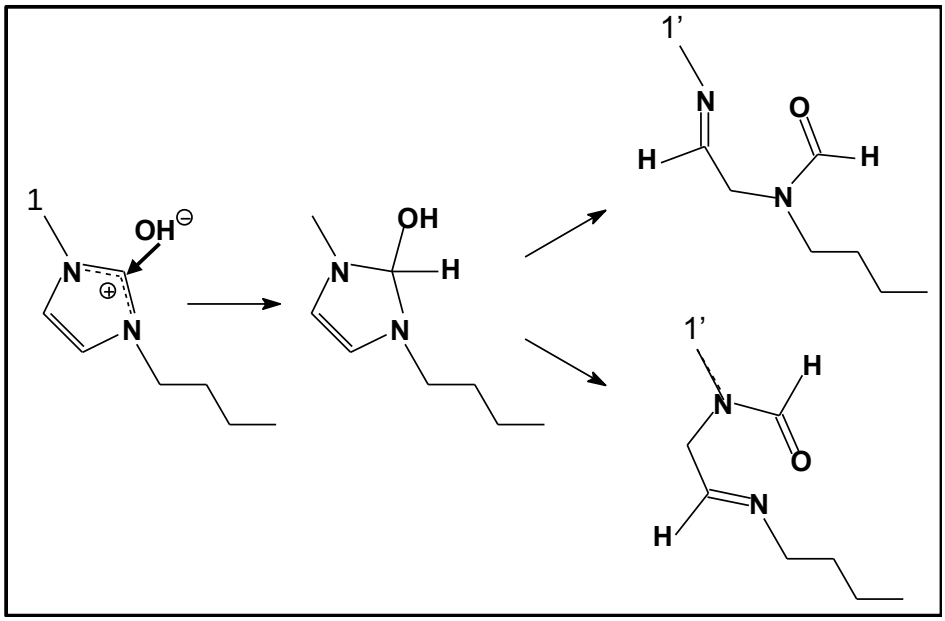

Figure 3.3 shows ^{1}H NMR spectra of each ionic salt in this study after 168 h exposure to 2 and 20 eq KOH/D_2O solutions at a higher temperature (80 °C). Degradation is accelerated by increased temperature, as seen in Figure 3.3A-B, where at 80 °C, both imidazolium salts show earlier signs of ring opening reactions with 0.5% degradation for 2 eq, compared with 0.0% at 30 °C at this KOH concentration. For 20 eq and 80 °C, degradation is further increased to 98.7% and 7.5% (compared with 20.0% and 2.0% at 30 °C) for $BMIm^+$ Cl^- and $BDMIm^+$ Cl^-, respectively. $BDMIm^+$ Cl^- appears to be the more chemically stable imidazolium salt at high temperature as well as low temperature.

Figures 3.2C-D and 3.3C-D show ^{1}H NMR spectra for ammonium-based ionic salts, TMA^+ Cl^- and $BTMA^+$ Cl^-, after 168 h exposure to KOH/D_2O at 30 and 80 °C, respectively. Though cation peaks do shift as expected after addition of hydroxide, no

other changes were observed as the original cation peaks are still present and no new peaks appear under any measured conditions, indicating high alkaline stability in up to at least 50 eq KOH/D_2O at 30 °C and 20 eq KOH/D_2O at 80 °C. It is possible to show chemical degradation of ammonium salts *via* nucleophilic attack at higher temperatures or with other solvents (*e.g.*, methanol);[28] however, for consistency within this study, the ionic salts were degraded under the same conditions as the PILs, which were degraded in the conditions most applicable to a fuel cell (*e.g.*, water, 80°C), that would also not cause precipitation of the degraded polymer. The phosphonium analog to TMA^+ Cl^-, TMP^+ Cl^- (Figure 3.2G and 3.3G), likewise shows no chemical degradation after 168 h under similar measured conditions: 2, 20, and 50 eq KOH/D_2O at 30 °C; 2 and 20 eq KOH/D_2O at 80 °C.

Figures 3.2E and 3.3E show ^1H NMR spectra for guanidinium ionic salt, HMG^+ Cl^-, after 168 h exposure to KOH/D_2O at 30 and 80 °C, respectively. As observed for the imidazolium salts, degradation increased with increasing hydroxide concentration, as well as increasing temperature. In Figure 3.2E, new peaks observed at ~1.8 ppm (labeled 1') were attributed to a nucleophilic-substitution reaction as described in the literature.[32] Scheme 3.6 shows the S_N2 degradation of HMG^+ Cl^- in alkaline media, where the new peak was attributed to the protons at position 1'. The degree of degradation was determined by the relative integrations of ^1H resonances of the degraded and non-degraded cation (*i.e.*, 2(1')/(3(1) + 2(1')), Scheme 3.6), and was found to be 0.7%, 10.2% and 66.4% in 2, 20, and 50 eq KOH/D_2O solutions, respectively, at 30 °C for 168 h. Figure 3.3E

shows that as temperature increased to 80 °C, degradation increased to 60.9% and 100% for 2 and 20 eq, respectively.

Similar to results for ammonium and phosphonium salts, the pyrrolidinium salt, BMP^+ Cl^- in Figure 3.2F and 3.3F shows no chemical degradation in alkaline media. This is an interesting result, as other ring-structures (imidazolium salts) show quantifiable degradation by ring opening reaction under the same conditions. One potential explanation for improved chemical stability is increased resistance to bond breakage due to lack of polarizability in the resonance-free ring structure of a pyrrolidinium versus the conjugated bonds of the imidazolium ring; steric hindrance as a result of the butyl and methyl substituents in the N1 position may also be providing protection from hydroxide attack.

Overall, high alkaline chemical stability was observed in the ammonium, phosphonium, and pyrrolidinium ionic salts, TMA^+ Cl^-, $BTMA^+$ Cl^-, TMP^+ Cl^-, BMP^+ Cl^-, as no quantifiable degradation was evidenced in as much as 50 eq KOH/D_2O at 30 °C and 20 eq KOH/D_2O at 80 °C. Of the remaining salts, the C2-methyl substituted imidazolium, $BDMIm^+$ Cl^- was observed to be the most chemically stable, with 7.5% degradation at 20 eq KOH/D_2O at 80 °C, compared with 98.7% and 100% degradation for $BMIm^+$ Cl^- and HMG^+ Cl^-, respectively, under the same conditions. A summary of the alkaline chemical degradation results for the small molecule ionic salts is listed in Table 3.1.

Table 3.1 Alkaline Chemical Degradation Results for Ionic Salts.

Ionic salt	Temp. (°C)	KOH conc. (mol. eq.)	KOH conc. (M)	NMR Spectrum Figure	Degradation[a] (%)	Degradation pathway Scheme
$BMIm^+ Cl^-$	30	2	0.29	3.2A	0.0	3.5
	30	20	2.86	3.2A	20.0	
	30	50	7.16	3.2A	88.1	
	80	2	0.29	3.3A	0.4	
	80	20	2.86	3.3A	98.7	
$BDMIm^+Cl^-$	30	2	0.27	3.2B	0.0	3.5[b]
	30	20	2.65	3.2B	2.0	
	30	50	6.63	3.2B	13.8	
	80	2	0.27	3.3B	0.8	
	80	20	2.65	3.3B	7.5	
$TMA^+ Cl^-$	30	2	0.46	3.2C	0	
	30	20	4.56	3.2C	0	
	30	50	11.41	3.2C	0	
	80	2	0.46	3.3C	0	
	80	20	4.56	3.3C	0	
$BTMA^+ Cl^-$	30	2	0.27	3.2D	0	
	30	20	2.69	3.2D	0	
	30	50	6.74	3.2D	0	
	80	2	0.27	3.3D	0	
	80	20	2.69	3.3D	0	
$HMG^+ Cl^-$	30	2	0.29	3.2E	0.7	3.6
	30	20	2.86	3.2E	10.2	
	30	50	7.16	3.2E	66.4	
	80	2	0.29	3.3E	60.9	
	80	20	2.86	3.3E	100	
$BMP^+ Cl^-$	30	2	0.28	3.2F	0	
	30	20	2.81	3.2F	0	
	30	50	7.03	3.2F	0	
	80	2	0.28	3.3F	0	
	80	20	2.81	3.3F	0	
$TMP^+ Cl^-$	30	2	0.39	3.2G	0	
	30	20	3.89	3.2G	0	
	30	50	9.72	3.2G	0	
	80	2	0.39	3.3G	0	
	80	20	3.89	3.3G	0	

[a]All samples were degraded for 168 h. [b]Analogous to degradation pathway of similar ionic salt.

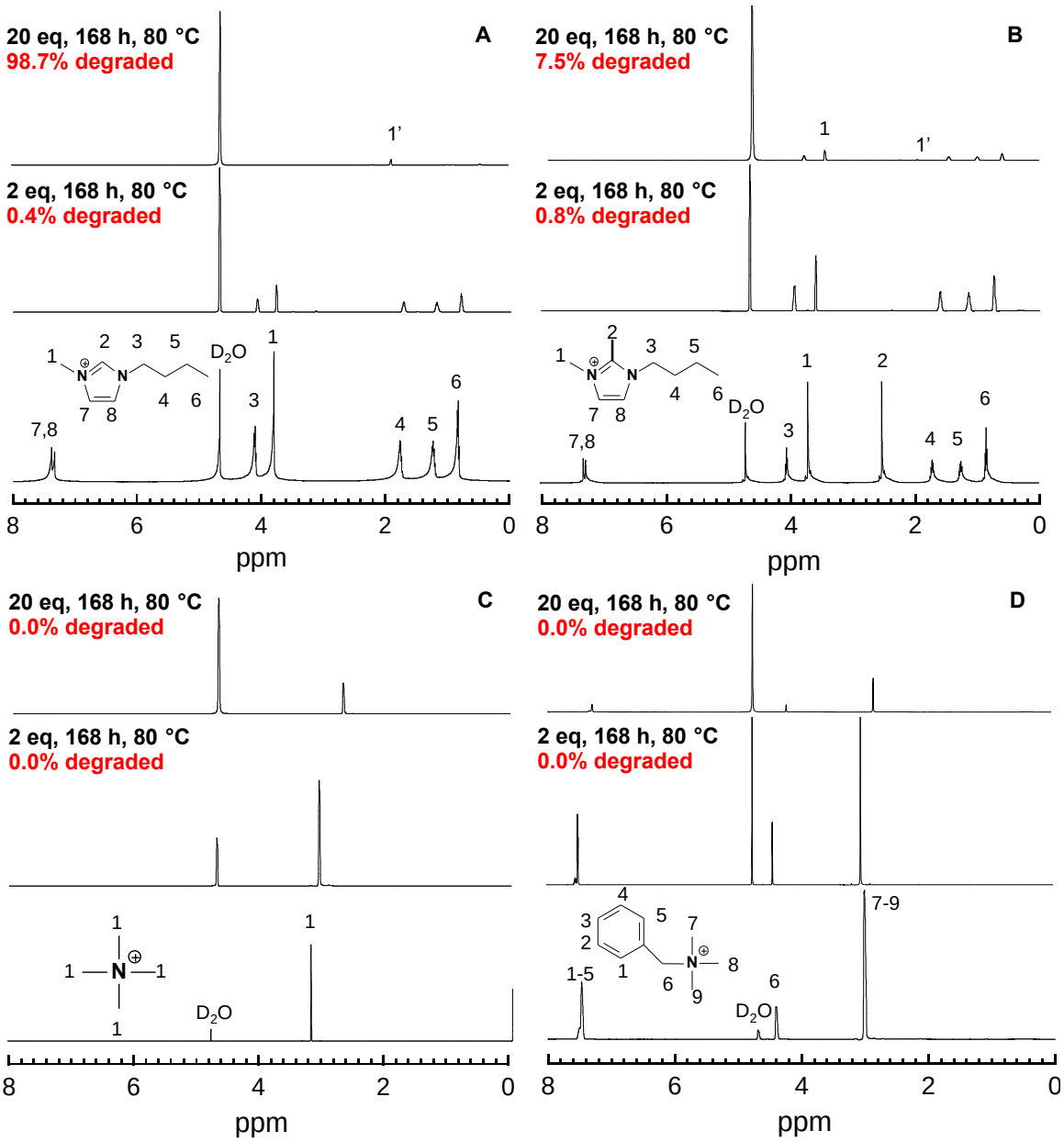

Figure 3.3 ^{1}H NMR spectra for (A) $BMIm^{+}$ Cl^{-}, (B) $BDMIm^{+}$ Cl^{-}, (C) TMA^{+} Cl^{-}, (D) $BTMA^{+}$ Cl^{-}, (E) HMG^{+} Cl^{-}, (F) BMP^{+} Cl^{-}, (G) TMP^{+} Cl^{-} in 2 and 20 eq KOH/D_2O at 80 °C for 168 h.

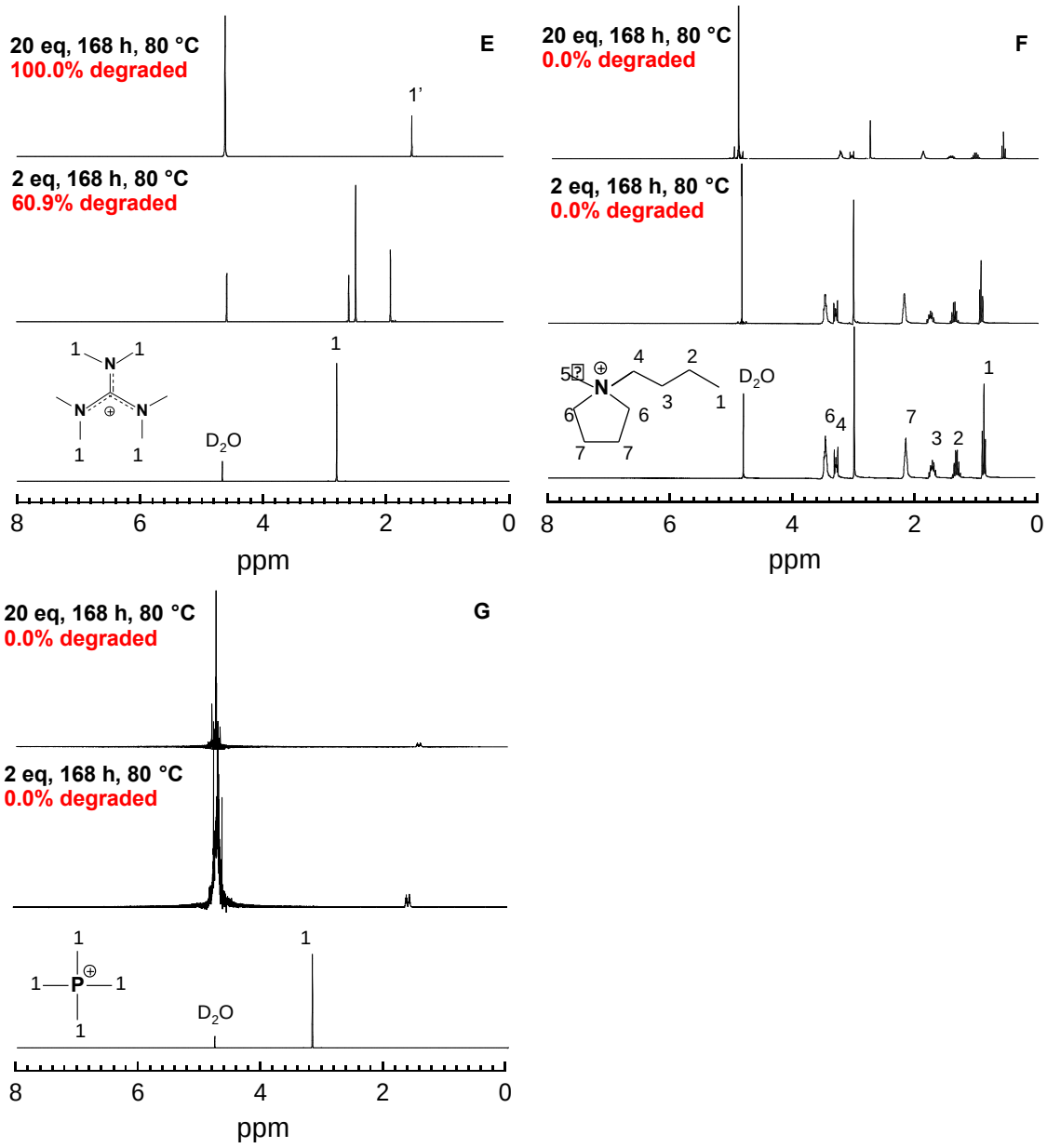

Figure 3.3 Continued

Scheme 3.6 Nucleophilic substitution reaction of hexamethylguanidinium.

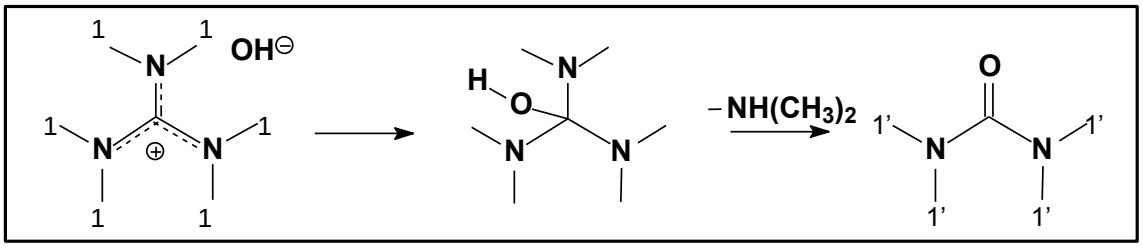

3.3.2 PIL Alkaline Chemical Stability

We synthesized and investigated the chemical stability of methacrylate-based PILs consisting of various covalently attached cations: butylimidazolium, butylmethylimidazolium, trimethylammonium, pentamethylguanidinium, butylpyrrolidinium, trimethylphosphonium; cations analogous to the ionic salts in this study. The purity, chemical structure, and degree of functionalization of these PILs were confirmed by ^{1}H NMR prior to alkaline chemical stability experiments (see Figure 3.1). PIL cation degradation was also quantified by ^{1}H NMR spectroscopy, where the effects of alkaline concentration and reaction temperature on the alkaline chemical stability of the covalently tethered cations were investigated.

Figures 3.4 and 3.5 show ^{1}H NMR spectra of each PIL after 168 h exposure to 2 and 20 eq KOH/D_2O solutions at 30 °C and 80 °C, respectively. In Figure 3.4A, the ^{1}H NMR spectra of poly(MEBIm-Br) show two new peaks at ~7.5 and ~8.43 ppm (labeled f' and e', respectively), where these peaks are attributed to ring-opening degradation as seen in the analogous small molecule salt and described in literature.[5] Likewise, in Figure 3.4B, two new peaks appear at ~7.48 and ~8.42 ppm (labeled h' and g', respectively) in the ^{1}H

NMR spectra of poly(MEBMIm-Br), also indicating a ring-opening mechanism. Alkaline degradation by this ring-opening reaction was calculated by the relative integrations of the indicated ^{1}H resonances (*i.e.*, f'/(f + f') for poly(MEBIm-Br) and g'/(g + g') for poly(MEBMIm-Br); degradation mechanism shown in Scheme 3.7), and was calculated as 12.1% and 22.3% for poly(MEBIm-Br) and 15.5% and 23.9% for poly(MEBMIm-Br) at 2 and 20 eq, respectively, at 30 °C for 168 h. Figures 3.5A-B shows the same new peaks arising under high temperature conditions; extent of degradation was calculated as 19.4% and 33.5% for poly(MEBIm-Br) and 31.3% and 38.2% for poly(MEBMIm-Br) at 2 and 20 eq, respectively, at 80 °C for 168 h. In contrast to the ionic salt chemical stability results, the C2-methyl-substituted cation showed slightly higher degradation at each condition compared to the unsubstituted cation, indicating that the resistance to ring-opening mechanism provided by steric hindrance of additional moieties in the C2 position that has been seen in the small molecule studies may not translate to covalently tethered cations. It should be noted that for both imidazolium polymers in KOH/D_2O solution, the proton peaks associated with the C2, C4, and C5 positions of imidazole rings diminished more rapidly than could be attributed solely to ring opening degradation, due to an accompanying hydrogen/deuterium (H/D) exchange reaction. It has been shown in previous studies that it is possible to suppress this H/D exchange in order to accurately calculate cation degradation by including 10 wt% H_2O (relative to mass of polymer).[5] Therefore, for the imidazolium PILs only, 80 mg of D_2O was replaced with 80 mg of H_2O, to maintain a total of 1 mL water (deuterated and non-deuterated), while also preventing H/D exchange. Additional ^{1}H NMR spectra (Appendix B, Figure B2-3) confirm that the

exchange is fully suppressed for the imidazolium PILs when H_2O is included. For the remaining three PILs, ^1H NMR spectra (Appendix B Figure B4-5) confirm that, as anticipated, there is no H/D exchange in D_2O at 80° C for 168 h, such that any reduction in the cation peaks in the presence of KOH can be attributed solely to alkaline degradation reaction; it is therefore not necessary to include H_2O in the solution. It was also confirmed (Appendix B, Figure B6) that including H_2O would not change the results for these PILs, and thus the imidazolium results in KOH/D_2O/H_2O solutions are analogous to results for the other three PILs in KOH/D_2O solutions. Similar results were obtained for the imidazolium salts, where no difference in degradation was observed between D_2O or H_2O solutions (Appendix B, Figure B7).

Figures 3.4C and 3.5C show ^1H NMR spectra for the quaternary ammonium-based PIL, poly(METMA-Br), after 168 h exposure to KOH/D_2O at 30 and 80 °C, respectively. Two major degradation reactions are generally accepted for pendant quaternary ammonium cations: 1) nucleophilic substitution (S_N2 reaction) *via* hydroxide attack on the α carbons resulting in amine and alcohol byproducts and 2) Hofmann degradation (E2 elimination) from the removal of the β hydrogen by hydroxide, resulting in amine and alkene byproducts (Scheme 3.8).[109] The S_N2 reaction and E2 elimination occur simultaneously, leading to a mixture of byproducts; one mechanism may be preferential depending upon the chemical structure and degradation conditions. In Figure 3.4C, nucleophilic substitution reactions were observed for the trimethylammonium cation as new peaks appeared at ~3.92 ppm (labeled i') and ~2.09 ppm (labeled i'') in solutions of 2 and 20 eq KOH/D_2O at 30 °C; Hofmann elimination reaction was not observed at 30 °C. Extent of

degradation of the cation, defined as the relative integrated intensities of corresponding ^{1}H NMR peaks (*i.e.*, (9i' + 3i'')/(2i + 9i' + 3i'')), was 46.4% and 75.5% for 2 or 20 eq, respectively, at 30 °C. At 80 °C, in addition to the degradation peaks seen in Figure 3.4C, Figure 3.5C shows two additional peaks located at ~5.45 ppm and ~5.67 ppm (labeled i'''). These new peaks indicate degradation by Hofmann elimination occurred at this higher temperature condition; subsequently, relative integration ratios include the new peaks (*i.e.*, (9i' + 3i''+ 9i''')/(2i + 9i' + 3i'' + 9i'''). Cation degradation was quantified as 72.1% and 94.8% upon exposure to 2 and 20 eq KOH/D_2O solutions, respectively, at 80 °C. While degradation increased with increasing temperature, the S_N2 reaction, specifically the pathway that resulted in a pendant hydroxyl and an amine byproduct, was the primary degradation mechanism at both low and high temperatures.

The guanidinium-based PIL, poly(MEPMG-Br), was not water-soluble and was therefore excluded from the chemical stability study. For the pyrrolidinium-based PIL, poly(MEBP-Br), in Figure 3.4D and 3.5D, limited degradation was observed in the ^{1}H NMR spectra after 168 h exposure to 2 or 20 eq KOH/D_2O at 30 °C and 80 °C, respectively, as a new peak arises at ~5.60 ppm (labeled j'). Similar degradation has been described in literature; proposed Hofmann elimination mechanism shown in Scheme 3.9.[35] The degree of degradation of the cation can be calculated by the relative integrated intensities of corresponding ^{1}H NMR peaks (*i.e.*, j'/(k + j')) and was 9.3% and 10.3% for 2 and 20 eq, respectively, at 80 °C, indicating a high alkaline chemical stability at these conditions. Hofmann elimination reaction was further confirmed by the minimal

degradation at 30 °C (1.5% and 3.1% for 2 and 20 eq, respectively), as this mechanism is known to favor higher temperatures.

Figures 3.4E and 3.5E show ^{1}H NMR spectra for the quaternary phosponium-based PIL, poly(METMP-Br), at 30 and 80 °C, respectively, after 168 h exposure to 2 and 20 eq KOH/D_2O solutions. The phosphonium cation is known to degrade by the Cahours-Hofmann reaction, where hydroxide attacks the phosphonium tetrahedron, resulting in phosphine oxide and an alkyl group as byproducts (Scheme 3.10).[110,111] In both Figure 3.4E and 5E, the two new peaks appearing at ~3.84 and ~3.77 ppm (labeled l') are associated with the -CH_2- of the alkyl chain remaining on the polymer after the phosponium group has been cleaved, while the new peak at ~1.12ppm (labeled l'') is associated with the small molecule byproduct, trimethylphosphonium oxide. Integration of the degradation peaks relative to the remaining covalently tethered polymer cation peak (*i.e.*, 9l'/(l + 9l')) yields degradation degrees of 63.4% and 93.1% for 2 or 20 eq, respectively, at 30 °C. At 80 °C, degradation could not be quantified, because the polymer precipitated from solution and the precipitate was black in color. A summary of the alkaline chemical degradation results for the PILs with various cations are listed in Table 3.2.

Table 3.2 Alkaline Chemical Degradation Results for PILs with Various Cations.

PIL	T (°C)	KOH conc.[a] (mol. eq.)	KOH conc. (M)	NMR Spectra Figure	Cation Degradation[b] (%)	Degradation pathway Scheme
Poly(MEBIm-Br)	30	2	0.05	3.4A	12.1	3.7[c]
	30	20	0.50	3.4A	22.3	
	80	2	0.05	3.5A	19.4	
	80	20	0.50	3.5A	33.5	
Poly(MEBMIm-Br)	30	2	0.05	3.4B	15.5	3.7
	30	20	0.48	3.4B	23.9	
	80	2	0.05	3.5B	31.3	
	80	20	0.48	3.5B	38.2	
Poly(METMA-Br)	30	2	0.06	3.4C	46.4	3.8
	30	20	0.63	3.4C	75.5	
	80	2	0.06	3.5C	72.1	
	80	20	0.63	3.5C	94.8	
Poly(MEBP-Br)	30	2	0.05	3.4D	1.5	3.9
	30	20	0.50	3.4D	3.1	
	80	2	0.05	3.5D	9.3	
	80	20	0.50	3.5D	10.3	
Poly(METMP-Br)	30	2	0.06	3.4E	63.4	3.10
	30	20	0.59	3.4E	93.1	
	80	2	0.06	3.5E	[d]	
	80	20	0.59	3.5E	[d]	

[a]In samples of poly(MEBIm-Br) and poly(MEBMIm-Br), 80 mg of D_2O was replaced with 80 mg of H_2O to suppress H/D exchange. [b]All samples were degraded for 168 h; amounts refer to both cleaved and uncleaved cation, see Supporting Information for backbone degradation due to hydrolysis. [c]Degradation pathway of poly(MEBIm-Br) is analogous to degradation pathway of poly(MEBMIm-Br). [d]Polymer precipitated under these conditions.

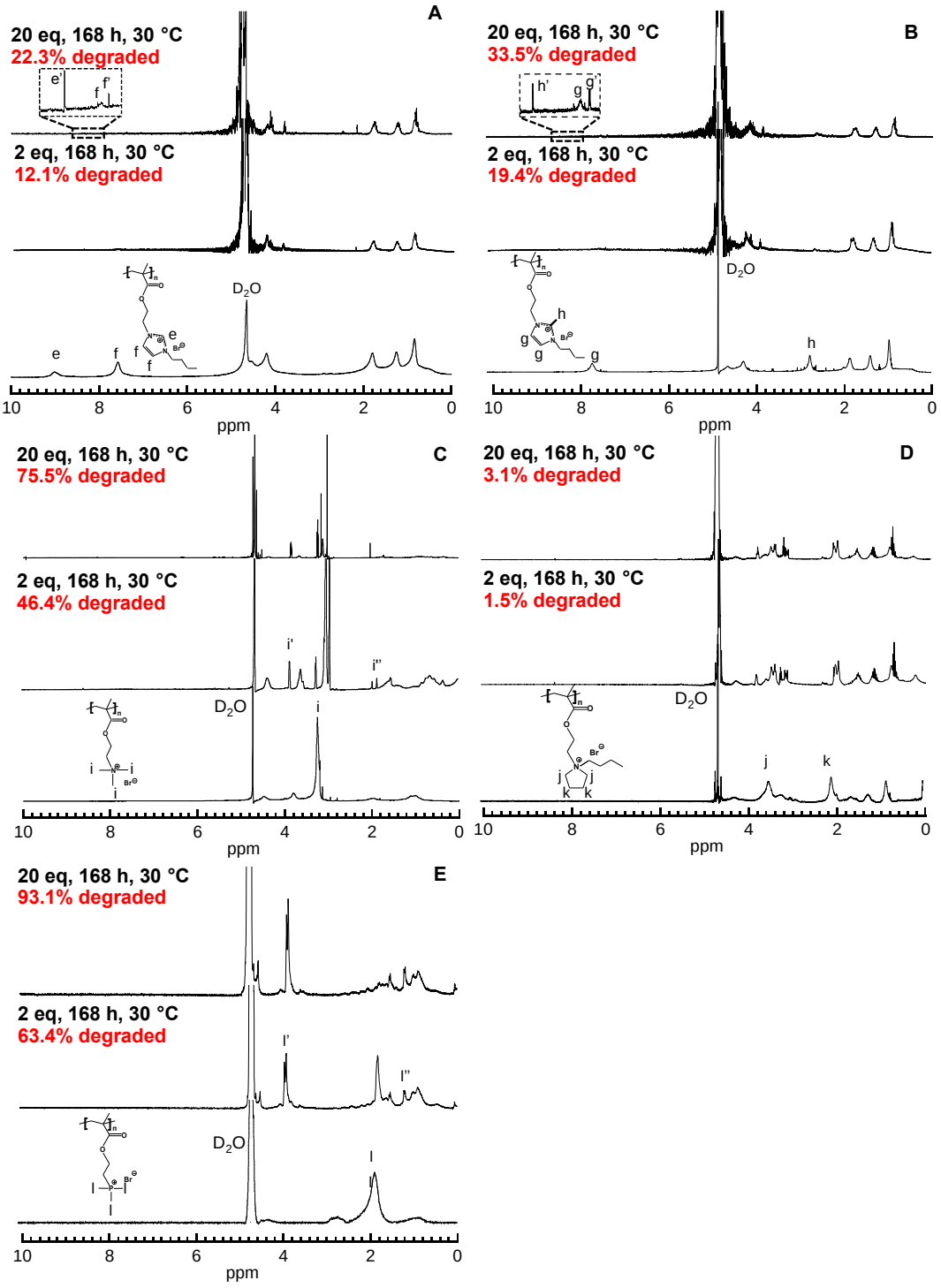

Figure 3.4 ^{1}H NMR spectra for (A) poly(MEBIm-Br), (B) poly(MEBMIm-Br), (C) poly(METMA-Br), (D) poly(MEBP-Br) and (E) poly(METMP-Br) in 2 and 20 eq KOH/D_2O at 30 °C for 168 h.

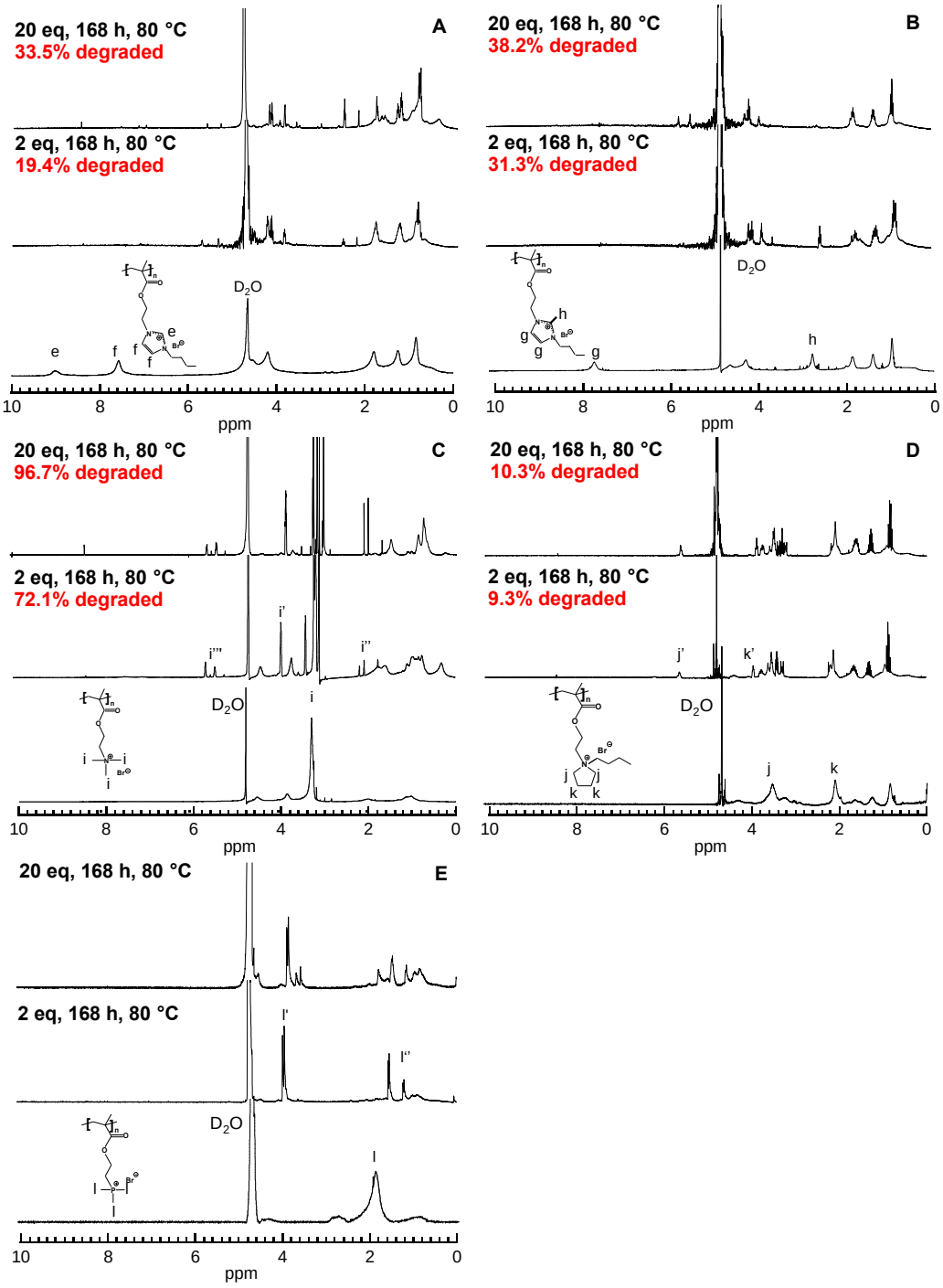

Figure 3.5 ^{1}H NMR spectra for (A) poly(MEBIm-Br), (B) poly(MEBMIm-Br), (C) poly(METMA-Br), (D) poly(MEBP-Br) and (E) poly(METMP-Br) in 2 and 20 eq KOH/D_2O at 80 °C for 168 h.

Scheme 3.7 Ring opening reaction of poly(MEBMIm-Br).

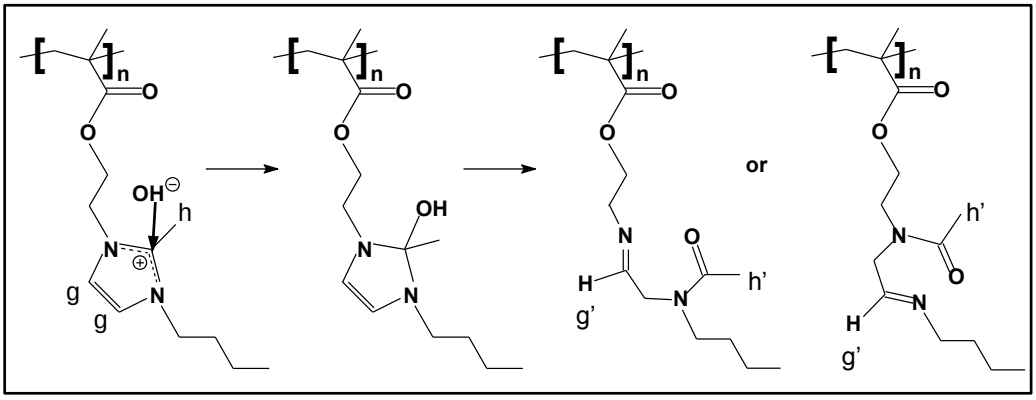

Scheme 3.8 Degradation reactions of poly(METMA-Br).

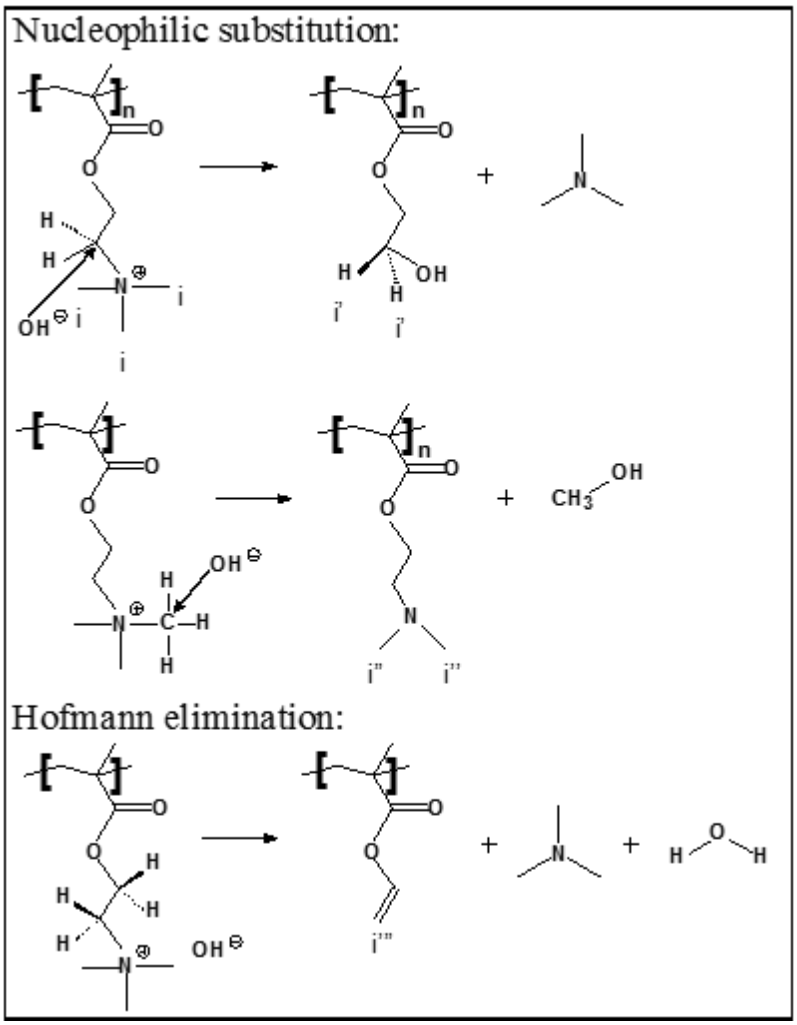

Scheme 3.9 Hofmann elimination reaction of poly(MEBP-Br).

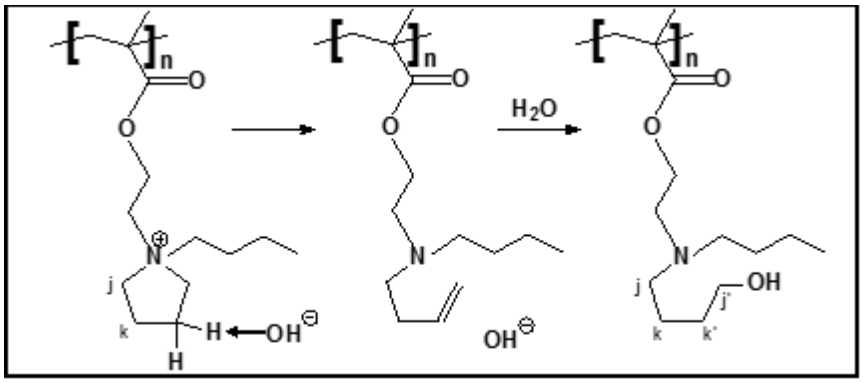

Scheme 3.10 Cahours-Hofmann reaction of poly(METMP-Br).

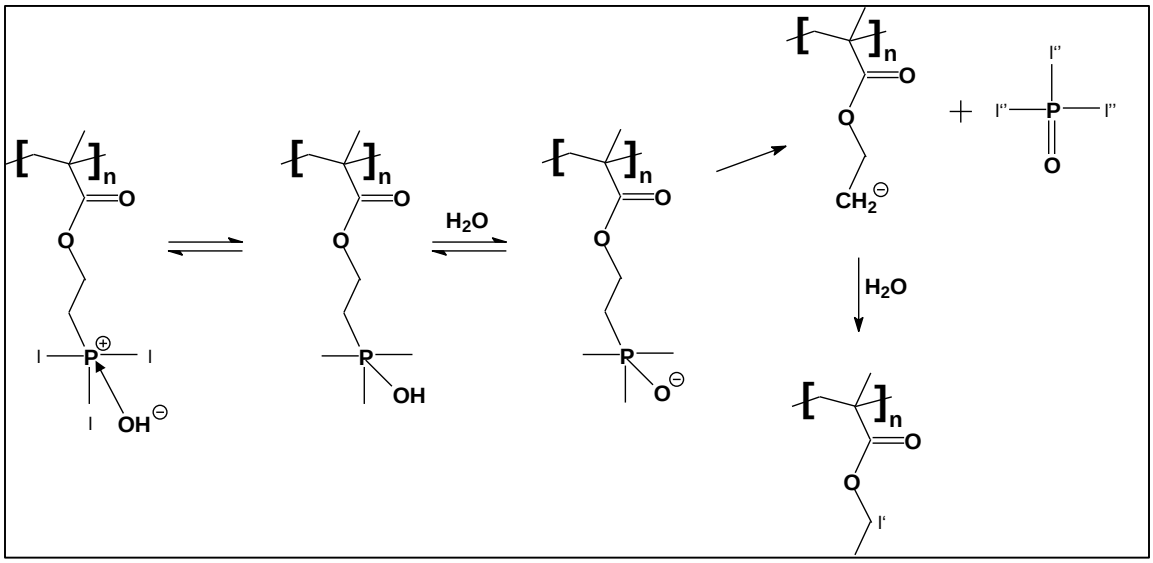

Note that, in addition to the chemical stability of cations, another potential concern is hydrolysis degradation of the carboxylate ester linkage of the methacrylate-based PIL backbone under alkaline conditions. Although the hydrolysis of a polymeric ester has been reported in literature, it typically occurs at a much slower rate compared to small molecule esters;[112] degradation rate is significantly dependent on the structure of the polymer

backbone, with the hydrolysis of a methacrylate-based polymer observed to occur at a significantly slower rate compared to the acrylate analog.[113] For poly(methyl methacrylate) (PMMA), studies have confirmed that ~9% of the monomer units are susceptible to hydrolysis.[113] Previous research has suggested ester hydrolysis of the hydroxide-exchanged methacrylate-based PIL, poly(MEBIm-OH), occurs after the ring-opening mechanism of the butylimidazolium cation, as ring-opened imidazolium byproducts were present in both covalently attached (non-hydrolyzed) and cleaved (hydrolyzed) forms; ~30% of the ring-opened byproducts (~11% of the total monomer units) were cleaved from the polymer *via* ester hydrolysis after 168 h at 80 °C and 1 M KOH.[5] In this study, for the imidazolium-based PILs, poly(MEBIm-Br) and poly(MEBMIm-Br), ~18% and ~15% of the total monomer units (~55% and ~40% of the ring-opened byproducts), respectively, had cleaved from the polymer after 168 h at 80 °C and 20 eq KOH (see Figure B8 and Schemes B1 and B2 in Appendix B).; these results are in relatively good agreement with results for PMMA and poly(MEBIm-OH). For poly(MEBP-Br), after 168 h in 20 eq KOH/D_2O at 80 °C, evidence of significant hydrolysis is noted in the undegraded cation peaks, as well as the peaks that arise due to the E2 elimination reaction; overall, 65.5% of the backbone undergoes hydrolysis (see Figures B9 and B10 and Scheme B3 in Appendix B). This could provide a potential explanation for the extraordinarily high chemical stability of poly(MEBP-Br), as the small molecule byproduct of hydrolysis may have higher resistance to hydroxide attack, keeping the pyrrolidinium ring intact. However, of the cations that remained tethered to the polymer backbone in 20 eq KOH/D_2O at 80 °C for 168 h, only 24.1% underwent E2

elimination; butylpyrrolidinium remains the most chemically stable polymeric cation of those considered. Ester hydrolysis was not identified as a primary mechanism of degradation in the ammonium-based PIL (see Figure B11 in Appendix B).

3.4 Conclusions

The alkaline chemical stability of PILs with various cations was examined with ^{1}H NMR spectroscopy in comparison with their analogous ionic salts. Results show enhanced chemical stability of imidazolium- and pyrrolidinium-based PILs relative to quaternary ammonium- and phosphonium-based PILs. Results for the ionic salts are in stark contrast to the PILs, as the imidazolium salts showed significantly more degradation than the quaternary ammonium and phosphonium salts at all conditions examined, while the pyrrolidinium-based salt showed degradation equivalent to that of the ammonium- and phosphonium-based salts. Another inconsistency between salt and polymer was observed when comparing the two imidazolium cations; ionic salt results showed that methyl-substitution in the C2 position significantly lessened degradation, while the PIL with unsubstituted imidazolium actually showed higher chemical stability under all conditions measured compared to its substituted PIL counterpart. Overall, the alkaline chemical stability of the free cations in solution investigated in this study show no correlation to that of the tethered cations on the PILs, suggesting that small molecule studies may not provide a solid basis for comparison of relative cation stability as a preliminary screening tool for determining the most promising cations.

This study answers an important question regarding AEM alkaline chemical stability: whether chemical stability of small molecule salts can be extrapolated to polymeric cations, as is commonly practiced in literature. This study suggests that there is no clear correlation, highlighting the importance of the backbone type in designing AEM chemistries and suggests that assessments of alkaline chemical stability can only be accurate for the particular polymer backbone/cation pairing being assessed. Further investigation into backbone/cation pairings could produce increased alkaline chemical stability in AEMs, as well as improved transport properties.

CHAPTER IV

ALKALINE CHEMICAL STABILITY AND ION TRANSPORT IN POLYMERIZED IONIC LIQUIDS WITH VARIOUS BACKBONES AND CATIONS

4.1 Introduction

Achieving long-lifetime AFC performance will require that both the polymer backbone, as well as the attached cation, maintain long-term chemical stability in alkaline media at moderate temperatures (60 to 80 °C). Additionally, AEMs for AFC applications require sufficient hydroxide transport (*i.e.*, conductivities > 10 mS cm^{-1}) and adequate mechanical properties (*i.e.*, limited membrane swelling from water sorption). Further investigation is required to determine the optimal backbone and cation pairings for long-term AEM stability in the presence of hydroxide, in conjunction with high hydroxide ion conductivity at moderate water uptakes, in order to achieve peak AFC performance.

In the previously discussed study,[36] we synthesized polymerized ionic liquids (PILs) with an ethyl methacrylate backbone containing various covalently attached cations: butylimidazolium, butylmethylimidazolium, trimethylammonium, butylpyrrolidinium, trimethylphosphonium. The alkaline chemical stability of these PILs was investigated and compared to their analogous ionic salts: 1-butyl-3-methylimidizolium chloride, 1-butyl-2,3-dimethylimidazolium chloride, tetramethylammonium chloride, benzyltrimethylammonium chloride, 1,1-butylmethylpyrrolidinium chloride, tetramethylphosphonium chloride. The degradation pathways and extent of chemical

stability of the PILs and ionic salts were determined using ^{1}H NMR spectroscopy after exposure to 2 or 20 molar equivalents (eq) of KOH per cation at 30 °C or 80 °C for 168 h. This tandem study of AEMs alongside analogous small molecule cations established that small molecules do not necessarily provide accurate representations of the alkaline chemical stability behavior of polymeric cations, thus emphasizing the importance of considering polymer backbone type and cation attachment to the backbone with regard to alkaline chemical degradation. Additionally, in this previous study, pyrrolidinium-based cations demonstrated significant improvements in alkaline chemical stability, motivating future exploration of these cations.

In this study, we synthesized twelve polymerized ionic liquids (PILs) with four backbones (ethyl methacrylate (Scheme 4.1a), undecyl methacrylate (Scheme 4.1b), undecyl acrylate (Scheme 4.1c), styrene (Scheme 4.1d)) and three covalently tethered cations on each backbone (butylimidizolium, trimethylammonium, butylpyrrolidinium). The alkaline chemical stability and degradation pathways of these PILs were determined using ^{1}H NMR spectroscopy after exposure to 20 molar eq of KOH (0.5 M) per cation at 60 °C for 168 h. Bromide ion conductivity and water uptake of the twelve PILs were evaluated *via* impedance spectroscopy and dynamic vapor sorption, respectively, at 60 °C and 90% RH. These results provide a consistent measure of relative alkaline chemical stability and transport properties of three major cation types (pyrrolidinium, imidazolium, ammonium), as well as four major backbone types (ethyl methacrylate, undecyl methacrylate, undecyl acrylate, styrene).

Scheme 4.1. Chemical structures of PILs with various backbones and pendant cations.

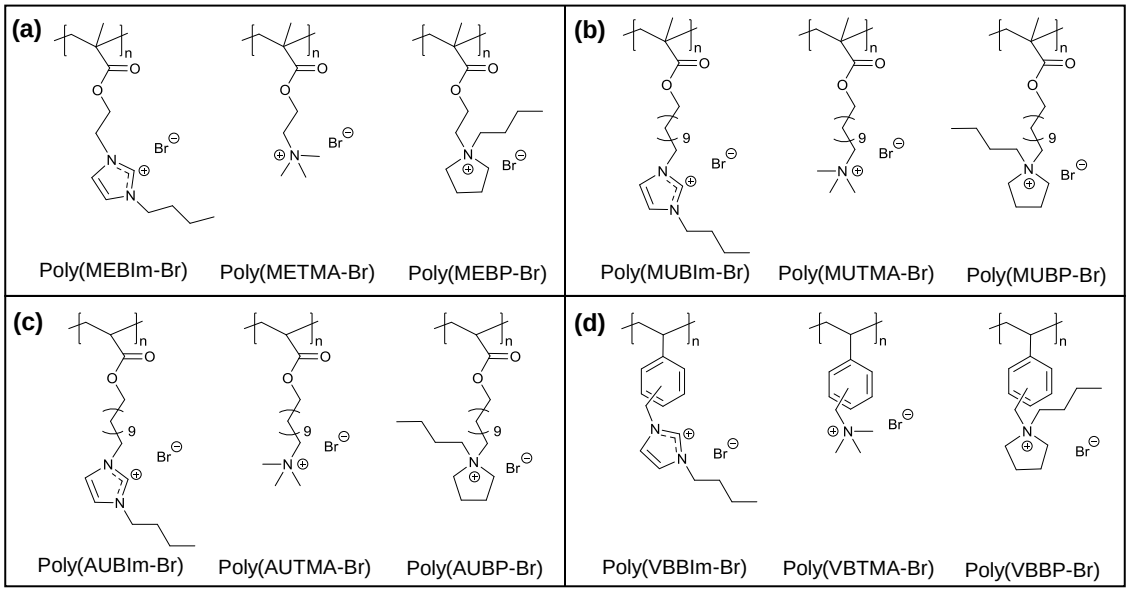

4.2 Experimental Section

4.2.1 Materials

2-(Dodecylthiocarbonothioylthio)-2-methylpropionic acid (chain transfer agent (CTA), 98%, HPLC), 11-bromo-1-undecanol (98%), magnesium sulfate (anhydrous, ReagentPlus®, 99%), triethylamine (≥99.5%), methacryloyl chloride (97%, stabilized with 200 ppm monomethyl ether hydroquinone (MEHQ)), dichloromethane (ACS reagent, ≥99.5%, contains 50 ppm amylene stabilizer), poly(vinylbenzyl chloride) (60/40 mixture of 3- and 4-isomers, M_n ~55.0 kg mol^{-1}, M_w ~100 kg mol^{-1} by GPC/MALLS), N-dimethylformamide (DMF, ACS Reagent, ≥99.8%), 1-butylimidazole (98%), trimethylamine solution (45 wt% in H_2O), 1-butylpyrrolidine (98%), hexane (ACS Reagent, ≥98.5%), tetrahydrofuran (THF, ≥99.9%), methanol (ACS Reagent, ≥99.8%,), diethyl ether (anhydrous, ≥99.7%, contains 1 ppm BHT inhibitor), potassium hydroxide

(KOH, ≥90%, reagent grade), deuterium oxide (D_2O, 99.98 atom% D), dimethyl-d_6 sulfoxide (DMSO-d_6, 99.9 atom% D, contains 0.03% v/v TMS), and tetrahydrofuran (THF, HPLC grade, ≥99.9%) were used as received from Sigma-Aldrich. Azobis(isobutyronitrile) (AIBN, 98%, Sigma-Aldrich) was purified by recrystallization twice from methanol.

4.2.2 Synthesis of Poly(BrEMA) and Ethyl Methacrylate PILs

Synthesis of the non-ionic precursor monomer, 2-bromoethyl methacrylate (BrEMA) was performed according to a procedure in literature.[41] The synthesis and characterization of the non-ionic precursor homopolymer, poly(BrEMA) is well documented in the previous study, along with the synthesis and characterization of the following post-functionalized PILs: poly(MEBIm-Br) [MEBIm-Br = 1-[(2-methacryloyloxy) ethyl]-3-butylimidazolium bromide], poly(METMA-Br) [MEBIm-Br = 1-[(2-methacryloyloxy) ethyl]-3-trimethylammonium bromide], and poly(MEBP-Br) [MEBIm-Br = 1-[(2-methacryloyloxy) ethyl]-3-butylpyrrolidinium bromide] (Scheme 4.2(a); NMR, Figure 4.1).[36]

4.2.3 Synthesis of Poly(BrUMA)

Synthesis of the non-ionic precursor monomer, 11-bromoundecyl methacrylate (BrUMA) and the non-ionic precursor homopolymer, poly(BrUMA) is well documented in a previous study.[4] The synthesis of the non-ionic precursor homopolymer, poly(BrUMA), was performed using conventional free-radical polymerization as shown

in Scheme 4.2(b). A typical example is given as follows. 16.0 g (50.3mmol) of BrUMA monomer in DMF (BrUMA/DMF 1/2 w/w) and 41.6 mg (0.25 mmol) AIBN were mixed in a 200 mL round bottom Schlenk flask and reacted under N_2 for 1 h at 65 °C. The resulting polymer was twice precipitated in methanol, filtered and then dried under vacuum in an oven at room temperature for 24 h. Yield: ~3 g (~19%); resulting polymer was adhesive to reaction vial and thus yield could only be estimated. ^{1}H NMR (500 MHz, $CDCl_3$, 23 °C) δ (ppm): 4.15-3.75 (s, 2H, Br-CH_2-CH_2-$(CH_2)_7$-CH_2-C*H*$_2$-O), 3.69-3.38 (m, 2H, Br-C*H*$_2$-CH_2-$(CH_2)_7$-CH_2-CH_2-O), 2.11-1.70 (m, 2H, C*H*$_2$-C(CH_3)), 1.70-1.51 (s, 2H, Br-CH_2-CH_2-$(CH_2)_7$-C*H*$_2$-CH_2-O), 1.51-1.39 (s, 2H, Br-CH_2-C*H*$_2$-$(CH_2)_7$-CH_2-CH_2-O), 1.39-1.22 (s, 2H, Br-CH_2-CH_2-(C*H*$_2$)$_7$-CH_2-CH_2-O), 1.13-0.71 (m, 2H, C*H*$_2$-C(CH_3)) (NMR, Appendix C, Figure C1). SEC (THF, 40 °C): M_n = 41.96 kg mol^{-1}, M_w/M_n = 2.23 (against PS standards).

4.2.4 Synthesis of Poly(MUBIm-Br)

Synthesis of the PIL homopolymer, poly(MUBIm-Br) [MUBIm-Br = 1-[(2-methacryloyloxy) undecyl]-3-butylimidazolium bromide], is shown in Scheme 4.2(b), *i.e.*, functionalization of non-ionic precursor homopolymer, 2-bromoundecyl methacrylate, to form an ionic homopolymer. A typical example is given as follows. 0.500 g (1.57 mmol) of poly(BrUMA) was first dissolved in ~5 mL DMF in a 50 mL vial. 0.973 g (7.83 mmol) of 1-butylimidazole (poly(BrUMA)/1-butylimidazole, 1/5 mol/mol) was then mixed into the vial. The solution was stirred at 80 °C for 48 h. The resulting polymer was precipitated twice into hexane followed by multiple washes with diethyl ether and dried under vacuum

in an oven at room temperature for 24 h. Yield: 0.399 g (0.900 mmol) of solid particles (57.5%). ^{1}H NMR (500 MHz, D_2O, 23 °C) δ (ppm): 7.90-7.50 (s, 2H, N-C*H*=C*H*-N), 4.54-4.04 (m, 4H, N-C*H*$_2$-$(CH_2)_9$-CH_2-O, N-C*H*$_2$-CH_2-CH_2-CH_3), 1.81 (s, 4H, C*H*$_2$-C(CH_3), N-CH_2-C*H*$_2$-CH_2-CH_3), 1.69-1.00 (s, 20H, N-CH_2-(C*H*$_2$)$_9$-CH_2-O N-CH_2-CH_2-C*H*$_2$-CH_3, 1.00-0.65 (s, 6H, N-CH_2-CH_2-CH_2-C*H*$_3$, CH_2-C(C*H*$_3$)) (NMR, Figure 4.1).

4.2.5 Synthesis of Poly(MUTMA-Br)

Synthesis of the PIL homopolymer, poly(MUTMA-Br) [MUTMA-Br = 1-[(2-methacryloyloxy) undecyl]-trimethylammonium bromide], is shown in Scheme 4.2(b). A typical example is given as follows. 0.500 g (1.57 mmol) of poly(BrUMA) was first dissolved in ~2 mL DMF in a 50 mL vial. 1.029 g (7.83 mmol) of trimethylamine in aqueous solution (poly(BrUMA)/trimethylamine, 1/5 mol/mol) was then mixed into the vial. The solution was stirred at room temperature for 48 h. The resulting polymer was precipitated twice into diethyl ether and dried under vacuum in an oven at room temperature for 24 h. Unlike the other eleven PILs, poly(MUTMA-Br) was not water soluble, and therefore NMR was performed in DMSO-d_6; the TMA cation peak was consequently coupled with the water peak (which was present due to the hygroscopic nature of PILs with bromide counter ions) and therefore full functionalization was confirmed *via* elemental analysis (EA) by comparing the molar ratios of N to Br. Yield: 0.478 g (1.26 mmol) of solid particles (80.6%). ^{1}H NMR (500 MHz, DMSO-d_6, 23 °C) δ (ppm): 4.40-4.07 (s, 2H, N-CH_2- $(CH_2)_9$-C*H*$_2$-O), 4.06-3.79 (s, 2H, N-CH_2-$(CH_2)_9$-C*H*$_2$-O), 3.78-3.37 (s, 9H, N-(C*H*$_3$)$_3$), 2.16-1.93 (m, 2H, C*H*$_2$-C(CH_3)), 1.93-1.77 (s, 2H, N-

CH_2-CH_2-$(CH_2)_7$-CH_2-CH_2-O), 1.77-1.28 (s, 16H, N-CH_2-CH_2-(CH_2)$_7$-CH_2-CH_2-O), 1.28-0.88 (s, 2H, CH_2-C(CH_3)) (NMR, Figure 4.1). EA Calculated: C, 57.12; H, 9.61; N, 3.70; Br, 21.11; EA Found: C, 53.40; H, 9.80; N, 3.46; Br, 16.13.

4.2.6 Synthesis of Poly(MUBP-Br)

Synthesis of the PIL homopolymer, poly(MUBP-Br) [MUBP-Br = 1-[(2-methacryloyloxy) undecyl]-1-butylpyrrolidinium bromide], is shown in Scheme 4.2(b). A typical example is given as follows. 0.500 g (1.57 mmol) of poly(BrUMA) was first dissolved in ~2 mL DMF in a 50 mL vial. 0.598 g (4.70 mmol) of 1-butylpyrrolidine (poly(BrUMA)/1-butylpyrrolidine, 1/3 mol/mol) was then mixed into the vial. The solution was stirred at 80 °C for 24 h. The resulting polymer was precipitated twice into hexane, followed by multiple washes with diethyl ether, and dried under vacuum in an oven at room temperature for 24 h. Yield: 0.567 g (1.27 mmol) of solid particles (81.1%). ^{1}H NMR (500 MHz, D_2O, 23 °C) δ (ppm): 3.68-2.91 (s, 8H, N-CH_2-CH_2-CH_2-CH_2-N, N-CH_2-CH_2-CH_2-CH_3, N- CH_2-$(CH_2)_9$-CH_2-O), 2.25-1.97 (s, 7H, N-CH_2-CH_2-CH_2-CH_2-N, CH_2-C(CH_3)), 1.72-1.53 (s, 2H, N-CH_2-CH_2-CH_2-CH_3), 1.46-1.06 (s, 20H, N-CH_2-CH_2-CH_2-CH_3, N-CH_2-(CH_2)$_9$-CH_2-O, 0.99-0.80 (s, 5H, N-CH_2-CH_2-CH_2-CH_3, CH_2-C(CH_3)) (NMR, Figure 4.1).

4.2.7 Synthesis of 11-bromoundecyl acrylate monomer (BrUA)

A typical synthesis method for the bromine terminated monomer, 11-bromoundecyl acrylate (BrUA), includes: adding 51.9 g (206.6 mmol) 11-bromo-1-undecanol and 100

mL dichloromethane (DCM) to a three-neck 500 mL flask in an ice bath. Under nitrogen, a mixture of 21.1 g (208.5 mmol) triethylamine and 55 mL dichloromethane was slowly added to the flask, followed by a slow addition of a mixture of 18.9 g (208.8 mmol) of acryloyl chloride and 38 mL of dichloromethane using an addition funnel. The reaction mixture was stirred at room temperature for 18 h and then filtered. The liquid filtrate was washed with 250 mL 0.1 M sodium bicarbonate ($NaHCO_3$) two times followed by washes with 250 mL DI water four times. The water layer was removed using a separation funnel and the residual water in the organic layer was removed with anhydrous magnesium sulfate. The organic solvent was removed by vacuum, yielding a transparent yellow-tinted liquid product, 11-bromoundecyl acrylate (BrUA). Yield 41.1 g (65.1 %). ^{1}HNMR (500 MHz, $CDCl_3$, 23 °C) δ(ppm): 6.45-6.36 (d 1H, *H*CH=CH), 6.18-6.07 (m, 1H, HCH=C*H*), 5.85-5.79 (d, 1H, HC*H*=CH), 4.2-4.12 (t, 2H , O-CH_2-), 3.7-3.36 (t, 2H,-CH_2-Br), 1.91-1.82 (s, 3H, CH_2=C(CH_3)), 1.8-1.75 (m, 2H, O-CH_2-CH_2), 1.7-1.56 (m, 2H, -CH_2-CH_2-Br), 1.5-1.2 (m, 14H, O-CH_2-CH_2-(CH_2)$_7$-CH_2-CH_2-Br) (NMR, Appendix C, Figure C1).

4.2.8 Synthesis of Poly(BrUA)

The synthesis of the non-ionic precursor homopolymer, poly(BrUA), was performed using reversible addition-fragmentation chain-transfer (RAFT) polymerization as shown in Scheme 4.2(c). A typical example is given as follows. 5 g of BrUA (16.4 mmol), 11.95 mg of CTA (0.033 mmol), 1.35 mg of AIBN (0.008 mmol) were mixed with 0.5 mL THF in a 250 mL single-neck Schlenk flask. The flask was subjected to three freeze-pump-thaw degassing cycles followed by sealing the reactor and carrying out the reaction under static

vacuum at 70 °C for 4 h. The resulting polymer was twice precipitated in DI water, filtered and then dried under vacuum in an oven at room temperature for 24 h. Yield: ~1 g (~20%); resulting polymer was adhesive to reaction vial and thus yield could only be estimated. ^{1}H NMR (500 MHz, $CDCl_3$, 23 °C) δ (ppm): 4.16-3.84 (s, 2H, Br-CH_2-CH_2-$(CH_2)_7$-CH_2-C*H*$_2$-O), 3.59-3.34 (m, 2H, Br-C*H*$_2$-CH_2-$(CH_2)_7$-CH_2-CH_2-O), 2.42-2.18 (m, 2H, CH_2-C*H*), 1.96-1.72 (m, 2H, C*H*$_2$-CH), 1.72-1.51 (s, 2H, Br-CH_2-CH_2-$(CH_2)_7$-C*H*$_2$-CH_2-O), 1.51-1.37 (s, 2H, Br-CH_2-C*H*$_2$-$(CH_2)_7$-CH_2-CH_2-O), 1.37-1.22 (s, 2H, Br-CH_2-CH_2-(C*H*$_2$)$_7$-CH_2-CH_2-O) (NMR, Appendix C, Figure C1). SEC (THF, 40 °C): M_n = 40.0 kg mol^{-1}, M_w/M_n = 3.76 (against PS standards).

4.2.9 Synthesis of Poly(AUBIm-Br)

Synthesis of the PIL homopolymer, poly(AUBIm-Br) [AUBIm-Br = 1-[(2-acryloyloxy) undecyl]-3-butylimidazolium bromide], is shown in Scheme 4.2(c), *i.e.*, functionalization of non-ionic precursor homopolymer, poly(BrUA), to form an ionic homopolymer. A typical example is given as follows. 0.460 g (1.51 mmol) of poly(BrUA) was first dissolved in ~5 mL DMF in a 50 mL vial. 0.936 g (7.53 mmol) of 1-butylimidazole (poly(BrUA)/1-butylimidazole, 1/5 mol/mol) was then mixed into the vial. The solution was stirred at 80 °C for 48 h. The resulting polymer was precipitated twice into hexane, followed by multiple washes with diethyl ether, and dried under vacuum in an oven at room temperature for 24 h. Yield: 0.399 g (0.790 mmol) of solid particles (52.4%). ^{1}H NMR (500 MHz, D_2O, 23 °C) δ (ppm): 7.88-7.50 (s, 2H, N-C*H*=C*H*-N), 4.51-4.04 (m, 4H, N-C*H*$_2$-$(CH_2)_9$-CH_2-O, N-C*H*$_2$-CH_2-CH_2-CH_3), 2.06-1.69 (s, 4H, C*H*$_2$-C(CH_3), N-

CH_2-CH_2-CH_2-CH_3), 1.69-0.95 (m, 20H, N-CH_2-(CH_2)$_9$-CH_2-O N-CH_2-CH_2-CH_2-CH_3, 1.00-0.65 (s, 6H, N-CH_2-CH_2-CH_2-CH_3) (NMR, Appendix C, Figure C1).

4.2.10 Synthesis of Poly(AUTMA-Br)

Synthesis of the PIL homopolymer, poly(AUTMA-Br) [AUTMA-Br = 1-[(2-acryloyloxy) undecyl]-trimethylammonium bromide], is shown in Scheme 4.2(c). A typical example is given as follows. 0.400 g (1.37 mmol) of poly(BrUA) was first dissolved in ~2 mL DMF in a 50 mL vial. 0.902 g (6.87 mmol) of trimethylamine in aqueous solution (poly(BrUA)/trimethylamine, 1/5 mol/mol) was then mixed into the vial. The solution was stirred at room temperature for 48 h. The resulting polymer was precipitated twice into diethyl ether and dried under vacuum in an oven at room temperature for 24 h. Yield: 0.307 g (0.875 mmol) of solid particles (63.7%). ^{1}H NMR (500 MHz, D_2O, 23 °C) δ (ppm): 4.24-3.75 (s, 2H, N-CH_2-(CH_2)$_9$-CH_2-O), 3.74-3.24 (s, 2H, N-CH_2-(CH_2)$_9$-CH_2-O), 3.27-2.93 (s, 9H, N-(CH_3)$_3$), 1.96-1.50 (m, 2H, CH_2-CH, N-CH_2-CH_2-(CH_2)$_7$-CH_2-CH_2-O), 1.50-0.98 (s, 16H, N-CH_2-CH_2-(CH_2)$_7$-CH_2-CH_2-O)) (NMR, Appendix C, Figure C1).

4.2.11 Synthesis of Poly(AUBP-Br)

Synthesis of the PIL homopolymer, poly(AUBP-Br) [AUBP-Br =1-[(2-acryloyloxy) undecyl]-1-butylpyrrolidinium bromide], is shown in Scheme 4.2(c). A typical example is given as follows. 0.360 g (1.30 mmol) of poly(BrUA) was first dissolved in ~2 mL DMF in a 50 mL vial. 0.496 g (3.90 mmol) of 1-butylpyrrolidine (poly(BrUA)/1-

butylpyrrolidine, 1/3 mol/mol) was then mixed into the vial. The solution was stirred at 80 °C for 24 h. The resulting polymer was precipitated twice into hexane, followed by multiple washes with diethyl ether, and dried under vacuum in an oven at room temperature for 24 h. Yield: 0.408 g (1.01 mmol) of solid particles (77.8%). ^{1}H NMR (500 MHz, D_2O, 23 °C) δ (ppm): 3.69-3.12 (s, 8H, N-C*H*$_2$-CH_2-CH_2-C*H*$_2$-N, N-C*H*$_2$-CH_2-CH_2-CH_3, N-C*H*$_2$-CH_2-$(CH_2)_7$-CH_2-CH_2-O), 2.26-2.03 (s, 5H, N-CH_2-C*H*$_2$-C*H*$_2$-CH_2-N, CH_2-C*H*), 1.79-1.53 (s, 6H, N-CH_2-C*H*$_2$-CH_2-CH_3, C*H*$_2$-CH, N-CH_2-C*H*$_2$-$(CH_2)_7$-CH_2-CH_2-O), 1.50-1.11 (s, 18H, N-CH_2-CH_2-C*H*$_2$-CH_3, N-CH_2-CH_2-(C*H*$_2$)$_7$-C*H*$_2$-CH_2-O, 1.01-0.83 (s, 3H, N-CH_2-CH_2-CH_2-C*H*$_3$) (NMR, Figure 4.1).

4.2.12 Synthesis of Poly(VBBIm-Br)

Synthesis of the PIL homopolymer, poly(VBBIm-Br) [VBBIm-Br = vinylbenzylbutylimidazolium bromide], is shown in Scheme 4.2(d), *i.e.*, functionalization of non-ionic precursor homopolymer, poly(vinylbenzylchloride) (PVBC), to form an ionic homopolymer, followed by anion exchange metathesis. A typical example is given as follows. 2.00 g (13.1 mmol) of PVBC was first dissolved in ~15 mL DMF in a 100 mL flask. 8.14 g (0.066 mol) of 1-butylimidazole (PVBC/1-butylimidazole, 1/5 mol/mol) was then mixed into the vial. The solution was stirred at 80 °C for 48 h. The resulting polymer was precipitated twice into hexane, followed by multiple washes with diethyl ether, and dried under vacuum in an oven at room temperature for 24 h. Yield: 3.29 g (11.9 mmol) of solid particles (90.6%). Subsequently, anion exchange metathesis was performed on the dried polymer, poly(VBBIm-Cl), to exchange from chloride to bromide form. 0.500 g

(1.81 mmol) of poly(VBBIm-Cl) was stirred in 200 mL of 0.1 M LiBr in acetone for 24 h, followed by 24 h stirring in 200 mL acetone. The resulting polymer was filtered and dried under vacuum in an oven at room temperature for 24 h. The efficacy of anion exchange from Cl^- to Br^- was confirmed by EA and determined to be 96% bromide-exchanged. Yield: 0.245 g (0.762 mmol) of solid particles (42.2%). ^{1}H NMR (500 MHz, D_2O, 23 °C) δ (ppm): 7.67-7.33 (s, 2H, N-C*H*=C*H*-N), 7.33-6.74 (m, 4H, C_6H_4), 5.42-4.91 (s, 2H, C_6H_4-CH_2-N), 4.29-3.95 (s, 2H, N-CH_2-CH_2-CH_2-CH_3), 1.91−1.44 (m, 3H, CH_2-C*H*, N-CH_2-CH_2-CH_2-CH_3), 1.24−0.82 (m, 4H, CH_2-CH, N-CH_2-CH_2-CH_2-CH_3), 0.82-0.35 (s, 3H, N-CH_2-CH_2-CH_2-CH_3) (NMR, Figure 1). EA Calculated: C, 56.25; H, 7.10; N, 5.47; Br, 31.18; Cl, 0.00. Found: C, 54.95; H, 7.42; N, 5.08; Br, 29.06; Cl, 1.28.

4.2.13 Synthesis of Poly(VBTMA-Br)

Synthesis of the PIL homopolymer, poly(VBTMA-Br) [VBBIm-Br = vinylbenzyltrimethylammonium bromide], is shown in Scheme 4.2(d), *i.e.*, functionalization of non-ionic precursor homopolymer, poly(vinylbenzylchloride) (PVBC), to form an ionic homopolymer, followed by anion exchange metathesis. A typical example is given as follows. 2.00 g (13.1 mmol) of PVBC was first dissolved in ~15 mL DMF in a 100 mL flask. 8.61 g (3.87 g TMA; 0.066 mol TMA) of 45 wt% trimethylamine in aqueous solution (PVBC/trimethylamine, 1/5 mol/mol) was then mixed into the vial. The solution was stirred at room temperature for 48 h. The resulting polymer was precipitated twice into diethyl ether and dried under vacuum in an oven at room temperature for 24 h. Yield: 2.19 g (10.3 mmol) of solid particles (78.9%). Subsequently,

anion exchange metathesis was performed on the dried polymer, poly(VBTMA-Cl), to exchange from chloride to bromide form. 2.00 g (9.45 mmol) of poly(VBTMA-Cl) was stirred in 200 mL of 0.1 M LiBr in acetone for 24 h, followed by 24 h stirring in 200 mL acetone. The resulting polymer was filter and dried under vacuum in an oven at room temperature for 24 h. The efficacy of anion exchange from Cl^- to Br^- was confirmed by EA and determined to be 94% bromide-exchanged. Yield: 1.57 g (6.12 mmol) of solid particles (64.8%). 7.62-6.28 (m, 4H, C_6H_4), 4.58-4.00 (s, 2H, C_6H_4-CH_2-N), 3.13−2.44 (s, 9H, N-$(CH_3)_3$), 1.82−0.89 (s, 3H, CH_2-CH, CH_2-CH) (NMR, Figure 4.1). EA Calculated: C, 59.81; H, 6.60; N, 8.72; Br, 24.87; Cl, 0.00. Found: C, 57.69; H, 6.70; N, 8.21; Br, 23.06; Cl, 1.36.

4.2.14 Synthesis of Poly(VBBP-Br)

Synthesis of the PIL homopolymer, poly(VBBP-Br) [VBBP-Br = vinylbenzylbutylpyrroldinium bromide], is shown in Scheme 4.2(d), *i.e.*, functionalization of non-ionic precursor homopolymer, poly(vinylbenzylchloride) (PVBC), to form an ionic homopolymer, followed by anion exchange metathesis. A typical example is given as follows. 2.00 g (13.1 mmol) of PVBC was first dissolved in ~15 mL DMF in a 100 mL flask. 8.34 g (0.066 mol) of 1-butylpyrrolidine (PVBC/butylpyrrolidine, 1/5 mol/mol) was then mixed into the vial. The solution was stirred at 80 °C for 48 h. The resulting polymer was precipitated twice into hexane, followed by multiple washes with diethyl ether, and dried under vacuum in an oven at room temperature for 24 h. Yield: 3.67 g (9.54 mmol) of solid particles (72.8%). Subsequently, anion exchange metathesis was performed on the

dried polymer, poly(VBBP-Cl), to exchange from chloride to bromide form. 2.00 g (7.15 mmol) of poly(VBBP-Cl) was stirred in 200 mL of 0.1 M LiBr in acetone for 24 h, followed by 24 h stirring in 200 mL acetone. The resulting polymer was filter and dried under vacuum in an oven at room temperature for 24 h. The efficacy of anion exchange from Cl^- to Br^- was confirmed by EA and determined to be ~96% bromide-exchanged. Yield: 0.909 g (2.80 mmol) of solid particles (39.3%). 7.50-6.18 (m, 4H, C_6H_4), 4.54-4.01 (s, 2H, C_6H_4-CH_2-N), 3.71-2.52 (m, 6H, N-CH_2-CH_2-CH_2-CH_2-N, N-CH_2-CH_2-CH_2-CH_3), 2.33−1.87 (s, 4H, N-CH_2-CH_2-CH_2-CH_2-N), 1.87-1.35 (m, 3H, CH_2-CH, N-CH_2-CH_2-CH_2-CH_3), 1.35-0.91 (m, 4H, CH_2-CH, N-CH_2-CH_2-CH_2-CH_3), 0.91-0.56 (s, 3H, N-CH_2-CH_2-CH_2-CH_3) (NMR, Figure 4.1). EA Calculated: C, 62.95; H, 8.10; N, 4.32; Br, 24.63; Cl, 0.00. Found: C, 59.81; H, 8.09; N, 3.96; Br, 23.67; Cl, 0.95.

Scheme 4.2 Synthesis of PILs, (a) poly(MEX-Br), (b) poly(MUX-Br), (c) poly(AUX-Br), (d) poly(VBX-Br), X = various cations (A, B, C in bottom panel).

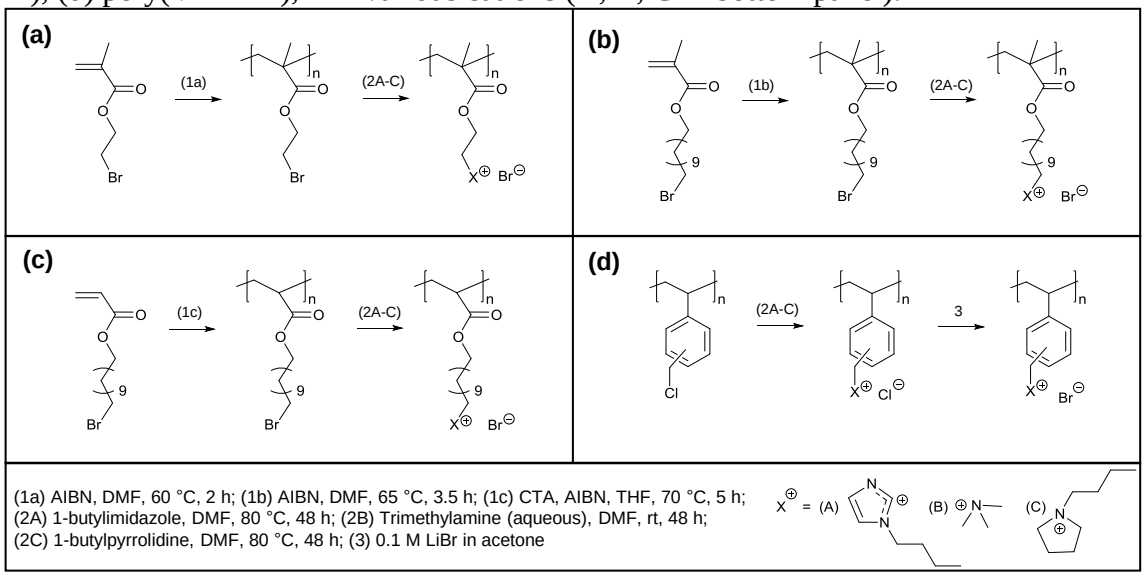

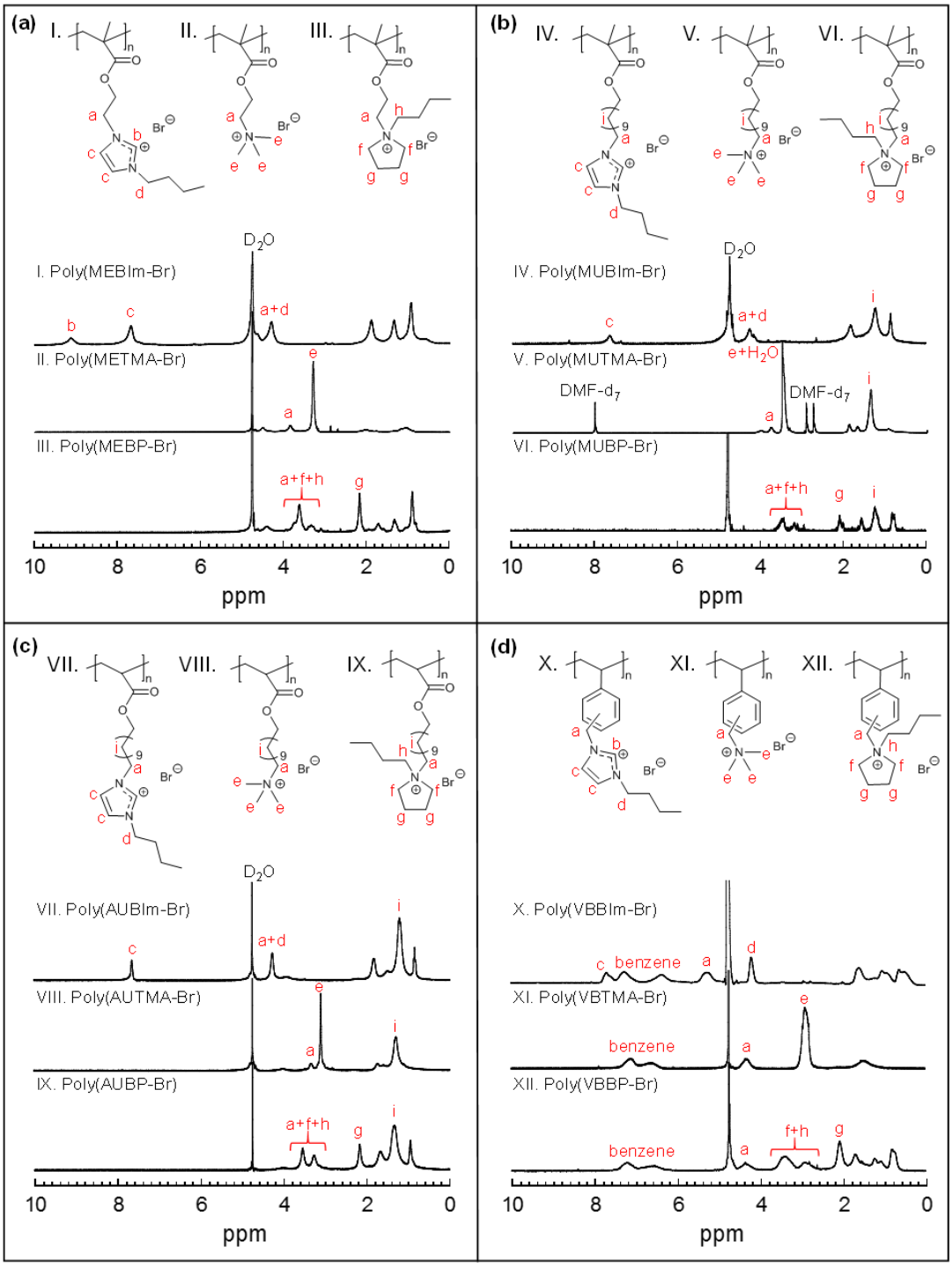

Figure 4.1 ^{1}H NMR spectra for PILs: (I) poly(MEBIm-Br), (II) poly(METMA-Br), (III) poly(MEBP-Br), (IV) poly(MUBIm-Br), (V) poly(MUTMA-Br), (VI) poly(MUBP-Br), (VII) poly(AUBIm-Br), (VIII) poly(AUTMA-Br), (IX) poly(AUBP-Br), (X) poly(VBBIm-Br), (XI) poly(VBTMA-Br), (XII) poly(VBBP-Br).

4.2.15 Solvent-Casting PIL Films

The twelve bromide-conducting PILs were first dissolved in various solvents (1-10% w/w) and cast onto glass substrates (*ca.* 40 mm (L) × 8 mm (W) × 1 mm (T)) under ambient conditions for 24 h and subsequently annealed under dynamic vacuum at 100 °C for 48 h; specific casting conditions (solvent and concentration) are listed in Appendix C in Table C1. These films were used to measure ionic conductivity. The film thicknesses, ranging between approximately 30 to 80 μm, were measured with a Mitutoyo digital micrometer with ± 1 μm accuracy.

4.2.16 Characterization

Chemical structures of the PIL homopolymers were characterized by ^{1}H NMR spectroscopy using a Varian 500 MHz spectrometer at 23 °C with D_2O as the solvent. The chemical shifts were referenced to water at 4.75 ppm. Chemical structures of poly(BrUMA), poly(BrUA), and BrUA were characterized by ^{1}H NMR spectroscopy and referenced to $CDCl_3$ at 7.27 ppm, and the chemical structure of poly(MUTMA-Br) was referenced to DMF-d_7 at 8.03 ppm. Elemental analysis was performed by Atlantic Microlab, Inc., Norcross, GA. The molecular weights and molecular weight distributions of non-ionic precursor homopolymers were determined by size exclusion chromatography (SEC) using a Waters GPC system equipped with a THF Styragel column (Styragel@HR 5E, effective separation of molecular weight range: 2 to 4000 kg mol^{-1}) and a 2414 reflective index (RI) detector. All measurements were performed at 40 °C, where THF was used as the mobile phase at a flow rate of 1.0 mL/min. PS standards (Shodex, Japan)

with molecular weights ranging from 2.97 to 983 kg mol^{-1} were used for calibration. Glass transition temperatures (T_gs) were determined by differential scanning calorimetry (DSC; TA Instruments, Q200) over a temperature range of -40 to 180 °C at a heating/cooling rate of 10 °C/min under a N_2 environment using a heat/cool/heat method. T_g was determined using the midpoint method from the second thermogram heating cycle.

The ionic conductivities of the polymer films were measured with electrochemical impedance spectroscopy (EIS; Solartron, 1260 impedance analyzer, 1287 electrochemical interface, Zplot software) over a frequency range of 10^2 Hz to 10^6 Hz at 10 mV. Conductivities were collected under humidified conditions, where temperature and relative humidity were controlled by an environmental chamber (Espec, BTL-433 model). The in-plane conductivities of the PIL films were measured in a cell with four parallel electrodes (BekkTech, BTT-112, Scribner Associates, Inc.), where an alternating current was applied to the outer electrodes and the real impedance or resistance, *R*, was measured between the two inner reference electrodes. The resistance was determined from the x-intercept at high frequency of the semi-circle regression of the Nyquist plot. Conductivity was calculated by using the following equation: $\sigma = L/AR$, where *L* and *A* are the distance between two inner electrodes and the cross sectional area of the polymer film ($A = Wl$; *W* is the film width and *l* is the film thickness), respectively. Samples were allowed to equilibrate for 2 h at 60 °C and 90% RH (relative humidity), followed by 6 measurements at the equilibrium condition. An average error of <5% was observed among these repeated measurements. The values reported are an average of these steady-state measurements, where experiments for each PIL film were repeated a second time.

Water uptake or content of the PILs was measured with dynamic vapor sorption (DVS, TA Instruments Q5000), at the same condition that conductivity was measured (60 °C and 90% RH). A dry sample of powder weighing ~1-3 mg was loaded into the DVS and preconditioned at 0% RH and 60 °C for 3 h; the weight of the PILs stabilized well before the end of the drying step (<0.1 wt% change for at least 30 min). The relative humidity was then systematically changed to a constant value of 90% RH at a fixed temperature of 60 °C, equilibrating at this condition for 2 h, where the weight was observed as stable (<0.1 wt% change for at least 30 min) after ~1 h. The polymer water content (uptake) [wt%; g H_2O/g dry polymer] was calculated as follows:

$$W_{H_2O} = \frac{W - W_0}{W_0} \times 100 \tag{4.1}$$

where W_0 and W are dry and wet polymer weights measured before and after the relative humidity change in the DVS experiment, respectively.

4.2.17 Alkaline Chemical Stability Analysis

The chemical stability of the PILs was examined using ^{1}H NMR spectroscopy with D_2O as the solvent. The stability study was performed under alkaline conditions in NMR tubes. PILs (0.025 mmol) were exposed to 20 molar eq KOH in 1 mL D_2O (0.5 M KOH) at 60 °C for 168 h, followed by ^{1}H NMR experiments to quantify chemical degradation.

4.3 Results and Discussion

4.3.1 PIL Alkaline Chemical Stability

We synthesized and investigated the chemical stability of ethyl methacrylate-, undecyl methacrylate-, undecyl acrylate-, and styrene-based PILs consisting of various covalently attached cations: butylimidazolium, trimethylammonium, butylpyrrolidinium. The chemical structure and purity of these PILs were confirmed by ^{1}H NMR prior to alkaline chemical stability experiments (see Figure 1). All twelve PILs were determined to be fully functionalized by ^{1}H NMR, EA, or both. IECs [mmol g^{-1}] of the PILs were calculated as the moles of cation per gram of polymer. PIL degradation was quantified by ^{1}H NMR spectroscopy, where the effect of alkaline media (20 eq (0.5 M) KOH/D_2O) at moderate temperature (60 °C) on the chemical stability of the various backbone types, as well as the covalently tethered cations, was investigated. The PILs were considered to be hydroxide-exchanged during the course of this alkaline chemical stability study due to the excess of hydroxide anions (20 eq) and were not pre-exchanged to hydroxide form.

Figure 4.2 shows ^{1}H NMR spectra of each PIL after 168 h exposure to 20 eq KOH/D_2O at 60 °C. In Figure 2a, the ^{1}H NMR spectra of the butylimidazolium ethyl methacrylate-based PIL, poly(MEBIm-OH), shows a new peak at ~7.41 ppm, which is attributed to degradation by ring-opening mechanism as described in literature.[5] Alkaline degradation by this ring-opening reaction was calculated by the relative integrations of the ring-opened byproducts to the intact imidazolium rings (*i.e.*, $2c^3/(2c^3 + c + c^4)$; degradation mechanism shown in Scheme 4.3a-b) as 33.3%. Scheme 3b, Figure S2, and Figure S3 contain a degradation pathway and NMRs showing new peaks (labeled c', c", c^4) that result from

backbone ester hydrolysis of the butylimidazolium ethyl methacrylate-based PIL. The data suggests that hydrolysis and the ring-opening mechanism occurred simultaneously, such that the cleaved cations may be intact or may be ring-opened degradation byproducts. For poly(MEBIm-OH), ~63.7% of the total monomer units have cleaved from the polymer; further details regarding ester hydrolysis are available in the Supporting Information. Note that for the imidazolium-functionalized PILs in KOH/D_2O solution, the proton peaks associated with the C2, C4, and C5 positions of imidazole rings may undergo a hydrogen/deuterium (H/D) exchange reaction, and therefore for the imidazolium PIL degradation reactions only, 10 wt% H_2O (relative to mass of polymer) replaced an equal weight of D_2O within the solution, as this has been shown in previous studies to suppress H/D exchange.[5,36] It was also noted in a previous study that extent of degradation in D_2O was equivalent to degradation in H_2O.[36] In summary, 63.7% of poly(MEBIm-OH) degraded by ester hydrolysis, while 33.3% of the PIL degraded by ring opening mechanism; both degradation mechanisms were occurring simultaneously, such that these two degradation values overlap for the 20.6% (both hydrolyzed and ring-opened), for an overall total of 76.4% degradation (63.7% ester hydrolysis + 33.3% ring opening – 20.6% overlap = 76.4% total degradation).

Figure 4.2b shows ^{1}H NMR spectra for the trimethylammonium ethyl methacrylate-based PIL, poly(METMA-OH), after 168 h exposure to 20 eq KOH/D_2O at 60 °C. Two major degradation pathways for pendant quaternary ammonium cations are generally recognized and were also observed in this study: 1) Hofmann elimination (E2 elimination) through the removal of the β hydrogens by hydroxide, resulting in amine and alkene

byproducts (Scheme 4.3c), and 2) nucleophilic substitution (S_N2 reaction) *via* hydroxide attack on the α carbons resulting in amine and alcohol byproducts (Scheme 4.3d).[114] This results in a mixture of degradation byproducts, as S_N2 reaction and E2 elimination occur simultaneously, with S_N2 favored at lower temperatures. In Figure 4.2b, nucleophilic substitution reactions were observed for the trimethylammonium cation as new peaks appeared at ~3.88 ppm (Scheme 4.3c; labeled a'') and ~2.15 ppm (Scheme 4.3c; labeled e'); Hofmann elimination reaction was also observed, as two additional peaks were detected at ~5.42 ppm and ~5.63 ppm (Scheme 4.3c; labeled a'). Overall cation degradation was calculated from relative integration ratios (*i.e.*, (9a' + 3e'+ 9a'')/(2e + 9a' + 3e' + 9a'')) and was quantified as 80.9%. Ester hydrolysis of the polymer backbone was not observed for the trimethylammonium ethyl methacrylate-based PIL, likely due to the intensity of competing cation degradation mechanisms, and thus 80.9% represents the total degradation observed in the PIL.

For the butylpyrrolidinium ethyl methacrylate-based PIL, poly(MEBP-OH), in Figure 4.2c, cation degradation *via* Hofmann elimination was noted in the ^{1}H NMR spectra after 168 h exposure to 20 eq KOH/D_2O at 60 °C. Two new peaks appeared at ~5.57 ppm (Scheme 4.3e; labeled f') and ~3.82 ppm (Scheme 4.3e; labeled g'); similar degradation by E2 elimination has been observed in literature.[35,36] The degree of degradation of the cation can be calculated by the relative integrated intensities of corresponding ^{1}H NMR peaks (*i.e.*, 4f'/((a + f + h)*+4f'), see Figure 4.2c, where (a + f +h)* = (a + f + h + a'' + f'' + h''), see Figure C4) and was 23.4%. Significant ester hydrolysis (65.5%) was observed in a previous study where poly(MEBP-OH) was exposed for 168 h to 20 eq KOH/D_2O at

80 °C.[36] In this study, at a lower temperature of 60 °C, 37.0% hydrolysis was observed (degree of hydrolysis = (f" + h")/(f + h + f" + h"), see Figure C4). It was also noted that the new peaks resulting from E2 elimination (f', g') did not exhibit the same shouldering that was observed at 80 °C in the previous study, and therefore in this study, the portion of PIL that underwent cation degradation did not also undergo hydrolysis. In summary, 23.4% of poly(MEBP-OH) degraded by Hofmann elimination, while an additional 37.0% of the PIL degraded by backbone ester hydrolysis, for an overall total of 60.4% degradation.

Figure 4.2d shows ^{1}H NMR spectra for the butylpyrrolidinium undecyl methacrylate-based PIL, poly(MUBP-OH), after 168 h exposure to 20 eq KOH/D_2O at 60 °C. The peaks that were noted in the degraded ^{1}H NMR spectra of the ethyl methacrylate analogue, poly(MEBP-OH), as an indication of cation degradation by an E2 mechanism were not observed in poly(MUBP-OH); no other evidence of cation degradation is present in the degraded ^{1}H NMR spectra. Increased sharpness of the polymer peaks is evident, indicating the presence of small molecules (*i.e.*, indicating the backbone has been hydrolyzed at the ester bond to some extent.) Additionally, two new peaks were observed at ~2.45 ppm and ~2.39 ppm (Scheme 4.3e; labeled f' and h', respectively), which are associated with protons of the butylpyrrolidinium in the hydrolysis small molecule byproduct. Backbone degradation was calculated from relative integration ratios (*i.e.*, 4(f' + h')/(3(a + f + h) + 4(f' + h'))) as 16.8%, accounting for total degradation of poly(MUBP-OH).

Similarly to poly(MUBP-OH), Figure 4.2e shows no signs of cation degradation in the ^{1}H NMR spectra of the butylpyrrolidinium undecyl acrylate-based PIL, poly(AUBP-OH),

after 168 h exposure to 20 eq KOH/D_2O at 60 °C. Likewise, the peaks present are significantly sharper than those observed prior to degradation, indicating hydrolysis (*i.e.*, indicating a significant concentration of small molecules); all of the cation peaks are also shifted slightly upfield in the degraded NMR relative to the non-degraded NMR, another indicator that these groups are no longer attached to the polymer backbone. Additionally, the splitting pattern of the peaks becomes fully apparent, which was not the case for non-degraded polymeric material, and the peaks at 1.79-1.11 ppm split from 3 broad peaks to 5 sharp peaks, where the polymer backbone peaks become evident (labeled j' and k'; Scheme 4.3f). It was determined that 100% of the PIL degraded *via* ester hydrolysis, with the cation remaining fully intact. In summary, the butylpyrrolidinium undecyl acrylate-based PIL proved to be exceedingly more susceptible to ester hydrolysis relative to butylpyrrolidinium undecyl methacrylate-based PIL. Lower alkaline stability of acrylate-based polymers compared to methacrylate-based polymers have been previously observed in literature.[113]

The additional undecyl methacrylate and undecyl acrylate PILs (imidazolium- and ammonium-based cations) were only soluble in water at low polymer concentrations (<0.025 M) and therefore their alkaline chemical stability was not measured by ^{1}H NMR.

The butylimidazolium styrene-based PIL, poly(VBBIm-OH), showed visible signs of degradation after 168 h exposure to 20 eq KOH/D_2O at 60 °C. Specifically, the PIL turned black and precipitated from solution, and therefore it was not possible to use ^{1}H NMR to accurately access degradation (Figure 4.2f).

Degradation of the benchmark cation, BTMA, on the styrene-based PIL, poly(VBTMA-OH), is shown in Figure 4.2g. BTMA has been shown in literature to degrade by a number of mechanisms, such as nucleophilic displacement (S_N2), Stevens and Sommelet-Hauser rearrangements, and direct ylide degradation, with E2 (Hofmann) elimination not being a feasible route due to the lack of a β hydrogen.[115,116] ^{1}H NMR experiments after 168 h exposure to 20 eq KOH/D_2O at 60 °C show degradation *via* nucleophilic substitution, *i.e.*, show the displacement of the tertiary amine to form benzyl alcohol, as there is a new peak representing the tertiary amine byproduct present at ~2.19 ppm (labeled e'), and there is a reduction of the covalently tethered quaternary ammonium peak (labeled e) relative to the benzyl protons. The alternative degradation pathways shown by others were not identified in the degraded NMRs for this polymer, and therefore were not likely major contributors to this specific PIL degradation. Relative integration of the polymeric ammonium protons to the benzyl protons (*i.e.*, 4e/(4e + 9(benzene)) indicates an overall degradation of 13.2% for poly(VBTMA-OH). There is no indication of backbone degradation. For the trimethylammonium cation, the styrene-based backbone leads to significant improvements in alkaline stability over ethyl methacrylate-based backbone (13.2% degradation for styrene vs. 80.9% degradation for ethyl methacrylate).

In Figure 4.2h, there is no degradation present in the ^{1}H NMR spectra of the butylpyrrolidinium styrene-based PIL, poly(VBBP-OH), after 168 h exposure to 20 eq KOH/D_2O at 60 °C. Specifically, no new peaks have appeared in the spectra, and the relative integration ratio of backbone peak "a" to cation peaks "f + h" remains constant. A second experiment was performed where the experimental polymer concentration was

halved to 0.0125 M to prevent precipitation, and the hydroxide equivalents were increased 4-fold, exposing poly(VBBP-OH) to 80 eq KOH/D_2O (1 M; 4-fold increase in hydroxide eq results in 2-fold increase in molarity since polymer concentration was also halved, *i.e.*, 0.0125 M x 80 hydroxide eq = 1 M, compared to previous experiments where 0.0250 M x 20 hydroxide eq = 0.5 M.) at 60 °C; the ^{1}H NMR spectra is reported in Appendix C (Figure C5). Again, no cation or backbone degradation was observed. A similar third experiment was performed to enable identification of degradation pathways; poly(VBBP-OH) (0.0125 M) was exposed to 8-fold OH equivalents, 160 eq (2 M) KOH/D_2O, but the PIL almost immediately precipitated with no color change, indicating that the solution was likely at the solubility limit. Overall, poly(VBBP-OH) shows significant improvements in alkaline chemical stability relative to all other PILs examined. The combination of the butylpyrrolidinium cation with the styrene-based backbone yielded the highest alkaline chemical stabilities among the backbone/cation combinations that could be investigated *via* NMR in this study. Multiple factors may contribute to the improved chemical stability of styrene/butylpyrrolidinium relative to styrene/BTMA: the heterocyclical ring structure of butylpyrrolidonium results in a nonpolarizable moiety, which is highly resistant to hydroxide attack, while its butyl substituent also provides steric hindrance. Additionally, the reduced chemical stability of the ethyl methacrylate/butylpyrrolidinium pairing relative to the styrene/butylpyrrolidinium pairing lends insight into the contribution of backbone chemistry to cation stability. The ester group of the methacrylate backbone is an electron-withdrawing group, and therefore can reduce electron density from the cation and contributes to more electrophilicity, and thus more susceptible to nucleophilic

hydroxide anion attack. In contrast, the benzene ring of the styrene backbone acts as an electron-donating group creating a more nucleophilic cation, and thus more stable under hydroxide attack. Similarly, for the undecyl methacrylate/butylpyrrolidinium pairing, the 11-carbon spacer between the cation and ester group results in the cation not experiencing as significant of an effect of electron withdrawing of the ester group, and instead receiving increased electron density from its alkyl attachment and thus achieving increased cation stability. A summary of the extent of PIL alkaline chemical degradation resulting from both backbone and cation degradation (Figure 4.2) is listed in Table 4.1.

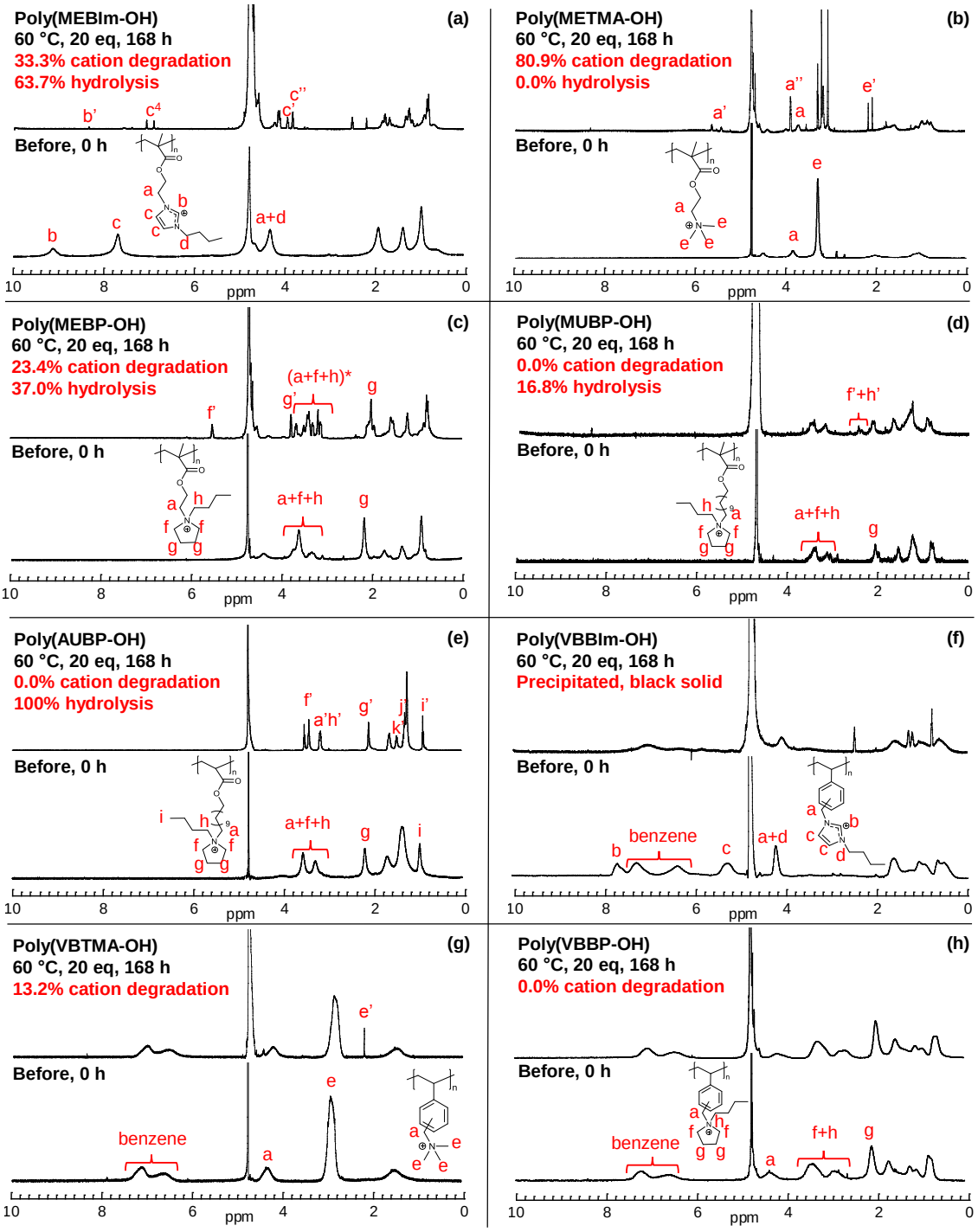

Figure 4.2 ^{1}H NMR spectra for (a) poly(MEBIm-OH), (b) poly(METMA-OH), (c) poly(MEBP-OH), (d) poly(MUBP-OH), (e) poly(AUBP-OH), (f) poly(VBBIm-OH), (g) poly(VBTMA-OH), (h) poly(VBBP-OH) degraded in 20 eq (0.5 M) KOH/D_2O at 60 °C for 168 h.

Scheme 4.3 PIL Degradation Reaction Pathways

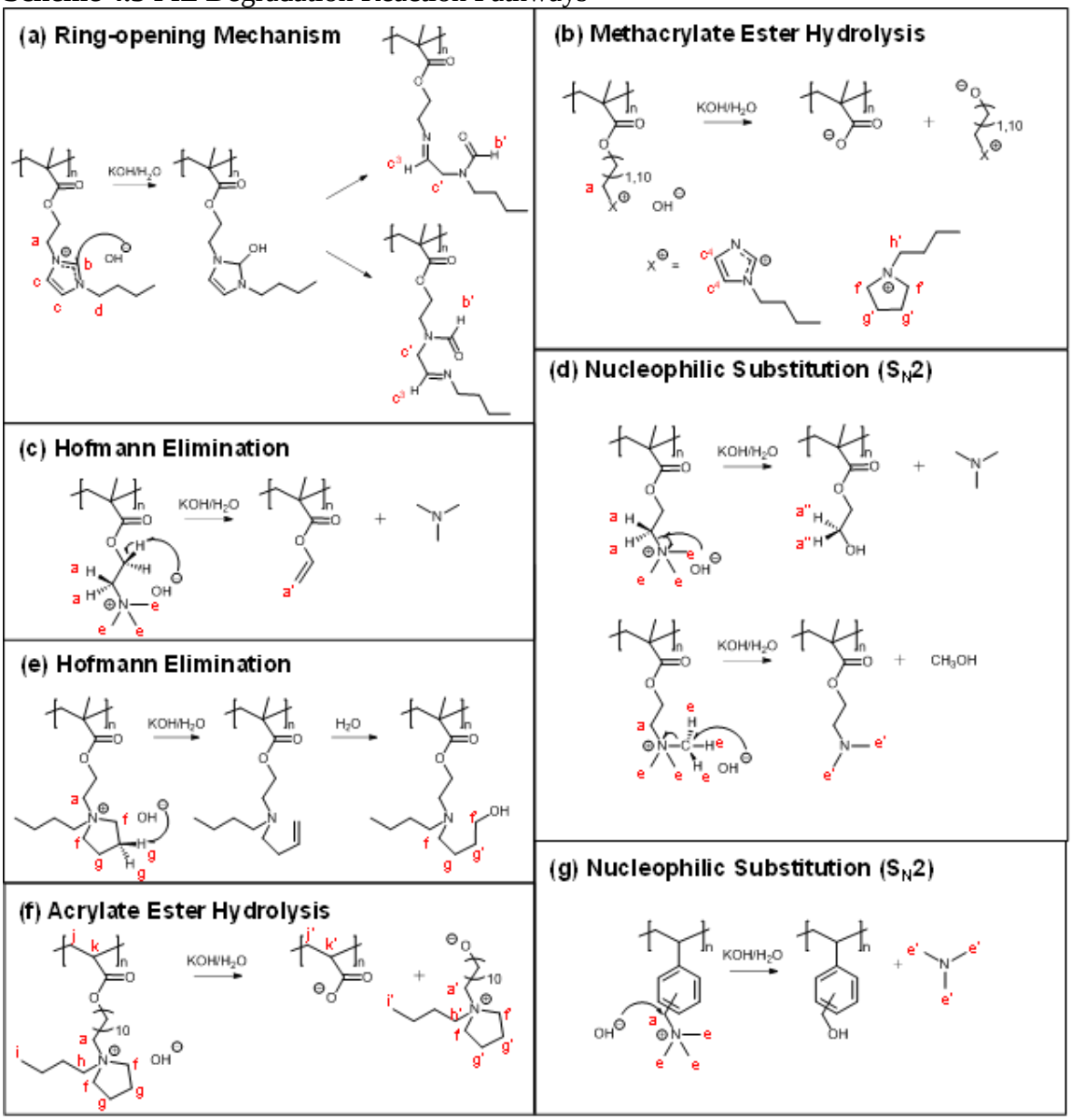

Table 4.1 Alkaline Chemical Degradation of PILs.

Polymer	Degraded Cation (%)[a]	Hydrolysis (%)[a]	Degraded Overall (%)[a]	NMR Fig.	Degradation Scheme
poly(MEBIm-OH)	33.3	63.7	76.4	4.2a	4.3a-b, C2-3
poly(METMA-OH)	80.9	0.0	80.9	4.2b	4.3c-d
poly(MEBP-OH)	23.4	37.0	60.4	4.2c	4.3b, 4.3e, C4
poly(MUBIm-OH)	*b*	*b*	*b*	*b*	*b*
poly(MUTMA-OH)	*b*	*b*	*b*	*b*	*b*
poly(MUBP-OH)	0.0	16.8	16.8	4.2d	4.3b
poly(AUBIm-OH)	*b*	*b*	*b*	*b*	*b*
poly(AUTMA-OH)	*b*	*b*	*b*	*b*	*b*
poly(AUBP-OH)	0.0	100	100	4.2e	4.3f
poly(VBBIM-OH)	*c*	N/A	*c*	4.2f	*c*
poly(VBTMA-OH)	13.2	N/A	13.2	4.2g	4.3g
poly(VBBP-OH)	0.0	N/A	0.0	4.2h	N/A
poly(VBBP-OH)[d]	0.0	N/A	0.0	C5	N/A

[a]Samples were degraded at 60 °C and 20 eq (0.5 M) KOH/D_2O for 168 h. [b]Degradation was not quantified, due to limited water solubility of polymers. [c]Degradation was not quantified, because degraded polymer precipitated from solution. [d]Sample was degraded at 60 °C and 80 eq (1 M) KOH/D_2O for 168 h.

4.3.2 PIL Ion Conductivity and Water Uptake

Figure 4.3 shows the bromide ion conductivity (σ, mS cm^{-1}) versus normalized water uptake or hydration number (λ, mol H_2O/mol cation) of the twelve PILs investigated in this study at a condition of 90% RH at 60 °C. Figure 3a specifically shows the bromide conductivity as a function of hydration number for the three ethyl methacrylate-based PILs. The bromide conductivity increases with increasing water content for these PILs, where the PIL with trimethylammonium, poly(METMA-Br), which has the highest hydration number (6.4), as well as the highest absolute water uptake (45.9 wt%), yields

the highest bromide conductivity of 21.3 mS cm^{-1} among the methacrylate-based PILs. The positive correlation between conductivity and water content can be attributed to a water-assisted transport mechanism similar to water-Nafion systems. A similar trend of increasing IECs with increasing conductivity is observed for these PILs, where the IECs are 4.2, 4.2, and 5.8 mmol g^{-1} for the butylimidazolium, butylpyrrolidinium, and trimethylammonium polymers, respectively.

When the alkyl chain spacers of the methacrylate-based PILs are increased from ethyl to undecyl, a correlation between conductivity and water content was no longer observed. Figure 4.3b shows the bromide conductivity as a function of hydration number for the three undecyl methacrylate-based PILs. The hydration number among the three PILs is relatively constant (ranging from 3.9 to 4.0). However, the bromide conductivity shows a 2-fold increase from 6.9 to 12.4 mS cm^{-1} from the butylimidazolium to the trimethylammonium cation, and greater than 4-fold increase from butylimidazolium to butylpyrrolidinium cation, where a high bromide conductivity of 29.7 mS cm^{-1} was observed for the butylpyrrolidinium undecyl methacrylate-based PIL, poly(MUBP-Br). Likewise, no trend relating conductivity and IEC was observed for these PILs (IECs = are 2.7, 2.7, and 3.4 mmol g^{-1} for the butylimidazolium, butylpyrrolidinium, and trimethylammonium polymers, respectively). IECs decreased from the ethyl methacrylate to undecyl methacrylate PILs because of the increased molecular weight due to the long alkyl side chains. Still, IECs remain relatively high compared to Nafion (IEC = 0.9 mmol g^{-1}), with relatively low water uptakes ($\lambda \approx 4$ for PILs versus $\lambda \approx 8$-12 for Nafion at 90%

RH, 30 °C[117,118]), yielding a desired combination of AEM properties (high ion conductivity at low water contents).

Although the only change in chemistry between the undecyl methacrylate and undecyl acrylate PILs is the methyl group attached to the backbone, a reduction in bromide conductivity is observed in Figure 4.3c for all three cation types. Particularly, for butylpyrrolidinium PILs, the conductivity decreases ~4-fold from 29.7 mS cm^{-1} for the undecyl methacrylate to 7.9 mS cm^{-1} for the undecyl acrylate. The decrease in conductivity cannot be attributed to water content; for each cation type, hydration number values actually increased (between 0.1 to 0.9) and absolute water content increased (between 0.6 wt% to 6.0 wt%) from the undecyl methacrylate to undecyl acrylate backbone. IEC also increased by ~0.1 mmol g^{-1} for each PIL. Overall, the long-chain acrylate showed no advantages over the long-chain methacrylate backbones in terms of ion conductivity or water uptake.

In Figure 4.3d, the bromide ion conductivity of the three styrene-based PILs is shown as a function of hydration number. The conductivity and hydration number values for these PILs are similar to the values for the ethyl methacrylate-based PILs, however a clear trend between conductivity and hydration number was not observed. Specifically, the butylimidazolium and butylpyrrolidinium possessed conductivity and hydration numbers of 10.1 mS cm^{-1} and 14.5 mS cm^{-1} and 4.7 and 5.6, respectively. Interestingly, the trimethlyammonium possessed the lowest conductivity of all twelve PILs explored, regardless of also having the highest hydration number, highest absolute water uptake, and second highest IEC of the twelve PILs. Specifically, poly(VBTMA-Br) possessed a

conductivity, hydration number, and IEC of 2.7 mS cm^{-1}, 8.1, and 5.7 mmol g^{-1}. These results indicate that several other cation/backbone combinations, particularly butylpyrrolidinium/styrene, trimethylammonium/ethyl methacrylate, and butylpyrrolidinium/undecyl methacrylate, may yield improvements in transport properties over the standard benzyl trimethylammonium/styrene (benzyl trimethylammonium). A summary of the transport properties of the PILs at 60 °C and 90% RH is listed in Table 4.2. Note that in this study, only bromide conductivity was measured rather than hydroxide conductivity, as it is common practice in literature to measure ion conductivity of anion forms which are stable under atmospheric conditions (e.g., bromide, chloride, bicarbonate); hydroxide is known to convert rapidly to bicarbonate form upon exposure to the carbon dioxide present in air. Previous conductivity data for the ethyl methacrylate butylimidazolium PIL showed an approximate 4-fold increase in conductivity at 60 °C and 90% RH when the PIL was exchanged from bromide to hydroxide form.[48] A similar increase in conductivity may have resulted from the exchange of the PILs in this study from bromide to hydroxide form, but was not measured in this study. Additionally, glass transition temperatures (T_gs) of the twelve PILs measured by DSC are listed in Appendix C (Figure C6, Table C2).

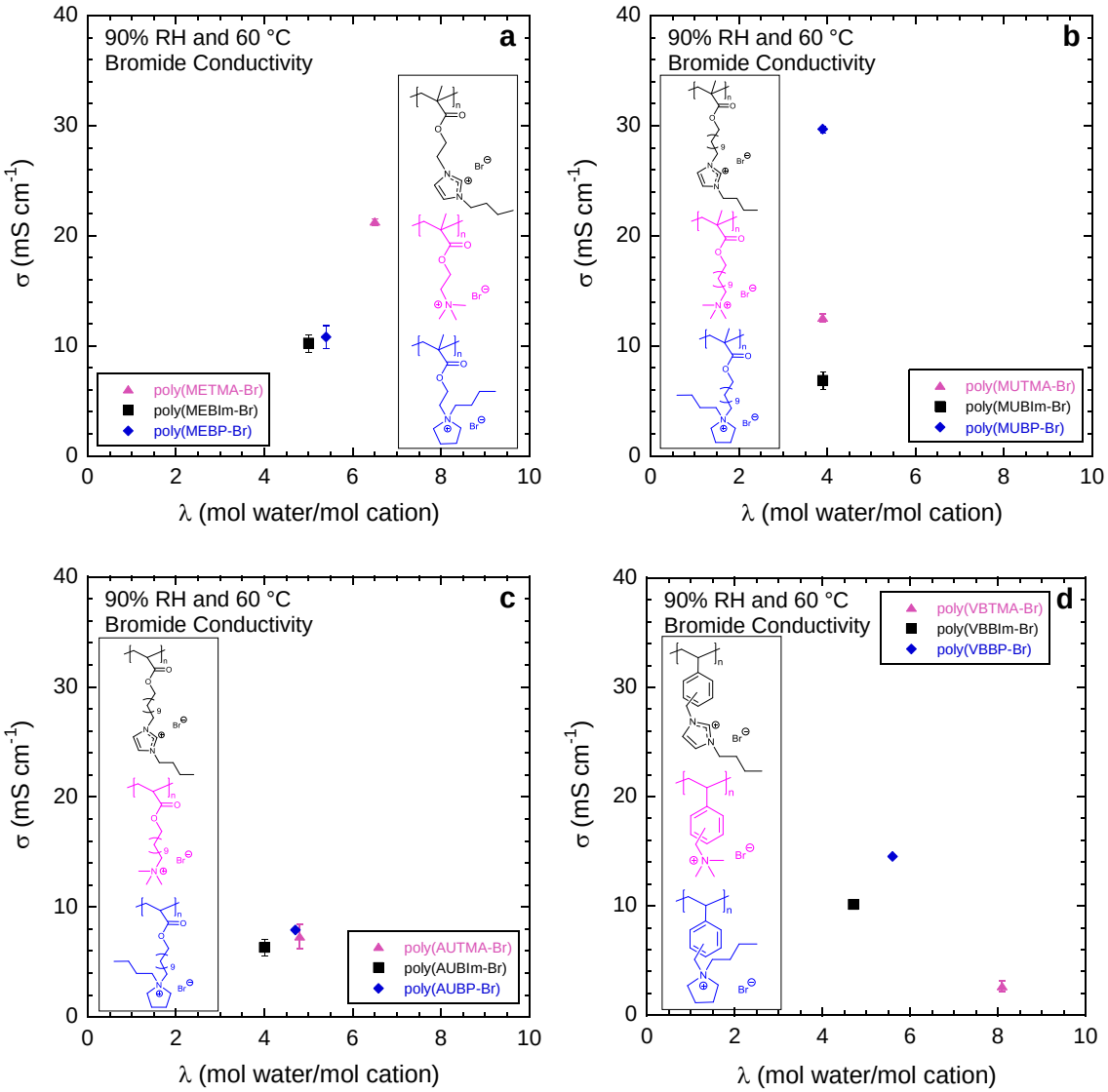

Figure 4.3 Bromide ion conductivity versus hydration number for (a) ethyl methacrylate- (b) undecyl methacrylate- (c) undecyl acrylate- and (d) styrene-based PILs with various cations at 60 °C and 90% RH.

Table 4.2 Ion Conductivity and Water Content of PILs.

Polymer	σ (mS cm^{-1})[a]	Water Uptake (wt%) [a]	λ (mol H_2O/mol cation)	Calculated IEC (mmol g^{-1})
poly(MEBIm-Br)	10.3	28.6	5.0	4.2
poly(METMA-Br)	21.3	45.9	6.4	5.8
poly(MEBP-Br)	10.5	30.2	5.4	4.2
poly(MUBIm-Br)	6.9	22.2	3.9	2.7
poly(MUTMA-Br)	12.6	28.1	3.9	3.4
poly(MUBP-Br)	29.7	25.2	4.0	2.7
poly(AUBIm-Br)	6.3	22.8	4.0	2.9
poly(AUTMA-Br)	7.3	34.1	4.8	3.5
poly(AUBP-Br)	7.9	26.2	4.7	2.8
poly(VBBIM-Br)	10.1	26.7	4.7	4.1
poly(VBTMA-Br)	2.7	57.8	8.1	5.7
poly(VBBP-Br)	14.5	31.5	5.6	4.1

[a]Conductivity and water uptake were measured at 60 °C and 90% RH.

4.4 Conclusions

A series of twelve PILs containing four backbones (ethyl methacrylate, undecyl methacrylate, undecyl acrylate, styrene) and three covalently attached cations (butylimidazolium, trimethylammonium, butylpyrrolidinium) were synthesized and characterized. Alkaline chemical stability of the PILs was examined *via* ^{1}H NMR spectroscopy to quantify the extent of degradation and identify the specific degradation pathways in regards to backbone/cation pairings and their synergistic impact on chemical stability. Regarding backbone pairing for the butylpyrrolidinium cation, ethyl and undecyl methacrylate backbones proved to be more stable than the undecyl acrylate backbone, and the long chain carbon spacer of undecyl methacrylate also enhanced alkaline chemical

stability relative to ethyl methacrylate. Overall, the butylpyrrolidinium styrene-based PIL had the highest alkaline chemical stability, exhibiting 0% degradation after 168 h of exposure to 80 eq KOH/D_2O at 60 °C; the benchmark styrene/BTMA pairing degraded 13.2% under the same conditions. The high alkaline chemical stability of styrene/butylpyrrolidinium was attributed to the synergistic stability-enhancing properties of this PIL: the nonpolarizable pyrrolidinium ring, the sterically hindering butyl substituent, and the electron donating benzyl attachment. Additionally, this highly chemically stable PIL also achieved a high bromide ion conductivity of 14.5 mS cm^{-1} at 60 °C and 90% RH. Numerous improvements are noted for the styrene/butylpyrrolidinium pairing relative to the popular styrene/BTMA pairing: higher conductivity, higher chemical stability, and lower water uptake. Like BTMA, butylpyrrolidinium is also attachable by a facile functionalization reaction with a commercially available chemical that can be simply incorporated into popular AEM styrene backbones.

This study provides a comparison of alkaline chemical stability and transport properties of four major polymer backbone types paired with three major cation types and shows that the butylpyrrolidinium styrene-based AEM chemistry is ideal for achieving improved longevity and performance of solid-state AFCs. Additional improvements to conductivity may also be achieved by incorporating a pyrrolidinium-functionalized styrene block into a PIL block copolymer, as the microphase-separated morphology present in PIL block copolymers was previously shown in this work to enhance conductivity. The block copolymer structure would also provide the opportunity for incorporating a mechanically

strengthening block to produce robust AEMs. Incorporating the styrene/pyrrolidinium pairing into a PIL block copolymer structure warrants further exploration.

CHAPTER V

ION TRANSPORT IN POLYMERIZED IONIC LIQUID MULTI-BLOCK COPOLYMER ANION EXCHANGE MEMBRANES WITH METHYLPYRROLIDINIUM CATIONS

5.1 Introduction

Previous studies in this work have shown that enhanced conductivity in AEMs can be achieved through ion confinement within PIL microdomains of nanostructed PIL block copolymers. Studies in this work have also examined alkaline chemical stability in AEMs to reveal the merit of a styrene/pyrrolidinium backbone/cation pairing, for its resistivity to chemical degradation at high pH. Results indicate that the most desirable AEM properties may be achieved by incorporating a pyrrolidinium-functionalized styrene block into a PIL block copolymer; however, this specific chemistry has not currently been explored in literature.

In this study, a polymerized ionic liquid (PIL) ABCBA pentablock terpolymer, poly(tbS-*b*-EB-*b*-VBMP-Br-*b*-EB-*b*-tbS), was investigated and contains tert-butyl-styrene as the A outer blocks (tert-butyl-styrene: tbS), a random copolymer of ethylene butylene blocks (ethylene butylene: EB) as the B blocks, and a pyrrolidinium-functionalized styrene PIL midblock (vinylbenzylmethypyrrolidinium bromide: VBMP-Br) as the inner C block (Figure 5.1).. Ion exchange metathesis of the bromide-conducting PIL block polymer to hydroxide form allowed for the investigation of ion conductivity and water uptake of the hydroxide form of the solid-state anion exchange membrane (AEM), *via* electrochemical

impedance spectroscopy (EIS) and dynamic vapor sorption (DVS), respectively. To access alkaline chemical stability, AEMs were exposed to high pH (0.5 M and 1 M KOH) at 60 °C for 168 h (1 week), followed by reexamination of the ion conductivity *via* EIS, as well as analysis of the chemical structure *via* Fourier transform infrared-attenuated total reflectance (FTIR-ATR) spectroscopy. The effect of carbon dioxide on conductivity of the hydroxide-conducting AEM was monitored *via* EIS. Thermal properties of the PIL block polymer were measured using TGA (thermal gravimetric analysis) and DSC (differential scanning calorimetry).

5.2 Experimental Section

5.2.1 Materials

Potassium hydroxide (KOH, ≥90%, reagent grade) was used as received from Sigma-Aldrich. Deionized (DI) water was used as appropriate. Poly(tbS-*b*-EB-*b*-VBMP-Br-*b*-EB-*b*-tbS) AEM was used as received from Kraton Performance Polymers, Inc: IEC ~1.8 mmol g^{-1}, M_n ~ 76 kg mol^{-1} where M_n of respective blocks is 15-13-16-14-18 kg mol^{-1}.

5.2.2 Preparation of Thin Films

The AEM was received in the form of a thin film sheet (*ca.* 30 cm (L) × 20 cm (W)). Multiple measurements across the film thickness indicated a uniform thickness of 38 μm. For conductivity testing, films were cut into rectangular strips (*ca.* 40 mm (L) × 8.5 mm (W)). For infrared analysis before and after exposure to high pH, films were cut into squares ((*ca.* 20 mm (L) × 20 mm (W))).

5.2.3 Alkaline Chemical Stability

In order to assess alkaline chemical stability of the AEMs, films were exposed to 50 mL solutions of 0.5 M and 1 M KOH at 60 °C for 168h. These solutions were argon purged and stored in jars maintained at 60 °C in an oven. Conductivity and chemical structure were then analyzed relative to films that were stored in argon purged DI water at room temperature for 168 h. Multiple square (for IR) and rectangular (for EIS) films were stored in each jar.

5.2.4 Anion Exchange Metathesis

AEMs were anion exchanged from bromide to hydroxide form, in order to collect hydroxide ion transport data. Films were placed in a 40 mL vial with freshly prepared 0.2 M KOH aqueous solution, which was purged with argon beforehand and continuously purged with argon during the exchange, for 1 h. The KOH solution was replaced with a new argon purged solution using a syringe every 1 h and this was repeated 3 times. The KOH solution was then removed by syringe and replaced with argon saturated deionized (DI) water for 1 h by syringe; this was repeated with a fresh batch of DI water 3 times, to extensively wash the hydroxide-exchanged polymer. The film was then stored in argon-purged DI water at room temperature. AEMs were approximately 91% hydroxide-exchanged, based on the residual bromide found in elemental analysis (EA). EA, bromide form: C, 68.05; H, 8.93; N, 2.40; Br, 17.93; EA, hydroxide form: C, 71.78; H, 9.78; N, 2.11; Br, 1.55.

5.2.5 Characterization

EA was performed by Atlantic Microlab, Inc., Norcross, GA. The ionic conductivities of polymer films were measured with electrochemical impedance spectroscopy (EIS; Solartron, 1260 impedance analyzer, 1287 electrochemical interface, Zplot software) over a frequency range of 10^2–10^6 Hz at 10 mV. Conductivities were collected in an environmental chamber (Espec, BTL-433 model), where temperature and relative humidity were controlled. The in-plane conductivities of the polymer films were measured in a cell with four-parallel electrodes, where an alternating current was applied to the outer electrodes and the real impedance or resistance, *R*, was measured between the two inner reference electrodes. The resistance was determined from a high x-intercept of the semicircle regression of the Nyquist plot. Conductivity was calculated by using the following equation: $\sigma = L/AR$, where L is the distance between two inner electrodes and A is the cross-sectional area of the polymer film ($A = Wl$; W is the film width and l is the film thickness). Samples were allowed to equilibrate for 2 h at each temperature and humidity followed by six measurements at the equilibrium condition. The values reported are an average of these steady-state measurements. An average error of < 5% was observed among repeated experiments. Note that CO_2 was not removed from humid air in these experiments, except where otherwise noted.

Water uptake or content was measured with dynamic vapor sorption (DVS, TA Instruments Q5000). A dry film sample was first loaded into the DVS and preconditioned at 0% RH and 30 °C until equilibrium was reached; equilibrium was established as <0.05 wt% change for at least 30 min for all conditions. The relative humidity was then

systematically changed to values of 30%, 45%, 60%, 75%, 95%, and 90% RH at a fixed temperature of 60 °C, and subsequently maintained at 90% RH, while temperature was systematically changed to 50 °C, 40 °C, and 30°C, equilibrating at each condition. Equilibrium time for each step was less than the 2 h (the time allotted for conductivity measurement steps). The polymer water content (uptake) [wt%; g H_2O/g dry polymer] was calculated as follows:

$$W_W = \frac{W - W_0}{W_0} \times 100 \tag{5.1}$$

where W_0 and W are dry and wet polymer weights measured before and after the DVS experiment, respectively. To measure saturated liquid water uptake, a film weighing ~13 mg was soaked in argon purged DI water at 60 °C for 24 h. To determine water content, the film was removed from the water, patted dry, and immediately placed in the DVS, where it was dried at 60 °C and 0% RH until equilibrium (<0.5% wt loss for 30 min.) was reached. The weight loss observed from drying the film was interpreted as the saturated liquid water uptake.

Chemical structures of the polymers were investigated with infrared spectroscopy using a Fourier transform infrared (FTIR) spectrometer (Nicolet 6700 Series; Thermo Electron) equipped with a single reflection diamond ATR accessory (Specac; Quest). All spectra were collected using a liquid nitrogen-cooled mercury-cadmium-telluride (MCT) detector at 32 scans per spectrum with a resolution of 4 and a data spacing of 1.925 cm^{-1}. Samples were clamped with an anvil at a constant load of 68.9 MPa onto the surface of the ATR crystal (1.8 mm diameter). Before each experiment, a background spectrum of the bare

ATR crystal was collected, and all subsequent collected spectra were subtracted from this spectrum.

Glass transition temperatures (T_gs) were measured by differential scanning calorimetry (DSC; TA Instruments, Q200) over a temperature range of -100 to 180 °C at a heating/cooling rate of 10 °C/min under a N_2 environment using a heat/cool/heat method. Thermal degradation of the AEMs was measured by thermal gravimetric analysis (TGA; TA Instruments, Q50) over a temperature range of 30 to 1000 °C at a heating rate of 10 °C/min under a N_2 environment. The results of the thermal characterization of the bromide- and hydroxide- conducting AEMs are shown in Appendix D, Figure D3.

5.3 Results and Discussion

In this study, the transport properties and alkaline chemical stability of a hydroxide-exchanged PIL pentablock terpolymer or multi-block polymer AEM, poly(tbS-*b*-EB-*b*-VBMP-OH-*b*-EB-*b*-tbS) (chemical structure shown in Figure 5.1), were examined. In Figure 5.2, ion conductivity and water uptake data is presented for the hydroxide-exchanged PIL multi-block polymer AEM, after anion exchange metathesis, no additional efforts were made to prevent membrane carbonation from exposure to CO_2, except where otherwise noted. Figure 5.2a and 5.2c shows a comparison of temperature-dependent ion conductivity and water uptake values, respectively, for the PIL block polymer at 90% RH. Measurements were conducted at various temperatures ranging from 30 to 80 °C. In Figure 5.2a, hydroxide conductivity follows an Arrhenius behavior with temperature at high humidity promoted by the thermal activation of water-assisted ion transport with an

activation energy of 25.0 kJ mol^{-1}. Water uptake (Figure 5.2c) was observed to be relatively constant over the measured temperature range of 30 to 60 °C, with values ranging from 26.1 to 23.9 wt%, respectively.

Figure 5.2b and 5.2d shows a comparison of humidity-dependent ion conductivity and water uptake values, respectively, for the PIL block polymer at 90% RH. Measurements were conducted at various humidities ranging from 30% RH to 95% RH (green squares) and in liquid water (green diamond) at 60 °C. The humidity-dependent data were extrapolated to 100% RH (dashed line) for comparison with the measured saturated liquid water results; both correspond to a water activity of one. Additionally, a second saturated liquid water conductivity experiment at 60 °C was performed under argon purge to prevent exchange of the hydroxide anion to carbonate and/or bicarbonate forms, and the data is shown in Figure 5.2b (red diamond); experimental details, as well as time-dependent hydroxide ion conductivity measurements for this experiment, can be found in Appendix D, where ion conductivity over time is shown in Figure D1. Figure 5.2b shows that, as expected, the ion conductivity increases over three orders of magnitude as humidity increases from 60% RH to 95% RH. This increase can be attributed to a water-assisted transport mechanism, where an increase in water uptake (6.5 wt% to 26.4 wt%; Figure 5.2d) was observed over this humidity range. Interestingly, when the results were extrapolated to 100% RH and compared with samples measured in liquid water, there was a discontinuous increase in both the conductivity and water uptake data. For the experiment where membrane carbonation was not prevented, the observed liquid conductivity of the AEM at 60 °C was 29.3 mS cm^{-1}, which corresponds to a 141%

increase from the extrapolated 100% RH results. Similarly, a 109% increase was observed for the saturated liquid water uptake experiments, where the observed water uptake was 64.0 wt% higher than the extrapolated 100% RH results. This phenomena has been commonly observed in PEMs, such as Nafion, *i.e.*, higher water uptake in liquid water relative to 100% RH conditions; this has been referred to as the Schroeder's paradox. Further increases relative to the extrapolated data were observed in the liquid water conductivity measurements for the experiment where membrane carbonation was prevented (*i.e.*, purge with argon); the observed liquid conductivity of the AEM at 60 °C was 44.4 mS cm^{-1}, which corresponds to a 256% increase from the extrapolated results at 100% RH, and a 52% increase compared to the liquid water conductivity with no CO_2 control (*i.e.*, no purge with argon). From the discontinuity between the experiments with and without CO_2 control, it can be inferred that some degree of carbonation of the AEM may have occurred during the non-controlled conductivity experiments, resulting in somewhat reduced conductivity values, where both hydroxide and exchanged anion form (carbonate, bicarbonate) conductivities are being measured.

In order to assess alkaline chemical stability of the AEM, films were exposed to high pH (0.5 M and 1 M KOH) at 60 °C for 168 h. Subsequently, films were washed with DI water and their conductivity was measured after 2 h at 60 °C and 90% RH. It was observed that the film that was never exposed to KOH or elevated temperatures had a conductivity of 4.7 mS cm^{-1} at 60 °C and 90% RH. The conductivity was relatively unchanged in the films that were placed in 0.5 M and 1 M KOH; conductivity values were measured as 4.8 mS cm^{-1} and 5.0 mS cm^{-1}, respectively, after 1 week at these conditions. Figure 5.3 shows

pictures of the AEMs in the bromide form, as well as in the hydroxide form before and after exposure to high pH conditions. The films remained physically intact for all conditions explored; a slight color change from light yellow to a darker yellow was observed for films that were exposed to high pH. FTIR-ATR spectroscopy was used to analyze the chemical structure of the AEMs before and after high pH exposure. Some changes were noted in the spectra, and this is further discussed in Appendix D (FTIR-ATR spectra shown in Figure D2.) Overall, AEMs maintained their hydroxide conductivity in alkaline conditions up to 1 M KOH at 60 °C for 168 h, indicating high levels of alkaline chemical stability.

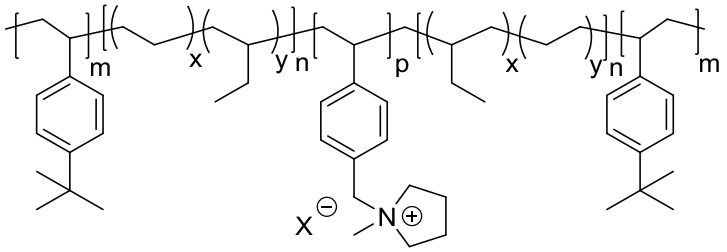

Figure 5.1 Chemical structure of PIL multiblock polymer, poly(tbS-*b*-EB-*b*-VBMP-X-*b*-EB-*b*-tbS), where X represents the mobile anion: bromide (Br^-) or hydroxide (OH^-).

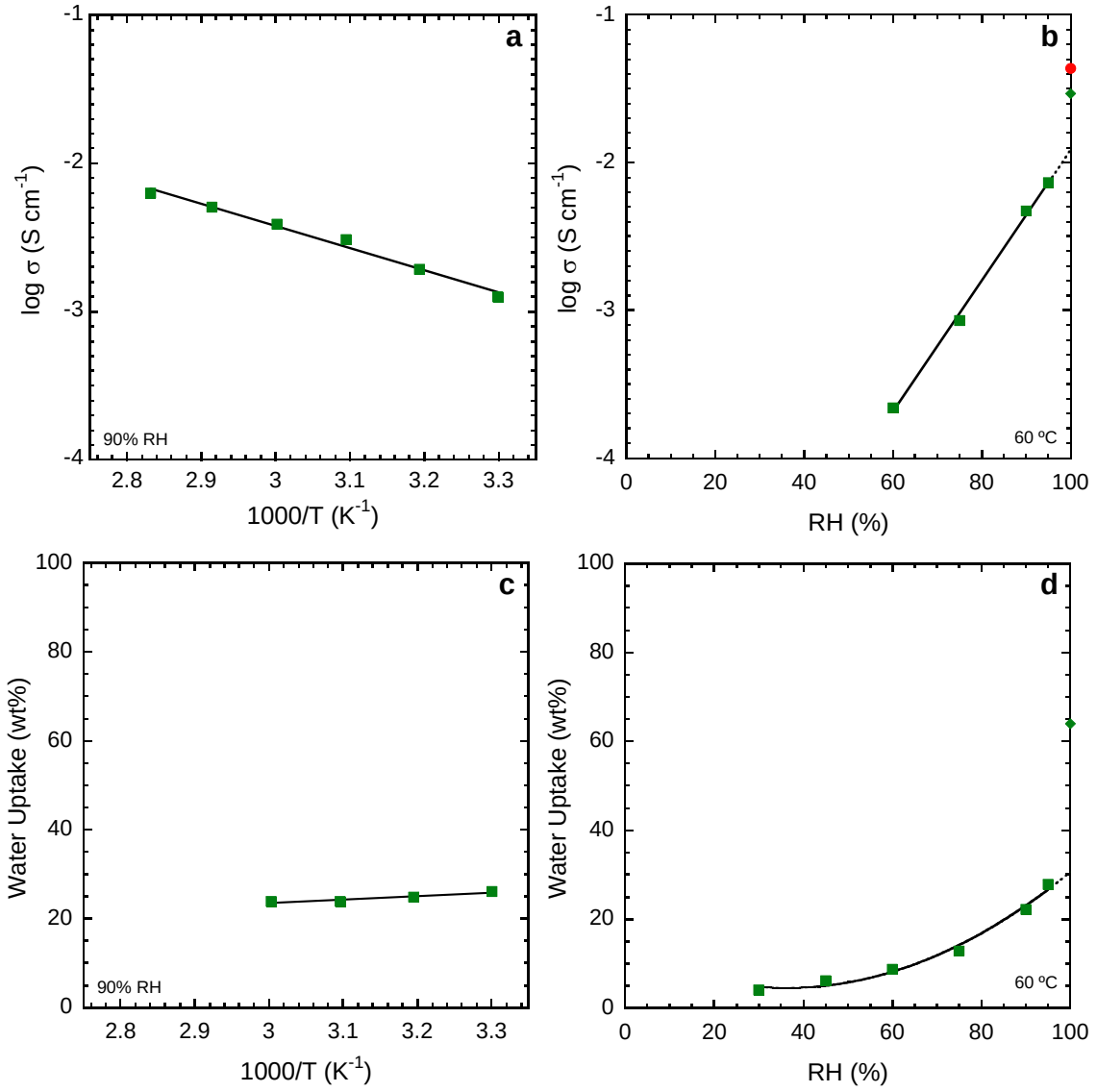

Figure 5.2 Temperature-dependent (a) ion conductivity and (c) water uptake at 90% RH and humidity-dependent (b) ion conductivity and (d) water uptake at 60 °C for hydroxide-conducting PIL multi-block polymer, poly(tbS-*b*-EB-*b*-VBMP-OH-*b*-EB-*b*-tbS). Solid lines represent trend lines of the data, and dashed lines represent an extrapolation of that trend to 100% RH. The measured conductivities and water uptakes are represented by green squares at humidified conditions and green diamonds at saturated liquid water conditions. During experiments, no efforts were taken to prevent hydroxide conversion to bicarbonate and/or carbonate forms in air, except in the case of one saturated liquid water conductivity experiment (red diamond).

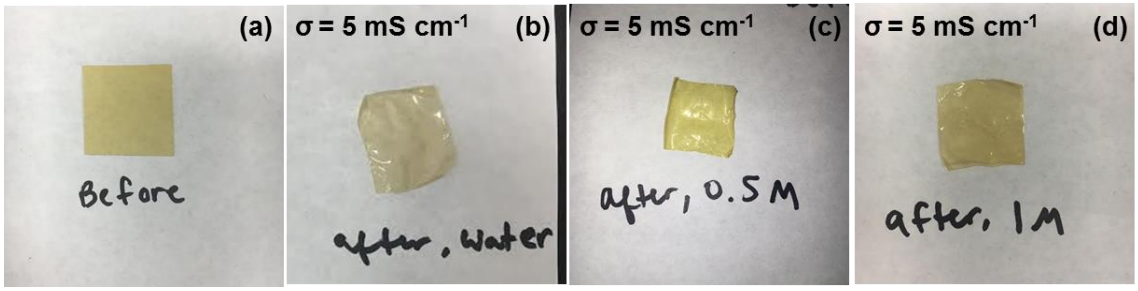

Figure 5.3 (a) Bromide-conducting PIL multi-block polymer AEM, poly(tbS-*b*-EB-*b*-VBMP-Br-*b*-EB-*b*-tbS), at ambient conditions, as received. Hydroxide-exchanged AEMs, poly(tbS-*b*-EB-*b*-VBMP-OH-*b*-EB-*b*-tbS), after 168 h in (b) DI water at room temperature, (c) 0.5 M KOH at 60 °C, (d) 1 M KOH at 60 °C. Conductivity measurements were performed at 60 °C and 90% RH.

5.4 Conclusions

The hydroxide ion conductivity and alkaline chemical stability of a PIL multi-block polymer (ABCBA pentablock terpolymer) AEM with a styrene/pyrrolidinium-based PIL block was investigated. A high hydroxide conductivity of 43.4 mS cm^{-1} at 60 °C in liquid water was achieved and no physical degradation or loss of conductivity was observed in the membrane after 168 h in 1 M KOH at 60 °C. Overall, the results from this study indicate the PIL block copolymer utilizing a styrene/pyrrolidinium backbone/cation pairing in the PIL block is a promising chemistry for producing highly conductive, chemically stable, robust AEMs for implementation in future solid-state AFCs.

CHAPTER VI

SULFONATED POLYMERIZED IONIC LIQUID BLOCK COPOLYMERS

6.1 Introduction

In addition to PIL block copolymers, another type of ion-conducting block copolymer of significant interest has been sulfonated block copolymers.[119] Sulfonated block copolymers are block copolymers where one block consists of a covalently attached sulfonic acid moiety with a mobile counter cation (typically protons). These polymers have been investigated over the past several decades for a variety of applications, most notably as membrane separators for proton exchange membrane fuel cells.[119]

Similar to PIL block copolymers and sulfonated block copolymers, which both contain positively and negatively charged ions and thus an overall net neutral charge, another class of block copolymer known as zwitterionic block copolymers has been prepared in literature, and contains both covalently attached anions and cations (*i.e.*, no mobile counter ions; both cation and anion are covalently attached to the polymer).[120-125] Also, in contrast to PILs where imidazolium has been the most explored cation, the cationic moieties most frequently employed in polyzwitterions are quaternized or protonated ammonium groups, while anionic groups are typically phosphates, sulfonates, and carboxylates.[126] Although zwitterionic block copolymers are hydrophilic similar to other ion-containing polymers, such as sulfonated polymers, they have no mobile ions and thus behave more closely to non-ionic polar polymers rather than polyelectrolytes.[127]

One potential route for synthesizing a new type of ion-conducting block copolymer is to combine the concept of zwitterionic block copolymers with current ion-conducting block copolymers. In other words, synthesize a block copolymer, where one block contains a covalently attached cation and mobile counter anion and the other block contains a covalently attached anion and mobile counter cation, e.g., *via* sulfonation of a PIL block copolymer. A sulfonated PIL block copolymer that simultaneously conducts both free cations and anions, has never been previously synthesized and thus represents an exciting new opportunity for exploration within ion-conducting block copolymers, specifically, for applications where both mobile cations and mobile anions may be advantageous (*e.g.*, drug delivery, electrodialysis, bipolar membranes, solid-state capacitors, *etc.*).

In this study, a sulfonated PIL diblock copolymer, poly(SS-Li-*b*-AEBIm-TFSI), consisting of an ionic PIL component (1-[(2-acryloyloxy)ethyl]-3-butylimidazolium bis(trifluoromethylsulfonyl)imide) (AEBIm-TFSI) and an ionic sulfonated styrenic component (SS) (Scheme 1), was successfully synthesized *via* the RAFT polymerization technique. Thermal properties of the sulfonated PIL block copolymer and non-sulfonated PIL block copolymer (polymer prior to sulfonation) were measured using TGA (thermal gravimetric analysis) and DSC (differential scanning calorimetry). The conductivity, water uptake, and morphology of poly(SS-Li-*b*-AEBIm-TFSI) films (cast with 1 M Li-TFSI in ionic liquid) were investigated. Transport and morphological properties were compared to results from a previous study of the non-sulfonated PIL block copolymer at a similar PIL composition.

6.2 Experimental Section

6.2.1 Materials

4-cyano-4-[(dodecylsulfanylthiocarbonyl)sulfanyl]pentanoic acid (chain transfer agent (CTA), >97%, HPLC), tetrahydrofuran (THF, ≥99.9%, HPLC), methanol (99.8%), 1-butylimidazole (98%), N,N-dimethylformamide (DMF, 99.9%, HPLC), hexanes (≥98.5%), lithium bis(trifluoromethanesulfonyl)imide (LiTFSI, 97%), acetonitrile (anhydrous, 99.8%), dichloromethane (DCM, ACS reagent, >99.5%), magnesium sulfate (anhydrous, 99%), deuterated chloroform ($CDCl_3$, 99.96 atom % D, contains 0.03% v/v TMS), and dimethyl-d_6 sulfoxide (DMSO-d_6, 99.9 atom % D, contains 0.03% v/v TMS) were used as received from Sigma-Aldrich. 1-Ethyl-3-methylimidazolium bis(trifluoromethylsulfonyl)imide, (EMIm-TFSI, 99%) was used as purchased from IoLiTec. Azobis(isobutyronitrile) (AIBN, 98%, Sigma-Aldrich) was purified by recrystallization twice from methanol. Styrene (S, 99%, Sigma-Aldrich) was purified by distillation over calcium hydride (CaH_2, 95%, Sigma-Aldrich) at a reduced pressure. Ultrapure deionized (DI) water was used as appropriate. 2-bromoethyl acrylate (BrEA) monomer[56] and acetyl sulfate[128] were prepared according to procedures described in literature.

6.2.2 PS Macro-CTA Synthesis

The preparation of polystyrene (PS) macro-chain transfer agent (macro-CTA) is shown in Scheme 6.1(1). 5.00 g of styrene (0.048 mol) was mixed with 384.4 mg of CTA (0.952 mmol) in a 100 mL single-neck Schlenk flask. The flask was subjected to four

freeze−pump−thaw degassing cycles followed by sealing the reactor and carrying out the reaction under static nitrogen at 100 °C for 18 h. The resulting polymer was precipitated in methanol and dried under vacuum in an oven at room temperature for 24 h. Yield: 3.78 g of solid particles (70.2%). ^{1}H NMR (500 MHz, $CDCl_3$, 23 °C) δ (ppm): 7.30−6.30 (m, 5H, C_6H_5), 2.42−1.71 (m, 1H, CH_2CH), 1.71−1.10 (m, 2H, CH_2CH) (NMR, Figure 6.1(I)); SEC (THF, 40 °C): M_n = 4.36 kg mol^{-1}, M_w/M_n = 1.07 (against PS standards) (SEC, Appendix E, Figure E1).

6.2.3 Diblock Copolymer Poly(S-*b*-BrEA) Synthesis

The synthesis of the block copolymer (poly(S-*b*-BrEA)) is shown in Scheme 6.1(2). 3.083 g of BrEA monomer (17.202 mmol), 0.500 g of PS macro-CTA (0.115 mmol), and 1.9 mg of AIBN (0.012 mmol) were mixed with 16 mL of THF in a 50 mL Schlenk flask and subjected to four freeze-pump-thaw degassing cycles. After degassing, the reactor was sealed, and the reaction was then carried out under static nitrogen at 55 °C for 6 h. The resulting copolymer was precipitated in methanol, filtered, and then dried under vacuum in an oven at 50 °C for 24 h. The composition of the copolymer was calculated by ^{1}H NMR as shown in Figure 6.1 by relative integrations of resonance “e” versus resonance “a” (*i.e.*, e/(e + a)), and was determined to be 25.3 mol% BrEA. Yield: 0.339 g of solid particles (9.0%). ^{1}H NMR (500 MHz, $CDCl_3$, 23 °C) δ (ppm): 7.32−6.27 (m, 5H, C_6H_5), 4.40 (s, 2H, O−CH_2−CH_2−Br), 3.55 (s, 2H, O−CH_2−CH_2−Br), 2.60−1.66 (m, 1H, CH_2CH), 1.66−0.73 (m, 2H, CH_2CH), (NMR, Figure 6.1(II)); SEC (THF, 40 °C): M_n = 5.81 kg mol^{-1}, M_w/M_n = 1.20 (against PS standards) (SEC, Appendix E, Figure E1).

6.2.4 PIL Diblock Copolymer Poly(S-*b*-AEBIm-TFSI)

The synthesis of poly(S-*b*-AEBIm-Br) *via* post-functionalization of poly(S-*b*-BrEA) with 1-butylimidazole is shown in Scheme 6.1(3). The same procedure that is well documented in literature was used.[56] Yield: 0.365 g of solid particles (95.8%). Complete functionalization of the BrEA units with butylimidazole was confirmed and calculated by ^{1}H NMR as shown in Figure 6.1 by relative integrations of resonance "a+b+c" versus resonance "g" (*i.e.*, g/2/(g/2 + (a+b+c)/5)). The anion exchange of poly(S-*b*-AEBIm-Br) to poly(S-*b*-AEBIm-TFSI) is shown in Scheme 6.1(4). The same procedure that is well documented in literature was used.[56] Yield: 0.224 g of solid particles (67.2%). Complete exchange of Br^- to $TFSI^-$ was confirmed by elemental analysis, where no Br^- was observed in the final product. ^{1}H NMR (500 MHz, DMSO-d_6, 23 °C) δ (ppm): 9.32-8.98 (s, 1H, N−C*H*=N), 7.89−7.53 (d, 2H, N−C*H*=C*H*−N), 7.35−6.23 (m, 5H, C_6H_5), 4.64−4.05 (m, 4H, N−CH_2−CH_2−O, N−CH_2−CH_2−CH_2−CH_3), 3.69-3.45 (s, 4H, N−CH_2−CH_2−O, N−CH_2−CH_2-CH_2−CH_3), 2.34−1.66 (m, 1H, CH_2C*H*), 1.66−1.06 (m, 2H, CH_2CH), 0.95−0.77 (m, 5H, N−CH_2−CH_2−CH_2−CH_3, N−CH_2−CH_2−CH_2−CH_3) (NMR, Figure 6.1 III). Elemental Analysis (EA) Calculated: C, 55.71; H, 5.31; N, 5.18; F, 14.06; S, 7.91; Br, 0.00; EA Found: C, 57.52; H, 5.45; N, 4.59; F, 12.00; S, 6.97; Br, 0.00.

6.2.5 Preparation of Poly(S-b-AEBIm-TFSI) + Li-TFSI/IL Thin Films

Nonsulfonated PIL block copolymer, poly(S-b-AEBIm-TFSI), was dissolved in acetonitrile (~4% w/w) and a solution of 1 M Li-TFSI salt dissolved in EMIm-TFSI (~50% w/w salt/IL to polymer) was added to the polymer solution. The final material will be referred to as poly(S-b-AEBIm-TFSI) + Li-TFSI/IL. This solution was cast onto

Kapton film substrates (ca. 30 mm (L) × 5 mm (W) × 0.130 mm (H)), subsequently covered for 24 h, exposed to ambient conditions for 12 h, and further annealed at 50 °C under vacuum for 48 h.

6.2.6 Sulfonated PIL Diblock Copolymer Poly(SS-H-*b*-AEBIm-TFSI)

The sulfonation of poly(S-*b*-AEBIm-TFSI) to synthesize poly(SS-H-*b*-AEBIm-TFSI) (H refers to proton or acid form of sulfonated styrene) was performed following a procedure from literature[128] and is shown in Scheme 6.1(5). A 1% (w/v) solution of poly(S-*b*-AEBIm-TFSI) (148.3 mg) in dry dichloromethane (15 ml) was prepared. The solution was stirred and refluxed at approximately 40 °C, while acetyl sulfate (7 mol acid/mol S; 0.465 g acetic anhydride, 0.446 g H_2SO_4) in dry dichloromethane was added dropwise to begin the sulfonation reaction. After approximately 4 h, the solution had changed from a yellow color to a dark amber brown color and the reaction was terminated by slowly adding 5 mL of methanol. The sulfonated polymer was then precipitated with hexane. The precipitate was washed several times with hexane and then dried in a vacuum oven at 50 °C for 24 h. Pictures of the PIL block copolymer before and after sulfonation can be found in Appendix E in Figure E3. Yield: 0.168 g of solid particles (>100%, based on 15% sulfonation, which was estimated from EA results).

6.2.7 Sulfonated PIL Diblock Copolymer Poly(SS-Li-*b*-AEBIm-TFSI)

The cation exchange of poly(SS-H-*b*-AEBIm-TFSI) to poly(SS-Li-*b*-AEBIm-TFSI) is shown in Scheme 6.1(6). Poly(SS-H-*b*-AEBIm-TFSI) (0.148 g, 0.470 mmol H^+) and Li-

TFSI (0.723 g, 2.518 mmol) were mixed with DMF (3 mL) and stirred at 50 °C for 24 h. The reaction mixture was precipitated into methanol/water (1/1 v/v) and washed extensively with hexane. The resulting polymer was filtered and dried under vacuum in an oven at 50 °C for 24 h. Yield: 0.094 g of solid particles (63.2%, based on 15% sulfonation, which was estimated from EA results for this block copolymer. The degree of sulfonation (DS) of the PSS block was estimated as approximately 0.15 (mol sulfonic acid/mol PS). EA was used to determine DS, by matching calculated relative ratios of N, S, and F to those found. A significant degree of sulfonation is also apparent from the desulfonation reaction in the TGA thermograph for the sulfonated polymer relative to the nonsulfonated polymer in the range of 150 °C to 285 °C (See Appendix E Figure E2). ^{1}H NMR (500 MHz, DMSO-d_6, 23 °C) δ (ppm): 9.37-8.91 (s, 1H, N−C*H*=N), 7.91−7.57 (d, 2H, N−C*H*=C*H*−N), 7.38−6.20 (m, 5H, C_6H_5), 4.67−3.92 (m, 4H, N−CH_2−CH_2−O, N−CH_2-CH_2−CH_2−CH_3), 3.59 (s, 4H, N−CH_2−CH_2−O, N−CH_2−CH_2−CH_2−CH_3), 2.04−1.66 (m, 1H, CH_2C*H*), 1.66−1.06 (m, 2H, CH_2CH), 1.03−0.57 (m, 5H, N−CH_2−CH_2−CH_2−CH_3, N−CH_2−CH_2−CH_2−CH_3) (NMR, Figure 6.1 IV). EA Calculated (based on 15% sulfonation, estimated from EA results): C, 53.375.63; H, 5.214.73; N, 4.9617; F, 6.7913.47; S, 6.189.25; Br, 0.00; EA Found: C, 61.91; H, 6.49; N, 3.02; F, 7.95; S, 5.45; Br, 0.00. Presence of excess C and H, as well as lower than expected values for N, F, and S, is likely due to residual solvent. Relative ratios of elements N, F, and S indicate 15% sulfonation. EA Ratios Calculated (15% sulfonation): N/S, 0.54; F/S, 1.46; N/F, 0.37. EA Ratios Found: N/S, 0.55; F/S, 1.46; N/F, 0.38.

6.2.8 Preparation of Poly(SS-Li-*b*-AEBIm-TFSI) + Li-TFSI/IL Thin Films

Sulfonated PIL block copolymer, poly(SS-Li-*b*-AEBIm-TFSI), was dissolved in acetonitrile (~7% w/w) and cast onto Teflon substrates (*ca.* 40 mm (L) × 7.5 mm (W) × 0.525 mm (H)). A slow drying procedure was employed, where films were covered and a solvent reservoir was placed next to the cast films, such that the solvent was allowed to slowly evaporate over 168 h. Despite the slow drying procedure, films were glassy and exhibited significant cracking. In order to plasticize the material, a solution of 1 M Li-TFSI salt dissolved in EMIm-TFSI (~30% w/w salt/IL to polymer) was added to the polymer solution. The final material will be referred to as poly(SS-Li-*b*-AEBIm-TFSI) + Li-TFSI/IL. This solution was cast onto Kapton film substrates (*ca.* 40 mm (L) × 7.5 mm (W) × 0.130 mm (H)), subsequently covered for 24 h, exposed to ambient conditions for 12 h, and further annealed at 50 °C under vacuum for 48 h.

6.2.9 Characterization

A detailed description of the experimental characterization procedures can be found in Appendix E.

6.3 Results and Discussion

A sulfonated acrylate-based PIL block copolymer was synthesized *via* the following route (Scheme 6.1): (1,2) sequential RAFT polymerization, (3) post-functionalization reaction, (4) anion exchange reaction, (5) sulfonation reaction, (6) cation exchange reaction. Overall, the synthesis route is similar to our previous work,[56] where the major

difference is the sulfonation of the polystyrene block, which allows for the inclusion of a tethered anion (SO_3^-) and mobile cation (Li^+), in addition to the tethered cation (BIm^+) and mobile anion ($TFSI^-$) of the PIL block. The chemical structures of the sulfonated PIL block copolymer and precursors were analyzed by ^1H NMR (Figure 6.1). A composition of 25.3 mol% PIL was determined from relative integrations of proton resonances of the imidazolium ring at C(4,5) (g) positions versus the sum of all styrenic proton resonances at ortho (a), meta (b), and para positions (c) (Figure 6.1 III). The PIL composition matched the composition of acrylate in the neutral block copolymer, determined from relative integrations of proton resonance of the acrylate at 4.40 ppm (O−CH_2−CH_2−Br, labeled (e)) versus the styrenic proton resonance at ortho positions (a) (Figure 6.1 II). Therefore, the block copolymer was fully functionalized with butylimidazolium. The efficacy of ion exchange from the Br anion form to TFSI anion form was confirmed by EA. From EA of the block copolymers before and after sulfonation,, it was also determined that the S block was approximately 15 mol% sulfonated; TGA (Appendix E, Figure E2) and Fourier transform infrared-attenuated total reflectance (FTIR-ATR) spectroscopy further confirmed significant sulfonation (Appendix E, Figure E4-6). Post-sulfonation, a color change in the polymer from yellow to dark amber brown was also noted (Appendix E, Figure E3, as well as differences in the observed T_gs from DSC experiments (Figure 6.2a). The molecular weight, determined by SEC (Appendix E, Figure E1), of the neutral block copolymer, poly(S-*b*-BrEA), was 5.81 kg mol^{-1} with polydispersity of 1.20. As a result, molecular weights of the precursor PIL block copolymer, poly(S-*b*-AEBIm-TFSI), and

the final sulfonated PIL block copolymer, poly(SS-Li-*b*-AEBIm-TFSI) (15% sulfonation), were calculated to be 9.71 kg mol^{-1} and 10.13 kg mol^{-1}, respectively.

Scheme 6.1 Synthesis of sulfonated PIL block copolymer, poly(SS-Li-*b*-AEBIm-TFSI)

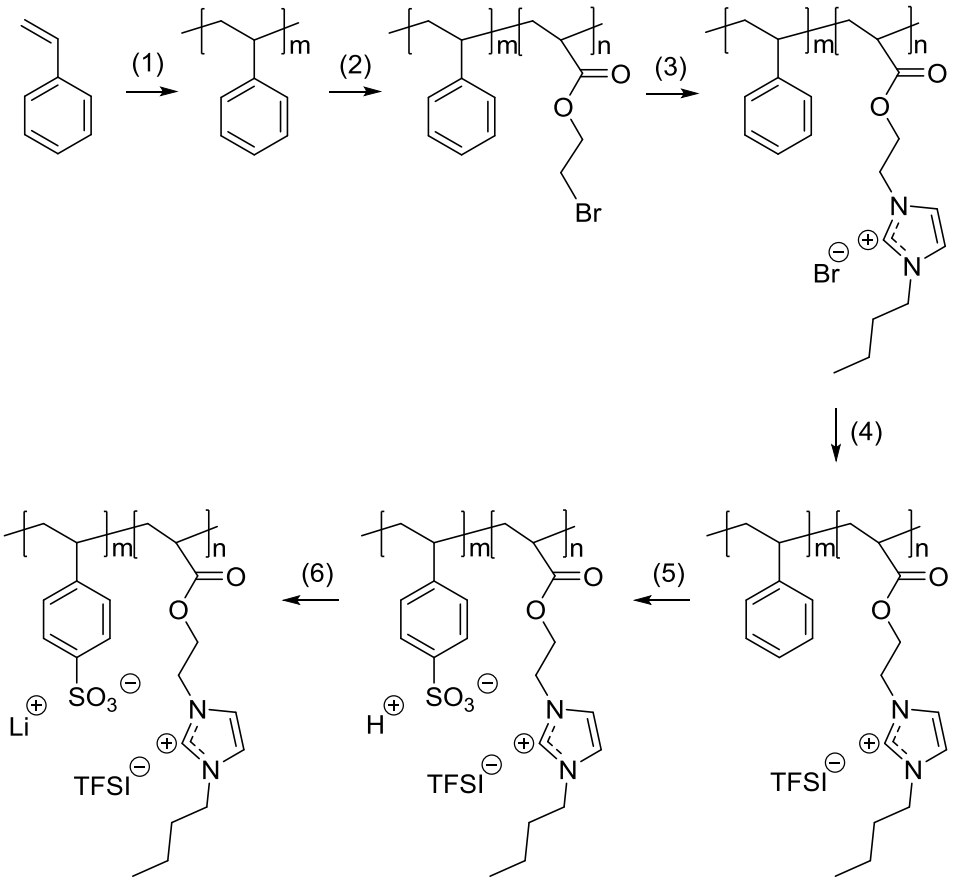

(1) CTA, 100 °C, 18 h; (2) BrEA, AIBN, THF, 55 °C, 6 h; (3) Butylimidazole, DMF, 80 °C, 48 h; (4) Li-TFSI, DMF, 50 °C, 24 h (5) DCM, acetyl sulfate, 4 h; (6) Li-TFSI, DMF, 50 °C, 24 h.

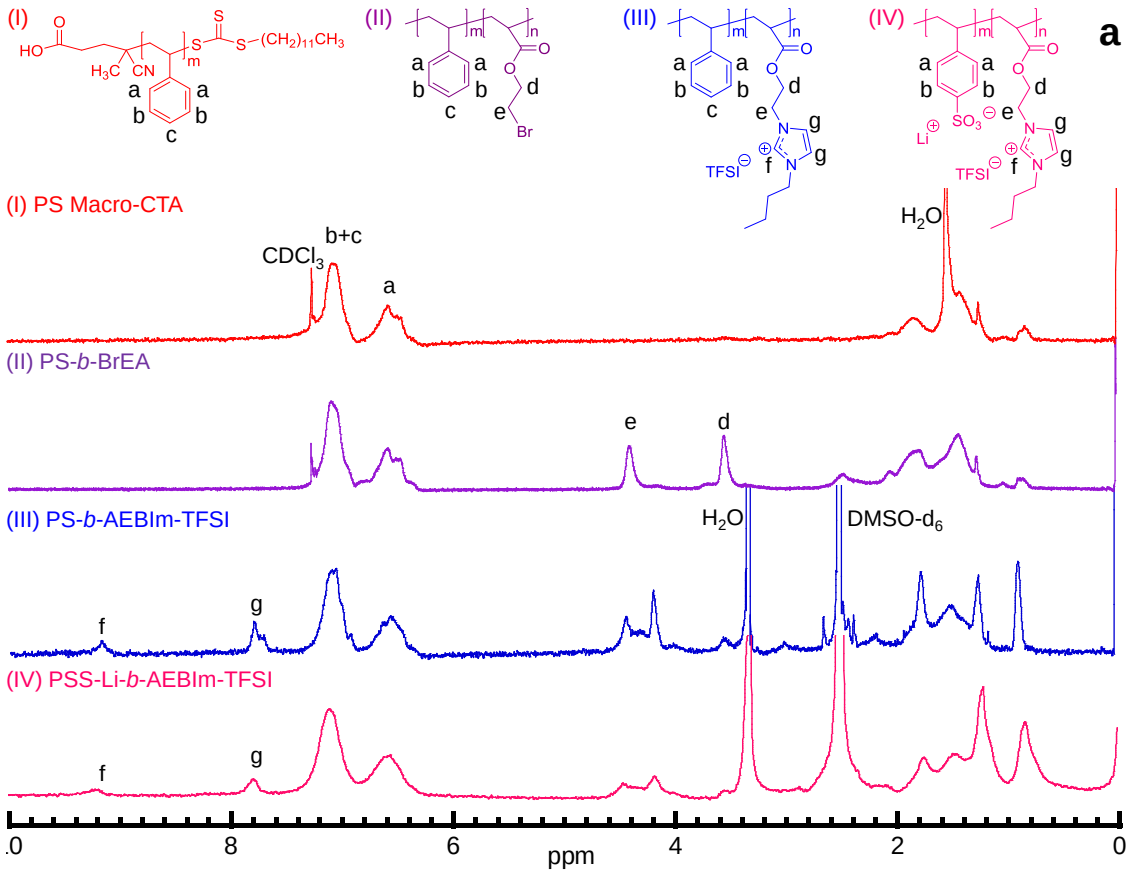

Figure 6.1 ^{1}H NMR spectra for (I) polystyrene Macro-CTA (red), (II) poly(S-*b*-BrEA) (purple), (III) poly(S-*b*-AEBIm-TFSI) (blue), (IV) poly(SS-Li-*b*-AEBIm-TFSI) (pink).

In Figure 6.2a, the non-sulfonated PIL diblock copolymer, poly(S-*b*-AEBIm-TFSI), shows two distinct glass transition temperatures (T_gs); the observed T_gs correspond to the PS block (76 °C) and the PIL block (17 °C), where the PS block T_g is comparable to that of the PS-CTA homopolymer (79 °C). These results suggest microphase separation in the poly(S-*b*-AEBIm-TFSI) diblock copolymer. Similarly, in our previous research concerning non-sulfonated PIL diblock copolymer poly(S-*b*-AEBIm-TFSI) at a comparable composition of 23.6 mol% PIL (relative to 25.3 mol% in this study), two distinct T_gs were observed.[56] Strong microphase separation was evidenced by small-angle

X-ray scattering (SAXS) in this previous study, where interestingly, at the 23.6 mol% PIL composition, poly(S-*b*-AEBIm-TFSI) exhibited two distinct primary scattering peaks with comparable intensity, suggesting a coexistence of two different morphologies. The observed scattering peaks contained a broad shoulder at q*, 2q*, and 4q*, indicating lamellar morphology, while the second set of scattering peaks at q* and 2q*, or the shoulder, were without higher order reflections such that morphology could not be assigned solely from SAXS; TEM images, however, clearly showed a coexisting lamellar and network morphology at this composition. Contrastingly, in this study, the SAXS profile in Figure 6.2b of the sulfonated PIL block copolymer with IL/salt (poly(SS-Li-*b*-AEBIm-TFSI) solution cast with 1 M Li-TFSI/EMIm-TFSI) shows one broad scattering peak at $q^* = 0.33\ nm^{-1}$, suggesting a weak microphase separation without long-range order; Bragg spacing, or correlation distance, was calculated by $d^* = 2\pi/q^*$ to be $d^* = 19.0$ nm. The lack of strong microphase separation may be attributed to attraction between the sulfonated block and the PIL block, *e.g.*, complexing between the negatively charged sulfonic acid moieties and the positively charged imidazolium moeities. Similarly, the DSC data for poly(SS-Li-*b*-AEBIm-TFSI) in Figure 6.2a shows one T_g at 50 °C, occurring between the two T_gs observed prior to sulfonation, further suggesting that a complexation between covalently attached cations and anions may frustrate the formation of a block copolymer morphology with long-range order. After the inclusion of salt/IL, no T_g was observed for poly(SS-Li-*b*-AEBIm-TFSI) + Li-TFSI/IL, where the additional ionic interactions between charged groups on the polymer and the salt/IL may inhibit the ability to clearly measure thermal transitions with DSC.

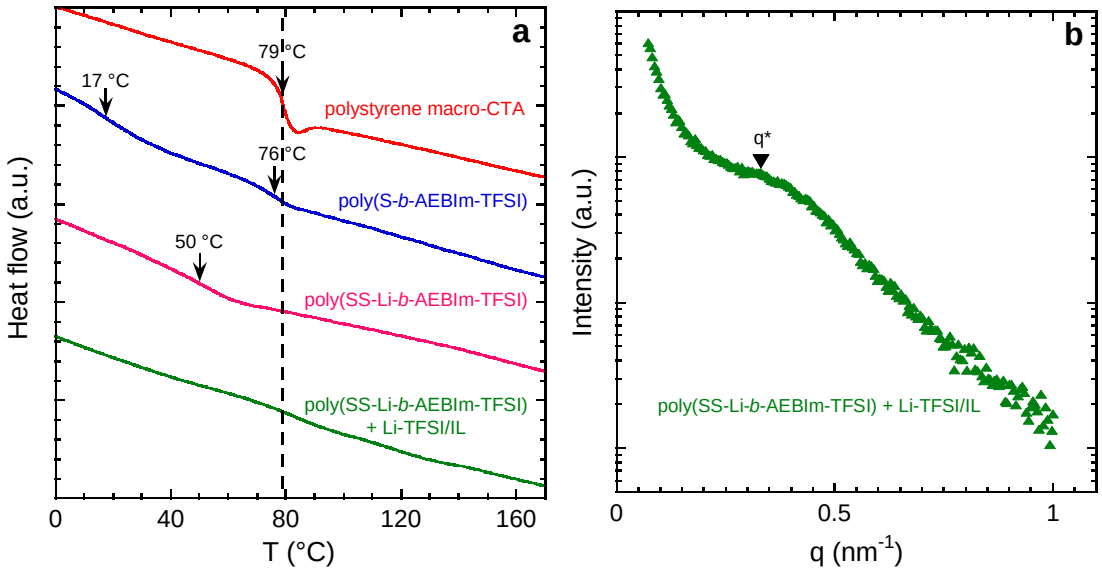

Figure 6.2 (a) DSC thermograms of polystyrene macro-CTA (red), poly(S-*b*-AEBIm-TFSI) (blue), poly(SS-Li-*b*-AEBIm-TFSI) (pink), poly(SS-Li-*b*-AEBIm-TFSI) + Li-TFSI/IL (green). (b) SAXS profile at room temperature under vacuum for poly(SS-Li-*b*-AEBIm-TFSI) + Li-TFSI/IL (green triangles). The inverted triangle (▼) indicates primary peak position at q*.

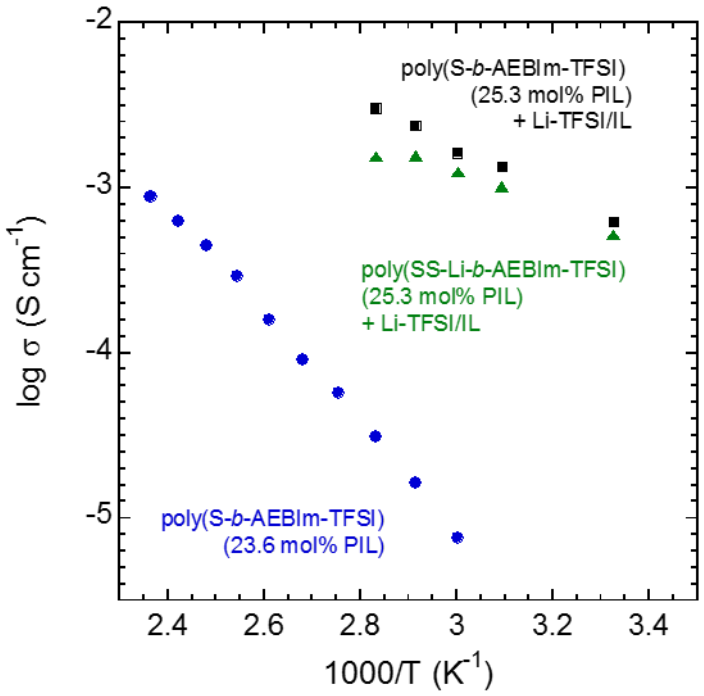

Figure 6.3 Temperature-dependent anhydrous ion conductivity for nonsulfonated PIL block copolymer with salt/IL: poly(S-*b*-AEBIm-TFSI) + Li-TFSI/IL (black squares), sulfonated PIL block copolymer with salt/IL: poly(SS-Li-*b*-AEBIm-TFSI) + Li-TFSI/IL (green triangles) and non-sulfonated PIL block copolymer: poly(S-*b*-AEBIm-TFSI) (23.6 mol% PIL)[56] (blue circles).

Figure 6.3 shows the temperature-dependent anhydrous ion conductivity of poly(SS-Li-*b*-AEBIm-TFSI) + Li-TFSI/IL. The ion conductivity of poly(S-*b*-AEBIm-TFSI) + Li-TFSI/IL and the nonsulfonated PIL block copolymer, poly(S-*b*-AEBIm-TFSI), from a previous study with a similar PIL composition to this study are also shown in Figure 6.3.[56] Recent work by Segalman and coworkers[132] with a similar styrene-based PIL block copolymer with mobile TFSI anions at a comparable PIL composition of 26 mol% PIL shows comparable anhydrous ion conductivity to poly(S-*b*-AEBIm-TFSI) over the same temperature range. In comparison to the non-sulfonated PIL block copolymer, the anhydrous ion conductivity for poly(SS-Li-*b*-AEBIm-TFSI) + Li-TFSI/IL is over 2 orders

magnitude higher at moderate temperatures (60 °C). The temperature dependence of ion conductivity between the two polymers is also significantly different. For poly(SS-Li-*b*-AEBIm-TFSI) + Li-TFSI/IL, ion conductivity increases with increasing temperature (27.5 °C to 70 °C) by only *ca.* 1/2 order of magnitude plateauing at an ion conductivity of 1.56 mS cm^{-1} at 70 °C and 80 °C. In contrast, ion conductivity increased by over 2 orders of magnitude with temperature (30 °C to 150 °C) for the non-sulfonated PIL block copolymer; specifically, from 60 °C to 80 °C, the conductivity increased 4-fold from 7.57 x 10^{-3} mS cm^{-1} to 3.11 x 10^{-2} mS cm^{-1}, compared to poly(SS-Li-*b*-AEBIm-TFSI) + Li-TFSI/IL, where from 60 °C to 80 °C, the conductivity remained relatively constant from 1.26 mS cm^{-1} to 1.56 mS cm^{-1}. Across this temperature range, the conductivity of poly(SS-Li-*b*-AEBIm-TFSI) + Li-TFSI/IL was ~2 orders of magnitude greater than the conductivity of the non-sulfonated PIL block copolymer from the previous study. This may be a direct consequence of the increase in ion concentration or ion exchange capacity (IEC) from sulfonation of the polymer and casting with Li-TFSI/IL. Relative to the non-sulfonated polymer from the previous study with an IEC of 1.78 meq/g, the non-sulfonated polymer in this study has a comparable, but slightly increased IEC of 1.91 meq/g, because of the slightly higher PIL composition. Sulfonation results in a sulfonated PIL block copolymer with an increased IEC of 2.16 meq/g. Finally, the addition of 1 M Li-TFSI salt dissolved in EMIm-TFSI to the sulfonated PIL block copolymer (~30% w/w salt/IL to polymer; 0.801 mol polymer: 0.041 mol salt: 0.158 mol IL) increases the IEC to 2.72 meq/g, whereas the addition of 1 M Li-TFSI salt dissolved in EMIm-TFSI to the nonsulfonated PIL block copolymer (~50% w/w salt/IL to polymer; 0.643 mol polymer:

0.073 mol salt: 0.284 mol IL) increases the IEC to 3.17 meq/g, which is higher than the IEC of the sulfonated PIL block copolymer with salt/IL (2.72 meq/g) and also results in a slightly higher conductivity. Overall, it is apparent that the inclusion of additional charged species in the solid-state, and subsequent increase in IEC of the material, resulted in a significant increase in ion conductivity.

6.4 Conclusions

In summary, the successful synthesis of the first sulfonated PIL diblock copolymer, poly(SS-Li-*b*-AEBIm-TFSI), is reported; a block copolymer with covalently attached cations (BIm^+) in one block and covalently attached anions (SO_3^-) in the other block with both mobile counter anions ($TFSI^-$) and mobile counter cations (Li^+), respectively. Chemical analysis reveals 100 mol% post-functionalization with BIm^+ in relation to PIL block, 15 mol% sulfonation SO_3^- in relation to styrene block. The sulfonated PIL block copolymer, cast with a solution of 1 M Li-TFSI/EMIm-TFSI possessed a high anhydrous ionic conductivity >1.5 mS cm^{-1} at 70 °C and the X-ray data revealed one broad scattering peak, indicating a weakly microphase-separated morphology. These conductivity results were over two orders of magnitude higher than the non-sulfonated PIL block copolymer, which possessed strongly microphase-separated morphology with long-range order. Overall, this new block copolymer (sulfonated PIL block copolymer) presents a new chemistry with both mobile cations and mobile anions for future exploration for a variety

of applications (*e.g.*, drug delivery, electrodialysis, bipolar membranes, solid-state capacitors, *etc.*).

CHAPTER VII

CONCLUSIONS AND FUTURE OUTLOOK

7.1 Summary

This work demonstrated the synthesis and characterization of AEMs for electrochemical applications; PILs and PIL block copolymers as AEMs for AFCs were of particular interest. The transport properties, self-assembled morphology, and alkaline chemical stability of these AEMs were investigated. Significant progress was achieved toward targeting the optimal chemistry for attaining highly hydroxide conductive, chemically stable, robust AEMs.

PIL diblock copolymers functionalized with butylimidazolium cations at various PIL compositions were synthesized from the direct copolymerization of an IL monomer and a nonionic monomer. Bromide and hydroxide ion conductivity in the PIL block copolymers were examined in relation to ion transport in the analogous PILs. Surprisingly, ion conductivity was observed to be higher in the PIL block copolymer relative to the analogous PIL hompolymer, despite the lower ionic content and water uptake of the PIL block copolymer. Morphology factor analysis and percolation theory were applied to the transport data; it was hypothesized that ion confinement in PIL microdomains yields accelerated ion transport properties in PIL block copolymers relative to the analogous PIL homopolymer.

In another study, the alkaline chemical stability was investigated in a set of ethyl methacrylate-based PILs with five different cation types: butylimidazolium,

butylmethylimidazolium, trimethylammonium, butylpyrrolidinium, trimethylphosphonium. The alkaline chemical stability of these PILs was examined in tandem with their analogous ionic salts: 1-butyl-3-methylimidizolium chloride, 1-butyl-2,3-dimethylimidazolium chloride, tetramethylammonium chloride, benzyltrimethylammonium chloride, 1,1-butylmethylpyrrolidinium chloride, tetramethylphosphonium chloride. Despite the primary focus of many literature studies on alkaline chemical stability of cations, it was determined that there was no correlation between the chemical stability of the polymeric cations and their free cation analogs. Butylpyrrolidinium proved to be the most chemically stable of the five polymeric cation types investigated.

The stability analysis was expanded to compare the alkaline chemical stability and transport properties of a total of twelve PILs with ethyl methacrylate, undecyl methacrylate, undecyl acrylate, and polystyrene-based backbones with various covalently attached cations: butylimidazolium, trimethylammonium, butylpyrrolidinium. The results of this study further emphasized the relevance of both the backbone and cation type in assessing alkaline chemical stability. A styrene/butylpyrrolidinium backbone/cation pairing was discovered as particularly chemically stable, surpassing the alkaline chemical stability of the benchmark styrene/BTMA pairing. Coupled with high ion transport, results for the styrene/butylpyrrolidinium pairing indicated high promise regarding its suitability for AFCs, upon incorporation of this particular chemistry into a PIL block copolymer structure that can provide sufficient mechanical integrity to the membrane material.

The results of these studies led to the investigation of ion transport and alkaline chemical stability in a PIL multiblock polymer, where the PIL block consists of a styrene/pyrrolidinium backbone/cation pairing. This robust AEM proved to be highly hydroxide conductive, as well as highly chemically stable. Carbonation of the membrane was also considered, where a technique was developed to monitor hydroxide conductivity under inert conditions, as well as monitor the conductivity upon exposure to ambient conditions. As predicted, stability and transport results for this material further indicated the high promise of PIL block copolymers as AEMs for AFCs.

In an additional study regarding PIL block copolymers, the versatility of these materials, where significant changes in physical properties can be achieved *via* subtle changes in chemistry, was further evidenced. The synthesis and property characterization of a novel sulfonated PIL diblock copolymer was presented, where the polymer contained both sulfonated blocks and PIL blocks with both mobile cations and mobile anions. This material represents an exciting new opportunity in PIL block copolymers for applications where the use of both mobile cations and mobile anions would prove advantageous (*e.g.*, drug delivery, electrodialysis, bipolar membranes, solid-state capacitors).

7.2 Future Outlook

Multiple opportunities exist to expand upon the work presented in this dissertation. One opportunity for further development would be to expand the transport studies of the twelve PILs with various backbone and cation types (backbones: ethyl methacrylate, undecyl methacrylate, undecyl acrylate, styrene; cations: butylimidazolium, trimethylammonium,

butylpyrrolidinium) to include analysis of the dry ion conductivity of the PILs (*e.g.*, neutralized with fluorinated anions). Though several of these PILs were determined unsuitable for AFC application due to low alkaline chemical stability, some of those same PILs still proved to have high ion transport. As dry ion transport applies to lithium ion battery technology, where conditions are neutral (*i.e.*, non-alkaline), these PILs may prove to be suitable candidates for dry ion transport applications.

It is well known that the dry ion conductivity of polymers is inversely proportional to the T_g, described by the Vogel-Fulcher-Tamman (VFT) relationship. As several of the PILs had low T_gs, well below room temperature, particularly the undecyl methacrylate and undecyl acrylate PILs, further investigation into their dry ion transport capabilities is warranted. Such a study would require that the PILs first be anion exchanged from bromide form to a fluorinated anion form (*e.g.*, TFSI, triflate, *etc.*). The PILs would be solution cast from acetonitrile into free-standing films such that dry ion conductivity data could be gathered at moderate to high temperatures (30 °C to 120 °C). Thermal analysis (DSC and TGA) would also be performed on the fluorinated-anion exchanged PILs. Using the dry ion conductivity data and T_gs, the transport behavior of the PILs could be fit to a VFT model.

It may also be possible to further decrease the T_gs of the PILs and in turn increase their ion conductivity, potentially by several orders of magnitude, by either casting the films with a solution of 1 M LiTFSI in EMIm TFSI or soaking the films in this solution. This solution plasticizes the material and includes additional ionic content in the films, while still keeping the material in the solid state. Overall, this study would allow for the

investigation of the dry ion conductivity of numerous backbone/cation pairings, over a wide range of T_gs.

Additionally, the work outlined here for the PIL pentablock terpolymer with the styrene/pyrrolidinium backbone/cation pairing can be expanded. This study would benefit from the inclusion of nanostructure or morphological analysis, preferably by SAXS and TEM, to determine morphology type. Additionally, this study has the opportunity to be expanded to include the analogous PIL, poly(vinylbenzylmethylpyrrolidinium-bromide), or poly(VBMP-Br). If transport studies of the PIL were included, it would be possible to perform a morphology factor analysis for the conductivity data, as well as apply percolation theory, similar to the approach applied in Chapter 2. With this additional information, it would be possible to determine whether transport properties in this PIL block polymer are also accelerated relative to its analogous PIL homopolymer, and to determine to what extent morphology contributes to this enhancement.

Through the incorporation of the results of all of the previous studies, a new PIL block polymer can now be synthesized to target all the desirable AEM properties: high hydroxide conductivity, high alkaline chemical stability, low water uptake, high mechanical strength, sufficient film flexibility. In particular, a pentablock (ABCBA) terpolymer represents an excellent chemical platform for producing a material with all of these qualities, as the pentablock structure allows for a significant increase in potential microphase separated morphology types, while the terpolymer chemistry allows for the incorporation of a PIL block (for high ion conductivity), a mechanically reinforcing block

(for robust films and processability), and a rubbery block (for increased flexibility and hydrophobicity *via* inclusion of a long alkyl spacer).

More specifically, in the pentablock terpolymer, the PIL block should contain a functionalized styrene backbone, where various heterocyclic cation types (similar to pyrrolidinium) are explored. Styrene represents a suitable option for a mechanically reinforcing block, as it would be compatible with the suggested PIL block, it is hydrophobic, chemically stable, and provides a high T_g. An amide block with a long alkyl substituent would be a good choice for a hydrophobic, rubbery block, as it would provide a low T_g for flexibility, and is compatible with styrene backbones in RAFT polymerization.

AEMs can be fabricated from this novel PIL pentablock terpolymer to measure the ion conductivity, morphology, thermal, and mechanical properties with a variety of experimental techniques (*e.g.*, EIS, SAXS, TEM, DVS, DSC, TGA, DMA). The transport-morphology-mechanical relationships can be investigated as a function of polymer chemistry parameters, such as block composition, degree of polymerization, alkyl side chain lengths, cation type. Additional opportunities to characterize this new material include alkaline chemical stability analysis with ^{1}H NMR spectroscopy and FTIR analysis, as well as monitoring of the AEM conductivity in high pH environments. Overall, the synthesis and characterization of this new material should result in the production of a highly hydroxide conductive, chemically stable, robust AEM, which can be tested as a solid-state separator in an AFC.

REFERENCES

(1) Varcoe, J. R.; Slade, R. C. T. *Fuel Cells* **2005**, *5*, 187.

(2) Merle, G.; Wessling, M.; Nijmeijer, K. *J Membrane Sci* **2011**, *377*, 1.

(3) Ye, Y.; Sharick, S.; Davis, E. M.; Winey, K. I.; Elabd, Y. A. *ACS Macro Lett.* **2013**, *2*, 575.

(4) Nykaza, J. R.; Ye, Y.; Elabd, Y. A. *Polymer* **2014**, *55*, 3360.

(5) Ye, Y. S.; Elabd, Y. A. *Macromolecules* **2011**, *44*, 8494.

(6) Chen, D.; Hickner, M. A. *ACS Appl. Mater. Interfaces* **2012**, *4*, 5775.

(7) Qiu, B.; Lin, B.; Si, Z.; Qiu, L.; Chu, F.; Zhao, J.; Yan, F. *J. Power Sources* **2012**, *217*, 329.

(8) Ran, J.; Wu, L.; Varcoe, J. R.; Ong, A. L.; Poynton, S. D.; Xu, T. *J. Membr. Sci.* **2012**, *415*, 242.

(9) Li, W.; Fang, J.; Lv, M.; Chen, C.; Chi, X.; Yang, Y.; Zhang, Y. *J. Mater. Chem.* **2011**, *21*, 11340.

(10) Lin, B.; Dong, H.; Li, Y.; Si, Z.; Gu, F.; Yan, F. *Chem. Mater.* **2013**, *25*, 1858.

(11) Gu, F.; Dong, H.; Li, Y.; Si, Z.; Yan, F. *Macromolecules* **2014**, *47*, 208.

(12) Qiu, B.; Lin, B.; Qiu, L.; Yan, F. *J. Mater. Chem.* **2012**, *22*, 1040.

(13) Zhang, F.; Zhang, H.; Qu, C. *J. Mater. Chem.* **2011**, *21*, 12744.

(14) Yang, C.; Wang, S.; Ma, W.; Jiang, L.; Sun, G. *J Mater Chem A* **2015**, *3*, 8559.

(15) Meek, K. M.; Sharick, S.; Ye, Y.; Winey, K. I.; Elabd, Y. A. *Macromolecules* **2015**, *48*, 4850.

(16) Nykaza, J. R.; Ye, Y.; Nelson, R. L.; Jackson, A. C.; Beyer, F. L.; Davis, E. M.; Page, K.; Sharick, S.; Winey, K. I.; Elabd, Y. A. *Soft Matter* **2016**.

(17) Nuñez, S. A.; Hickner, M. A. *ACS Macro Lett.* **2013**, *2*, 49.

(18) Vandiver, M. A.; Caire, B. R.; Poskin, Z.; Li, Y.; Seifert, S.; Knauss, D. M.; Herring, A. M.; Liberatore, M. W. *J. Appl. Polym. Sci.* **2015**, *132*, 41596.

(19) Yan, J.; Hickner, M. A. *Macromolecules* **2010**, *43*, 2349.

(20) Tsai, T.-H.; Maes, A. M.; Vandiver, M. A.; Versek, C.; Seifert, S.; Tuominen, M.; Liberatore, M. W.; Herring, A. M.; Coughlin, E. B. *J. Polym. Sci. Polym. Phys.* **2013**, *51*, 1751.

(21) Sturgeon, M. R.; Macomber, C. S.; Engtrakul, C.; Long, H.; Pivovar, B. S. *J. Electrochem. Soc.* **2015**, *162*, F366.

(22) Choe, Y.-K.; Fujimoto, C.; Lee, K.-S.; Dalton, L. T.; Ayers, K.; Henson, N. J.; Kim, Y. S. *Chem. Mater.* **2014**, *26*, 5675.

(23) Chen, D.; Hickner, M. A. *Macromolecules* **2013**, *46*, 9270.

(24) Hibbs, M. R. *J. Polym. Sci. Polym. Phys.* **2013**, *51*, 1736.

(25) Arges, C. G.; Ramani, V. *J. Electrochem. Soc.* **2013**, *160*, F1006.

(26) Arges, C. G.; Kulkarni, S.; Baranek, A.; Pan, K.-J.; Jung, M.-S.; Patton, D.; Mauritz, K. A.; Ramani, V. *ECS Trans.* **2010**, *33*, 1903.

(27) Cotanda, P.; Sudre, G.; Modestino, M. A.; Chen, X. C.; Balsara, N. P. *Macromolecules* **2014**, *47*, 7540.

(28) Noonan, K. J. T.; Hugar, K. M.; Kostalik, H. A.; Lobkovsky, E. B.; Abruña, H. D.; Coates, G. W. *J. Am. Chem. Soc.* **2012**, *134*, 18161.

(29) Gu, S.; Cai, R.; Luo, T.; Chen, Z.; Sun, M.; Liu, Y.; He, G.; Yan, Y. *Angew. Chem. Int. Ed.* **2009**, *48*, 6499.

(30) Wang, J.; Li, S.; Zhang, S. *Macromolecules* **2010**, *43*, 3890.

(31) Liu, L.; Li, Q.; Dai, J.; Wang, H.; Jin, B.; Bai, R. *J. Membr. Sci.* **2014**, *453*, 52.

(32) Kim, D. S.; Labouriau, A.; Guiver, M. D.; Kim, Y. S. *Chem. Mater.* **2011**, *23*, 3795.

(33) Sajjad, S. D.; Hong, Y.; Liu, F. *Polym. Advan. Technol.* **2014**, *25*, 108.

(34) Sudre, G.; Inceoglu, S.; Cotanda, P.; Balsara, N. P. *Macromolecules* **2013**, *46*, 1519.

(35) Gu, F.; Dong, H.; Li, Y.; Sun, Z.; Yan, F. *Macromolecules* **2014**, *47*, 6740.

(36) Meek, K. M.; Elabd, Y. A. *Macromolecules* **2015**, *48*, 7071.

(37) Price, S. C.; Williams, K. S.; Beyer, F. L. *ACS Macro Lett.* **2014**, *3*, 160.

(38) Arges, C. G.; Ramani, V. *Proceedings of the National Academy of Sciences* **2013**, *110*, 2490.

(39) Thomas, O. D.; Soo, K. J. W. Y.; Peckham, T. J.; Kulkarni, M. P.; Holdcroft, S. *J. Am. Chem. Soc.* **2012**, *134*, 10753.

(40) Ohno, H.; Ito, K. *Chemistry Letters* **1998**, 751.

(41) Ye, Y.; Elabd, Y. A. *Polymer* **2011**, *52*, 1309.

(42) Stancik, C. M.; Lavoie, A. R.; Schutz, J.; Achurra, P. A.; Lindner, P.; Gast, A. P.; Waymouth, R. M. *Langmuir* **2004**, *20*, 596.

(43) Stancik, C. M.; Lavoie, A. R.; Achurra, P. A.; Waymouth, R. M.; Gast, A. P. *Langmuir* **2004**, *20*, 8975.

(44) Weber, R. L.; Ye, Y.; Schmitt, A. L.; Banik, S. M.; Elabd, Y. A.; Mahanthappa, M. K. *Macromolecules* **2011**, *44*, 5727.

(45) Cheng, S.; Beyer, F. L.; Mather, B. D.; Moore, R. B.; Long, T. E. *Macromolecules* **2011**, *44*, 6509.

(46) Green, M. D.; Wang, D.; Hemp, S. T.; Choi, J.-H.; Winey, K. I.; Heflin, J. R.; Long, T. E. *Polymer* **2012**, *53*, 3677.

(47) Li, X.; Ni, X.; Liang, Z.; Shen, Z. *Journal of Polymer Science Part A: Polymer Chemistry* **2012**, *50*, 2037.

(48) Ye, Y.; Sharick, S.; Davis, E. M.; Winey, K. I.; Elabd, Y. A. *Acs Macro Letters* **2013**, *2*, 575.

(49) Yang, J.; Sun, W. L.; Lin, W. H.; Shen, Z. Q. *J Polym Sci Pol Chem* **2008**, *46*, 5123.

(50) Vijayakrishna, K.; Jewrajka, S. K.; Ruiz, A.; Marcilla, R.; Pomposo, J. A.; Mecerreyes, D.; Taton, D.; Gnanou, Y. *Macromolecules* **2008**, *41*, 6299.

(51) Mori, H.; Yahagi, M.; Endo, T. *Macromolecules* **2009**, *42*, 8082.

(52) Yuan, J.; Schlaad, H.; Giordano, C.; Antonietti, M. *Eur Polym J* **2011**, *47*, 772.

(53) Chanthad, C.; Masser, K. A.; Xu, K.; Runt, J.; Wang, Q. *J Mater Chem* **2012**, *22*, 341.

(54) Ye, Y.; Choi, J.-H.; Winey, K. I.; Elabd, Y. A. *Macromolecules* **2012**, *45*, 7027.

(55) Wang, Z.; Lai, H.; Wu, P. *Soft Matter* **2012**, *8*, 11644.

(56) Choi, J.-H.; Ye, Y.; Elabd, Y. A.; Winey, K. I. *Macromolecules* **2013**, *46*, 5290.

(57) Karjalainen, E.; Chenna, N.; Laurinmaki, P.; Butcher, S. J.; Tenhu, H. *Polym Chem-Uk* **2013**, *4*, 1014.

(58) Adzima, B. J.; Venna, S. R.; Klara, S. S.; He, H.; Zhong, M.; Luebke, D. R.; Mauter, M. S.; Matyjaszewski, K.; Nulwala, H. B. *J Mater Chem A* **2014**, *2*, 7967.

(59) Carrasco, P. M.; Tzounis, L.; Mompean, F. J.; Strati, K.; Georgopanos, P.; Garcia-Hernandez, M.; Stamm, M.; Cabanero, G.; Odriozola, I.; Avgeropoulos, A.; Garcia, I. *Macromolecules* **2013**, *46*, 1860.

(60) Carrasco, P. M.; de Luzuriaga, A. R.; Constantinou, M.; Georgopanos, P.; Rangou, S.; Avgeropoulos, A.; Zafeiropoulos, N. E.; Grande, H.-J.; Cabanero, G.; Mecerreyes, D.; Garcia, I. *Macromolecules* **2011**, *44*, 4936.

(61) Detrembleur, C.; Debuigne, A.; Hurtgen, M.; Jerome, C.; Pinaud, J.; Fevre, M.; Coupillaud, P.; Vignolle, J.; Taton, D. *Macromolecules* **2011**, *44*, 6397.

(62) Coupillaud, P.; Fevre, M.; Wirotius, A.-L.; Aissou, K.; Fleury, G.; Debuigne, A.; Detrembleur, C.; Mecerreyes, D.; Vignolle, J.; Taton, D. *Macromolecular rapid communications* **2014**, *35*, 422.

(63) Wiesenauer, E. F.; Phuc Tien, N.; Newell, B. S.; Bailey, T. S.; Nobleb, R. D.; Gin, D. L. *Soft Matter* **2013**, *9*, 7923.

(64) Wiesenauer, E. F.; Edwards, J. P.; Scalfani, V. F.; Bailey, T. S.; Gin, D. L. *Macromolecules* **2011**, *44*, 5075.

(65) Scalfani, V. F.; Wiesenauer, E. F.; Ekblad, J. R.; Edwards, J. P.; Gin, D. L.; Bailey, T. S. *Macromolecules* **2012**, *45*, 4262.

(66) Nguyen, P. T.; Wiesenauer, E. F.; Gin, D. L.; Noble, R. D. *J Membrane Sci* **2013**, *430*, 312.

(67) Suga, T.; Sakata, M.; Aoki, K.; Nishide, H. *ACS Macro Letters* **2014**, *3*, 703.

(68) Krogstad, D. V.; Choi, S.-H.; Lynd, N. A.; Audus, D. J.; Perry, S. L.; Gopez, J. D.; Hawker, C. J.; Kramer, E. J.; Tirrell, M. V. *The Journal of Physical Chemistry B* **2014**, *118*, 13011.

(69) Schneider, Y.; Modestino, M. A.; McCulloch, B. L.; Hoarfrost, M. L.; Hess, R. W.; Segalman, R. A. *Macromolecules* **2013**, *46*, 1543.

(70) Texter, J.; Vasantha, V. A.; Crombez, R.; Maniglia, R.; Slater, L.; Mourey, T. *Macromolecular Rapid Communications* **2012**, *33*, 69.

(71) Shi, Z.; Newell, B. S.; Bailey, T. S.; Gin, D. L. *Polymer* **2014**, *55*, 6664.

(72) Agudelo, N. A.; Elsen, A. M.; He, H.; López, B. L.; Matyjaszewski, K. *Journal of Polymer Science Part A: Polymer Chemistry* **2015**, *53*, 228.

(73) Karjalainen, E.; Khlebnikov, V.; Korpi, A.; Hirvonen, S.-P.; Hietala, S.; Aseyev, V.; Tenhu, H. *Polymer* **2015**, *58*, 180.

(74) Hann, N. D. *Journal of Polymer Science: Polymer Chemistry Edition* **1977**, *15*, 1331.

(75) Domard, A.; Rinaudo, M.; Rochas, C. *J Polym Sci Polym Phys Ed* **1979**, *17*, 673.

(76) Lai, A. N.; Wang, L. S.; Lin, C. X.; Zhuo, Y. Z.; Zhang, Q. G.; Zhu, A. M.; Liu, Q. L. *Acs Appl Mater Inter* **2015**, *7*, 8284.

(77) Trapa, P. E.; Huang, B.; Won, Y.-Y.; Sadoway, D. R.; Mayes, A. M. *Electrochemical and solid-state letters* **2002**, *5*, A85.

(78) Bouchet, R.; Maria, S.; Meziane, R.; Aboulaich, A.; Lienafa, L.; Bonnet, J.-P.; Phan, T. N.; Bertin, D.; Gigmes, D.; Devaux, D. *Nature materials* **2013**, *12*, 452.

(79) Soo, P. P.; Huang, B.; Jang, Y. I.; Chiang, Y. M.; Sadoway, D. R.; Mayes, A. M. *J Electrochem Soc* **1999**, *146*, 32.

(80) Yin, K.; Zhang, Z.; Li, X.; Yang, L.; Tachibana, K.; Hirano, S.-i. *J Mater Chem A* **2015**, *3*, 170.

(81) Bouchet, R.; Maria, S.; Meziane, R.; Aboulaich, A.; Lienafa, L.; Bonnet, J.-P.; Phan, T. N. T.; Bertin, D.; Gigmes, D.; Devaux, D.; Denoyel, R.; Armand, M. *Nat Mater* **2013**, *12*, 452.

(82) Li, M.; Yang, L.; Fang, S.; Dong, S.; Hirano, S. i.; Tachibana, K. *Polymer International* **2012**, *61*, 259.

(83) Li, M.; Yang, B.; Wang, L.; Zhang, Y.; Zhang, Z.; Fang, S.; Zhang, Z. *J Membrane Sci* **2013**, *447*, 222.

(84) Song, J.; Wang, Y.; Wan, C. *J Power Sources* **1999**, *77*, 183.

(85) Panday, A.; Mullin, S.; Gomez, E. D.; Wanakule, N.; Chen, V. L.; Hexemer, A.; Pople, J.; Balsara, N. P. *Macromolecules* **2009**, *42*, 4632.

(86) Gomez, E. D.; Panday, A.; Feng, E. H.; Chen, V.; Stone, G. M.; Minor, A. M.; Kisielowski, C.; Downing, K. H.; Borodin, O.; Smith, G. D. *Nano Lett* **2009**, *9*, 1212.

(87) Singh, M.; Odusanya, O.; Wilmes, G. M.; Eitouni, H. B.; Gomez, E. D.; Patel, A. J.; Chen, V. L.; Park, M. J.; Fragouli, P.; Iatrou, H. *Macromolecules* **2007**, *40*, 4578.

(88) Green, M. D.; Salas-de la Cruz, D.; Ye, Y. S.; Layman, J. M.; Elabd, Y. A.; Winey, K. I.; Long, T. E. *Macromol Chem Phys* **2011**, *212*, 2522.

(89) Elabd, Y. A.; Napadensky, E.; Walker, C. W.; Winey, K. I. *Macromolecules* **2006**, *39*, 399.

(90) Roy, A.; Hickner, M. A.; Yu, X.; Li, Y. X.; Glass, T. E.; McGrath, J. E. *Journal of Polymer Science Part B-Polymer Physics* **2006**, *44*, 2226.

(91) Ye, Y. S.; Choi, J. H.; Winey, K. I.; Elabd, Y. A. *Macromolecules* **2012**, *45*, 7027.

(92) Heiney, P. A. *Commission on Powder Diffraction Newsletter* **2005**, 9.

(93) Winey, K. I.; Thomas, E. L.; Fetters, L. J. *Journal of Chemical Physics* **1991**, *95*, 9367.

(94) Salas-de la Cruz, D.; Denis, J. G.; Griffith, M. D.; King, D. R.; Heiney, P. A.; Winey, K. I. *Review of Scientific Instruments* **2012**, *83*.

(95) Chen, L.; Hallinan, D. T., Jr.; Elabd, Y. A.; Hillmyer, M. A. *Macromolecules* **2009**, *42*, 6075.

(96) Wanakule, N. S.; Panday, A.; Mullin, S. A.; Gann, E.; Hexemer, A.; Balsara, N. P. *Macromolecules* **2009**, *42*, 5642.

(97) Singh, M.; Odusanya, O.; Wilmes, G. M.; Eitouni, H. B.; Gomez, E. D.; Patel, A. J.; Chen, V. L.; Park, M. J.; Fragouli, P.; Iatrou, H.; Hadjichristidis, N.; Cookson, D.; Balsara, N. P. *Macromolecules* **2007**, *40*, 4578.

(98) Choi, J. H.; Ye, Y. S.; Elabd, Y. A.; Winey, K. I. *Macromolecules* **2013**, *46*, 5290.

(99) Kim, O.; Kim, S. Y.; Ahn, H.; Kim, C. W.; Rhee, Y. M.; Park, M. J. *Macromolecules* **2012**, *45*, 8702.

(100) Park, M. J.; Kim, S. Y. *Journal of Polymer Science Part B: Polymer Physics* **2013**, *51*, 481.

(101) Tsai, T.-H.; Maes, A. M.; Vandiver, M. A.; Versek, C.; Seifert, S.; Tuominen, M.; Liberatore, M. W.; Herring, A. M.; Coughlin, E. B. *Journal of Polymer Science Part B: Polymer Physics* **2013**, *51*, 1751.

(102) Vorrey, S.; Teeters, D. *Electrochim Acta* **2003**, *48*, 2137.

(103) Chen, H.; Palmese, G. R.; Elabd, Y. A. *Chem Mater* **2006**, *18*, 4875.

(104) Elabd, Y. A.; Napadensky, E.; Sloan, J. M.; Crawford, D. M.; Walker, C. W. *Journal of Membrane Science* **2003**, *217*, 227.

(105) Kirkpatrick, S. *Reviews of Modern Physics* **1973**, *45*, 574.

(106) Hsu, W. Y.; Barkley, J. R.; Meakin, P. *Macromolecules* **1980**, *13*, 198.

(107) Duan, Q. J.; Ge, S. H.; Wang, C. Y. *Journal of Power Sources* **2013**, *243*, 773.

(108) Arges, C. G.; Ramani, V. *Proc. Natl. Acad. Sci. U. S. A.* **2013**, *110*, 2490.

(109) Yuesheng, Y.; Yossef, A. E. In *Polymers for Energy Storage and Delivery: Polyelectrolytes for Batteries and Fuel Cells*; American Chemical Society: 2012; Vol. 1096, p 233.

(110) Hofmann, A. W. C., A. *Philos. Trans. R. Soc. London* **1857**, *147*, 575.

(111) Zanger, M.; Vander Werf, C. A.; McEwen, W. E. *J. Am. Chem. Soc.* **1959**, *81*, 3806.

(112) Gaetjens, E.; Morawetz, H. *J. Am. Chem. Soc.* **1961**, *83*, 1738.

(113) Baines, F. C.; Bevington, J. C. *J. Polym. Sci. Polym. Chem.* **1968**, *6*, 2433.

(114) Ye, Y.; Elabd, Y. A. *ChemInform* **2013**, *44*.

(115) Chempath, S.; Einsla, B. R.; Pratt, L. R.; Macomber, C. S.; Boncella, J. M.; Rau, J. A.; Pivovar, B. S. *The Journal of Physical Chemistry C* **2008**, *112*, 3179.

(116) Long, H.; Kim, K.; Pivovar, B. S. *The Journal of Physical Chemistry C* **2012**, *116*, 9419.

(117) Mangiagli, P.; Ewing, C.; Xu, K.; Wang, Q.; Hickner, M. *Fuel Cells* **2009**, *9*, 432.

(118) Zawodzinski Jr, T. A.; Neeman, M.; Sillerud, L. O.; Gottesfeld, S. *The Journal of Physical Chemistry* **1991**, *95*, 6040.

(119) Elabd, Y. A.; Hickner, M. A. *Macromolecules* **2010**, *44*, 1.

(120) Gabaston, L.; Furlong, S.; Jackson, R.; Armes, S. *Polymer* **1999**, *40*, 4505.

(121) Liu, S.; Armes, S. P. *Langmuir* **2003**, *19*, 4432.

(122) Liu, S.; Armes, S. P. *Angewandte Chemie International Edition* **2002**, *41*, 1413.

(123) Bories-Azeau, X.; Armes, S. P.; van den Haak, H. J. *Macromolecules* **2004**, *37*, 2348.

(124) Jiménez, Z. A.; Yoshida, R. *Macromolecules* **2015**, *48*, 4599.

(125) Xin, X.; Wang, Y.; Liu, W. *Eur Polym J* **2005**, *41*, 1539.

(126) Laschewsky, A. *Polymers-Basel* **2014**, *6*, 1544.

(127) Kudaibergenov, S.; Jaeger, W.; Laschewsky, A. In *Supramolecular polymers polymeric betains oligomers* 2006, p 157.

(128) Elabd, Y. A.; Napadensky, E. *Polymer* **2004**, *45*, 3037.

(129) Younker, J. M.; Saito, T.; Hunt, M. A.; Naskar, A. K.; Beste, A. *J Am Chem Soc* **2013**, *135*, 6130.

(130) Xing, P.; Robertson, G. P.; Guiver, M. D.; Mikhailenko, S. D.; Wang, K.; Kaliaguine, S. *J Membrane Sci* **2004**, *229*, 95.

(131) Zaidi, S. J.; Mikhailenko, S.; Robertson, G.; Guiver, M.; Kaliaguine, S. *J Membrane Sci* **2000**, *173*, 17.

(132) Evans, C. M.; Sanoja, G. E.; Popere, B. C.; Segalman, R. A. *Macromolecules* **2016**, *49*, 395.

(133) Fetters, L. J.; Lohse, D. J.; Richter, D.; Witten, T. A.; Zirkel, A. *Macromolecules* **1994**, *27*, 4639.

(134) Ye, C.; Shreeve, J. M. *J. Phys. Chem. A* **2007**, *111*, 1456.

APPENDIX A

A1. ^{1}H NMR of PIL Block Copolymer

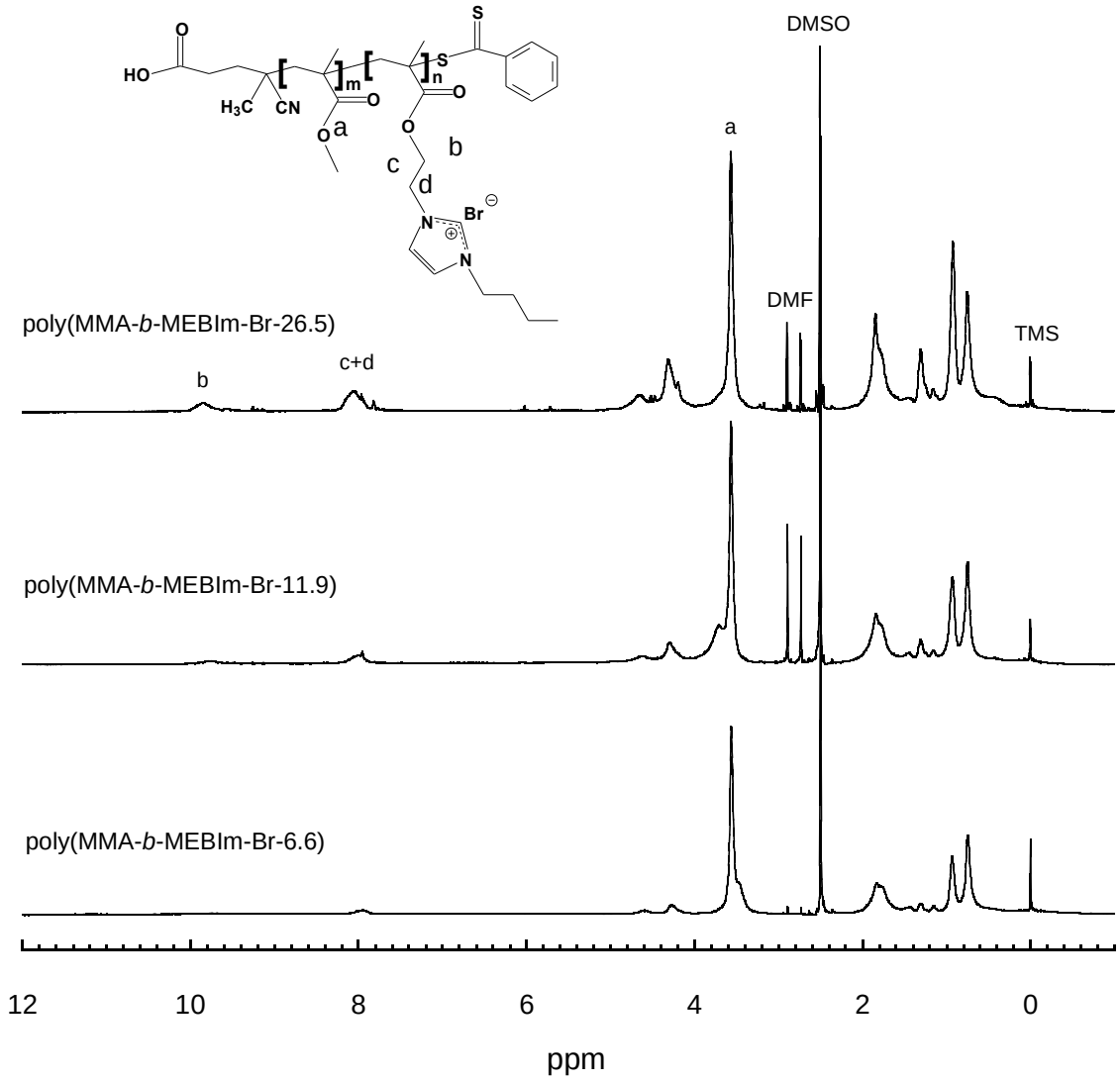

Figure A1. ^{1}H NMR spectra of various PIL compositions (6.6, 11.9, and 26.5 mol%) of PIL block copolymers: (top) (poly(MMA-*b*-MEBIm-Br-26.5)), (middle) (poly(MMA-*b*-MEBIm-Br-11.9)), and (bottom) PIL block copolymer (poly(MMA-*b*-MEBIm-Br-6.6)) in DMSO-d_6. PIL compositions are calculated from relative integrations of resonances "c + d" versus resonance "a" (i.e., (c + d)/2 /((c + d)/2 + a/3)).

A2. Density Estimation for Poly(MEBIm-Br) and Poly(MEBIm-OH) PILs

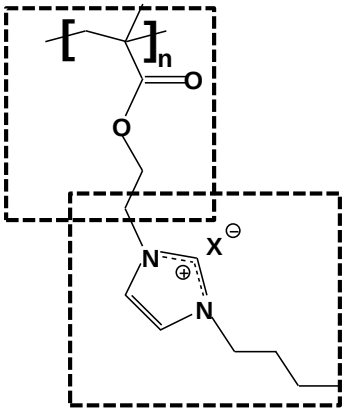

Figure A2. Chemical structure of poly(MEBIm-X) (X = Br^- or OH^-).

The densities of poly(MEBIm-Br) and poly(MEBIm-OH) were estimated using an additive contribution of two components to calculate the molar volume: poly(methyl methacrylate) (PMMA) and a tethered ionic part (*i.e.*, 1-butyl-3-methylimidazolium bromide or hydroxide, BMIm-Br or BMIm-OH) (Figure A2).[91]

$$\frac{1}{\rho_{\mathrm{PIL}}} = \frac{MW_{\mathrm{MMA}}/\left(MW_{\mathrm{MMA}} + MW_{\mathrm{BMIm-X}}\right)}{\rho_{\mathrm{PMMA}}} + \frac{MW_{\mathrm{BMIm-X}}/\left(MW_{\mathrm{MMA}} + MW_{\mathrm{BMIm-X}}\right)}{\rho_{\mathrm{BMIm-X}}} \quad \text{(A.1)}$$

where ρ_{PIL}, ρ_{PMMA}, and $\rho_{\mathrm{BMIm\text{-}X}}$ are the densities of PIL homopolymer (poly(MEBIm-X), X = OH^- or Br^-), PMMA, and BMIm-X, respectively. The density of PMMA (1.18 g cm^{-3})[133] was obtained from literature, while the density of BMIm-Br (1.24 g cm^{-3}) or BMIm-OH (1.05 g cm^{-3}) was estimated using the additive contribution method proposed by Ye and Shreeve.[134] With the molecular weight values of MW_{MMA} = 100.12 g mol^{-1}, $MW_{\mathrm{BMIm\text{-}Br}}$ = 219.12 g mol^{-1} and $MW_{\mathrm{BMIm\text{-}OH}}$ = 156.23 g mol^{-1}, the estimated density values are 1.22 g cm^{-3} for poly(MEBIm-Br) and 1.08 g cm^{-3} for poly(MEBIm-OH).

A3. Volume Fraction of Conducting Phase in Block Copolymers

Table A1. Bromide-Conducting and Hydroxide-Conducting PIL Block Copolymer Samples.

PIL Block Copolymers[a]	vol % PIL[b]	mol % PIL[c]	ϕ_{PIL+W} 30% RH[d]	ϕ_{PIL+W} 90% RH[d]
Poly(MMA-*b*-MEBIm-Br)	17.9	6.6	0.19	0.25
	29.2	11.9	0.31	0.38
	39.2	17.3	0.41	0.50
	52.5	26.5	0.54	0.61
Poly(MMA-*b*-MEBIm-OH)	16.4	6.6	0.18	0.25
	27.3	11.9	0.29	0.38
	36.7	17.3	0.38	0.47
	50.0	26.5	0.52	0.61

[a] Br = bromide counterion (Br^-), OH = hydroxide counterion (OH^-); [b] Volume fractions were calculated from density of PMMA (1.18 g cm^{-3}) and PIL homopolymers ($\rho_{poly(MEBIm-Br)}$ = 1.22 g cm^{-3} and $\rho_{poly(MEBIm-OH)}$ = 1.08 g cm^{-3}); [c] Determined from ^1H NMR spectroscopy. [d] Measured at 30 °C.

A4. Additional PMMA Macro-CTA and Block Copolymer Precursor Synthesis

Table A2. Reaction Conditions, Molecular Weights, and Composition of Macro CTAs and Precursor Block Copolymers.

Polymers	mol %[b]	Recipe	M_n (kg mol^{-1})	PDI	Yield (%)
PMMA Macro-CTA[a]	-	200:0.33:0.1[c]	30.6	1.23	66.1
	-	120:0.33:0.1[c]	22.8	1.19	55.9
	-	60:0.33:0.1[c]	17.0	1.16	83.6
	-	30:0.33:0.1[c]	8.57	1.12	64.7
Poly(MMA-*b*-BrEMA)[d]	30.0	200:1:0.1[e]	12.3	1.24	22.7
	30.9	200:1:0.1[e]	12.7	1.25	28.9
	36.6	200:1:0.1[e]	14.3	1.36	22.6

[a]CTA: 4-cyano-4-[(dodecylsulfanylthiocarbonyl)sulfanyl]pentanoic acid. [b]Mol% was determined from BrEMA present in ^{1}H NMR spectroscopy; [c]A:B:C = MMA:CTA:AIBN (in mol). [d]Block copolymers were synthesized from PMMA-CTA of *Mn* = 8.57 kg mol^{-1}. [e]A:B:C = BrEMA:PMMA-CTA:AIBN (in mol).

A5. Small Angle X-ray Scattering (SAXS)

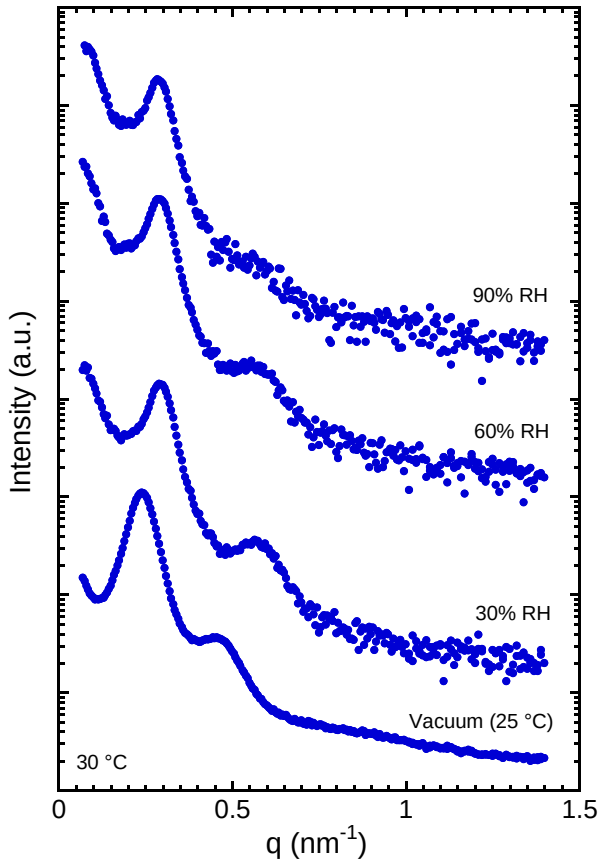

Figure A3. Representative *in situ* small-angle X-ray scattering data for poly(MMA-*b*-MEBIm-Br) with 18 vol% PIL at 30 °C as a function of relative humidity, indicating a microphase separated morphology over the investigated conditions. Data are offset vertically for clarity.

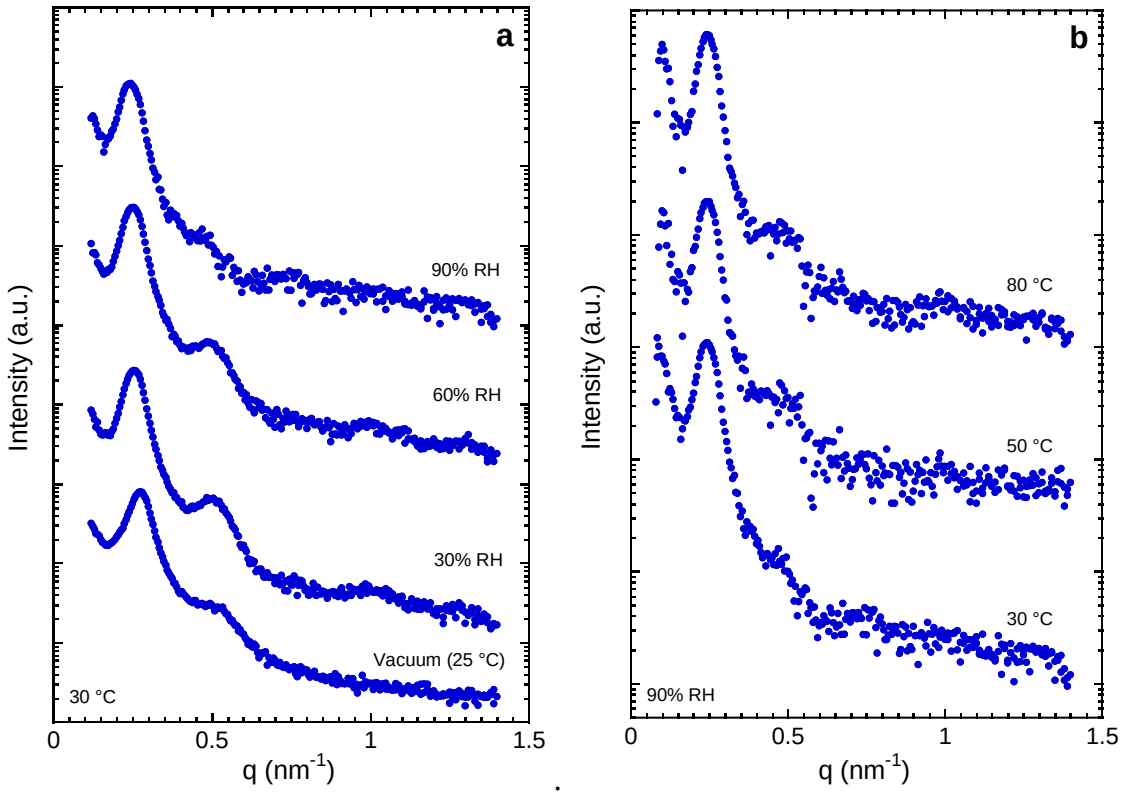

Figure A4. Representative *in situ* small-angle X-ray scattering data for poly(MMA-*b*-MEBIm-Br) with 29 vol% PIL (a) at 30 °C as a function of relative humidity and (b) at 90% RH as a function of temperature, indicating that a microphase separated morphology is maintained over all investigated relative humidity and temperatures. Data are offset vertically for clarity.

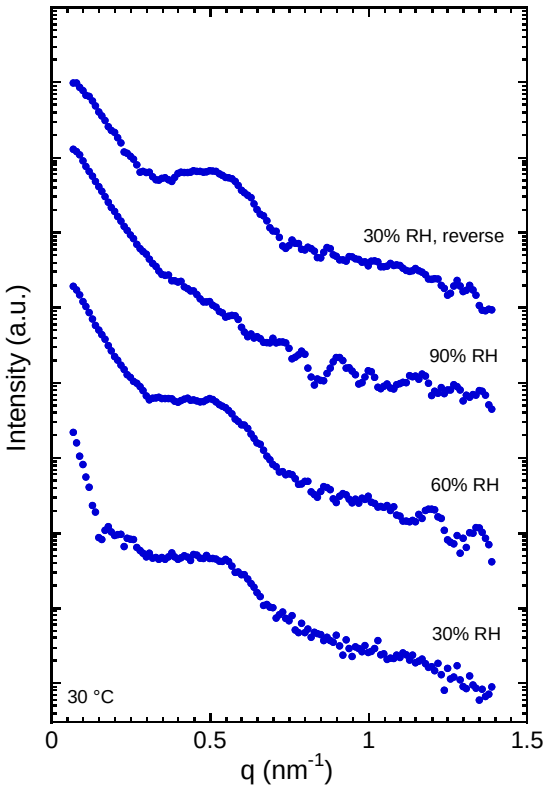

Figure A5. Representative *in situ* small-angle X-ray scattering data for poly(MMA-*b*-MEBIm-OH) with 16 vol% PIL (a) at 30 °C as a function of relative humidity, indicating that a microphase separated morphology is maintained over all investigated relative humidity and temperatures. Data are offset vertically for clarity.

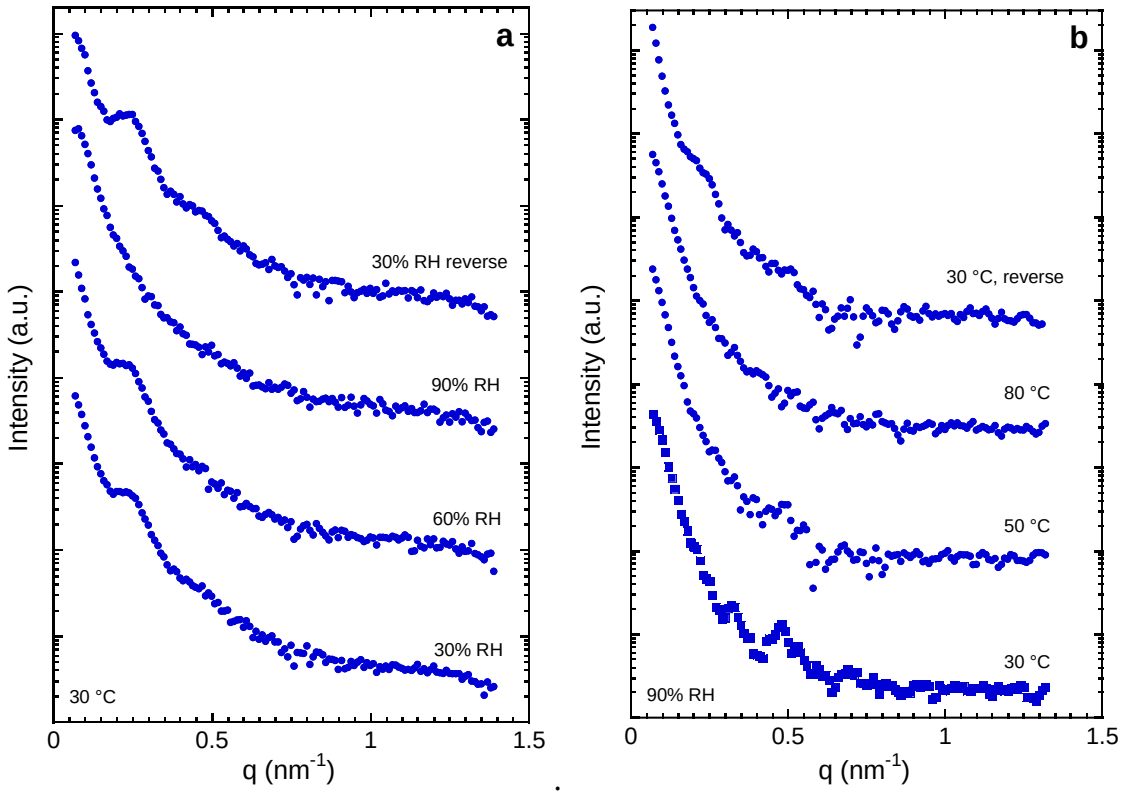

Figure A6. Representative *in situ* small-angle X-ray scattering data for poly(MMA-*b*-MEBIm-OH) with 27 vol% PIL (a) at 30 °C as a function of relative humidity and (b) at 90% RH as a function of temperature, indicating that a microphase separated morphology is maintained over all investigated relative humidity and temperatures. Data are offset vertically for clarity.

A6. Morphology Factor and Percolation Theory

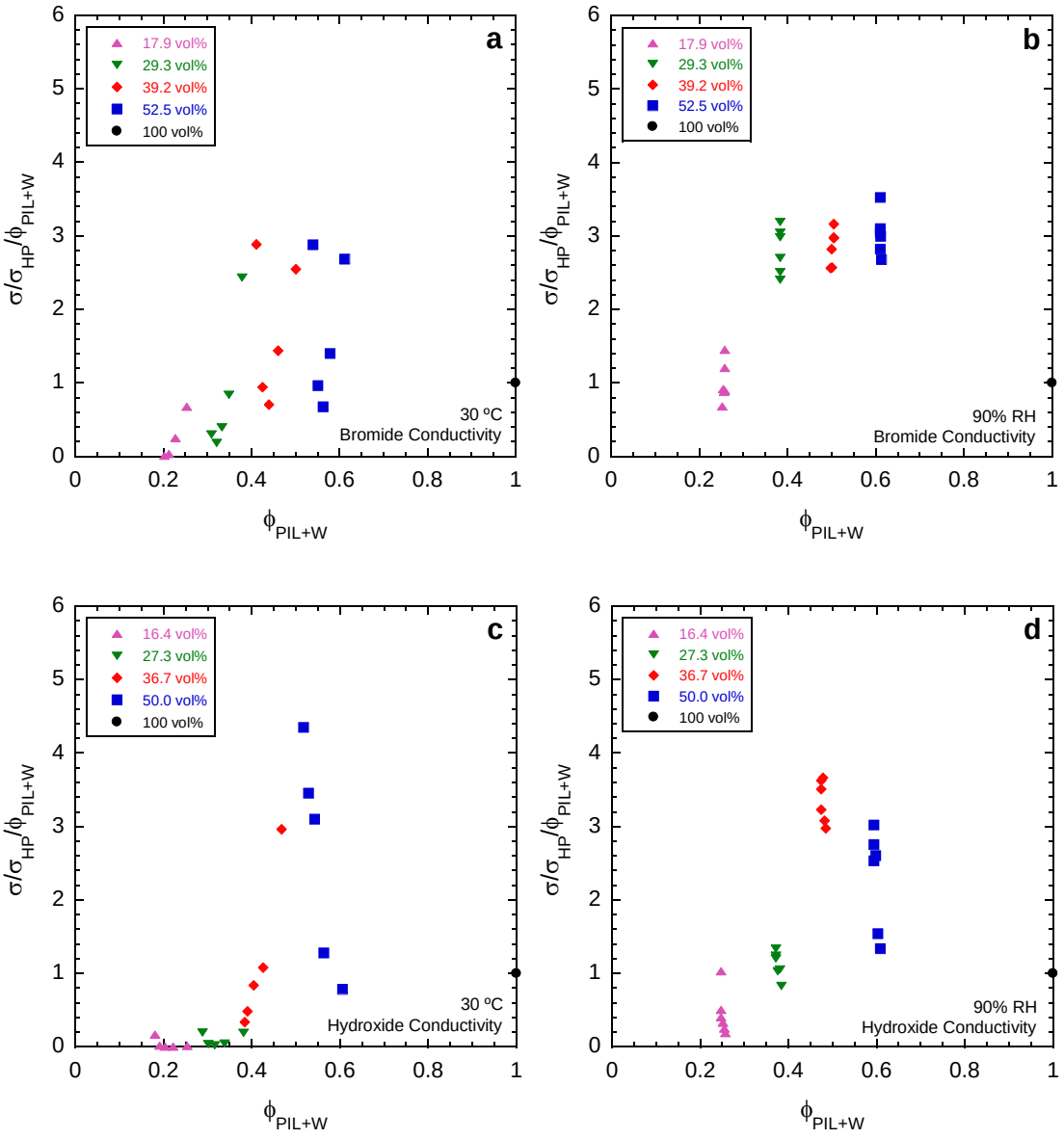

Figure A7. Normalized ionic conductivity as a function of volume fraction of the conducting phase (ϕ_{PIL+W}) at (a, c) 30 °C with varying RH and (b, d) 90% RH with varying temperature for (a, b) poly(MEBIm-Br) and poly(MMA-*b*-MEBIm-Br) and (c, d) poly(MEBIm-OH) and poly(MMA-*b*-MEBIm-OH). Conductivity normalized by homopolymer conductivity and volume fraction of conducting phase (ϕ_{PIL+W}).

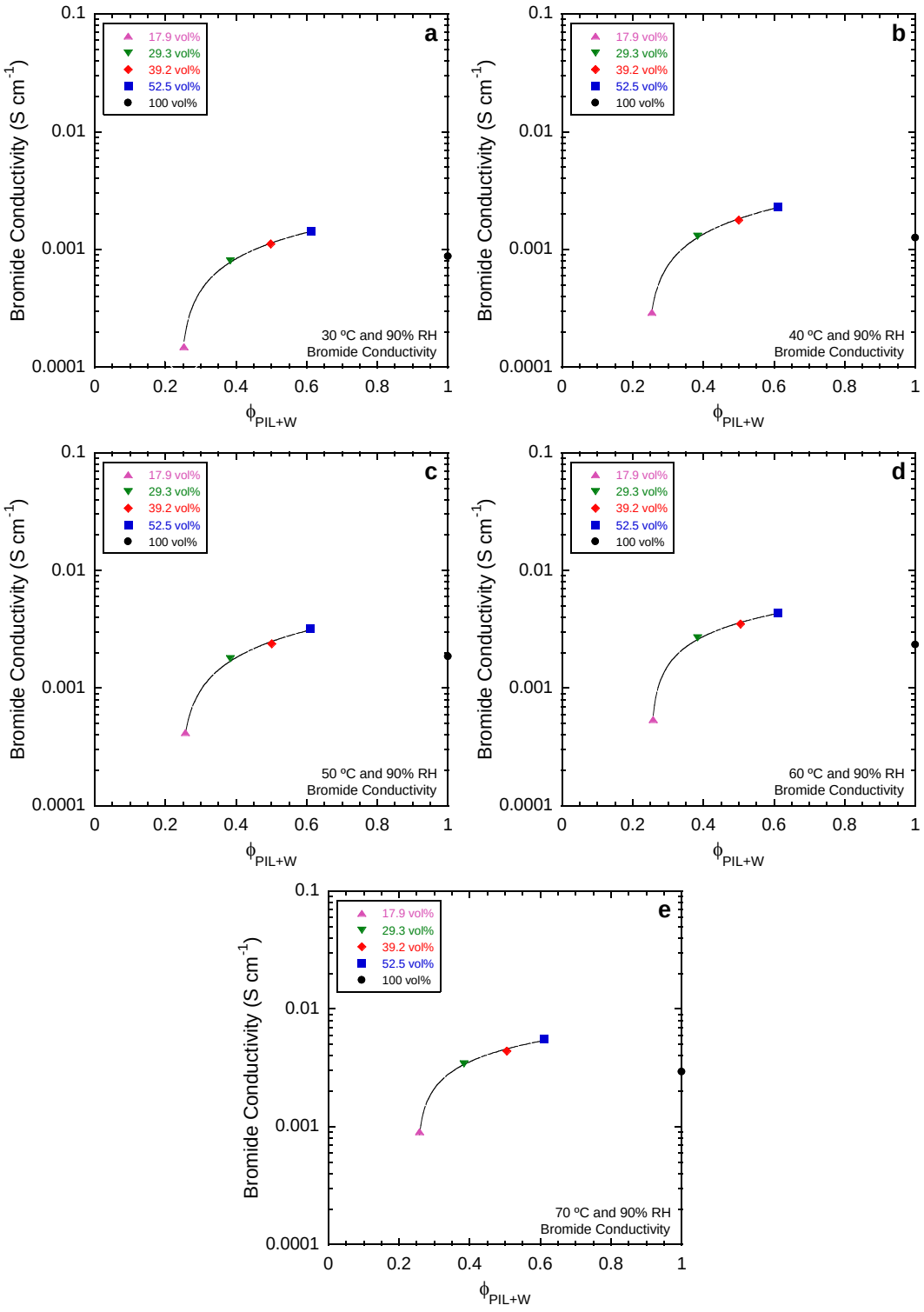

Figure A8. Ionic conductivity versus volume fraction of the conducting phase (ϕ_{PIL+W}) for poly(MMA-*b*-MEBIm-Br) and poly(MEBIm-Br) at (a-e) 30, 40, 50, 60, 70 °C.

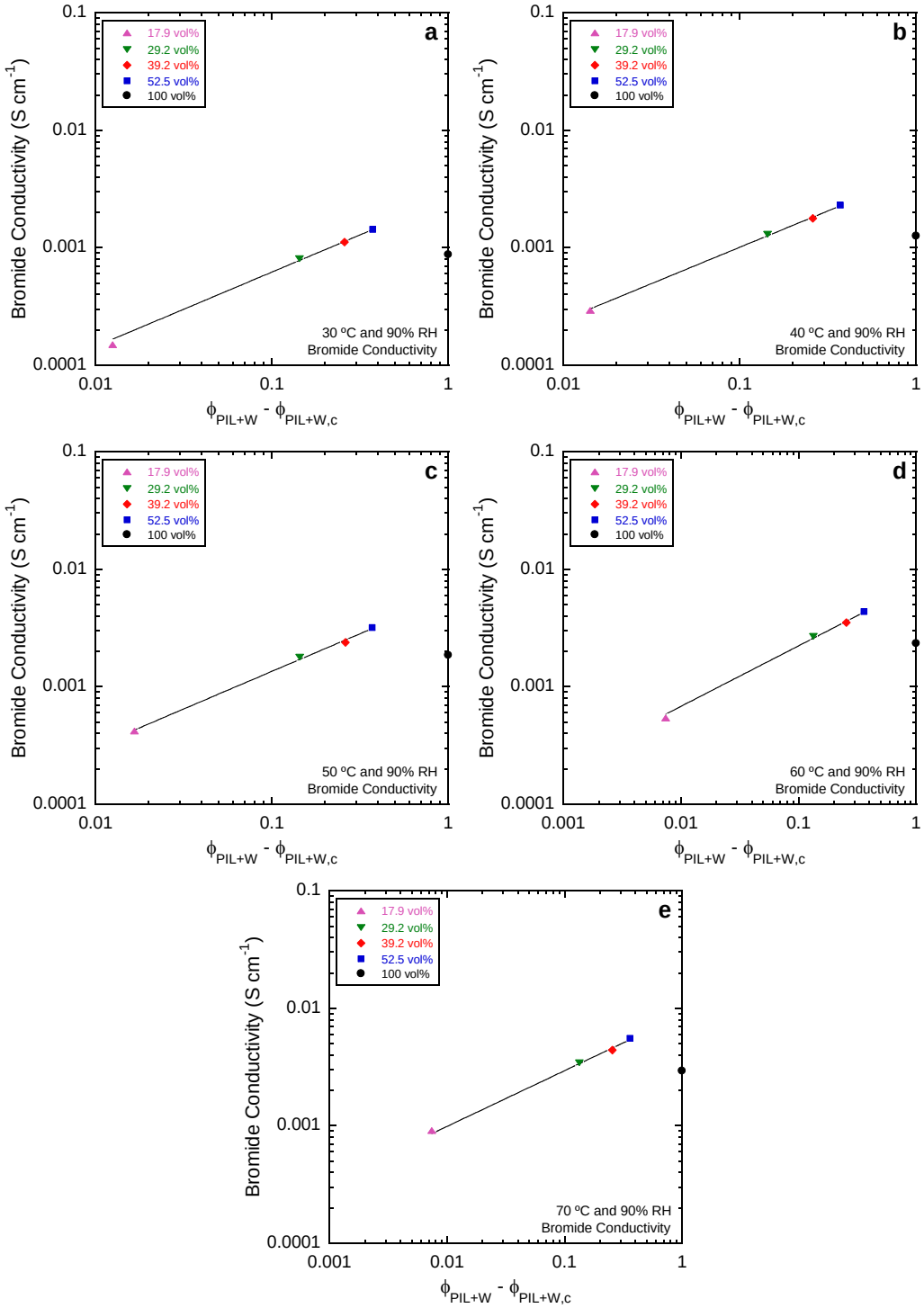

Figure A9. Conductivity versus volume fraction of the conducting phase (ϕ_{PIL+W}) minus the critical volume fraction ($\phi_{PIL+W,c}$) for poly(MMA-*b*-MEBIm-Br) and poly(MEBIm-Br) at (a-e) 30, 40, 50, 60, 70 °C.

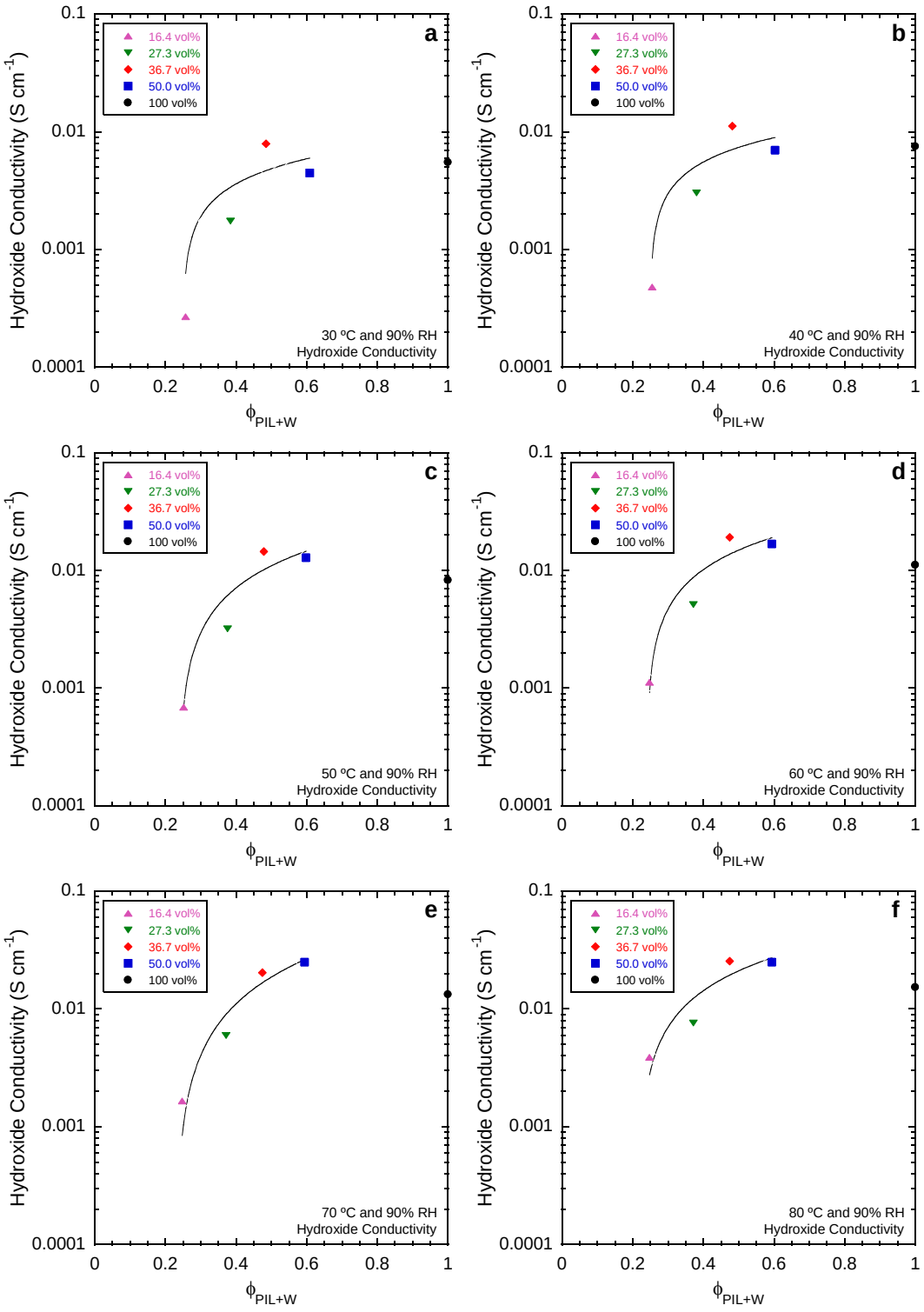

Figure A10. Ionic conductivity versus volume fraction of the conducting phase (ϕ_{PIL+W}) for poly(MMA-*b*-MEBIm-OH) and poly(MEBIm-OH) at (a-f) 30, 40, 50, 60, 70, 80 °C.

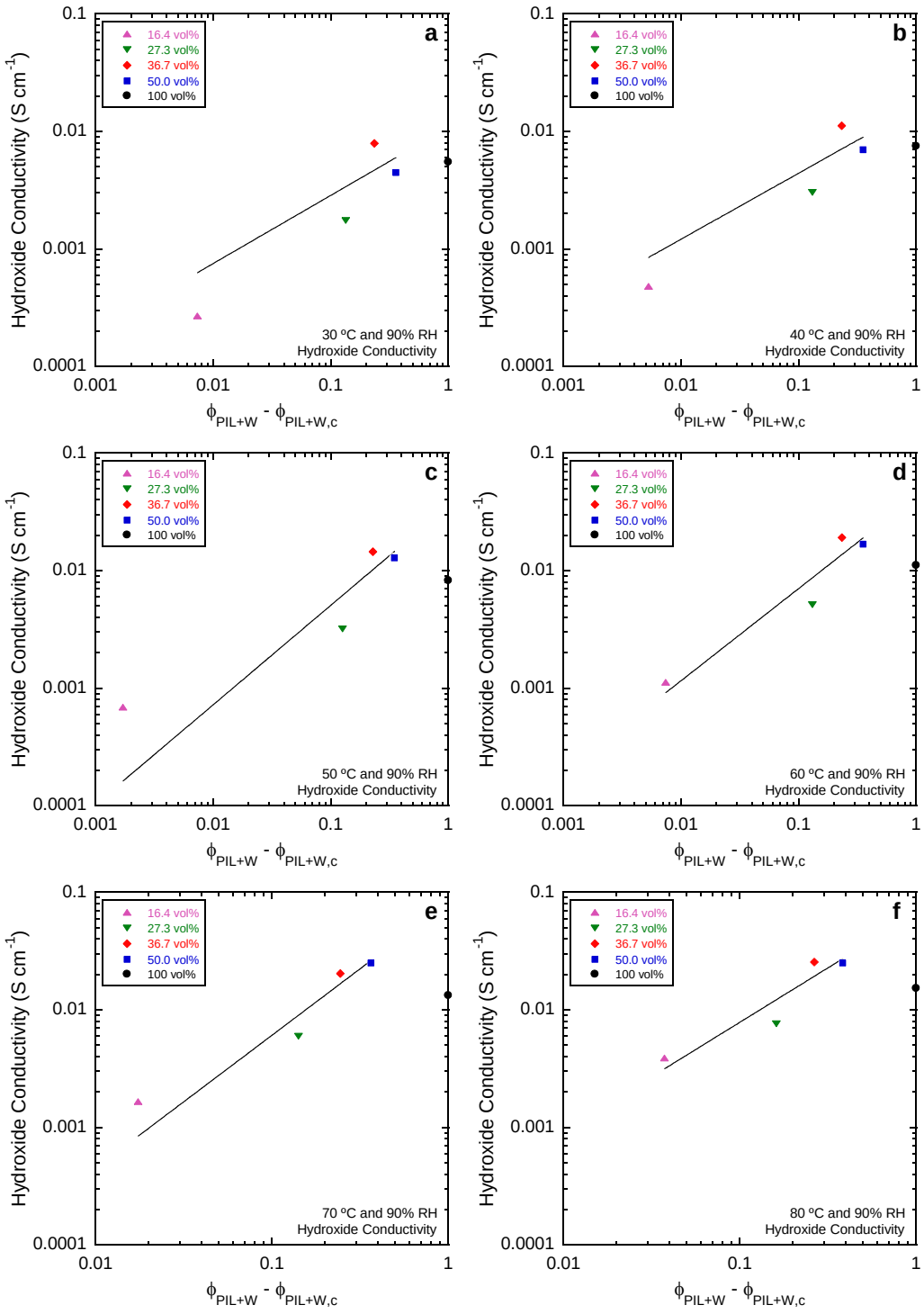

Figure A11. Conductivity versus volume fraction of the conducting phase (ϕ_{PIL+W}) minus critical volume fraction ($\phi_{PIL+W,c}$) for poly(MMA-*b*-MEBIm-OH) and poly(MEBIm-OH) at (a-f) 30, 40, 50, 60, 70, 80 °C.

APPENDIX B

B1. ^{1}H NMR of PMG and PMG PIL

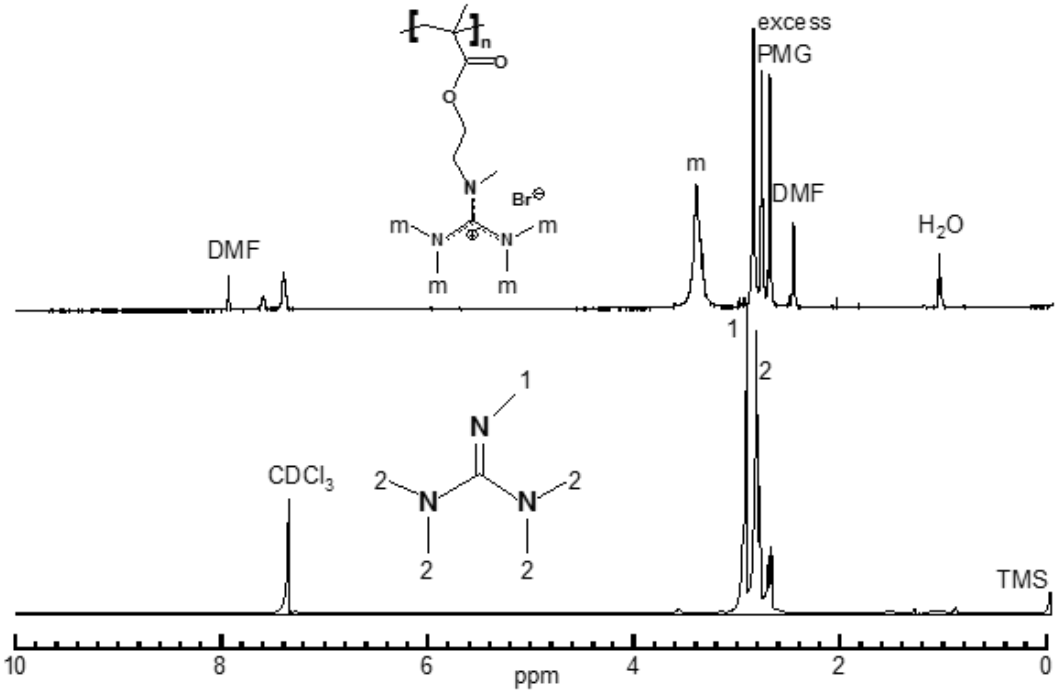

Figure B1. ^{1}H NMR spectra of 1,1,2,3,3-pentamethylguanidinium (PMG) in $CDCl_3$ (bottom) and PMG-functionalized PIL poly(MEPMG-Br) (top).

B2. Suppression of H/D exchange in imidazolium-based PILs

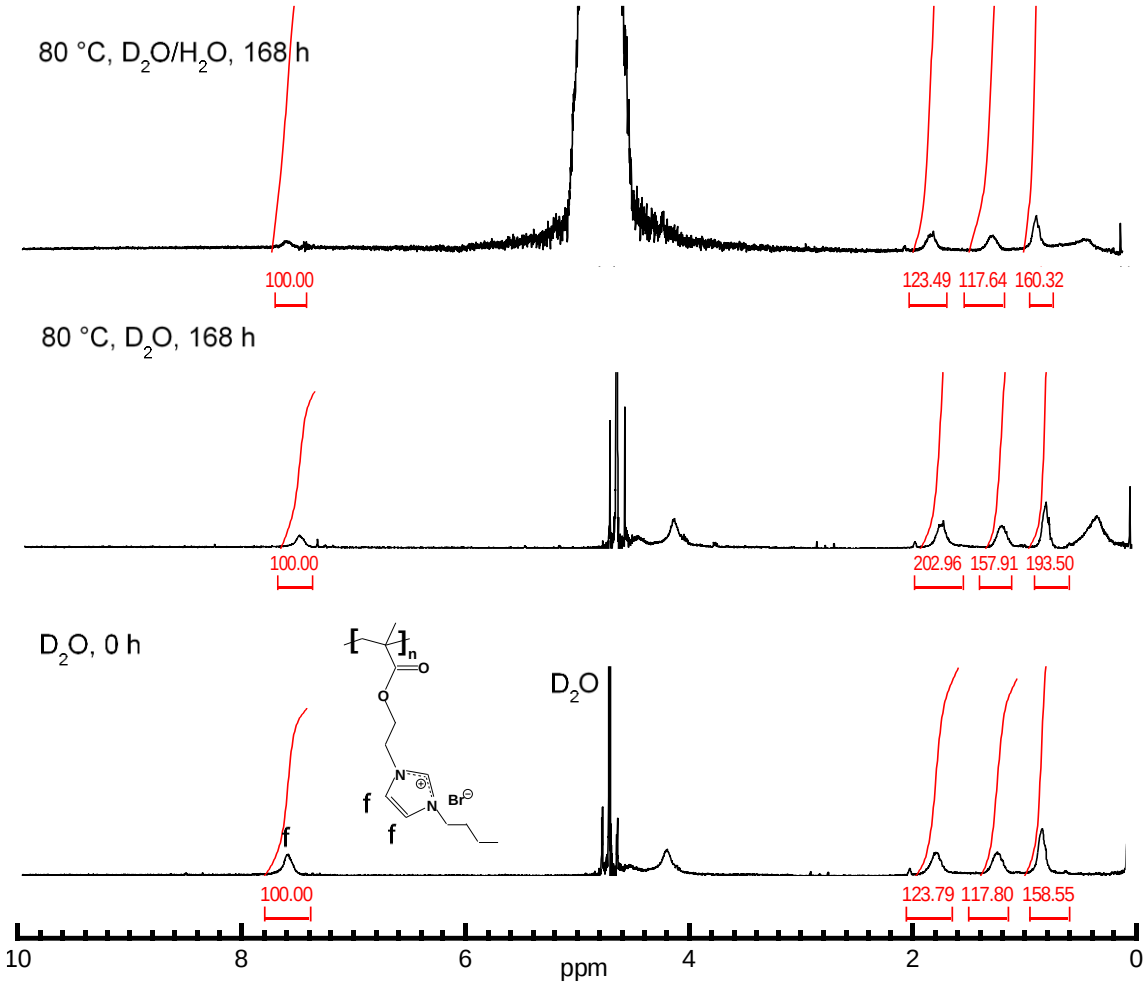

Figure B2. ^{1}H NMR spectra of butylimidazolium (BIm) functionalized PIL poly(MEBIm-Br) in D_2O before heat treatment (bottom), after 168 h at 80 °C (middle) and after 168 h at 80 °C with 80 mg of H_2O added (top). At 80 °C, an unidentified peak arises at low ppm, and is suppressed by the addition of H_2O.

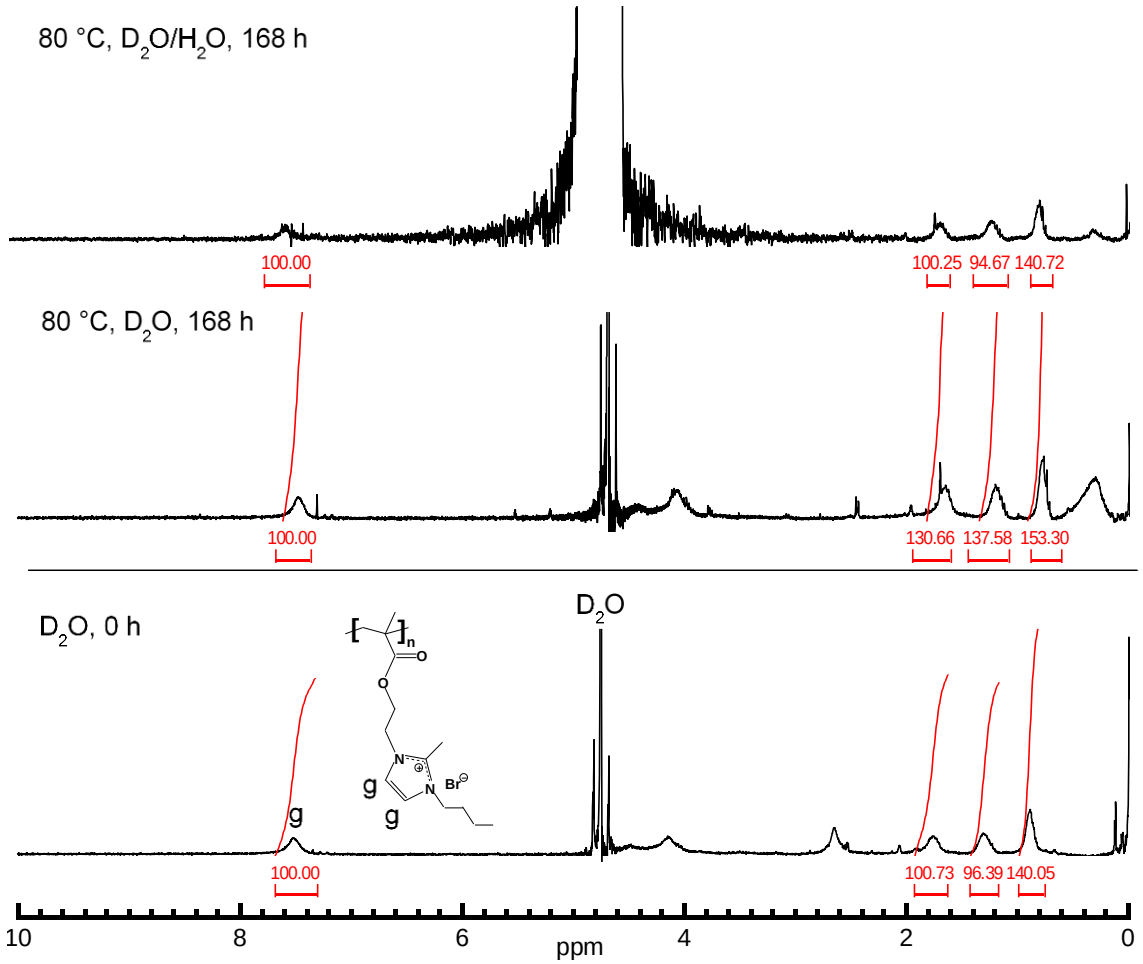

Figure B3. ^{1}H NMR spectra of butylmethylimidazolium (BMIm) functionalized PIL poly(MEBMIm-Br) in D_2O before heat treatment (bottom), after 168 h at 80 °C (middle) and after 168 h at 80 °C with 80 mg of H_2O added (top). At 80 °C, an unidentified peak arises at low ppm, and is suppressed by the addition of H_2O.

B3. Non-H/D exchanged PILs

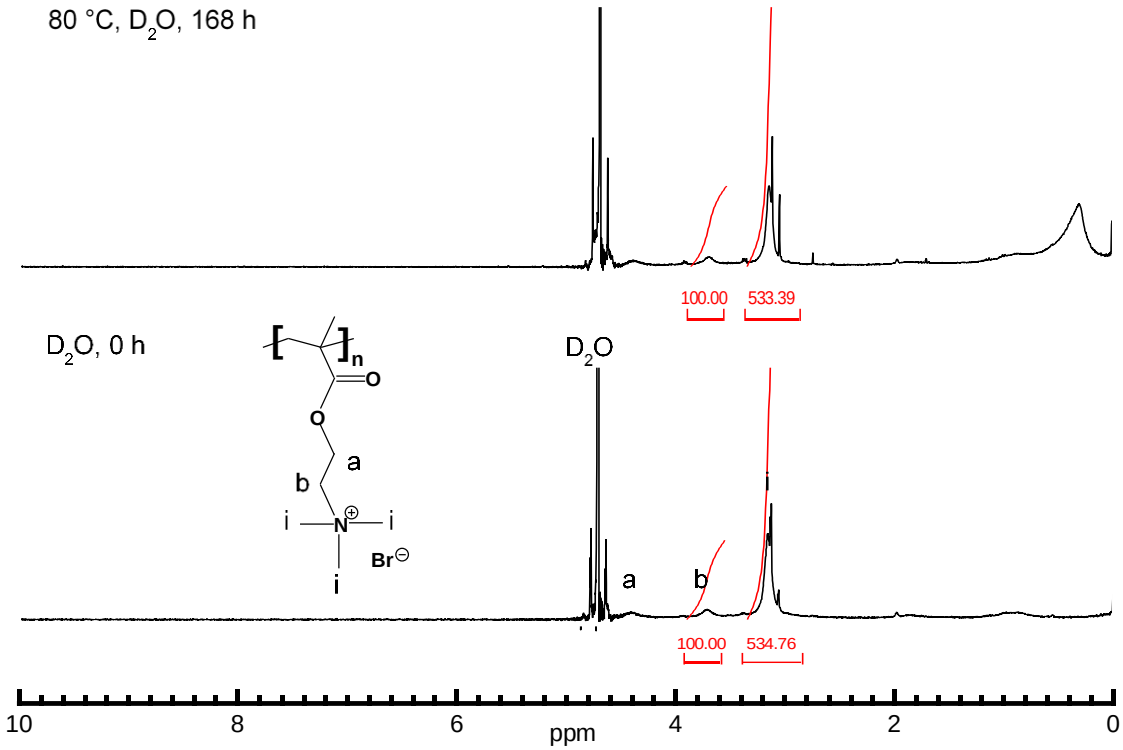

Figure B4. ^{1}H NMR spectra of trimethylammonium (TMA) functionalized PIL poly(METMA-Br) in D_2O before heat treatment (bottom) and after 168 h at 80 °C (top). At 80 °C, an unidentified peak arises at low ppm.

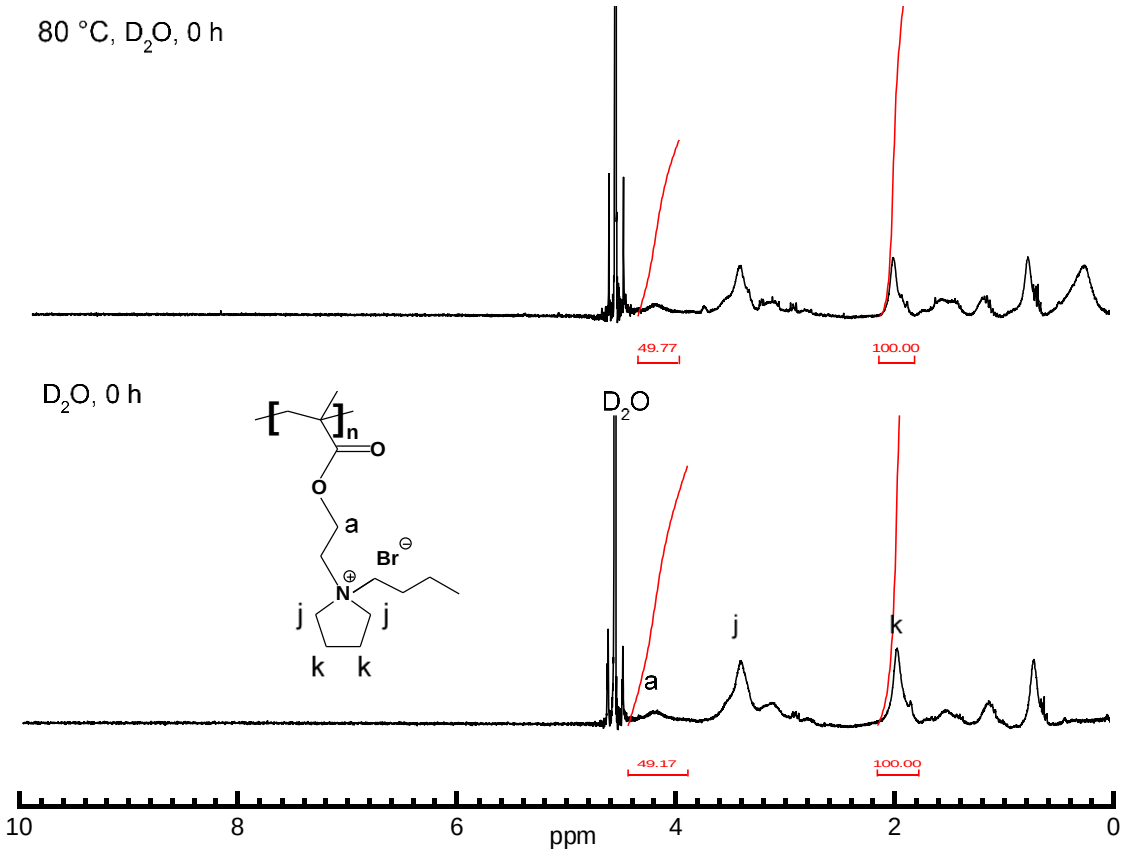

Figure B5. ^{1}H NMR spectra of butylpyrrolidinium (BP) functionalized PIL poly(MEBP-Br) in D_2O before heat treatment (bottom) and after 168 h at 80 °C (top). At 80 °C, an unidentified peak arises at low ppm.

B4. Effect of replacing 80 mg of D_2O with H_2O in non-H/D exchanged PIL

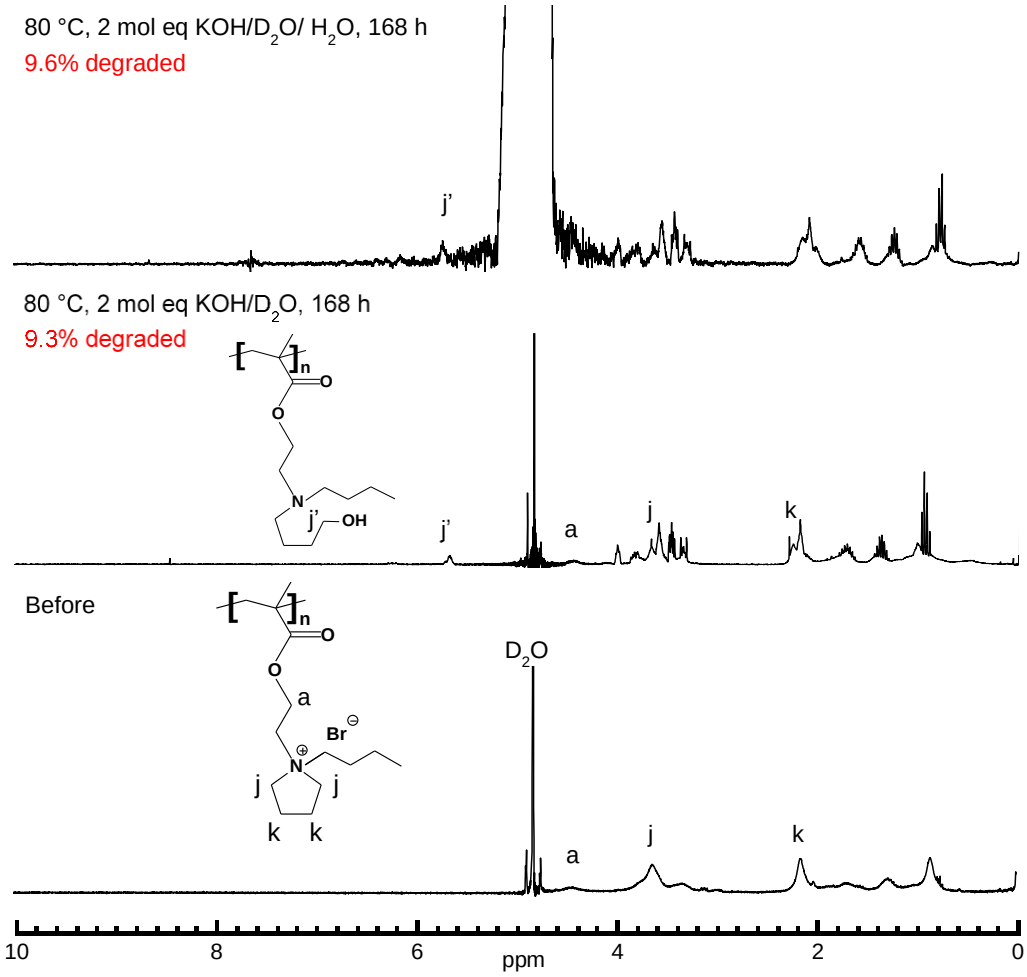

Figure B6. ^{1}H NMR spectra of butylpyrrolidinium (BP) functionalized PIL poly(MEBP-Br) in D_2O before degradation (bottom), after 168 h of degradation in 2 eq KOH/D_2O at 80 °C (middle), and after degradation in 2 eq KOH/D_2O/H_2O at 80 ° C (top).

B5. Comparison of Alkaline Stability between D_2O and H_2O for Imidazolium Salts

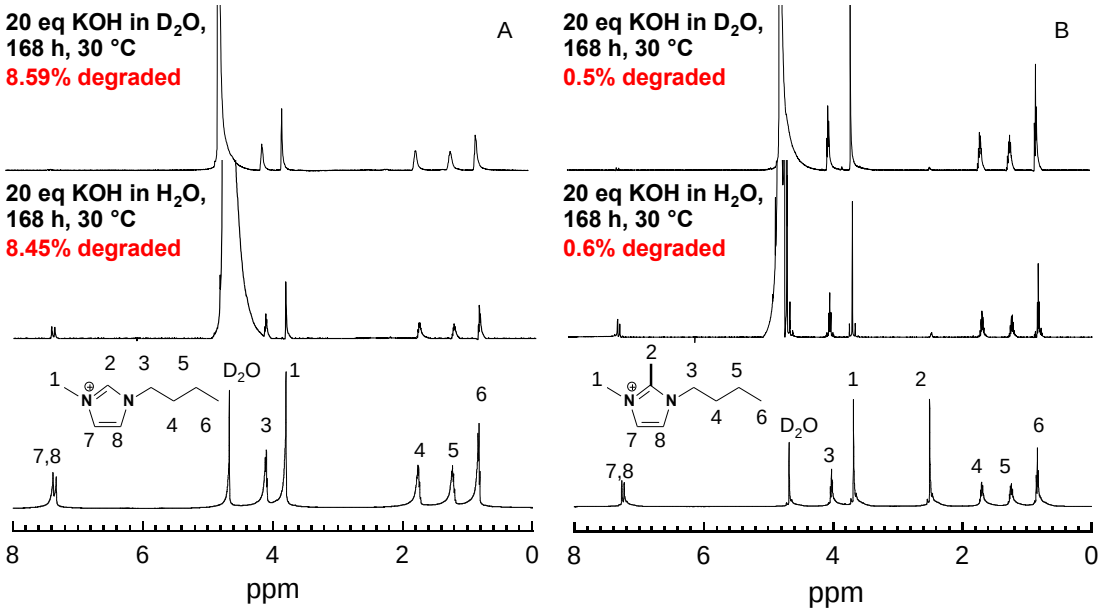

Figure B7. ^{1}H NMR spectra for (A) $BMIm^+ Cl^-$ and (B) $BDMIm^+ Cl^-$ in 20 eq KOH in D_2O and 20 eq KOH in H_2O at 30 °C for 168 h. Salts were degraded in pure D_2O or H_2O and then 100 mg aliquots of degraded solution were diluted with 1000 mg of D_2O to collect ^{1}H NMR spectra.

B6. Ester Hydrolysis

Carboxylate esters may hydrolyze to carboxylic acid and alcohol in an alkaline environment; the hydrolyzed byproducts are a carboxylic acid salt and an alkoxide salt. New peaks appearing at ~ 3.8 and ~3.9 ppm shown in Figure B8 may be assigned to -NCH_2- groups (f and f' along with g and g', for poly(MEBIm-Br and poly(MEBMIm-Br, respectively) that result from the ring opening products of covalently attached and cleaved imidazolium cations. This data suggests that hydrolysis likely occurs after the ring-opening mechanism, such that all cleaved cations have already undergone ring-opening degradation. For poly(MEBIm-Br) and poly(MEBMIm-Br), ~18% and ~15% of the total monomer units (~55% and ~40% of the ring-opened byproducts), respectively, had

cleaved from the polymer after 168 h at 80 °C and 20 eq KOH (see Schemes B1 and B2). For poly(MEBP-Br) under the same conditions, evidence of significant hydrolysis is noted in the undegraded cation peaks, as well as the degraded cation peaks that arise due to the E2 elimination reaction; overall, 65.5% of the backbone has undergone hydrolysis (see Figures B9 and B10 and Scheme B3). Note that Figure B9 shows NMR spectra for the condition of 2 eq, 80 °C rather than 20 eq, 80 °C (Figure B10); this is for ease of identifying peaks in the less degraded sample, but calculations were based on the NMR spectra for 20 eq, 80 °C. The high level of hydrolysis in the pyrrolidinium-based PIL may provide an explanation for its extraordinarily high chemical stability, as the small molecule byproduct of hydrolysis may have higher alkali stability. However, of the cations that remained tethered to the polymer backbone, only 24.1% underwent E2 elimination (see Scheme B3). Ester hydrolysis was not identified as a primary mechanism of degradation in the ammonium-based PIL (see Figure B11). Small molecule byproducts were not identified in the spectra that were not associated with cation degradation byproducts. This is likely due to the rate of degradation of the primary degradation mechanisms of poly(METMA-Br) occurring much faster than the hydrolysis reaction.

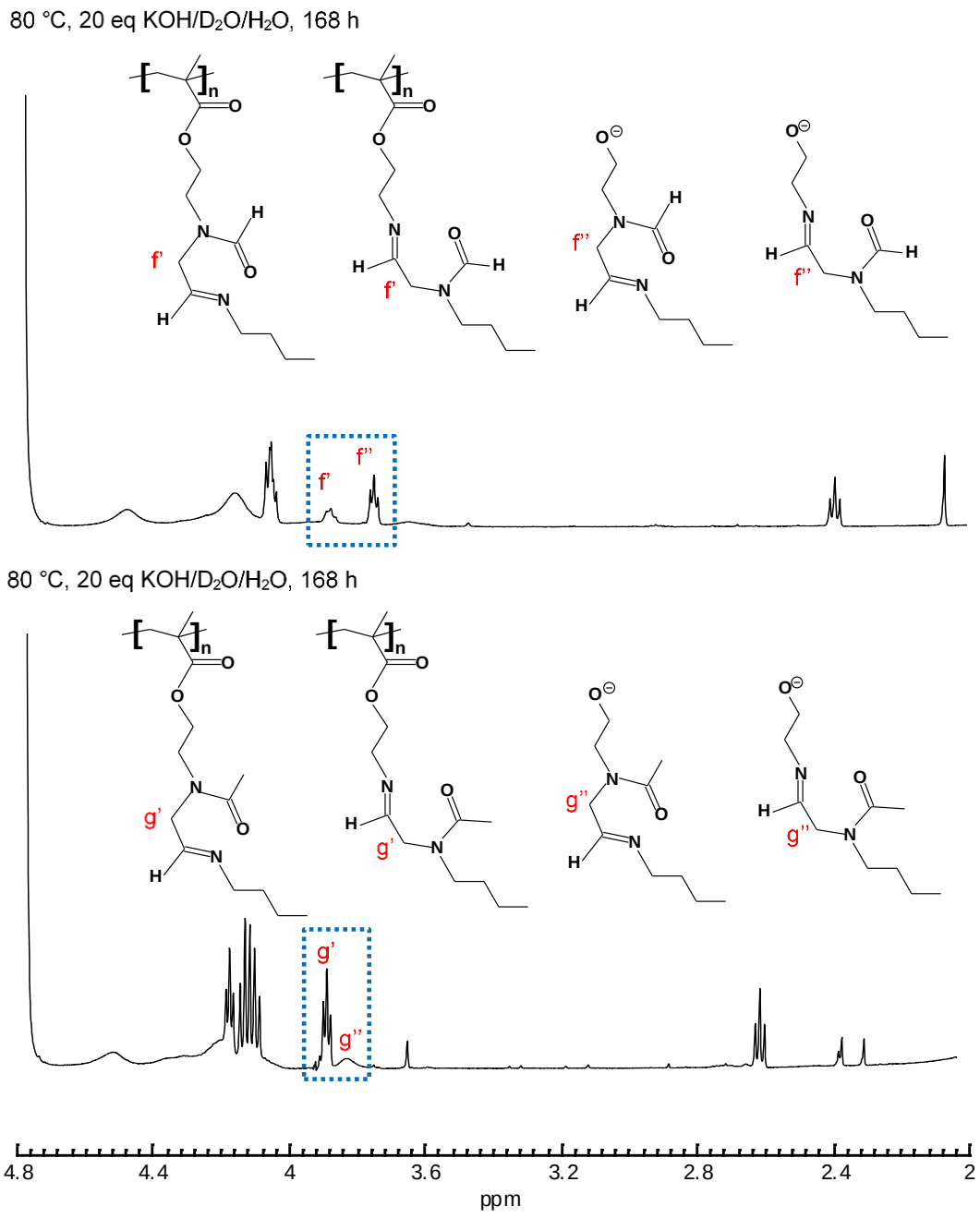

Figure B8. ^{1}H NMR spectra showing possible ester hydrolysis for poly(MEBMIm-Br) (bottom) and poly(MEBIm-Br) (top) after 168 h of degradation in 20 eq KOH/D_2O/H_2O at 80 °C.

Scheme B1. Poly(MEBIm-Br) structure after 168 h at 80 °C in 20 eq KOH/D_2O/H_2O.

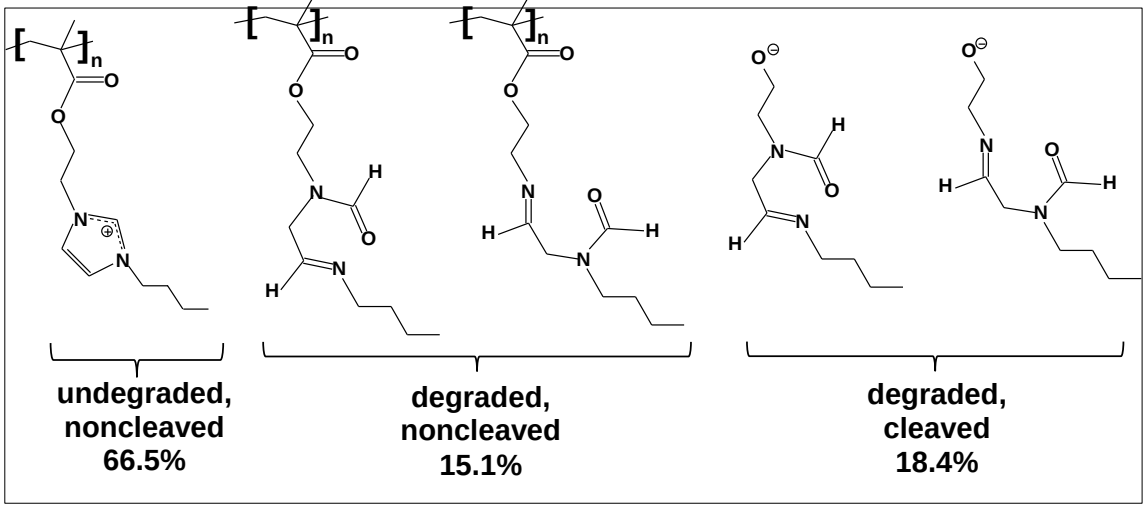

Scheme B2. Poly(MEBMIm-Br) structure after 168 h at 80 °C in 20 eq KOH/D_2O/H_2O.

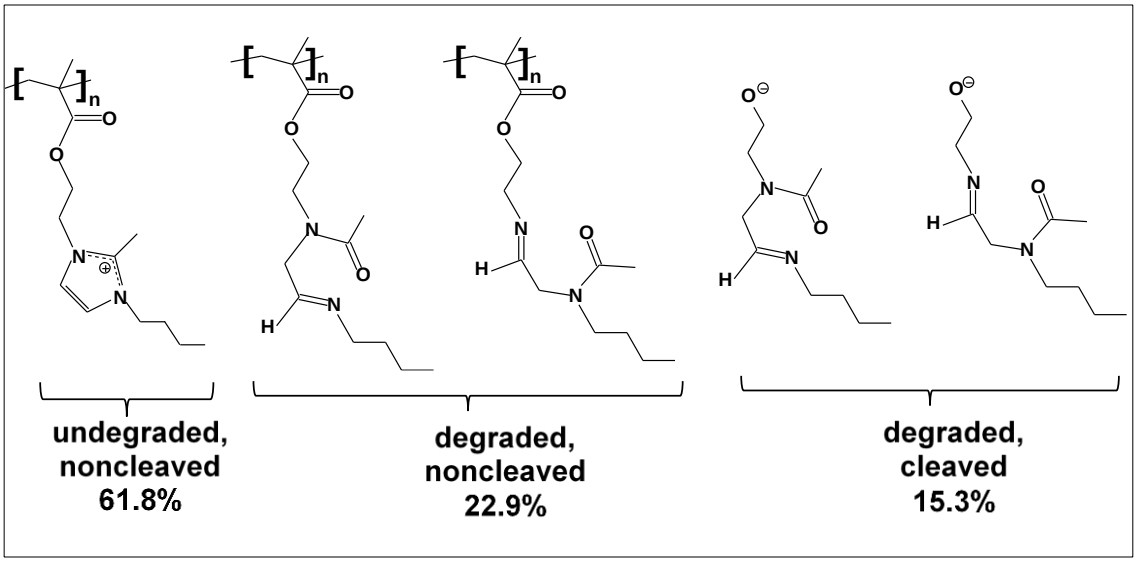

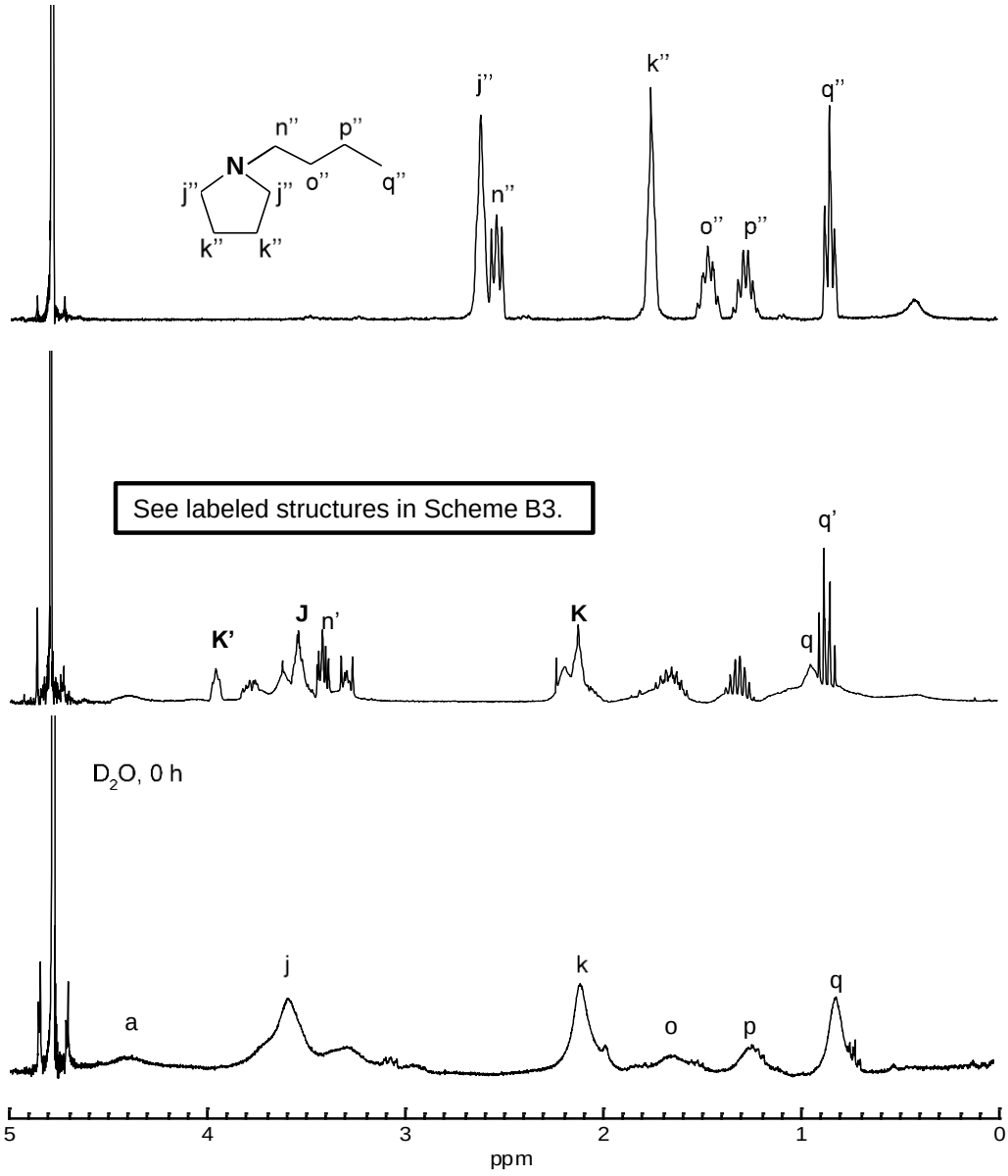

Figure B9. ^{1}H NMR spectra of possible ester hydrolysis for poly(MEBP-Br): before alkaline chemical stability study (bottom), 168 h in 2 eq KOH/D_2O at 80 °C (middle). ^{1}H NMR spectra of small molecule 1-butylpyrrolidinium (top).

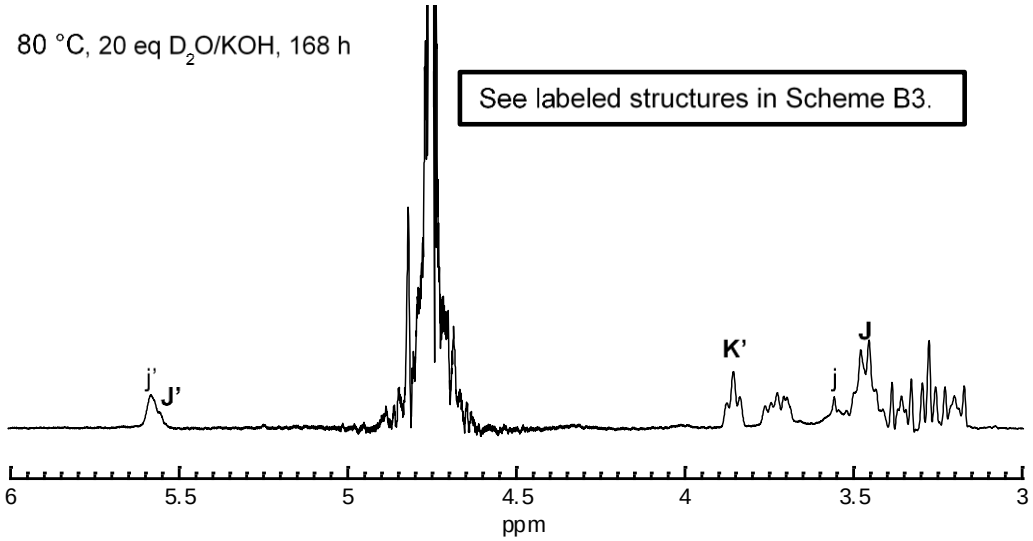

Figure B10. ^{1}H NMR spectra of possible ester hydrolysis for poly(MEBP-Br): after 168 h in 20 eq KOH/D_2O at 80 °C.

Scheme B3. Poly(MEBP-Br) structure after 168 h at 80 °C in 20 eq KOH/D_2O.

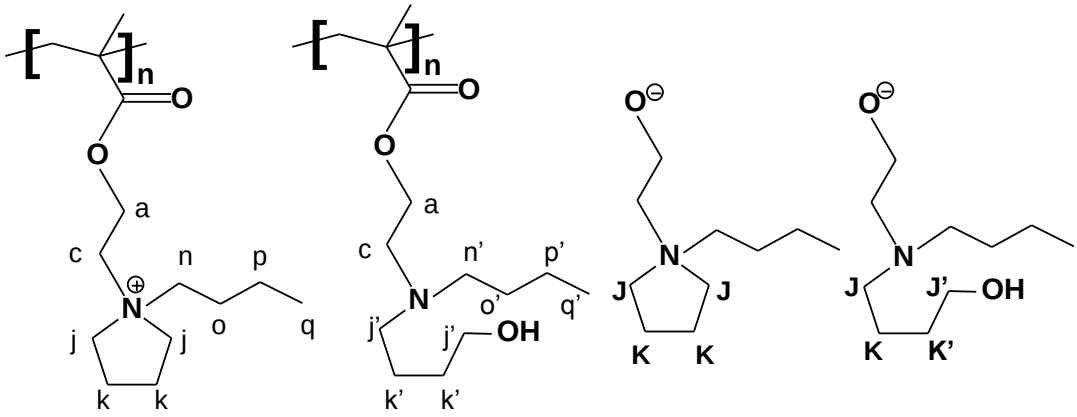

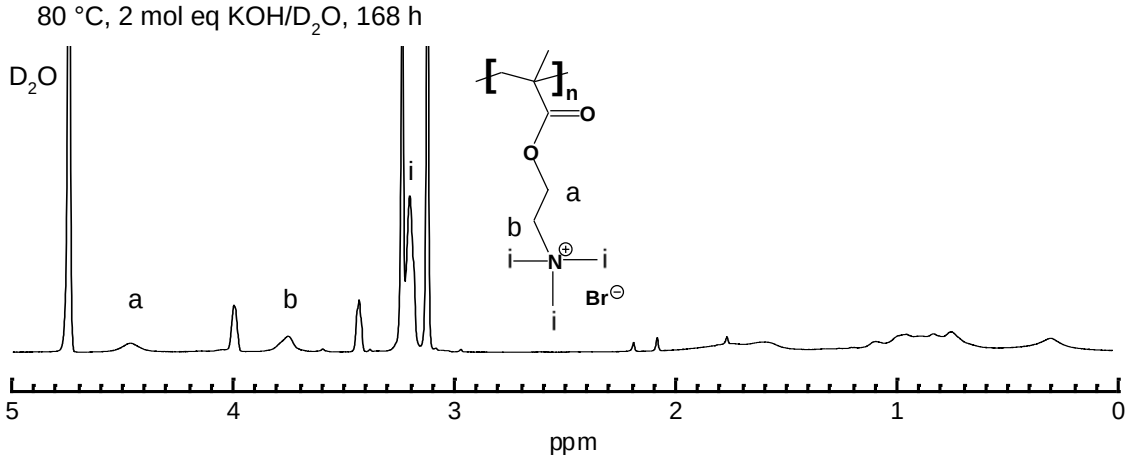

Figure B11. ^{1}H NMR spectra of possible ester hydrolysis for poly(METMA-Br) in 2 eq KOH/D_2O at 80 °C.

B7. An alternative degradation pathway through direct nucleophilic displacement

It may be possible that the OH^- ions attack the α-carbon located outside of the pyrrolidinium ring and form the byproduct 1-butylpyrrolidinium (BP) (Scheme B4). However, this byproduct is not present in the degraded ^{1}H NMR of poly(MEBP-Br) (see spectrum of commercially available 1-butylpyrroldinium in Figure B9), although similar peaks do appear. This small molecule byproduct has a very similar structure to the nondegraded, cleaved byproduct shown in Scheme B3 and therefore shares many of the same peaks. However, it is possible to comfirm these peaks are from the hydrolysis byproduct rather than BP byproduct from the ~1 ppm shift downfield of the hydrogens of the pyrrolidinium ring in comparison to the BP spectrum, due to the ring's proximity to the electronegative oxygen molecule. This suggests the direct nucleophilic replacement reaction is negligible and the primary degradation mechanisms for poly(MEBP-Br) are OH^- attack at the α-carbon located inside the pyrroldinium ring, and ester hydrolysis of

the polymer backbone. Similarly, Ye and Elabd confirmed that direct nucleophilic displacement was also negligible for poly(MEBIm-OH).[5] The same results were confirmed in this study for poly(MEBIm-Br) and poly(MEBMIm-Br), as 1-butylimidazole and 1-butyl-2-methylimidazole byproducts were not present in the degradation NMR spectra.

Scheme B4. Possible degradation pathway via direct nucleophilic displacement

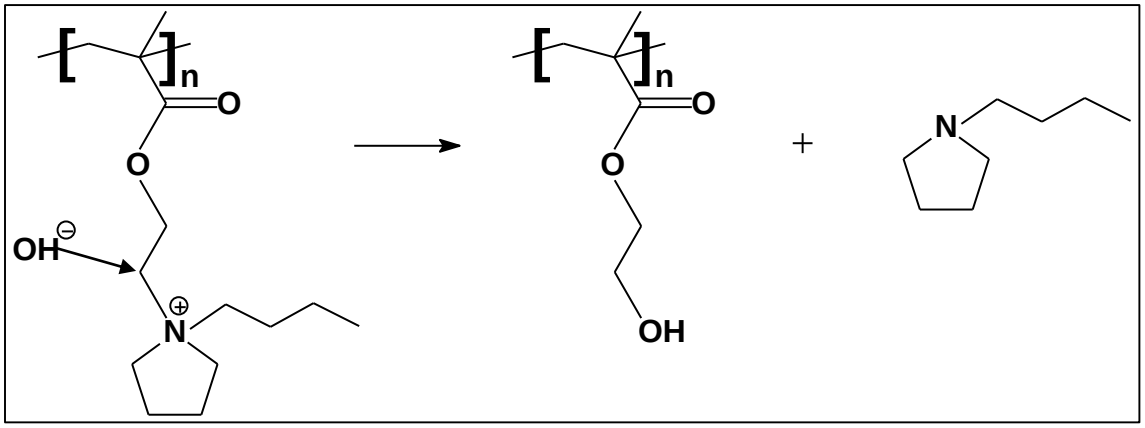

APPENDIX C

C1. ^{1}H NMR of BrUA, poly(BrUA), and poly(BrUMA).

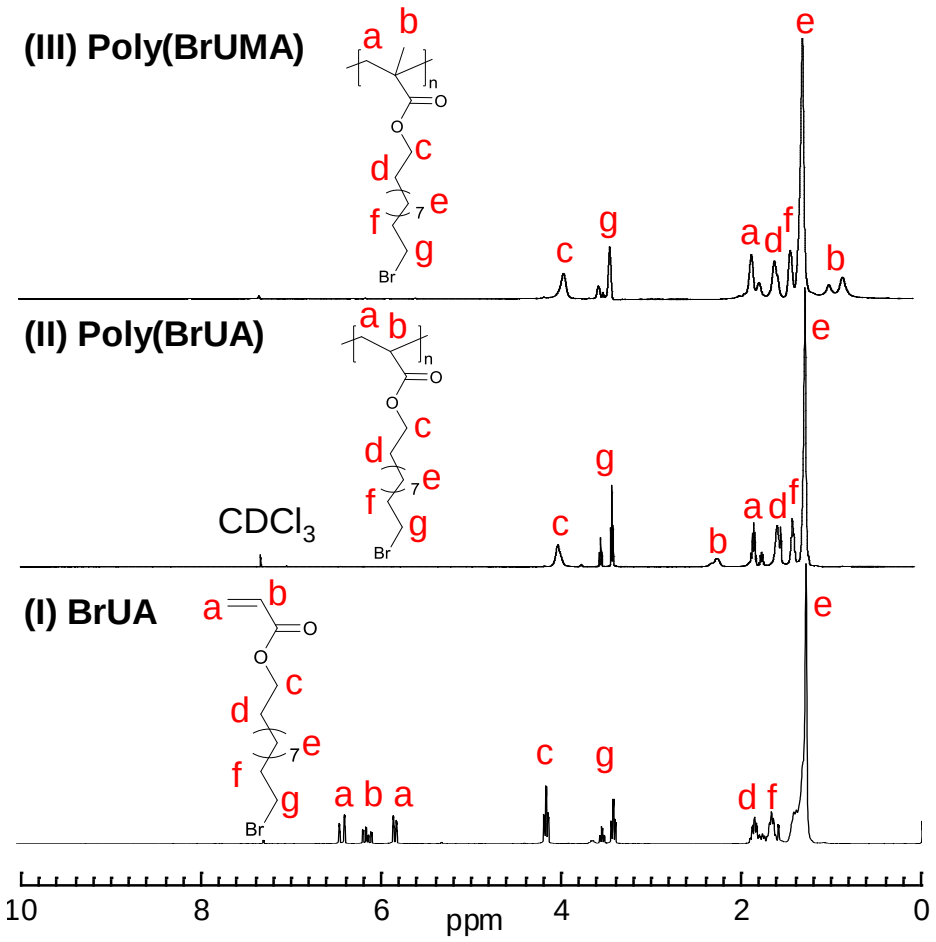

Figure C1. ^{1}H NMR spectra in $CDCl_3$ of (I) BrUA, (II) poly(BrUA), (III) poly(BrUMA).

C2. Ester Hydrolysis

Carboxylate esters may hydrolyze to carboxylic acid and alcohol in an alkaline environment; the hydrolyzed byproducts are a carboxylic acid salt and an alkoxide salt. New peaks appearing at ~3.8 and ~3.9 ppm shown in Figure C2 may be assigned to -NC*H*$_2$- groups (labeled c' and c") that result from the ring opening products of covalently

attached and cleaved imidazolium cations. Additionally, new peaks appearing at ~6.9 and ~7.1 ppm shown in Figure C3 may be assigned to C4 and C5 protons (labeled c^4) of the small molecule byproduct that results from the nondegraded imidazolium cations being cleaved from the polymer backbone, while the new peak appearing at ~7.41 ppm may be assigned to –N=C*H*- groups (c^3) that result from the ring opened byproducts of both covalently attached and cleaved imidazolium cations. This data suggests that hydrolysis and the ring-opening mechanism occured simultaneously, such that the cleaved cations may be intact or may be ring-opened degradation byproducts. For poly(MEBIm-OH), ~63.7% of the total monomer units have cleaved from the polymer after 168 h at 60 °C and 20 eq KOH/D_2O/H_2O.

In Figure C4, for poly(MEBP-OH) degraded under the same conditions, evidence of significant backbone hydrolysis is noted in the nondegraded cation peaks, by the presence of new peaks shifted slightly upfield (labeled a", f", g", h") from the original nondegraded protons (labeled a, f, g, h). No evidence of hydrolysis (*i.e.*, peak shouldering, peaks shifted upfield) was noted in the degraded cation peaks arising from the E2 elimination reaction. Overall, 37.0% of the backbone has undergone hydrolysis.

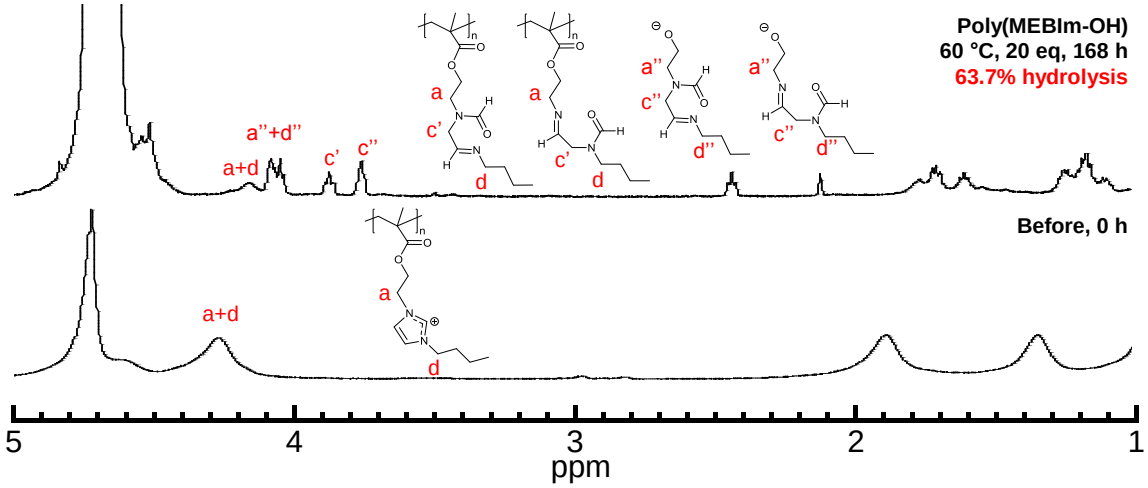

Figure C2. ^{1}H NMR spectra from 0 ppm to 5 ppm of (top) possible ester hydrolysis for poly(MEBIm-OH) after 168 h of degradation in 20 eq KOH/D_2O/H_2O at 60 °C and (bottom) poly(MEBIm-Br) before KOH exposure.

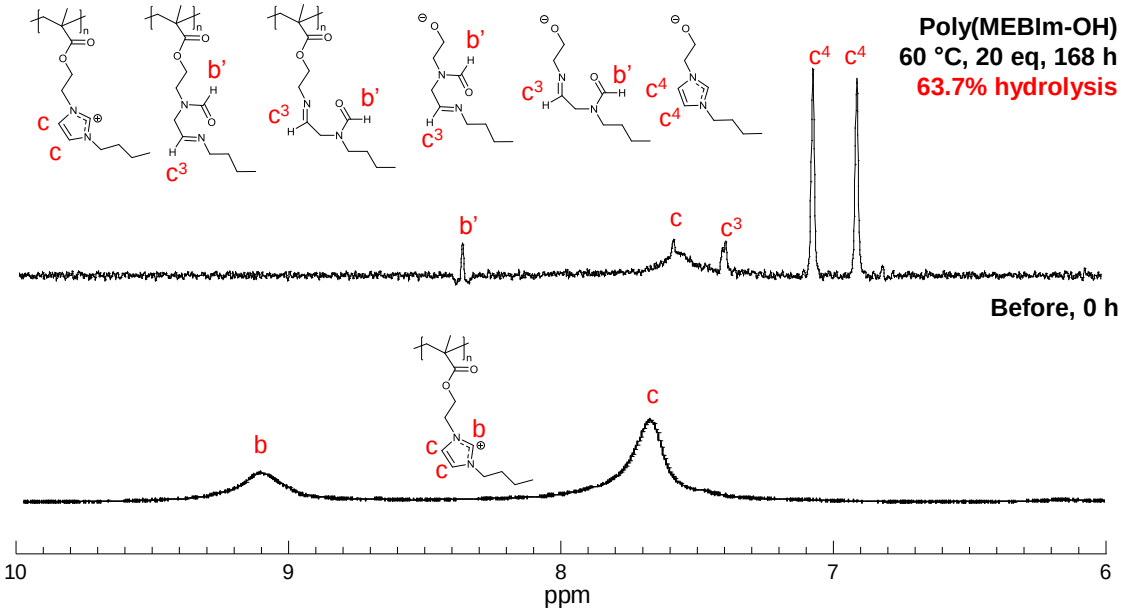

Figure C3. ^{1}H NMR spectra from 6 ppm to 10 ppm of (top) possible ester hydrolysis for poly(MEBIm-OH) after 168 h of degradation in 20 eq KOH/D_2O/H_2O at 60 °C and (bottom) poly(MEBIm-Br) before KOH exposure.

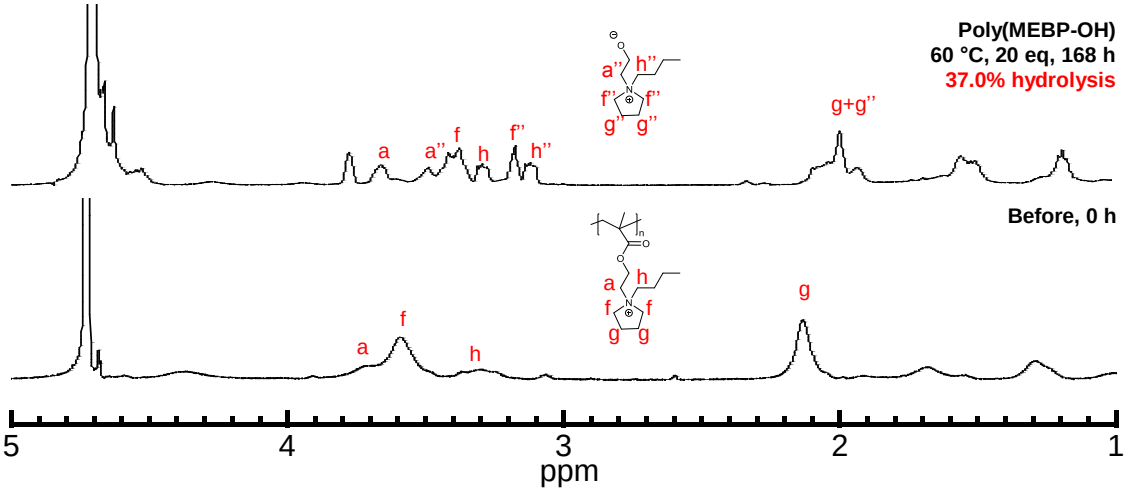

Figure C4. ^{1}H NMR spectra of (top) possible ester hydrolysis for poly(MEBP-OH) after 168 h of degradation in 20 eq KOH/D_2O at 60 °C and (bottom) poly(MEBP-Br) before KOH exposure.

C3. Harsher Degradation Conditions for Poly(VBBP-OH)

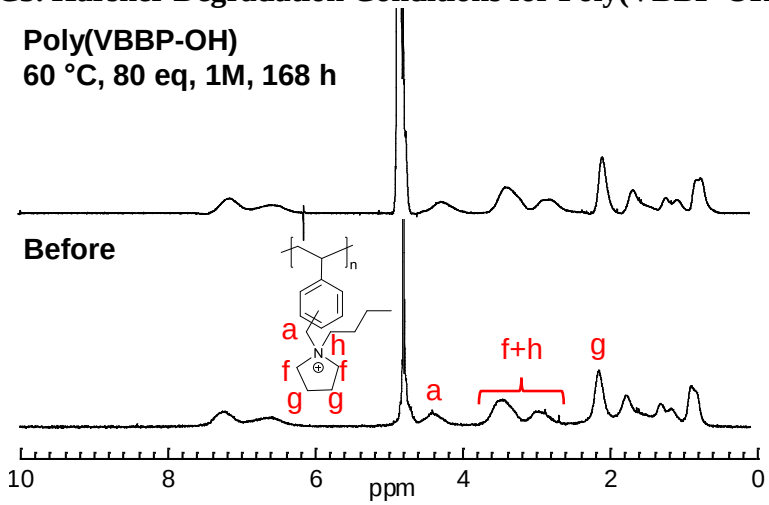

Figure C5. ^{1}H NMR spectra of (bottom) poly(MEBP-Br) before KOH exposure and (top) poly(MEBP-OH) after 168 h of degradation in 80 eq (1M) KOH/D_2O at 60 °C. New peak appearing at ~6.2 ppm is NMR center glitch, which appears due to low sample concentration, and is not a degradation peak. Cations peaks (labeled f, h, g) remain fully intact.

C4. Thermal Properties

Figure C6 shows glass transition temperatures (T_gs) of the twelve PILs measured by DSC. It is apparent when comparing Figure C4a (ethyl methacrylate) to Figure C6b (undecyl methacrylate PILs), that increasing the alkyl side-chain length resulted in a significant depression (~90 to 100 °C) of the T_g for the imidazolium and pyrrolidinium undecyl methacrylate PILs and a depression of 7 °C for the ammonium undecyl methacrylate PIL. Comparable to the undecyl methacrylate, where T_gs ranged from -5 °C to 67 °C, low T_gs ranging from -4 °C to 5 °C were observed for the undecyl acrylate PILs. The highest T_gs of the PILs were observed for the polystyrene backbone chemistries in Figure C6d, where T_gs ranged from 123 °C to 142 °C. In Figure C6a, the second highest T_gs of the PILs were observed for the ethyl methacrylate backbone chemistries, where T_gs ranged from 74 °C to 129 °C. Comparing all backbone types, no clear trend was present between cation type and T_g. Likewise, no clear trend was present between T_g and bromide ion conductivity. Thermal data for PILs is summarized in Table C1.

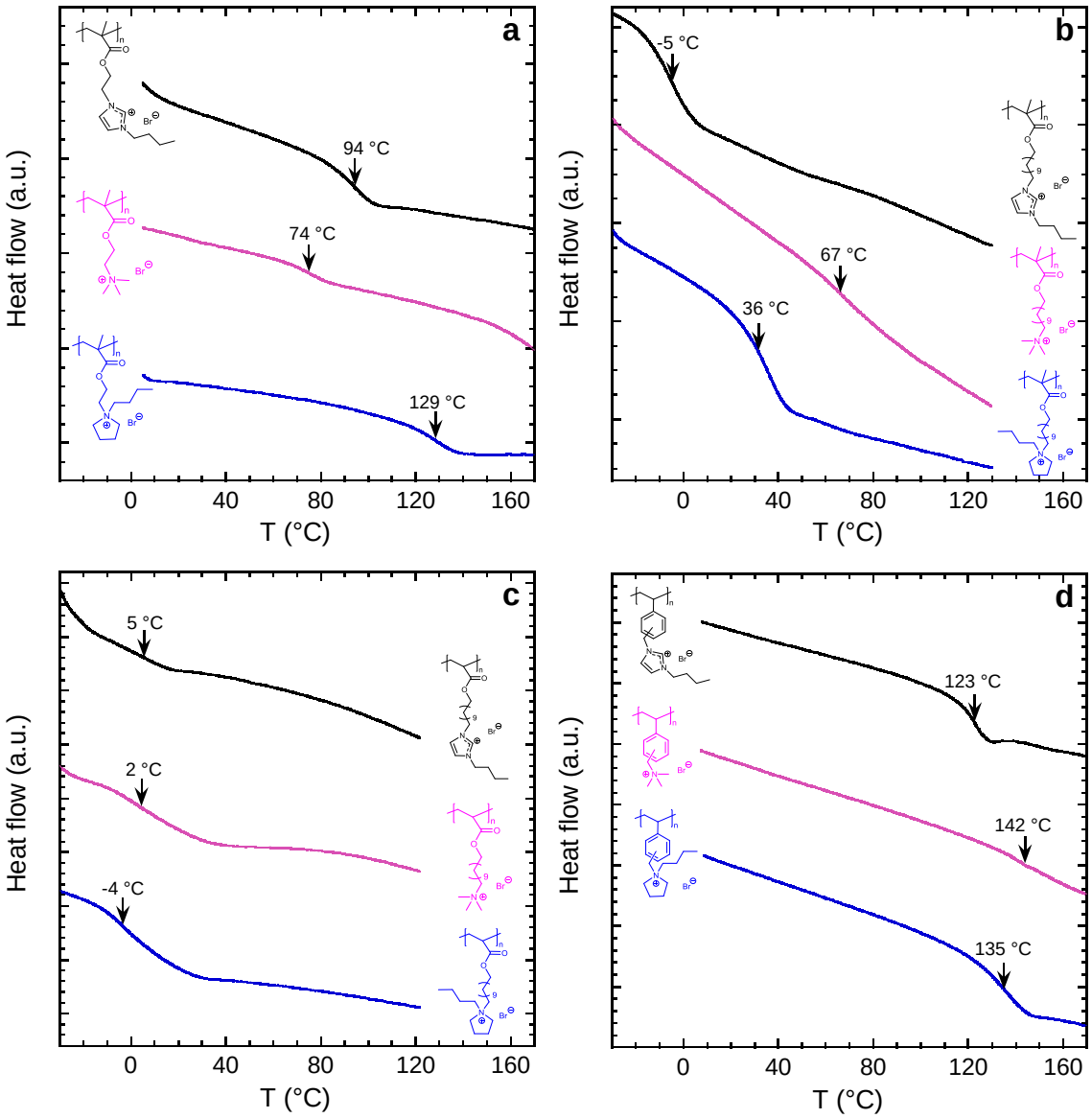

Figure C6. DSC thermograms of (a) ethyl methacrylate- (b) undecyl methacrylate- (c) undecyl acrylate- and (d) styrene-based PILs with various cations. Data offset for clarity.

Table C1. Glass transition temperatures of PILs.

Polymer	T_g (°C)
poly(MEBIm-Br)	94
poly(METMA-Br)	74
poly(MEBP-Br)	129
poly(MUBIm-Br)	-5
poly(MUTMA-Br)	67
poly(MUBP-Br)	36
poly(AUBIm-Br)	5
poly(AUTMA-Br)	2
poly(AUBP-Br)	-4
poly(VBBIM-Br)	123
poly(VBTMA-Br)	142
poly(VBBP-Br)	135

APPENDIX D

D1. Controlled Liquid Water Conductivity Experiment

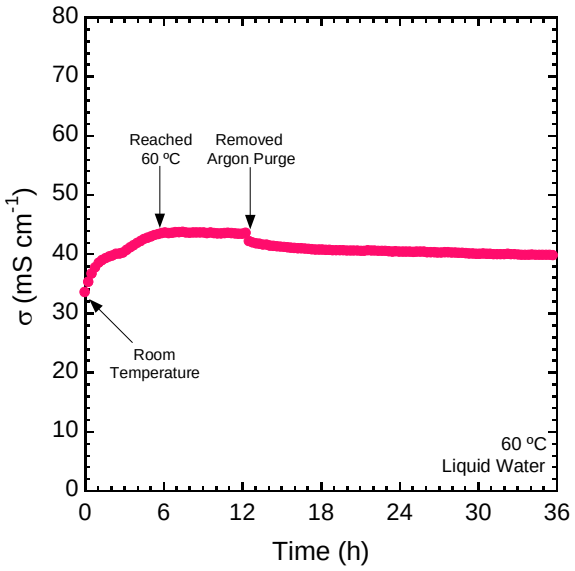

Figure D1. Time-dependent liquid water ion conductivity at 60 °C for hydroxide-conducting PIL multi-block polymer, poly(tbS-*b*-EB-*b*-VBMP-Br-*b*-EB-*b*-tbS), with argon purge for the first 12 h of the experiment. During the first 6 h, the conductivity increased as the water bath temperature increased from room temperature to 60 °C.

Figure D1 shows the results of an experiment that monitored the liquid water hydroxide ion conductivity of PIL multiblock polymer, poly(tbS-*b*-EB-*b*-VBMP-Br-*b*-EB-*b*-tbS), at 60 °C, for 36 h, where additional efforts were taken to prevent exchange of the hydroxide anion to bicarbonate and carbonate forms in air for the first 12 h. The AEM was exchanged using 0.2 M KOH in DI water, with argon bubbled into the solution continuously. Post-exchange, the AEM was stirred in DI water under argon purge to remove excess KOH. Efforts were made to prevent any exposure of the AEM to the atmosphere by using a syringe to remove and add solutions of fresh KOH or DI water. The KOH solutions and DI water were also purged with argon before being added with a syringe into the vial

containing the AEM. To begin the conductivity experiment, a water bath was purged with argon for 20 minutes. This argon purge was continued while the vial containing the AEM was opened under water in the water bath. The conductivity cell was assembled under water, then plastic wrap was used to cover the water bath, with a small opening allowed for the argon purge. The electrodes were able to pierce through the plastic wrap to allow for conductivity measurements. The water bath and conductivity cell setup were placed within the environmental chamber, which was preheated to 60 °C. Argon was continuously purged in the water bath throughout the experiment for the first 12 h. Initially, the conductivity rose in the first 6 h from 33.6 mS cm^{-1} to 43.6 mS cm^{-1} as the water bath heated from room temperature to 60 °C in the environmental chamber. The conductivity was then stable (changing <1%) at ~43 mS cm^{-1} from 6 h to 12 h; the argon gas was manually shut off at the regulator at 12 h and the plastic cover over the water bath was removed. The conductivity was monitored for 24 h more, with limited conductivity losses observed. The most significant conductivity loss (~4% loss) was observed in the first hour after the argon purge was removed (from hour 12 to hour 13) and 24 h after the purge was removed (hour 36), the conductivity had been stable (changing <1%) at ~40 mS cm^{-1} since hour 29.

In summary, limited effect of carbonation on the hydroxide ion conductivity of the AEM was observed in the controlled experiment. However, the conductivity after 24 h with no argon purge was still higher than the conductivity observed where no extra efforts were taken to prevent carbonation of the AEM (39.8 mS cm^{-1} versus 29.3 mS cm^{-1}, respectively. It is likely that limited CO_2 was absorbed into the water bath after the argon purge was

removed. Purging the water bath directly with air or CO_2 may have resulted in conductivity equivalent to that observed in the non-controlled experimental setup.

D2. FTIR-ATR Characterization of AEMs

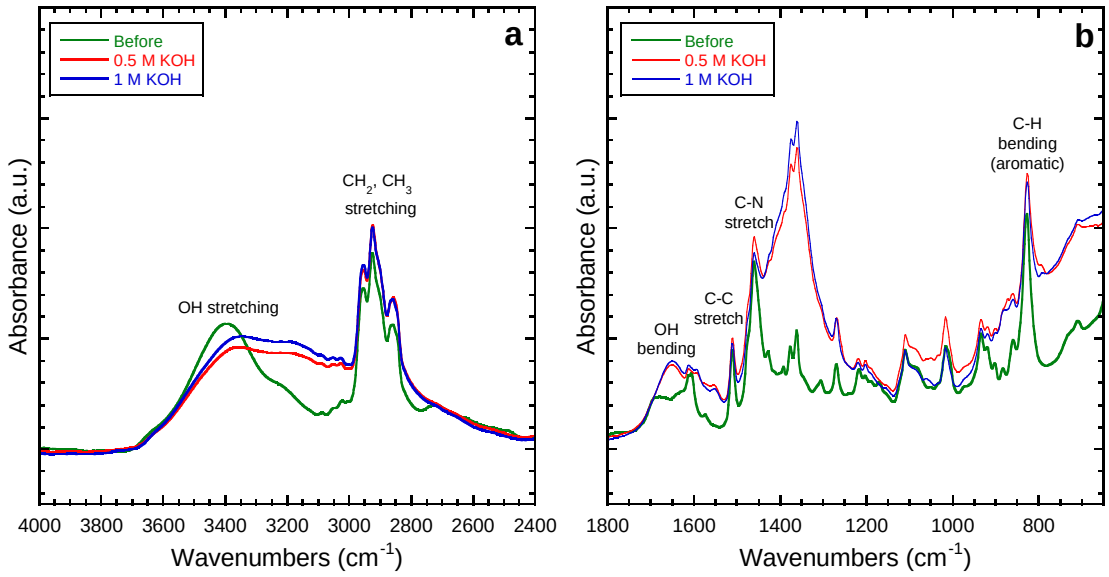

Figure D2. FTIR-ATR spectroscopy data of hydroxide-conducting PIL multi-block polymer, poly(tbS-*b*-EB-*b*-VBMP-OH-*b*-EB-*b*-tbS), before (green) and after exposure to 0.5 M KOH (red) and 1 M KOH (blue) at 60 °C for 168 h (blue) over wavenumbers (a) 2400 to 4000 cm^{-1} and (b) 650 to 1800 cm^{-1}.

Figure D2 shows the infrared data of hydroxide-conducting PIL multi-block polymer, poly(tbS-*b*-EB-*b*-VBMP-OH-*b*-EB-*b*-tbS), before and after exposure to 0.5 M KOH and 1 M KOH at 60 °C for 168 h. The most notable change in the spectra is observed for the infrared band located at *ca.* 1350 cm^{-1}, which is associated with the amine (C-N) group in the PIL block. This may indicate that the covalently tethered methylpyrrolidinium cation has undergone some degradation upon high pH exposure. However, results are

inconclusive, as membranes remained physically intact, and their conductivities did not change after high pH exposure.

D3. Thermal Characterization of AEMs

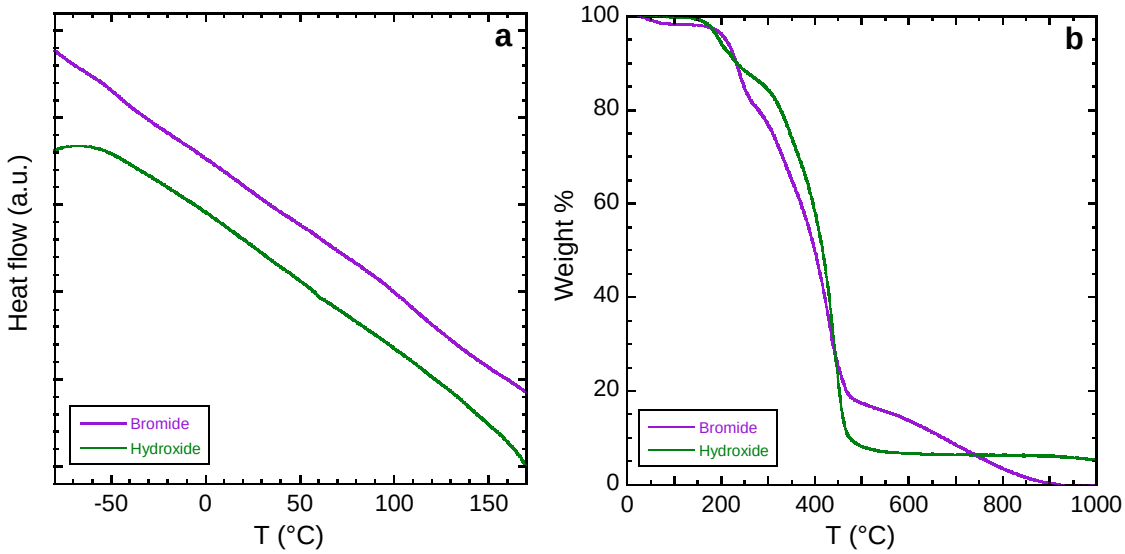

Figure D3. (a) DSC and (b) TGA thermograms of bromide- and hydroxide-conducting PIL multi-block polymers, poly(tbS-*b*-EB-*b*-VBMP-Br-*b*-EB-*b*-tbS) (purple) and poly(tbS-*b*-EB-*b*-VBMP-OH-*b*-EB-*b*-tbS) (green), respectively.

Figure D3 shows the results of thermal analysis of bromide- and hydroxide-conducting PIL multiblock polymers, poly(tbS-*b*-EB-*b*-VBMP-Br-*b*-EB-*b*-tbS) and poly(tbS-*b*-EB-*b*-VBMP-OH-*b*-EB-*b*-tbS), respectively. As shown in the DSC results in Figure D3a, no T_gs were measurable in the material for either anion form. TGA analysis (Figure D3b) was performed on the materials and it was observed that while no residual weight remained for the bromide form at 1000 °C, ~5 wt% of the hydroxide form remained.

APPENDIX E

E1. Characterization

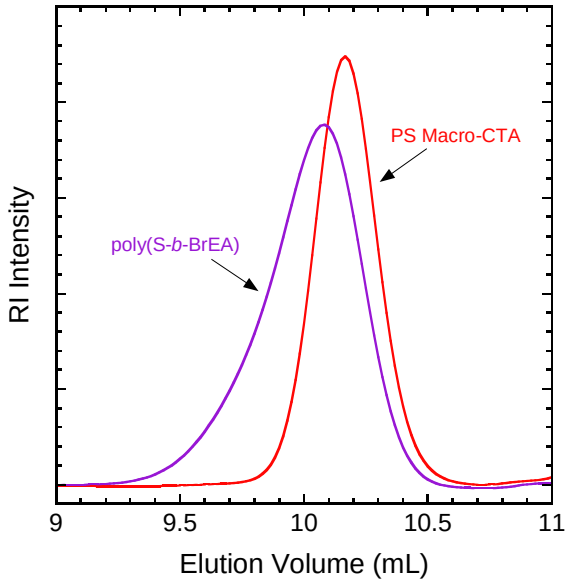

Figure E1. SEC chromatograms of PS macro-CTA (red) and poly(S-*b*-BrEA) (25.3 mol% PIL) (purple).

All chemical structures and PIL compositions were characterized by ^{1}H NMR spectroscopy using a Varian 500 MHz spectrometer at 23 °C with $CDCl_3$ or DMSO-d_6 as the solvent. The chemical shifts were referenced to tetramethylsilane (TMS). The molecular weights and molecular weight distributions of PS macro-CTA and poly(S-*b*-BrEA) were determined by size exclusion chromatography (SEC) using a Waters GPC system equipped with one THF Styragel column (Styragel HR 5E, effective separation of molecular weight range: 2,000 to 4,000,000 g mol^{-1}) and a 2414 reflective index (RI) detector. All measurements were performed at 40 °C at a flow rate of 1 mL/min. Polystyrene standards (Aldrich and Supelco Analytical) with molecular weights ranging from 2,500 to 983,400 g mol^{-1} were used for calibration. Glass transition temperatures

(T_gs) were determined by differential scanning calorimetry (DSC; TA Instruments, Q200) over a temperature range of -40 to 180 °C at a heating/cooling rate of 10 °C/min under a N_2 environment using a heat/cool/heat method. T_g was determined using the midpoint method from the second thermogram heating cycle. Thermal degradation of the PIL block copolymer before and after sulfonation (Figure E2) was measured by thermal gravimetric analysis (TGA; TA Instruments, Q50) over a temperature range of 30 to 900 °C at a heating rate of 10 °C/min under a N_2 environment.

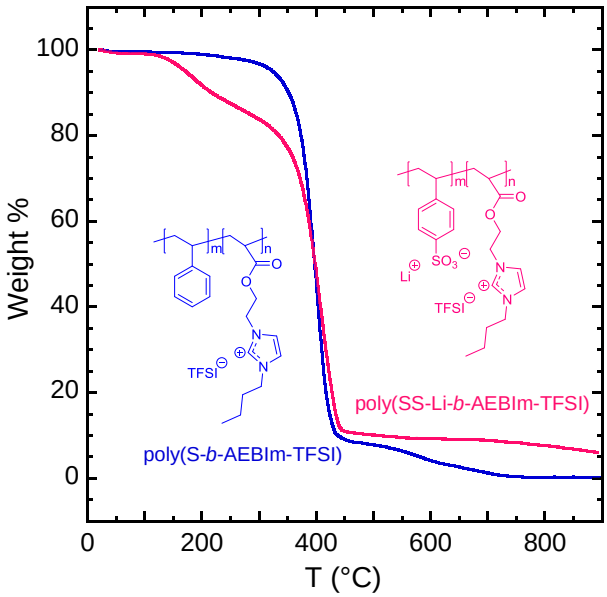

Figure E2. (a) TGA thermograms of poly(S-*b*-AEBIm-TFSI) (blue) and poly(SS-Li-*b*-AEBIm-TFSI) (pink).

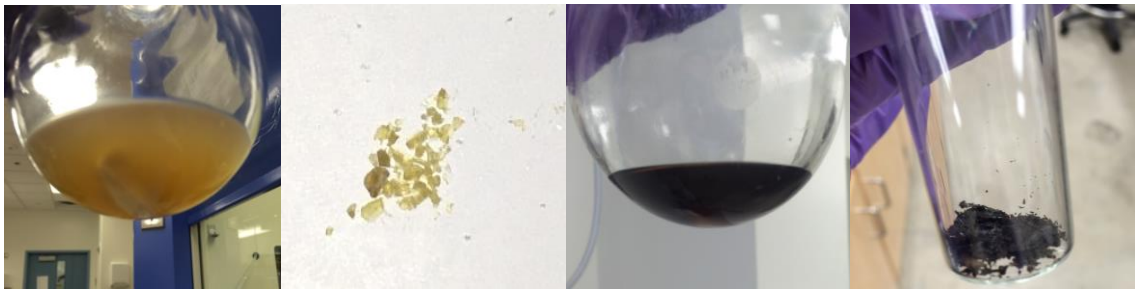

Figure E3. Pictures of the nonsulfonated block copolymer, poly(S-*b*-AEBIm-TFSI), in solution (far left) and as a powder (middle left) and the sulfonated polymer, poly(SS-Li-*b*-AEBIm-TFSI), in solution (middle right) and as a powder (far right).

The ionic conductivities of the polymer films were measured with electrochemical impedance spectroscopy (EIS; Solartron, 1260 impedance analyzer, 1287 electrochemical interface, Zplot software) over a frequency range of 10^2 Hz to 10^6 Hz at 10 mV. Conductivities were collected under dry conditions (<10% RH), where temperature and relative humidity were controlled by an environmental chamber (Espec, BTL-433 model). Specific temperature and humidity values are reported in Table E1. The in-plane conductivities of the polymer films were measured in a cell with four parallel electrodes, where an alternating current was applied to the outer electrodes and the real impedance or resistance, *R*, was measured between the two inner reference electrodes. The resistance was determined from the x-intercept at high frequency of the semi-circle regression of the Nyquist plot. Conductivity was calculated by using the following equation: $\sigma = L/AR$, where *L* and *A* are the distance between two inner electrodes and the cross sectional area of the polymer film ($A = Wl$; *W* is the film width and *l* is the film thickness), respectively. Samples were allowed to equilibrate for 2 h at each temperature and humidity followed by 6 measurements at the equilibrium condition. The values reported are an average of

these steady-state measurements. An average error of <5% was observed among repeated experiments. At 25 °C, the humidity chamber was unable to maintain humidity <10% RH (relative humidity), stabilizing instead at 25% RH; therefore a drybox was constructed to measure room temperature conductivity. Conductivity was measured within a Plexiglass box, purged with dry compressed air, in order to reach a temperature and relative humidity of 27.5 °C and 5% RH. These conditions were measured using a temperature/humidity sensor (Sensirion (SHT75)). Minimal difference (~2%) was observed in conductivity for conditions of 25 °C and 25% RH versus 27.5 °C and 5% RH; values were 0.509 mS cm^{-1} and 0.520 mS cm^{-1}, respectively.

Water uptake or content was measured with dynamic vapor sorption (DVS, TA Instruments Q5000), under the same conditions that conductivity was measured. Samples weighing ~1.3 mg were loaded into the DVS and preconditioned at 0% RH and 25 °C until equilibrium was reached; equilibrium was established as <0.05 wt% change for at least 30 min for all conditions. The relative humidity was then systematically changed to a constant value of 25% RH at a fixed temperature of 25 °C, and subsequently, 10% RH at 50 °C, 7% at 60 °C, and 5% at 27.5 °C, equilibrating at each condition. Equilibrium time per step varied by condition, from ~60 min to ~75 min (less than the 2 h equilibrium time allotted for conductivity measurements). The polymer water content (uptake) [wt%; g H_2O/g dry polymer] was calculated as follows:

$$W_{H_2O} = \frac{W - W_0}{W_0} \times 100 \qquad \text{(E.1)}$$

where W_0 and W are dry and wet polymer weights measured before and after the DVS experiment, respectively.

Table E1. Conductivity and Water Uptake Results.

Temperature (°C)	Relative Humidity (%)	Water uptake (wt%)[a]	Conductivity (mS cm^{-1})
25	25	0.89	0.509[b]
27.5	5	0.13	0.520[c]
50	10	0.42	1.01
60	7	0.25	1.26
70	8	-	1.56
80	10	-	1.56

[a]Water uptake measured by DVS at same condition as EIS. [b]Conductivity at this condition is not reported in Figure 6.4. [c]Experiment performed in drybox, not environmental chamber. Conductivity at this condition is reported in Figure 6.4.

Small-angle X-ray scattering (SAXS) was performed at the University of Houston on a Rigaku S-Max 3000 High Brilliance 3 Pinhole SAXS system with MicroMax-007HFM Microfocus rotating anode generator (Cu-Kα radiation, λ = 1.54 Å). SAXS data was collected under vacuum at room temperature in the through-plane direction of films cast on Kapton films (McMaster-Carr, 130 μm thickness) for 15 min. The intensities were first corrected for primary beam intensity, and then background scattering was subtracted (Kapton film). The isotropic 2-D scattering patterns were then azimuthally integrated to yield 1-D intensity versus scattering angle (q) profiles. The intensities were reported in arbitrary units (a.u.).

Chemical structures of the polymers were investigated with infrared spectroscopy using a Fourier transform infrared (FTIR) spectrometer (Nicolet 6700 Series; Thermo Electron) equipped with a single reflection diamond ATR accessory (Specac; Quest). All spectra were collected using a liquid nitrogen-cooled mercury-cadmium-telluride (MCT) detector at 32 scans per spectrum with a resolution of 4 and a data spacing of 1.925 cm^{-1}. Samples were clamped with an anvil at a constant load of 68.9 MPa onto the surface of the ATR crystal (1.8 mm diameter). Before each experiment, a background spectrum of the bare ATR crystal was collected, and all subsequent collected spectra were subtracted from this spectrum.

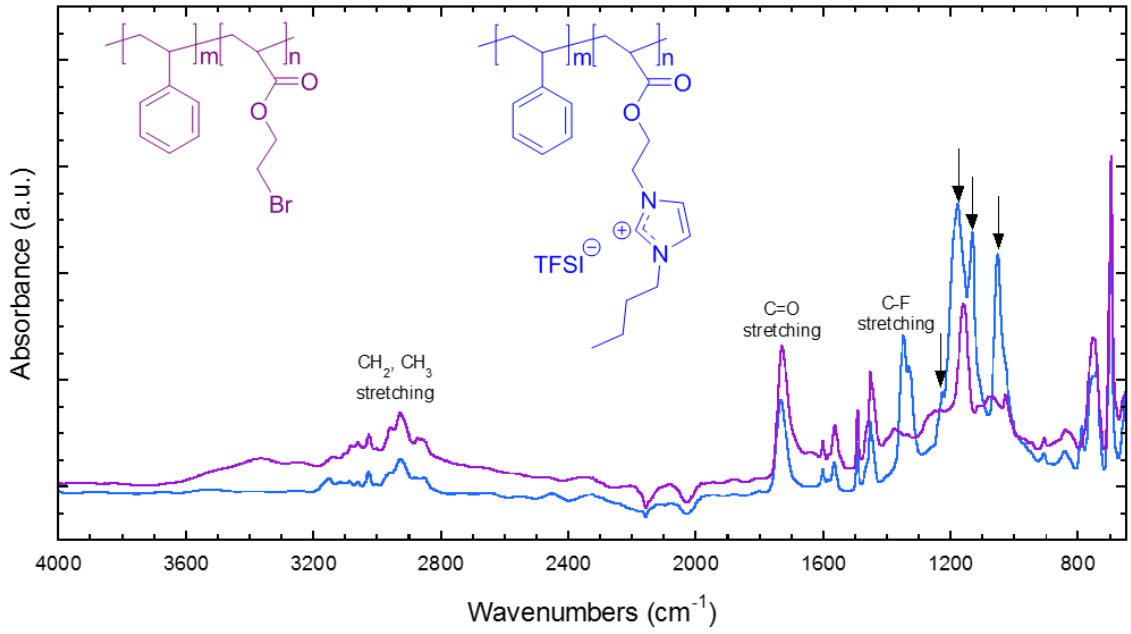

Figure E4. FTIR-ATR spectroscopy data of neutral precursor block copolymer, poly(S-*b*-BrEA) (purple), and the nonsulfonated PIL block copolymer, poly(S-*b*-AEBIm-TFSI) (blue) at ambient conditions. Four bands (indicated with arrows) are evident in the PIL block copolymer, 1222, 1178, 1132, 1051 cm^{-1}, representing the stretching vibrations of the sulfone groups of TFSI.

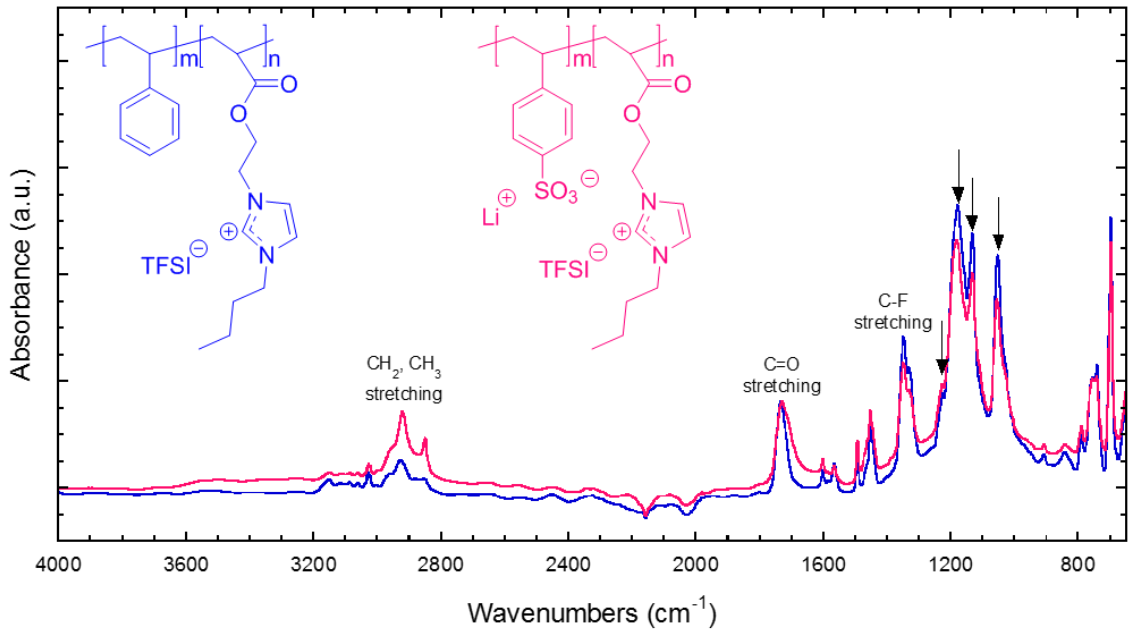

Figure E5. FTIR-ATR spectroscopy data of nonsulfonated PIL block copolymer, poly(S-*b*-AEBIm-TFSI) (blue), and the sulfonated PIL block copolymer, poly(SS-Li-*b*-AEBIm-TFSI) (pink) at ambient conditions.

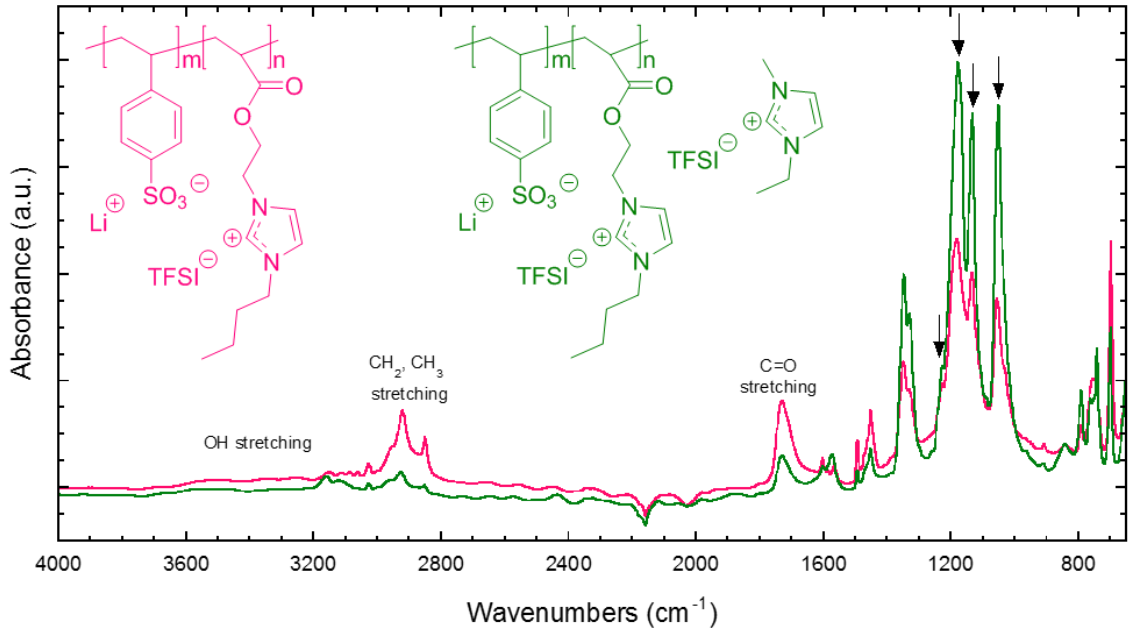

Figure E6. FTIR-ATR spectroscopy data of sulfonated PIL block copolymer, poly(SS-Li-*b*-AEBIm-TFSI) (pink), and the sulfonated PIL block copolymer cast with 1M Li-TFSI in EMIm-TFSI, poly(SS-Li-*b*-AEBIm-TFSI) + Li-TFSI/IL (green) at ambient conditions.

Figure E4 shows the infrared data of neutral precursor block copolymer, poly(S-*b*-BrEA) (purple), and the nonsulfonated PIL block copolymer, poly(S-*b*-AEBIm-TFSI) (blue) at ambient conditions. For the PIL block copolymer, four distinct bands are present from the sulfone groups of TFSI (1222, 1178, 1132, 1051 cm^{-1}). Additionally, the band at 1350 cm^{-1} represents the C-F stretching of TFSI.

Figure E5 shows the infrared data of the PIL block copolymer, before and after sulfonation. Minimal changes are noted in the spectra, as the peaks associated with sulfonation (the in-plane bending vibrations of the aromatic ring para-substituted with the sulfonate group and the sulfonate anion attached to the aromatic ring, and the symmetric and asymmetric stretching vibrations of the sulfonate group[1]) are already present at much

higher concentration from TFSI anion. Increase in bands in the CH_2, CH_3 stretching region post-sulfonation could be associated with sulfonation. However, they may also may be due to residual solvent, as was indicated by EA; however, it should be noted that additional drying of polymer was performed prior to FTIR experiments to prevent the presence of water in the spectra, which should have further removed residual solvents.

Figure E6 shows the infrared data of poly(SS-Li-*b*-AEBIm-TFSI) and poly(SS-Li-*b*-AEBIm-TFSI) + Li-TFSI/IL. In Figures E4-6, the infrared band located at *ca.* 1720 cm^{-1} is associated with the carbonyl (C=O) group in the PIL (acrylate-based) block. Although sulfonated styrene is hydrophilic and ionic, in Figure E5-6, limited water (<2 wt%) is absorbed and detected with FTIR-ATR spectroscopy in the sulfonated PIL block copolymer due to the presence of the lithium and TFSI mobile complexed ions, well as the small degree of sulfonation. The lack of any band located in the region of 3000-3700 cm^{-1}, which represents the O-H stretching of water, suggests minimal water uptake, which was confirmed by DVS experiments (Table E1). After the addition of Li-TFSI and EMIm-TFSI, there is a decrease in the intensity of the CH_2, CH_3 stretching and C=O stretching bands, because these functional groups are now less concentrated in the polymer composite, as well as an increase in the bands associated with sulfonation, because of the presence of sulfone functional groups in TFSI.